On the classification of cortical inhibitory neurons

Dissertation

der Mathematisch-Naturwissenschaftlichen Fakultät
der Eberhard Karls Universität Tübingen
zur Erlangung des Grades eines
Doktors der Naturwissenschaften
(Dr. rer. nat.)

vorgelegt von
Felipe Yáñez Lang
aus Santiago, Chile

Tübingen
2024

Gedruckt mit Genehmigung der Mathematisch-Naturwissenschaftlichen Fakultät der Eberhard Karls Universität Tübingen.

Tag der mündlichen Qualifikation:	24.02.2025
Dekan:	Prof. Dr. Thilo Stehle
1. Berichterstatter:	Prof. Dr. Jakob H. Macke
2. Berichterstatter:	Prof. Dr. Marcel Oberländer

To Hana, Mateo, and Ciro

Abstract

The brain's remarkable ability to process ambiguous information and transform it into meaningful behavior is a complex process largely performed by neurons. In computational neuroscience, this integration is investigated utilizing large-scale simulations constrained by realistic networks of excitatory and inhibitory neurons. In the cerebral cortex, inhibitory neurons exhibit high variability in cellular properties such as morphology, electrophysiology, and gene expression profiles. This diversity poses a challenge in terms of their characterization and classification across data modalities. While the major subtype specification of inhibitory neurons is given by their molecular identity, it is unknown whether morphological and electrophysiological properties systematically relate to molecular identity to organize the structure and function underlying cortical networks.

In this dissertation, I present a computational methodology to assess variations in morphological, electrophysiological, and molecular properties across the entire depth of rat barrel cortex. First, I standardize a comprehensive dataset of morphological and electrophysiological properties, and demonstrate that it is representative for the depth distribution of inhibitory neurons in a cortical column. Then, the molecular composition of the entire rat barrel cortex is acquired, and quantified at 50-micron resolution. For each neuron, I calculate a variety of morphological and electrophysiological features. Multimodal clustering is then utilized to assign neurons into subtypes. Cross-validation with several classifiers is applied to identified subtypes, demonstrating their robustness. The proposed methodology outperforms existing approaches, and its interpretable nature allows me to reliably link different cellular properties across cortical depth.

I found that the relative distributions of morphological and electrophysiological properties are similar at any given depth location. At the same time, these distributions systematically shift as a function of cortical depth. Regardless of subtype, the overall axonal and dendritic arborizations, as well as the firing frequency, increase with depth. In contrast, the firing frequency adaptation remains unaffected by depth. Surprisingly, these variations define depth-specific relationships that reveal the molecular identity of inhibitory neurons, which are conserved across species and cortex areas. Thus, simple organizing principles may largely account for the diversity of inhibitory neurons through the adjustment of their morphological and electrophysiological properties to their local environment within cortical circuits, providing novel insight for realistic network modeling.

Kurzfassung

Die bemerkenswerte Fähigkeit des Gehirns, mehrdeutige Informationen zu verarbeiten und in sinnvolles Verhalten umzuwandeln, ist ein komplexer Prozess, der hauptsächlich von Nervenzellen durchgeführt wird. In der Theoretischen Neurowissenschaft wird diese Integration mit Hilfe von groß angelegten Simulationen untersucht, die durch realistische Netzwerke von exzitatorischen und inhibitorischen Nervenzellen eingeschränkt sind. In der Großhirnrinde zeigen inhibitorische Nervenzellen eine hohe Variabilität in zellulären Eigenschaften wie Morphologie, Elektrophysiologie und Genexpressionsprofilen. Diese Vielfalt stellt eine Herausforderung in Bezug auf ihre Charakterisierung und Klassifizierung über verschiedene Datenmodalitäten hinweg dar. Obwohl inhibitorischer Nervenzellen hauptsächlich aufgrund ihrer molekulare Identität klassifiziert werden, ist unbekannt, ob morphologische und elektrophysiologische Eigenschaften systematisch mit der molekularen Identität zusammenhängen, und sodie Struktur und Funktion zugrunde liegender kortikaler Netzwerke organisieren.

In dieser Dissertation stelle ich eine Computermethodik vor, um Variationen in morphologischen, elektrophysiologischen, und molekularen Eigenschaften über die gesamte Tiefe des sogenannten Barrel-Kortex der Ratte zu bewerten. Zunächst standardisiere ich einen umfassenden Datensatz von morphologischen und elektrophysiologischen Eigenschaften und zeige, dass er repräsentativ für die Tiefenverteilung inhibitorischer Nervenzellen in einer kortikalen Säule ist. Anschließend wird die molekulare Zusammensetzung des gesamten Barrel-Kortex der Ratte gewonnen und in einer Auflösung von 50 Mikrometern quantifiziert. Für jede Nervenzelle berechne ich eine Vielzahl von morphologischen und elektrophysiologischen Merkmalen. Anschließend wird ein multimodales Clustering verwendet, um Nervenzellen in Subtypen einzuordnen. Eine Kreuzvalidierung mit mehreren Klassifizierern wird auf die identifizierten Subtypen angewendet, um ihre Robustheit zu demonstrieren. Die vorgeschlagene Methodik übertrifft die bestehenden Ansätze und ihre interpretierbare Natur ermöglicht es mir, verschiedene zelluläre Eigenschaften zuverlässig über die kortikale Tiefe hinweg zu verknüpfen.

Ich fand heraus, dass die relativen Verteilungen von morphologischen und elektrophysiologischen Eigenschaften an jeder gegebenen Tiefenposition ähnlich sind. Gleichzeitig verschieben sich diese Verteilungen systematisch als Funktion der kortikalen Tiefe. Unabhängig vom Subtyp nehmen die gesamten axonalen und dendritischen Verzweigungen sowie die Feuerrate mit der Tiefe zu. Im Gegensatz dazu bleibt

die Feuerratenadaptation von der Tiefe unbeeinflusst. Überraschenderweise definieren diese Variationen tiefenspezifische Beziehungen, die die molekulare Identität inhibitorischer Nervenzellen offenbaren, die über Spezies und Kortexarealen hinweg erhalten bleiben. Daher könnten einfache Organisationsprinzipien größtenteils die Vielfalt inhibitorischer Nervenzellen durch die Anpassung ihrer morphologischen und elektrophysiologischen Eigenschaften an ihre lokale Umgebung innerhalb kortikaler Netzwerke erklären, was neue Einblicke in die realistische Netzwerkmodellierung liefert.

Acknowledgments

Simplicity is about subtracting the obvious, and adding the meaningful (Maeda, 2006, Law 10). Neurobiological systems seem mysteriously complex, making the pursuit of simplicity a beautiful endeavor. First, I would like to thank my adviser, Prof. Dr. Marcel Oberlaender, who introduced me to all that is known about the brain. Thank you, Marcel, for your patience and support. But primarily for encouraging me to take risks with the aim of understanding, "just do your magic" was always a sign that I was going in the right direction.

My thesis advisory committee also included Prof. Dr. Jakob H. Macke and Prof. Dr. Dirk Feldmeyer. I am grateful for the time you dedicated examining my work. Your thoughtful feedback helped shaping the results presented in this dissertation. Jakob, your insightful comment about thinking in terms of probability distributions was key early on, many thanks. Dirk, you taught me how diversity looks in practice. I appreciate your support regarding the raw data, and for allowing me to install my classification tools in your lab.

I am also thankful to Egger *et al.* (2015); Helmstaedter *et al.* (2009a,b,c); Koelbl *et al.* (2015); Emmenegger *et al.* (2018); Arzt *et al.* (2018); Meyer *et al.* (2013); Egger *et al.* (2014); Udvary (2020); Udvary *et al.* (2022) whose raw data I used. Your hard work served as the foundation of mine. Dr. Guanxiao Qi, I appreciate your feedback on my SfN abstracts, your diligence in fixing ASCII files, and your kindness when I visited the lab in Jülich. Prof. Dr. Bert Sakmann, when I was starting my PhD, at a Max Planck-Hebrew University meeting in Frankfurt, you asked me what I was planning to do with those interneurons. I hope that this dissertation provides a better answer than I did then.

When I joined the MPI-NB, I shared the office with Dr. Rajeevan Therpurakal Narayanan and Dr. Daniel Udvary. Then, I moved with Dr. Fernando Messore into the interneuron office. Rajeev, you taught me so many things about living organisms. I appreciate your advice and friendship. Daniel, I admire your courage to tackle difficult problems without hesitation. Thank you for all your help with respect to inhibitory neurons. Fer, our conversations about natural versus artificial intelligence were most useful to frame my work. We had so much fun together, from our daily coffee breaks to sneaking into legendary events at SfN.

The "In Silico Brain Sciences" group is just great. The friendly and collaborative atmosphere that has been created over the years is truly remarkable. Many thanks to its current members in alphabetical order: Aman, Arco, Bjorge, Chantal, Rieke, María, Matt, Michelle, and Su. Aman, thank you for leading the lab and taking care of all the bits and pieces that make our time together as a group a great experience. Fiorella Gómez, even though you already left the lab, I want to highlight all the fun moments we had together, especially the coffee breaks. I will never forget your FELASA training! Thank you. Philipp Harth, you are an honorary member of the lab. Many thanks for the collaborative efforts over the years.

I had the pleasure of meeting Bettina Bosse, Dr. Corinna Bernsdorff, and Omar Valerio Minero at the MPI-NB. Bettina, I cannot describe the appreciation I have for the support you provided me during all these years. You are extremely efficient! I enjoyed talking with you, whether about work or learning about your vacations in France. You always made me smile. Corinna, thanks for the IT support. I remember deeply your love for Chile. Talking with you, or actually singing in Spanish with you, was very fun. Omar, many thanks for your friendship, teaching me about HPC, and leading the Spanish-speaking community at the MPI-NB. Thanks also to Sara Sorce and Dr. Leila Masri at the IMPRS-IS, who provided effective administrative support every time I needed it. I also appreciate you letting me coordinate the lightning talks at the IMPRS-IS Boot Camp after the pandemic; I really enjoyed it. Dr. Nima Dehghani, I am truly grateful for your patience and thoughtful advice, which I take very seriously. I am sincerely honored that the Kavli Foundation has trusted my vision and decided to support my next research project.

I am grateful to my parents, Luis y Paulina, who gave me the gift of being free. This freedom has allowed me to pursue my dreams. Approaching life from the perspective of an artist has been a treasure. Daniel, Vicky, Benja, María, and Bea: *gracias por todo, los quiero sogans*. I would also like to deeply thank my extended family in Chile, Czechia, Italy, US, and Canada, who provided me with love and support from a distance. Thanks to my friends in Santiago and Paris – you are all so accomplished and make me incredibly proud! Héctor, you are a true champion. Thanks for teaching me the importance of training the mind. In Frankfurt and Bonn, I was lucky to meet wonderful people who made my time unforgettable with countless fun memories. Special thanks to the Bonn Rugby Union Club, where I discovered the enriching experience of coaching the next generations. My deepest admiration to the ones that are no longer with us and that I remember with joy: Oldřich, *babi*, *abuelos*, *tía Silvia*, and *Chol*. My heartfelt gratitude to each and every one of you for your affection and encouragement.

The most important support came from my family, to whom I am forever grateful. Hana, you have always been there for me, from dancing until dawn in Ibiza to being next to me as I write these words. I admire your independence and generosity. These years by your side have been the most beautiful years of my life. *Děkuji.* Mateo, you are so passionate. From an early age, you have demonstrated character, which I greatly admire. Your thoroughness is present in everything you do, from learning to code to playing rugby. Ciro, you are so creative. You radiate beautiful emotions in whatever you decide to pursue, whether it is playing the violin or curating your diverse collection of rocks. I truly admire your empathy towards others. *Niños*, thank you for your interest in trying to understand what I do, from learning to knit and crochet interneuron sculptures, to drawing brains in my office. I can only hope that my work meets your standards, *los amo.*

Contents

List of Figures

List of Tables

Chapter 1

Introduction

One of the most impressive features of our central nervous system is its capacity to process noisy and ambiguous information, reliably transforming it into intended behaviors. Within the central nervous system, the brain's primary role is to process sensory information, control motor functions, and enable cognition and emotion. Just trying to understand how the brain represents sensory information has been and remains an enduring challenge. Pioneering work by Golgi (1885, 1903) and Ramón y Cajal (1899, 1903, 1909) focused on the anatomical organization of the brain's constituting parts, the neurons. Figure 1.1 illustrates hand drawings of human neurons in the cerebral cortex by Ramón y Cajal. These neurons were stained with the Golgi method and then placed under a microscope to be meticulously depicted. Neurons with diverse morphological characteristics were already observed in these drawings. For instance, small to large pyramidal neurons and non pyramidal short-axon neurons, currently referred as interneurons.

The focus on neuronal morphology has been and still is a common theme to better understand signal processing in the brain (Gouwens *et al.*, 2020; Scorcioni *et al.*, 2008). The interest arises from the complexity of individual neurons (Oberlaender, 2019). Besides the cell body, referred as soma, neurons have axonal and dendritic arborizations. Signals coming from thousands of synaptically connected neurons are sensed by either the soma or dendrites. Then, the neuron non-linearly integrates those inputs depending on its intrinsic properties. Finally, the output signal is projected to a large number of synaptically connected neurons across the brain. Naturally, multidisciplinary efforts have emerged in order to characterize other cellular modalities such as intrinsic physiology, gene expression profiles, connectivity patterns, and developmental history (Huang and Paul, 2019).

The rapid pace of technological development, combined with high throughput computing infrastructures, has resulted in large-scale multimodal databases. Extracting biological insight from them is challenging, because it demands technical (i.e., computer science) and domain-specific (i.e., neurobiology) expertise. The aim of this dissertation is to synthesize complex patterns of variation from large-scale multimodal data to a simple framework of neuronal organization, utilizing elements from applied mathematics, signal processing, and machine learning.

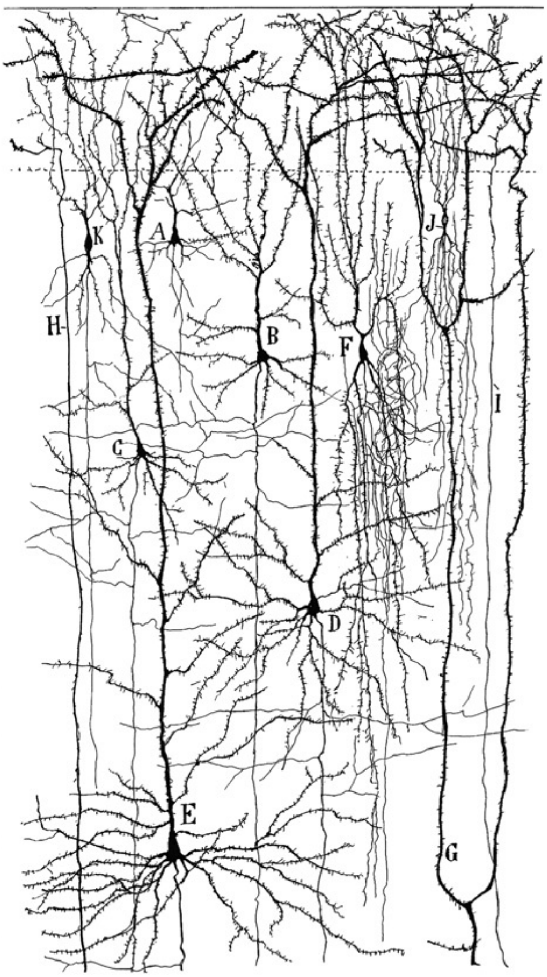

Figure 1.1: Hand drawings of human neurons in the cerebral cortex. Neurons with diverse morphology are presented, such as pyramidal (A to E) and non pyramidal (F, J, and K) neurons. Afferent and collateral fibers coming from the white matter are also outlined (G, H, and I). Adapted from Ramón y Cajal (1899).

1.1 *In silico* Brain Sciences

The complementarity between structure and function is a fundamental principle of biology (Swanson and Lichtman, 2016). Assessing it holistically is a daunting endeavor because one needs access to large amounts of high-dimensional multimodal data in the living brain. An effective alternative is to take advantage of the cytoarchitecture of the cortex (Brodmann, 1909) and utilize partial empirical observations to reconstruct an elementary processing unit of the brain, the cortical column (Sakmann, 2017). By systematically integrating the morphology (Oberlaender, 2019) and physiology (Sakmann, 1992) of different neurons as a function of cortical depth, a path towards better understanding how the cortex integrates sensory information is now available (Oberlaender, 2023). In contrast to experimental preparations *in vitro* (i.e., within the glass) and *in vivo* (i.e., within the living), *in silico* corresponds to experimental procedures performed via computer simulation, allowing a flexible and efficient exploration of signal flow in cortical circuits.

Figure 1.2 illustrates an *in silico* approach to systematically assess the relationships of the structure and function. The acquisition of *in vivo* recordings from identified neurons (Oberlaender *et al.*, 2012; Narayanan *et al.*, 2015; Egger *et al.*, 2015) provides the foundation to mechanistically investigate anatomical and physiological principles. The integration of different sources of data such as the cortical geometry (Egger *et al.*, 2012), cellular composition (Meyer *et al.*, 2013, 2010; Oberlaender *et al.*, 2009), and morphology of excitatory neurons (Narayanan *et al.*, 2015; Oberlaender *et al.*, 2012, 2011) defines a realistic cortical neuronal network (Udvary *et al.*, 2022; Egger *et al.*, 2014). Multiscale models of neuronal computation informed by realistic structural constraints generate plausible functional responses (Landau *et al.*, 2016; Bast and Oberlaender, 2022; Bast *et al.*, 2023). By comparing them with the actual physiology, mechanistic *in silico* predictions can be formulated and subsequently tested in the living brain (Egger *et al.*, 2020; Bast *et al.*, 2023).

Information processing in the brain combines excitatory and inhibitory neurons. The role of excitatory neurons is to transmit signals to other synaptically connected neurons (Narayanan *et al.*, 2017), whereas the role of inhibitory neurons is to modulate those transmitted signals (Feldmeyer *et al.*, 2018). The approach presented in Figure 1.2 primarily focused on excitatory neurons. Although some inhibitory neurons are currently present in the realistic neuronal network (Egger *et al.*, 2015; Helmstaedter *et al.*, 2009a,b,c; Koelbl *et al.*, 2015; Arzt *et al.*, 2018), a systematic assessment is still lacking. In order to enable experimentation involving inhibitory neurons, I integrate a large representative sample of neuronal morphologies, define robust multimodal class assignments based on well-established descriptive features, curate a morphological and electrophysiological assessment by a group of expert neuroscientists, provide the molecular composition of the rat barrel cortex, and propose a framework to better understand the diversity of inhibitory neurons.

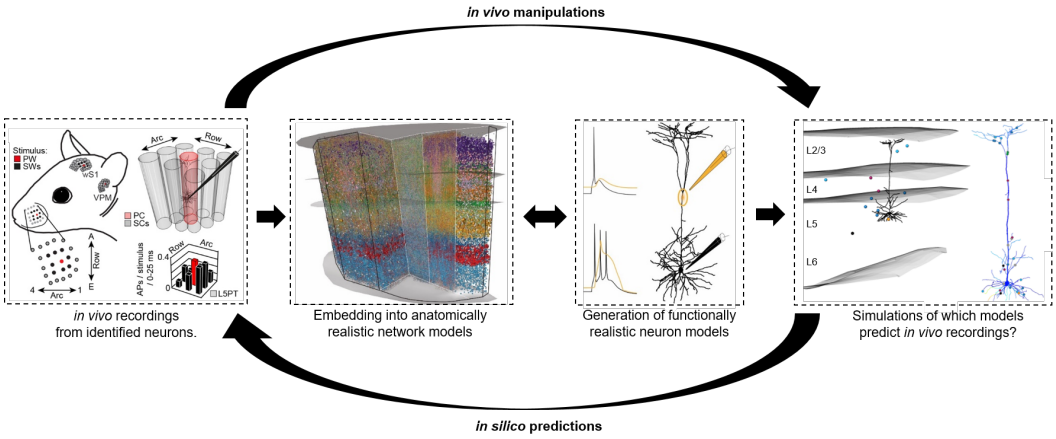

Figure 1.2: *In silico* approach to systematically link the structure and function. The acquisition of empirical measurements provides the foundation to investigate anatomical and physiological principles. The precise integration of different sources of data defines a realistic cortical neuronal network. Multiscale models of neuronal computation informed by realistic structural constraints generate plausible functional responses. By comparing them with the actual physiology, mechanistic *in silico* predictions can be formulated and subsequently tested in the living brain. Adapted from Egger *et al.* (2020); Udvary *et al.* (2022); Bast and Oberlaender (2022). Courtesy of Prof. Dr. Marcel Oberlaender.

1.2 Structure of the dissertation

This dissertation comprises 10 chapters. Following Chapter 1, Chapter 2, provides a concise background on the main concepts and ideas from the fields of Neurobiology, Computer Science, and Engineering that will be utilized in the following chapters.

Chapters 3 through 6 are pure methodological chapters. Chapter 3 (entitled: "Generation of a representative dataset") provides the technical details to generate a comprehensive dataset of morphological and electrophysiological properties of inhibitory neurons across all layers of rat barrel cortex. The dataset comprises 306 neurons, registered into a standardized 3D reference frame at a resolution of 50 µm (Egger *et al.*, 2012). Based on their registered soma depth, 9 neurons were located in L1, 53 in L2/3, 99 in L4, 74 in L5, and 71 in L6. The overall neuron number corresponded to $13.4 \pm 1.6\%$ (mean $\pm$ 95% CI) of the absolute number in an average column (Meyer *et al.*, 2013). The depth-distribution of somata was indistinguishable from the average soma density (Meyer *et al.*, 2013).

Chapter 4 (entitled: "Single-cell characterization") focuses on the characterization of both the registered axonal and dendritic morphology, and electrophysiological responses. For each inhibitory neuron, a total of 88 well-established features were extracted, 47 morphological and 31 electrophysiological. By adopting a similar characterization approach as in previous studies on mouse visual cortex (Gouwens *et al.*, 2019, 2020), analyses that will be proposed later in this dissertation can be readily extended across species and cortex areas.

Chapter 5 (entitled: "Multimodal class assignments") describes human and machine methodologies to group inhibitory neurons. Multimodal clustering based on previously defined features from a representative cortical column was utilized to capture the complexity and diversity of morphological and electrophysiological properties. As a result, inhibitory neurons were assigned to robust classes, 20 morphological (m-types), 13 electrophysiological (e-types), and 25 morphoelectric (me-types). A consensus of human experts, grouped the morphology and electrophysiology of these neurons into broader categories. The overall classification of both methods was in moderate agreement, indicating that they captured different but complementary aspects of inhibitory neuron diversity. The classification analysis allowed the identification of robust e-, m-, and me-types consistent with those reported for mouse visual cortex (Gouwens *et al.*, 2019, 2020).

Chapter 6 (entitled: "Molecular composition of barrel cortex") covers the methodology and quantification of the 3D distribution of the most predominant molecular markers for inhibitory neurons, namely parvalbumin (Pvalb), somatostatin (Sst), and vasoactive intestinal polypeptide (Vip). To validate the accuracy of this quantification methodology, the overall 3D distribution of inhibitory neurons was compared against a comprehensive previously reported study (Meyer *et al.*, 2013), obtaining remarkable correspondence. The distributions of Pvalb+, Sst+, and Vip+

neurons were heterogeneous across layers and barrel columns.

Chapters 7 and 8 provide the neurobiological results to build a new framework of neuronal organization. Chapter 7 (entitled: "Depth-dependent gradients of morphoelectric properties") presents the investigation of the role of different morphological and electrophysiological properties in inhibitory neuron diversity. Interestingly, some morphological features, such as the axon and dendrite vertical extent, increased with cortical depth, regardless of me-type. With regard to electrophysiological features, two well-established features such as the spike-frequency and the spike-frequency adaptation displayed smooth depth-dependent gradients. The former increased with cortical depth, while the latter was independent of it. Remarkable similarities were obtained when analyzing mouse visual cortex (Gouwens *et al.*, 2019, 2020), indicating that depth-dependent gradients of morphological and electrophysiological properties are conserved across species and cortex areas.

Chapter 8 (entitled: "The organizing principles") argues whether morphoelectric properties systematically relate to molecular identity to organize the structure underlying cortical circuits. A systematic assessment of the degree and character of the variability in morphoelectric properties across the entire depth of rat barrel and mouse visual cortices is performed. The variability has a particular structure that allows the definition of relationships that reveal the molecular identity of inhibitory neurons based on their respective morphoelectric properties. These relationships are conserved across layers, species, and cortex areas. Thus, simple organizing principles may largely account for the diversity of inhibitory neurons in cortex.

Chapter 9 discusses previous studies on cortical inhibitory neuron diversity, challenges and opportunities of reanalyzing previously published data, the impact of well-constrained inhibition, how to predict *in vivo* subtypes with missing information, homologies and divergences of inhibitory neurons across species, and closes with the question "are inhibitory neurons adjusting their cellular properties to local cortical circuits?" Chapter 10 provides the concluding remarks to the dissertation.

Chapter 2

Background

Complex patterns of variation emerge from the study of multimodal properties of neurons (Narayanan *et al.*, 2017; Kepecs and Fishell, 2014; Markram *et al.*, 2004). To synthesize them into a simple framework of neuronal organization, a multidisciplinary approach is required. This chapter comprises domain-specific elements from the field of neurobiology and a concise description of the mathematical and computational strategies utilized throughout the dissertation.

2.1 The somatosensory cortex

The selection of an appropriate model system to cast a particular question is paramount. Rodents have been widely utilized in neuroscience research to better understand the mechanisms by which the brain learns and refines different behaviors. In particular, the vibrissal part of the rat primary somatosensory cortex, also known as barrel cortex or vS1, comprises a wealth of anatomical and functional data, positioning it as the ideal model system to study diverse structural properties of neurons and their organization. For instance, Figure 2.1A illustrates the known pathway from deflecting a mystacial or facial whisker until reaching the barrel cortex. An interesting property of this cortical area is its somatotopic organization (Figure 2.1B). This means that each whisker on the rat's snout is mirrored in the barrel cortex (see how C2 is highlighted in panels A and B).

Furthermore, it known that the distribution of neurons throughout the entire depth of the barrel cortex is not stereotypic, but specific for each whisker (Meyer *et al.*, 2013). Figure 2.1C shows a semicoronal view of all neuron somata along the vertical column axis for columns in arc-2, namely A2, B2, C2, D2, and E2. Their precise location was obtained by reconstructing anatomical landmarks such as the pial surface, the white matter (WM) tract, and cytoarchitectonic layer borders (Oberlaender *et al.*, 2012). Striking differences can be found between excitatory and inhibitory neurons, when comparing a 2D average projection of the 3D neuron density (Figure 2.1D). For instance, for excitatory neurons, the L4 barrels are clearly visible as isolated high density regions (Meyer *et al.*, 2010). In contrast, for inhibitory neurons the distinction between barrels and septa is not evident.

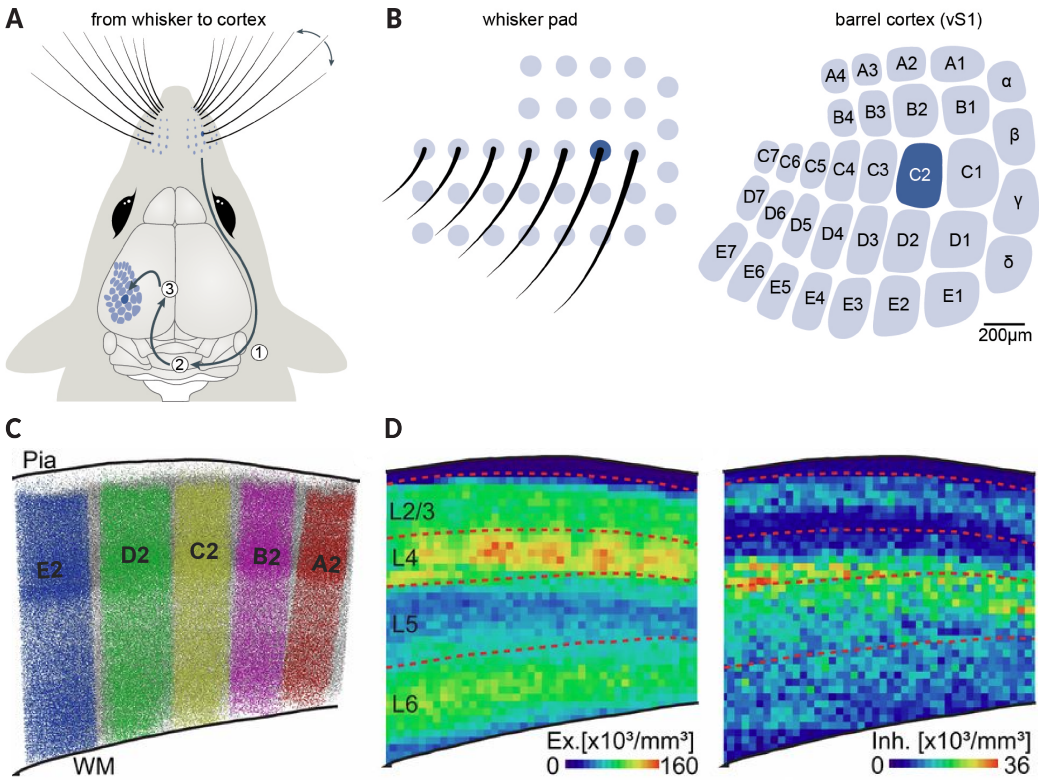

Figure 2.1: Organization of the vibrissal part of the primary somatosensory cortex. A. Signal evoked by the deflection of a facial whisker is relayed via the brain stem (1) to the thalamus (2) and then to the vibrissal part of the primary somatosensory cortex (3). B. The spatial arrangement of the whisker follicles at the rat's snout is conserved as anatomical structures termed "barrels" in layer 4. Barrels and whiskers are arranged into rows A to E and numbered arcs. C. Semicoronal view of all neuron somata along the vertical column axis for columns in arc-2. D. A 2D average projection of the 3D excitatory (left) and inhibitory (right) neuron density. Adapted from Petersen (2019); Udvary (2020); Meyer *et al.* (2013).

However, their distribution across layers is inhomogeneous, reminiscent of the "hot zones" of inhibition observed in L2 and L5A (Meyer *et al.*, 2011).

2.2 Diversity of cortical inhibitory neurons

Cortical inhibitory neurons correspond to less than 15% of the total number of cortical neurons (Meyer *et al.*, 2013; Feldmeyer *et al.*, 2018). Despite their low relative abundance in cortex, they have been consistently reported as a rich and diverse class of neurons (Fishell and Kepecs, 2020; Huang and Paul, 2019; Feldmeyer *et al.*, 2018; Tremblay *et al.*, 2016; Kepecs and Fishell, 2014; Ascoli *et al.*, 2008; Markram *et al.*, 2004; Gupta *et al.*, 2000). At the cellular level, attributes such as morphology, intrinsic physiology, gene expression profiles, connectivity patterns, and developmental history display high variability (Huang and Paul, 2019).

2.2.1 Morphology

The axonal and dentritic arborizations of inhibitory neurons may be remarkably different. Figure 2.2A illustrates the morphological reconstructions of axons (lighter shades) and dendrites (darkest shades) for each subtype (Gouwens *et al.*, 2019). Different morphological types can be observed across cortical layers, such as small and large basket cells (Kubota *et al.*, 1994; Kawaguchi and Kubota, 1997), chandelier cells (Szentágothai and Arbib, 1974; Somogyi, 1977; Somogyi *et al.*, 1982), bipolar and bitufted cells (Bayraktar *et al.*, 2000; Prönneke *et al.*, 2015), Martinotti cells (Martinotti, 1889), and neurogliaform cells (Tamás *et al.*, 2003), among others that seem less apparent.

2.2.2 Intrinsic physiology

The intrinsic properties of a cell are tightly related to how input signals are integrated. This integration is not unique in the inhibitory population. In Figure 2.2A, fast and non-fast spiking neurons are easily observed. Some of those neurons may also have regular or irregular spiking patterns, be adapting or non-adapting, with or without intrinsic burst firing, with or without stuttering discharge, among other properties (Ascoli *et al.*, 2008; DeFelipe *et al.*, 2013).

2.2.3 Gene expression profiles

Single-cell transcriptomics provides access to detailed genetic information that translates into approximately 60 different transcriptomic types for inhibitory neurons (Tasic *et al.*, 2016; Fishell and Kepecs, 2020; Yuste *et al.*, 2020; Mao and Staiger, 2024). Figure 2.2A shows that the major subtype specification of inhibitory

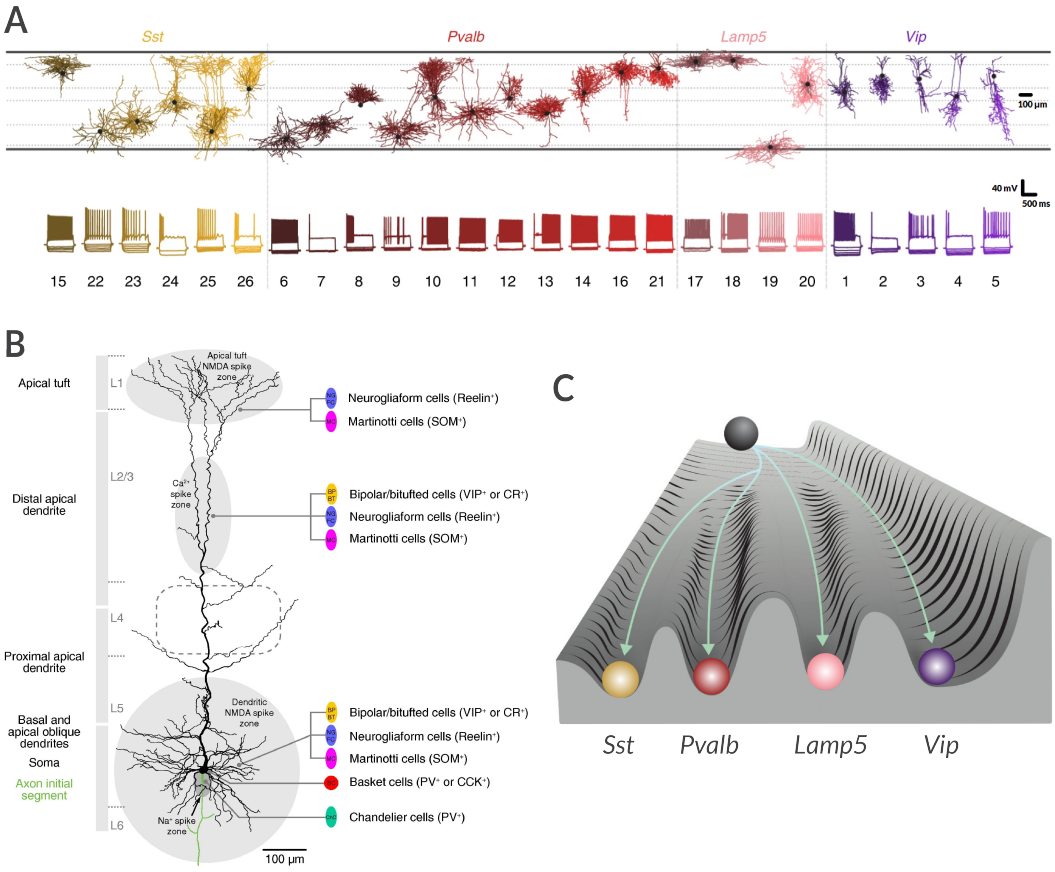

Figure 2.2: Diversity of cortical inhibitory neurons. A. Representative neurons from each transcriptomic-validated morphoelectric class. B. Subcellular organization of GABAergic synapses from several inhibitory subtypes onto a pyramidal neuron. C. Diagram showing the landscape of development as the energy function of an attractor gene regulatory network. Adapted from Gouwens *et al.* (2019); Feldmeyer *et al.* (2018); Fishell and Kepecs (2020). Further details can be found in text.

neurons is their molecular identity. Primarily, parvalbumin (Pvalb), somatostatin (Sst), vasoactive intestinal polypeptide (Vip), and lysosomal-associated membrane protein family member 5 (Lamp5). It is worth noting that others such as synuclein gamma (Sncg) are also being considered (Gouwens *et al.*, 2020; Zeng, 2022).

2.2.4 Connectivity patterns

Cortical output is mainly produced by pyramidal neurons, thus, it is important to understand what input patterns inhibitory neurons provide. Figure 2.2B illustrates the soma and dendrite of a L5 pyramidal neuron, where different inhibitory neuron subtypes target different compartments, such as soma, basal dendrites, or apical tuft dendrites. Inhibitory neurons have high wiring specificity. For instance, it is known that chandelier cells target the axon initial segment, or a specific type of basket cell exclusively targets other basket cells.

2.2.5 Developmental history

Inhibitory neurons originate from the medial and caudal ganglionic eminence (MGE and CGE). In MGE, Pvalb+ and Sst+ neurons are born, whereas in CGE, Vip+, Lamp5+ and Sncg+ neurons are born (Tasic *et al.*, 2018). They then disperse, independent of origin, throughout the brain to populate distinct structures, including cortex (Fishell and Kepecs, 2020; Hu *et al.*, 2017; Kepecs and Fishell, 2014). Remarkably, they integrate into cortical circuits following the arrival of excitatory neurons (Kwan *et al.*, 2012). Figure 2.2C illustrates how transcriptional networks can influence and even change the identity of inhibitory neurons after birth. This sequential and stochastic integration is a fundamental process in the development and organization of cortical circuits (Pouchelon *et al.*, 2021; Fishell and Kepecs, 2020; Kwan *et al.*, 2012).

2.3 Definition of cell types

The function of a neuron depends on the inputs to their soma or dendrites, intrinsic properties that integrate those inputs, and their axon that projects the output signal to local and distant neuron populations. Cell typing is an attempt to relate cellular attributes to functional properties in a cortical circuit. It is known that for excitatory neurons, this relationship holds true. For instance, Takahashi *et al.* (2020) show that pyramidal and intratelencephalic neuron populations (i.e., neurons with different axon and dendrite morphology) have distinct roles during a perceptual detection task. Thus, then the question is whether cell typing is also an effective approach for inhibitory neurons, given their cellular diversity (Zeng, 2022; Huang and Paul, 2019; Hardcastle *et al.*, 2017).

2.3.1 Consensus of experts

On the one hand, cell type definition by consensus of expert neuroscientists has produced ambiguous and sometimes arbitrary results (DeFelipe *et al.*, 2013), agreeing on well-established subtypes such as chandelier and Martinotti cells, but not reaching a clear consensus on the remaining subtypes such as basket cells. However, their classification grouped neurons into broad categories that have been reported to link to particular molecular identities (Fishell and Rudy, 2011; Kepecs and Fishell, 2014; Tremblay *et al.*, 2016). This assessment served as a starting point towards a generalized classification of inhibitory neurons.

2.3.2 Multimodal clustering

On the other hand, statistical methods based on descriptive features of cellular properties introduce an objective criteria to define classes. Furthermore, with the continuous advancement in the collection of large-scale datasets, scalable clustering methods across data modalities become a reliable option. Gouwens *et al.* (2019) proposed to simultaneously cluster the morphology and electrophysiology of inhibitory neurons utilizing a consensus of hierarchical, spectral, and Gaussian mixture model clustering with multiple parameter settings. The number of classes produced by this type of method is higher compared to human assessments. This is because they are designed to find boundaries in the data to define homogeneous groups. Thus, subtle perturbations to descriptive features or the addition of new neurons may change the overall number of classes (Gouwens *et al.*, 2020). Incorporating a new data modality can also increase the overall number of classes. Interestingly, different data modalities may group neurons similarly, allowing the identification of relationships between cellular properties. It is important to keep in mind that clustering cellular properties is an important step in defining inhibitory cell types, but it is not the only one. For instance, it is hypothesized that some aspects of specialized cortical circuits may be shaped by evolution (Hardcastle *et al.*, 2017), indicating that the observed data can be modulated by a yet unknown process. Thus, focusing on shared properties or relationships between classes could contribute to a better understanding of the diversity of inhibitory neurons.

2.3.3 Robustness

The predictability of class assignments from descriptive features provides an evaluation of the robustness of the underlying clustering results. A good compromise between bias and variance is obtained with 5-fold cross-validation. A 5-fold cross-validation means that the neurons characterized by descriptive features are split into 5 consecutive folds, with 80% of the data used for training a given classifier and the remaining 20% to test its accuracy. The resulting accuracy score reflects

how well a particular model structure can explain the relations between descriptive features and class assignments. This aspect is particularly important, as the focus of this dissertation is on finding shared properties across class assignments, rather than dissecting them even further. The evaluation may be performed across several classifiers, such as multilayer perceptrons, random forests, support vector machines, Gaussian processes, k-nearest neighbors, naive Bayes', and decision trees, among others. Different but complementary aspects of the representation of the data can be obtained when utilizing classifiers that are structurally very different.

2.4 Generation of realistic neuronal networks

In order to generate a large-scale dataset comprising realistic neuronal networks (Udvary *et al.*, 2022; Egger *et al.*, 2014), one can employ different strategies to collect the underlying "raw material." For instance, one aim might be to capture the diversity of reported inhibitory types, versus another one to produce a representative sample. Both approaches have benefits and compromises.

2.4.1 Homogeneous versus inhomogeneous scaling

The selected strategy has implications in the interpretation and generalization of downstream analyses. For instance, Markram *et al.* (2015) aimed at capturing the entire diversity of reported morphological and electrophysiological subtypes. The associated benefit is the unprecedented amount of detail that this effort provides. The associated cost is the inhomogeneous compensation of each subtype's relative abundance across layers. In contrast, Narayanan *et al.* (2015) aimed at capturing a representative random sample of excitatory neurons. The associated benefits are avoiding an over- and/or under-representation of subtypes, and extrapolating the results to larger structures by a homogeneous compensation across layers. The associated cost is not capturing all reported neuronal diversity.

2.5 Generalization via cross-area and cross-species validation

Due to the complexity of assessing cortical circuits, it is common that studies try focus on a single cortical layer, cortex area, or species. This makes it difficult to derive general mechanistic principles underlying cortical circuits. By extending the same analysis to a different cortical layer, cortex area, or species, it is possible to evaluate the out-of-distribution generalization of the underlying findings. This allows us to distinguish between specific and general observations (Hardcastle *et al.*, 2017), and to better constrain the organization of cortical circuits.

Chapter 3

Generation of a representative dataset

In collaboration with the laboratories of Prof. Dr. Bert Sakmann (Max Planck Institute for Biological Intelligence) and Prof. Dr. Dirk Feldmeyer (Research Center Jülich and RWTH Aachen University), we created a comprehensive dataset of morphological and electrophysiological properties of inhibitory neurons across all layers of rat barrel cortex. I analyzed the dendritic and axonal morphology, as well as spiking responses to somatic current injections for 306 inhibitory neurons from this collaborative project. I registered each neuron into a standardized 3D reference frame of rat barrel cortex at a resolution of 50 µm (Egger *et al.*, 2012), which allowed me to determine that 9 neurons were located in L1, 53 in L2/3, 99 in L4, 74 in L5, and 71 in L6. For each neuron, the voltage trace with an initial interspike interval closest to 100 Hz was selected for analysis (Beierlein *et al.*, 2003; Helmstaedter *et al.*, 2009b; Arzt *et al.*, 2018). This dataset comprised diverse morphoelectric properties of inhibitory neurons, ranging from neurons with small basket-like morphologies and fast-spiking firing patterns to neurons with Martinotti-like morphologies and non-fast-spiking firing patterns. The overall number of inhibitory neurons in this dataset corresponded to $13.4 \pm 1.6\%$ (mean $\pm$ 95% CI) of the absolute number in an average column of rat barrel cortex (Meyer *et al.*, 2013). The distribution of somata in this dataset was consistent with the soma density of an average column (Meyer *et al.*, 2013). Thus, this comprehensive dataset of morphological and electrophysiological properties was representative for the depth distribution of inhibitory neurons at 50 µm resolution bins.

The most important methodological results from Chapter 3 are:

- The standardization of morphology by registering 306 reconstructions at a resolution of 50 µm in a cortical column of rat barrel cortex.
- The standardization of electrophysiology by defining a common stimulus protocol across 100 Hz voltage traces.
- The representativeness of this dataset for the depth distribution of inhibitory neurons in an average column of rat barrel cortex.

3.1 Data sources

In order to create the dataset, I used 222 inhibitory neurons that were previously reported (Egger *et al.*, 2015; Helmstaedter *et al.*, 2009a,b,c; Koelbl *et al.*, 2015; Emmenegger *et al.*, 2018; Arzt *et al.*, 2018), along with an additional 84 inhibitory neurons provided by collaborators, namely the laboratories of Prof. Dr. Bert Sakmann and Prof. Dr. Dirk Feldmeyer, referred herein as new data.

Table 3.1 provides an overview of the available neuron number per data modality and study. The studies by Egger *et al.* (2015), Emmenegger *et al.* (2018), and Arzt *et al.* (2018) contained complete morphological and electrophysiological properties, including soma, axon, dendrite, and voltage traces. In the studies by Helmstaedter *et al.* (2009a,b,c), three dendritic reconstructions and one recording were not available from the original publications. For instance, a missing dendrite corresponded to a chandelier neuron, as illustrated in (Helmstaedter *et al.*, 2009a, Figure 5A). In the study by Koelbl *et al.* (2015), a dendrite was unintentionally merged with another neuron in the raw file, and recovery was not possible. From the new data contributed by collaborators, two experiments conducted in superficial L5 in early 2011 provided complete morphological reconstructions but lacked the corresponding recordings. Aggregating all the available data, there were 302 inhibitory neurons with complete morphology (i.e., axon and dendrites), and 303 with electrophysiology (i.e., at least one recording), and 299 with both morphology and electrophysiology (see Table 3.1 for details).

All experiments to acquire inhibitory neurons for this dataset were either (i) performed in accordance with the animal welfare guidelines of the Max Planck Society, (ii) performed in accordance with the guidelines of the Federation of European Laboratory Animal Science Association (FELASA), with the EU Directive 2010/63/EU, and with the German animal welfare act, and were approved by the *Northrhine-Westphalian Landesamt für Natur- und Verbraucherschutz* (LANUV), or (iii) approved by the Institutional Animal Care and Use Committee of the Max Planck Florida Institute for Neuroscience.

3.2 Standardization of morphology

For the purpose of acquiring neuron morphologies across all layers of rat barrel cortex, Egger *et al.* (2015), Helmstaedter *et al.* (2009a,b,c), Koelbl *et al.* (2015), Emmenegger *et al.* (2018), and Arzt *et al.* (2018) used male and female Wistar rats aged 17-35 days (P17-P35, m/f, Charles River Laboratories). After deep anesthetization and decapitation, the tissue was sliced at slow speed and high vibration frequency into either 100 µm thick tangential (Egger *et al.*, 2015), 300 µm thick semi-coronal (Land and Kandler, 2002), or 350 µm thick thalamocortical (Agmon

Study	Axon	Dendrite	Recording	Combined
Egger *et al.* (2015)	10	10	10	10
Helmstaedter *et al.* (2009a,b,c)	51	48	50	47
Koelbl *et al.* (2015)	45	44	45	44
Emmenegger *et al.* (2018)	48	48	48	48
Arzt *et al.* (2018)	68	68	68	68
New data	84	84	82	82
Total	306	302	303	299

Table 3.1: Data sources comprising the comprehensive dataset of inhibitory neurons. The dataset integrates 306 inhibitory neurons from previously reported studies and contributions by collaborators.

and Connors, 1991) slices of the vibrissal area of somatosensory cortex using a vibrating microslicer (DTK-1000, Dosaka, Kyoto, Japan or Slicer HR-2; Sigmann Elektronik, Hüffenhardt, Germany).

Neurons were visualized using an upright microscope (Zeiss, Göttingen, Germany or Olympus, Hamburg, Germany), and overview images of the barrels, pial surface and white matter (WM) were taken for subsequent analysis under bright field illumination at low magnification. Barrels in layer 4 are characterized by their appearance as light, hollow, barrel-like structures with narrow dark stripes in between (Feldmeyer *et al.*, 1999). To distinguish inhibitory from excitatory neuron types, inhibitory neurons were identified by their lack of apical dendrites (Helmstaedter *et al.*, 2009b) and dendritic spines (Marx and Feldmeyer, 2013). In layer 4, non-pyramidal excitatory neurons (i.e., spiny stellates) were identified and, therefore, excluded based on their wide action potential (AP) half-width and regular AP firing pattern (Connors *et al.*, 1982; Connors and Gutnick, 1990). Consequently, slices were treated with avidin–biotinylated horseradish peroxidase (ABC-Elite, Camon, Wiesbaden, Germany or Vectastain Elite ABC Kit, Vector Laboratories, Newark, CA, USA) solution and then biocytin-filled neurons with distinct axonal and dendritic branches were identified using the chromogen 3,3-diaminobenzidine tetrahydrochloride (DAB) (Horikawa and Armstrong, 1988). After that, slices were mounted, embedded using Mowiol (Hoechst AG, Frankfurt, Germany) or Eukitt (ORSAtec GmbH, Bobingen, Germany) medium, and enclosed with a coverslip.

Neurons were reconstructed manually using Neurolucida software (MBF Bioscience, Williston, VT, USA) attached to an Olympus BX50/51 or a Zeiss Axioplan microscope, equipped with a 100× oil immersion objective. To enhance contrast across different layers, the condenser aperture diaphragm was closed, which facilitated displaying the density and the size of the soma. The soma was traced in its largest 2D diameter. When axodendritic tracings were completed, the outlines of anatomical structures such as pial surface, barrels, and WM were traced. Each reconstruction was rotated so that the pial surface above the recorded neuron was aligned horizontally.

For instance, Figure 3.1 presents an example of the raw morphological data I was processing. The underlying inhibitory neuron was reconstructed in 3D from a 350 µm thick oblique coronal slice and included the soma (cell body in red), dendites (branches in red), and axon (branches in blue). The center of mass of the soma was located at 1532 µm from the pial surface and 454 µm from the white matter tract. Besides the neuronal reconstruction, several anatomical layouts were provided. In this case, the laminar location corresponded to superficial L6 or L6A, where the thickness of L6A was 328 µm. Similarly, three barrel contours were delineated. The central barrel corresponded to the home barrel where the soma was located and the other two (left and right) corresponded to adjacent barrels. The thickness of L4, the granular layer, was 190 µm. All other layer borders, and additional information

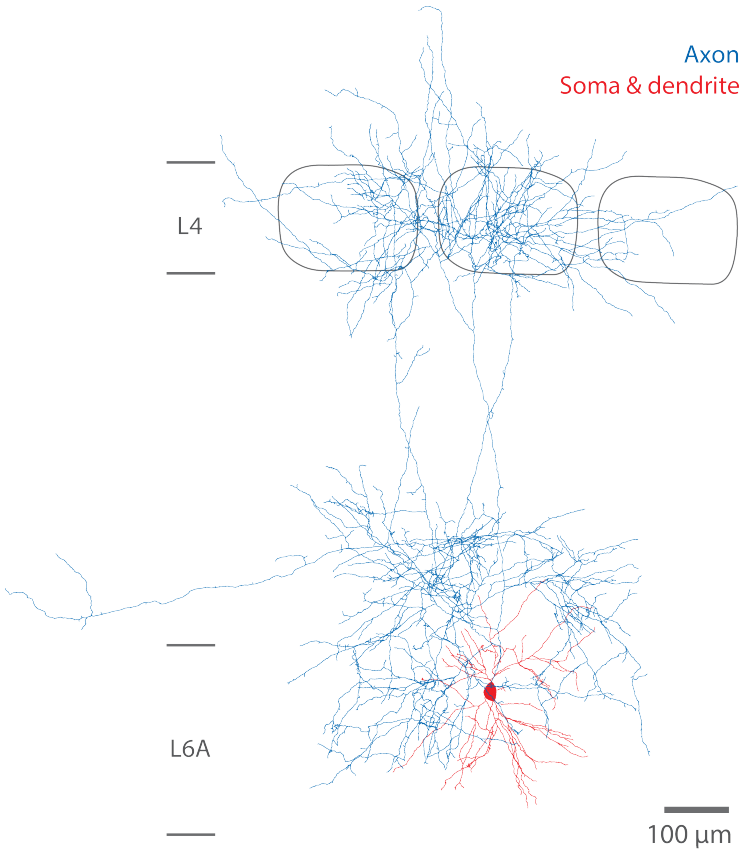

Figure 3.1: Example inhibitory neuron before morphological registration. The soma and dendrites are in red, whereas the axon in blue. Three L4 barrels are also outlined. The soma is located in L6 and the axon spans up to the supragranular layer and across cortical columns.

not relevant for this dissertation, were also available but not shown in Figure 3.1.

For each morphology, I first extracted the soma, dendrites (if available), and axon from the raw morphological file in Neurolucida ASCII-format and then transformed it to HOC-format (Carnevale and Hines, 2006). The HOC-format allows for seamless integration of morphologies into previously reported methodologies such as (Dercksen *et al.*, 2014; Egger *et al.*, 2012, 2014; Udvary *et al.*, 2022). After that, I extracted relevant anatomical information from the raw ASCII file to ultimately register the morphology in HOC-format to a standardized reference frame of rat barrel cortex (Egger *et al.*, 2012).

3.2.1 Anatomical landmarks

From the raw morphological data in ASCII-format, I extracted the outlines of anatomical structures such as the pial surface, L4 barrels, and WM. With identified barrels, I could determine the borders of the granular layer, namely the L3-L4 and L4-L5 borders. Table 3.2 shows the extracted anatomical landmarks per study.

For instance, Egger *et al.* (2015) traced the pia and L4 barrels for all their L1 inhibitory neurons. The raw data from Helmstaedter *et al.* (2009a,b,c) included the morphological reconstructions; however, anatomical landmarks were lacking. I inferred the distance from the soma to the pia and barrels by examining their published galleries for 44 out of 51 inhibitory neurons. For the remaining six inhibitory neurons, identification was not possible. I assumed, then, that the somata of these neurons were located in the center of L2/3, allowing the distance to the pia to be determined. Koelbl *et al.* (2015) traced the pial surfaces; thus, the pia-to-soma distance was available for all their L4 inhibitory neurons. Emmenegger *et al.* (2018) systematically outlined the L4 barrels. Arzt *et al.* (2018) provided the pia-soma distance as well as the L4/5, L5/6, and WM for all their L6 inhibitory neurons.

In the dataset comprising 84 new inhibitory neurons, all pia and WM borders were systematically outlined. These neurons were distributed from L4 to L6. For those in the granular layer, the barrels were traced as well (6 out of 6). For those in the infragranular layer (predominantly in L5), only some of the barrels were traced (26 out of 76).

3.2.2 Registration to cortical column

The 306 inhibitory neurons were registered to a standardized reference frame of rat barrel cortex (Egger *et al.*, 2012). This reference frame was established using reconstructions of the 3D geometry of the pial surface and WM, along with information on the locations, circumferences, and orientations of 24 barrel columns obtained from a sample of 12 Wistar rats. A preliminary assessment conducted by Dr. Daniel Udvary (Max Planck Institute for Neurobiology of Behavior – caesar)

Study	*N*	Pia	L3-L4	L4-L5	WM
Egger *et al.* (2015)	10	10	10	10	–
Helmstaedter *et al.* (2009a,b,c)	51	51	44	44	–
Koelbl *et al.* (2015)	45	45	–	–	–
Emmenegger *et al.* (2018)	48	–	48	48	–
Arzt *et al.* (2018)	68	68	–	68	68
New data	84	84	32	53	84

Table 3.2: Identified anatomical landmarks per study.

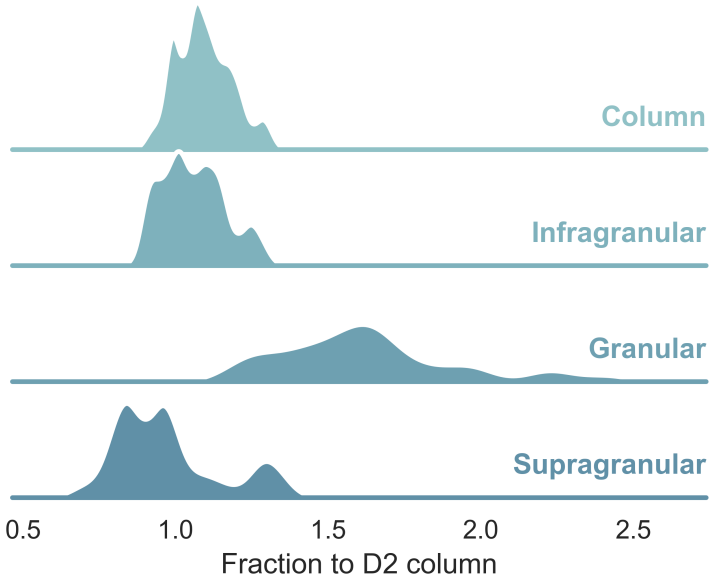

Figure 3.2: Comparison of unregistered anatomical landmarks to the D2 column for 32 inhibitory neurons (Table 3.2). Column corresponds to the pia to WM distance, infragranular to the L4/5 to WM distance, granular to the L3/4 to L4/5 distance, and supragranular to the pia to L3/4 distance.

identified the relevance of scaling along the cutting dimension to the original tissue thickness in order to compensate tissue shrinkage caused by fixation and mounting on microscope slides (Udvary, 2020). Thus, 296 inhibitory neurons were scaled prior to registration; those from Egger *et al.* (2015) were excluded because they were acquired *in vivo*. The registration of scaled morphologies involved aligning the relevant anatomical landmarks to a central column (i.e., D2) in the reference frame at a resolution of 50 µm (Egger *et al.*, 2012; Udvary, 2020).

The D2 column was approximated as a cylinder of height 1957 µm and diameter 397.34 µm. The granular layer had a thickness of 362 µm. I used the 32 inhibitory neurons that had all anatomical landmarks (see Table 3.2 for details) and compared them to the D2 column. Figure 3.2 shows that the pia to WM distances were similar to the D2 column height, and with low variability. Something similar occurred in the infragranular case (i.e., L4-L5 border to WM distances). The supragranular layer, representing distances between the pia and L3-L4 border, exhibited higher variability and a reduction in the underlying fraction. This suggests that the thickness of the supragranular layer in (Egger *et al.*, 2012) was smaller than those measured in (Helmstaedter *et al.*, 2009a,b,c; Koelbl *et al.*, 2015; Emmenegger *et al.*, 2018; Arzt *et al.*, 2018, and new data). The granular layer displayed even higher variability, resembling differences in the identification of layer borders from tangential slices (Egger *et al.*, 2012), and coronal slices (Helmstaedter *et al.*, 2009a,b,c; Koelbl *et al.*, 2015; Emmenegger *et al.*, 2018; Arzt *et al.*, 2018, and new data). As an example, for the inhibitory neuron shown in Figure 3.1, obtained from a coronal slice, the column fraction was 0.99, the infragranular fraction was 0.91, the granular fraction was 1.91, and the supragranular fraction was 0.85.

The registration for inhibitory neurons from Egger *et al.* (2015) was performed as in the original manuscript. As shown in Figure 3.2, the granular layer was highly variable for the remaining 296 inhibitory neurons. However, the pia to WM distance was similar to the D2 column. Using all the available data (Table 3.2), the underlying fraction with $n = 152$ was 1.07 ± 0.01 (mean $\pm$ 95% CI). Thus, I used the pia and WM as a reliable measurement to register inhibitory neurons. Specifically, for (Arzt *et al.*, 2018) and the new data, I used the outlined pia and WM borders. For (Helmstaedter *et al.*, 2009a,b,c) and (Koelbl *et al.*, 2015), I used the outlined pia and calculated the WM border using the height of the D2 column. Finally, for (Emmenegger *et al.*, 2018), the pia and WM borders were calculated by centering the empirical L4 borders to the D2 column. In Egger *et al.* (2012), the origin of the coordinate system was set at the center of the D2 barrel in L4. The same example inhibitory neuron from Figure 3.1 was registered and is presented in Figure 3.3. The pia, L4 barrels, and WM corresponded to the average barrel field (Egger *et al.*, 2012). The soma was located in the infragranular layer and the axon spanned up to the supragranular layer and across cortical columns.

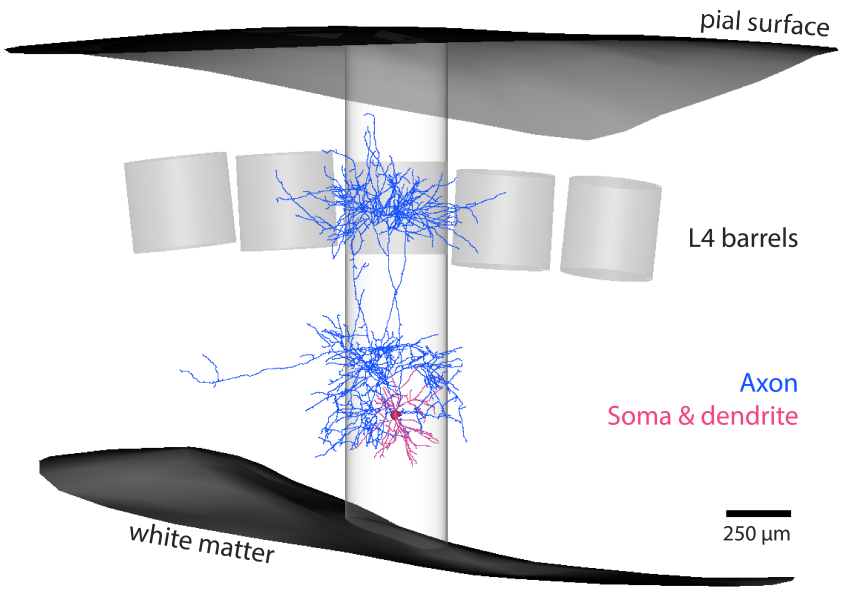

Figure 3.3: Example of a registered inhibitory neuron corresponding to the one in Figure 3.1. The pial surface and WM are depicted in black. Five L4 barrels, namely γ, D1, D2, D3, and D4, are highlighted in gray from left to right. The D2 column is illustrated in a lighter shade of gray.

3.2.3 Evaluation

Each individual study comprising the 306 inhibitory neurons was conducted in a layer-specific manner. For instance, Egger *et al.* (2015) targeted L1, Helmstaedter *et al.* (2009a,b,c) targeted L2/3, Koelbl *et al.* (2015) and Emmenegger *et al.* (2018) targeted L4, and Arzt *et al.* (2018) targeted L6. The new data contributed by collaborators, predominantly focused on L5.

Figure 3.4 presents the soma distribution of each study as a function of cortical depth. The soma position was calculated as the center of mass of its underlying 3D reconstruction. The bin size of the depth-histograms corresponded to 50 µm, which is the precision of the registration (Egger *et al.*, 2012). The borders for layers 1 to 6 were obtained from (Meyer *et al.*, 2013) (with $n = 4$). The D2 column height and granular layer thickness were consistent with (Egger *et al.*, 2012) ($n = 12$). For statistical stability, I used the average layer borders instead of the D2 layer borders (Meyer *et al.*, 2013); the results in both cases were qualitatively the same. Specifically, the pial surface was set at 0 µm. Then, the L1-L2 border was at 150 µm below the pia, the L3-L4 border at 551 µm, the L4-L5 border at 847 µm, the L5-L6 border at 1342 µm, and the L6-WM border at 1887 µm. With this, I determined that 9 inhibitory neurons were located in L1, 53 in L2/3, 99 in L4, 74 in L5, and 71 in L6. The specific distribution across layers is as follows: all 9 inhibitory neurons in L1 were from Egger *et al.* (2015); in L2/3, 1 inhibitory neuron was from Egger *et al.* (2015), 51 from Helmstaedter *et al.* (2009a,b,c), and 1 from Koelbl *et al.* (2015); in L4, 43 were from Koelbl *et al.* (2015), 47 from Emmenegger *et al.* (2018), and 9 from the new data; in L5, 1 was from Koelbl *et al.* (2015), 1 from Emmenegger *et al.* (2018), and 72 from the new data; and finally in L6, 68 were from Arzt *et al.* (2018), and 3 from the new data. As depicted in Figure 3.4, these studies were predominantly layer-specific. Consequently, there was a reduced amount of data close to the layer borders, regardless of the layer border definition (i.e., either average across columns or D2 column).

For each study, the depth distribution exhibited a unimodal pattern, with the peak varying in its location across layers. Thus, the distribution across layers was inhomogeneous, reminiscent of the "hot zones" of inhibition observed in L2 and L5A (Meyer *et al.*, 2011).

3.3 Standardization of electrophysiology

The electrophysiological recordings across all layers of rat barrel cortex were performed by Egger *et al.* (2015), Helmstaedter *et al.* (2009a,b,c), Koelbl *et al.* (2015), Emmenegger *et al.* (2018), and Arzt *et al.* (2018) using whole-cell patch-clamp (Neher and Sakmann, 1976; Hamill *et al.*, 1981). Slices were maintained at a temperature of 31–34 °C and continuously perfused with a recording artificial cerebral spinal

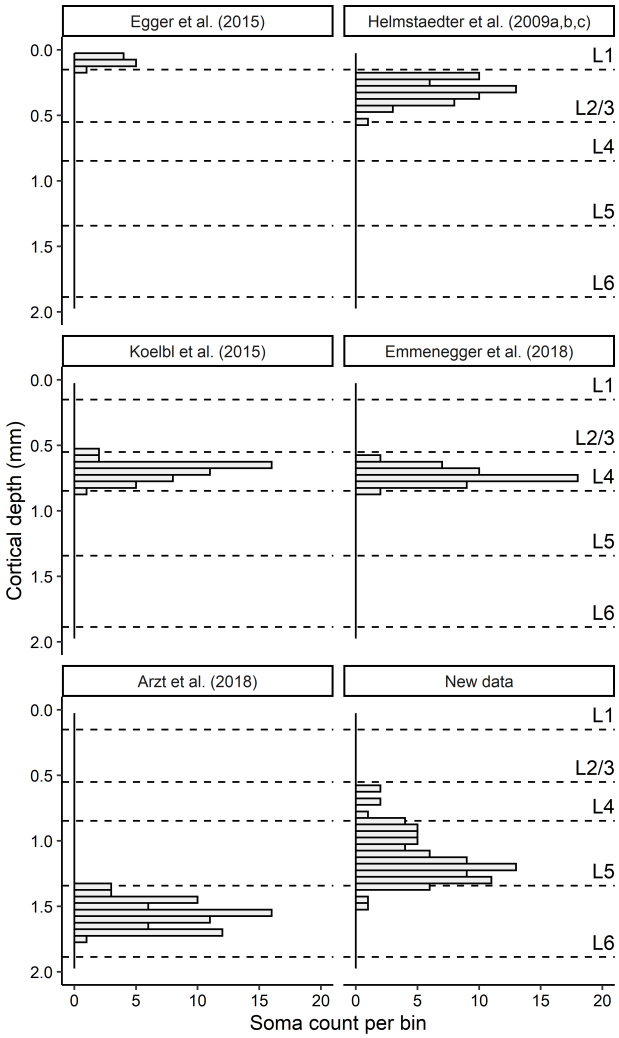

Figure 3.4: Depth distribution of registered inhibitory neuron somata per study. The bin size is 50 µm, and the layer borders are from (Meyer *et al.*, 2013).

fluid (ACSF). The solution was continuously bubbled with gas containing 95% O_2 and 5% CO_2. Whole-cell voltage recordings were performed using patch pipettes of 3.5–8 MΩ pulled from thick-wall borosilicate glass capillaries (outer diameter 2.0 mm; inner diameter 0.5–1.0 mm). Before recording, the electrodes were filled with an internal solution supplemented with 3–6 mg/mL biocytin (Sigma, Munich, Germany). Neurons were filled during 1–2 hours of recording. The patch pipettes were mounted on an Axopatch 200B (Molecular Devices, Sunnyvale, CA, USA) or an EPC10 (HEKA, Lambrecht, Germany) amplifier headstage. The firing responses to a series of current pulses, ranging from 0.5 to 1 s in duration and from −100 to 500 pA in amplitude, were recorded. The recordings were filtered and then sampled at 5–31.25 kHz. After recording, an overview image of the pipette positioned above the soma was taken.

3.3.1 Systematizing the unsystematic

The electrophysiological recordings were obtained from various studies. They were performed under similar but not identical experimental conditions and protocols, making it difficult to jointly analyze them. Thus, I identified both shared elements and differences among the utilized protocols.

Table 3.2 shows the electrophysiological protocols per study. *N* corresponds to the number of inhibitory neurons that were acquired in each study. The response time corresponds to the total recording time. Within that time frame, a stimulus was applied. The range of trials is also reported. For instance, Egger *et al.* (2015) performed current injections of inhibitory neurons *in vivo*. They recorded ten neurons, however, because of the difficulty of these experiments, the duration of stimuli and responses varied across experiments, and one trial was available for most of the experiments. The voltage traces as well as the corresponding injected currents were available. The sampling rate was 31.25 kHz.

The rest of the inhibitory neurons were acquired *in vitro*. There were two recording protocols. The first one had a response duration of 700 ms with a current pulse of 500 ms. The stimulus onset was at 100 ms and offset at 600 ms. The second one had a response duration of 1.6 s with a current pulse of 1 s. The stimulus onset was at 50 ms and offset at 1050 ms. The recordings from Helmstaedter *et al.* (2009a,b,c) used the first acquisition protocol. The raw data included 50 out of 51 inhibitory neurons. The missing one was described to have a burst regular firing pattern but it was only filled with biocytin. The recorded inhibitory neurons had a broad range of available voltage traces; however, the corresponding injected currents were lacking. The sampling rate was 10 kHz. Koelbl *et al.* (2015) also used the first protocol. The raw data included 45 out of 45 inhibitory neurons with an even broader range of available voltage traces per neuron. The corresponding injected currents were unavailable. The sampling rate was 10 kHz. On the other hand, Emmenegger *et al.*

Study	*N*	Response (s)	Stimulus (s)	Trials
Egger *et al.* (2015)	10	1.5–2	0.5–0.8	1–2
Helmstaedter *et al.* (2009a,b,c)	50	0.7	0.5	2–96
Koelbl *et al.* (2015)	45	0.7	0.5	2–158
Emmenegger *et al.* (2018)	48	1.6	1.0	5–25
Arzt *et al.* (2018)	68	0.7	0.5	1–16
New data (protocol one)	76	0.7	0.5	1–53
New data (protocol two)	6	1.6	1.0	10–15

Table 3.3: Electrophysiological protocols per study. *N* corresponds to the number of inhibitory neurons that were acquired in each study. Response corresponds to the total recording time in seconds. Stimulus corresponds to the pulse duration in seconds. Trials corresponds to the range of repetitions in each study.

(2018) used protocol two. The raw data included 48 out of 48 inhibitory neurons. The voltage traces as well as the corresponding injected currents were fully available. This dataset contained at least 5 trials per inhibitory neuron. The sampling rate was 20 kHz. Arzt *et al.* (2018) used protocol one. The raw data included 68 out of 68 inhibitory neurons. The voltage traces as well as the corresponding injected currents were fully available. This dataset comprised a narrow range of trials. The sampling rate was 5 kHz. In the new data provided by collaborators, the recordings were performed with both protocols. With the first protocol, 76 out of 78 inhibitory neurons were acquired. From those 76 recordings, 19 included both the voltage traces and the injected currents acquired at a sampling rate of 5 kHz, and 57 included only voltage traces acquired at a sampling rate of 10 kHz. The recordings comprised a broad range of available voltage traces. With the second protocol 6 out of 6 inhibitory neurons were acquired. The voltage traces as well as the corresponding injected currents were fully available. The recordings comprised a narrow range of voltage traces, with at least 10 trials per inhibitory neuron. The sampling rate was 20 kHz.

Identifying commonalities and differences among protocols allows for a unifying protocol to be developed, enabling consistent analysis across cortical layers.

3.3.2 Robust spike detection

Accurate and consistent spike detection is crucial for analyzing electrophysiological recordings. However, because of the variability in recording conditions and protocols, spike detection can be challenging and prone to errors. Thus, I developed a simple approach for robust spike detection.

The method begins by sorting the 100 Hz voltage trace within the stimulus window in descending order. I observed that it can be approximated with a piece-wise linear function. Upon further examination, I found that the second half of the sorted data could be discarded without any loss of information. This is because even in the theoretical limit of a binary spiking neuron, at least half of the time would be spent in the sub-threshold regime, which is not relevant for spike detection. Figure 3.5 illustrates the cut-off voltage approximation using a single change point for three example 100 Hz voltage traces (blue). However, I also found that using only one change point could result in false positive spikes (e.g. Example trace #3). To address this issue, I calculated the 95% CI of the voltage points above the cut-off to establish a proxy of minimum peak prominence against noisy approximations (green). This symbolic method is robust in detecting spikes, agnostic to absolute units, and relies only on the structure of a voltage trace.

From all the neurons analyzed in this dissertation (Egger *et al.*, 2015; Helmstaedter *et al.*, 2009a,b,c; Koelbl *et al.*, 2015; Emmenegger *et al.*, 2018; Arzt *et al.*, 2018; Gouwens *et al.*, 2019, 2020, and new data), my method had perfect accuracy.

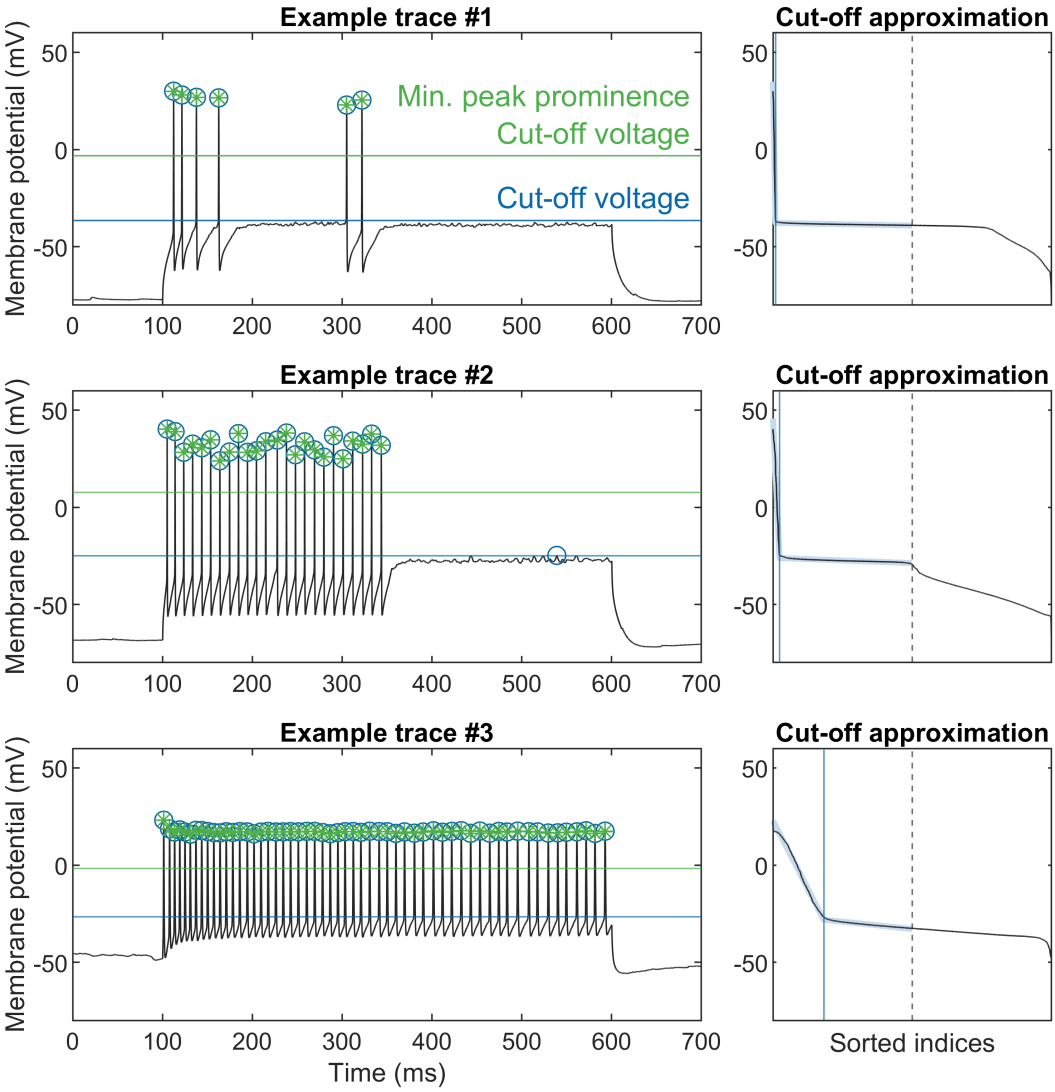

Figure 3.5: Robust spike detection for three example 100 Hz voltage traces.

3.3.3 A unifying protocol

In order to develop a common protocol that can be applied consistently across all inhibitory neurons, I first assessed experimental conditions and protocols of each study. Since the injected currents for each inhibitory neuron were not always available, I selected a single trial where the initial instantaneous firing rate was closest to 100 Hz (Beierlein *et al.*, 2003). According to Beierlein *et al.* (2003), even though the initial firing rates were set to 100 Hz significant differences in firing rates between cell types at every subsequent time point were found.

With this criteria, each inhibitory neuron had a single voltage trace and the injected currents were no longer needed to establish a common protocol across studies. Note that I defined the criteria in the frequency domain and not in the time domain (i.e., initial interspike-interval closest (ISI) to 10 ms) as in (Helmstaedter *et al.*, 2009b; Arzt *et al.*, 2018). To illustrate the differences, consider, for example, a perturbation of 10%. In the frequency domain, that would mean that 90 Hz and 110 Hz are indistinguishably good for the metric. However, in the time domain, now 11 ms and 9 ms are indistinguishable for the metric. This translates to 90.9 Hz and 111.1 Hz, making them asymmetric around 100 Hz. In this case, a symmetric metric does not favor the selection of higher frequencies.

Then, to address the issue of different protocols, I decided to adopt the previously defined protocol one for all inhibitory neurons, as it can be applied consistently. This means that only the first 500 ms after stimulus onset would be later used for analysis. The studies that were already using protocol one remain unchanged. However, in the studies using protocol two, I cropped the trace between 0–550 ms and 1050–1150 ms. Then, I combined them into a 650 ms long voltage trace. I made sure that the voltage at 550 ms was greater than or equal to the voltage at 1050 ms in order to have a smooth transition. Finally, I took the voltage at 0 ms and repeated its value for 50 ms in order to have the stimulus onset at 100 ms. I applied a similar methodology for (Egger *et al.*, 2015), I first kept the trace from stimulus onset until stimulus onset plus 500 ms. Then I combined it with the voltages from stimulus offset until stimulus offset plus 100 ms. Finally, I included the voltages from stimulus onset minus 100 ms until stimulus onset. The 303 inhibitory neurons were resampled at 100 kHz. Figure 3.6 illustrates the standardization procedure of the inhibitory neuron presented in Figure 3.1. The recording was performed using protocol two, acquiring 15 voltage traces at a sampling rate of 20 kHz. The selected 100 Hz voltage trace had an initial instantaneous firing rate of 104.71 Hz and an injected current of 444 pA.

Finally, all inhibitory neurons had a common protocol where the recording duration was 700 ms, with a current pulse of 500 ms and stimulus onset at 100 ms. Furthermore, they were also resampled at a rate of 100 kHz.

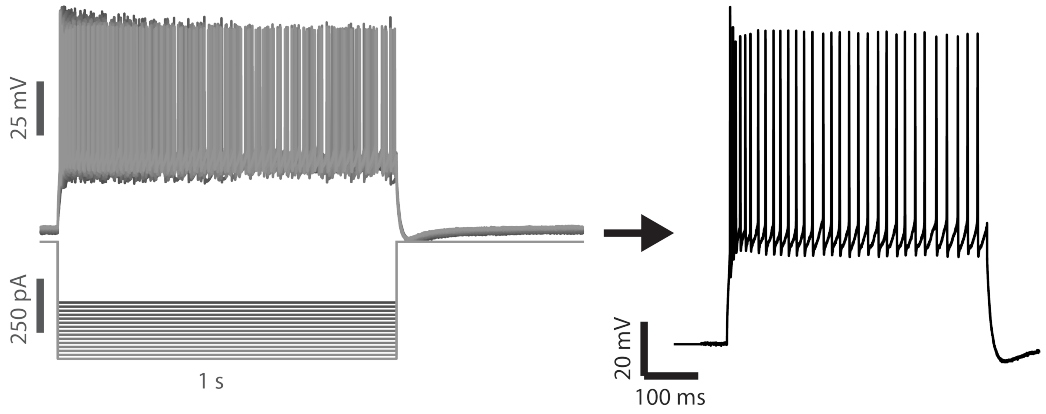

Figure 3.6: Example of a standardized electrophysiological recording corresponding to the inhibitory neuron in Figure 3.1. The selected 100 Hz voltage trace had an initial instantaneous firing rate of 104.71 Hz. See text for further details.

3.3.4 Evaluation

To evaluate the consistency of the unifying protocol, I assessed the initial firing frequency of inhibitory neurons across different studies, each conducted in a layer-specific manner. For instance, Egger *et al.* (2015) targeted L1, Helmstaedter *et al.* (2009a,b,c) targeted L2/3, Koelbl *et al.* (2015) and Emmenegger *et al.* (2018) targeted L4, and Arzt *et al.* (2018) targeted L6. The new data contributed by collaborators, predominantly focused on L5. All studies blindly recorded inhibitory neurons, except for Koelbl *et al.* (2015) which targeted fast-spiking (FS) neurons ($n = 45$) and Emmenegger *et al.* (2018) which targeted non-FS neurons ($n = 48$). However, it is worth noting that according to Markram *et al.* (2015), 41–67% of the inhibitory neurons in the granular layer, where both of these studies focused, were fast-spiking (see the Neocortical Microcircuit Collaboration Portal for details). This proportion is consistent with the fraction of FS and non-FS inhibitory neurons reported in these two studies (48%). Furthermore, by examining the data sources that composed L4, this means 43 inhibitory neurons from Koelbl *et al.* (2015), 47 from Emmenegger *et al.* (2018), and 9 from the new data, I calculated that the expected proportions range between 43% and 52%. This indicated that, in principle, the electrophysiological composition of the the granular layer in this dissertation is aligned with the overall diversity of reported inhibitory neuron subtypes in that layer (Markram *et al.*, 2015).

Table 3.4 presents the average initial firing frequency of each study. I calculated the initial firing frequency as the inverse of the time difference between the first two detected APs (i.e., initial ISI) in seconds. Each study comprised voltage traces with an initial firing rate close to 100 Hz (Beierlein *et al.*, 2003). The overall initial firing frequency of the dataset was 106 ± 4 Hz. To assess the consistency of the unifying protocol, I compared the average initial firing frequency of each study using a one-way ANOVA, revealing a significant difference between the studies (F-statistic: 2.84, p-value: 0.016). It is important to note that although the p-value was below the typical threshold of 0.05, it was still relatively close to it, indicating that the difference may not be highly significant. This difference may be explained in part whether it was an *in vivo* or *in vitro* recording. I repeated the analysis excluding the *in vivo* experiments by Egger *et al.* (2015), and obtained a non-significant difference among the means of the remaining studies. (F-statistic: 1.68, p-value: 0.155). This suggested that there may be some variability across studies, but it is not significant enough to conclude that there are true differences in initial firing frequency.

The evaluation demonstrated that the unifying protocol consistently captured the initial firing frequency of inhibitory neurons across different studies, and, thus, cortical layers. However, it is important to note the differences between experimental conditions among studies, and the potential biases they may introduce.

Study	N	Initial firing frequency (Hz)
Egger *et al.* (2015)	10	75 ± 27
Helmstaedter *et al.* (2009a,b,c)	50	104 ± 17
Koelbl *et al.* (2015)	45	99 ± 1
Emmenegger *et al.* (2018)	48	107 ± 9
Arzt *et al.* (2018)	68	116 ± 8
New data	82	106 ± 5
Total	303	106 ± 4

Table 3.4: Initial firing frequency evaluation involves calculating the inverse of the time difference between the first two detected APs, reported as mean ± 95% CI.

3.4 Representativeness per depth

The rat barrel cortex is a complex structure with a highly organized laminar architecture, and different cortical layers have distinct functional properties and connectivity patterns (Oberlaender *et al.*, 2012; Feldmeyer *et al.*, 2013; Narayanan *et al.*, 2017). The density of inhibitory neurons can vary significantly across the cortical mantle, and these variations can have important implications for the function of the cortical circuitry (Xu *et al.*, 2010; Meyer *et al.*, 2011, 2013; Tremblay *et al.*, 2016). Therefore, I first assessed whether the distribution of the 306 inhibitory neurons accurately represents the empirical distribution of inhibitory neurons across layers on an average cortical column. Table 3.5 compares the distribution of inhibitory neurons I standardized to an average column previously reported by Meyer *et al.* (2013), who provided the density and absolute number of inhibitory neurons in the entire rat barrel cortex at 50 µm resolution. I obtained the absolute numbers for an average column in each cortical layer from (Meyer *et al.*, 2013, Tables S2–S6), while the total number from (Meyer *et al.*, 2013, Table 1). For the dataset I standardized, each of the 306 inhibitory neurons was assigned to a cortical layer based on their soma depth. Average layer borders reported in (Meyer *et al.*, 2013) were utilized. The distribution of inhibitory neurons varied across layers, representing 13.4% of the average column in rat barrel cortex.

Then, I proceeded to compare their depth distribution, which refers to the one-dimensional profile of neuron counts or densities along the pia to WM direction. Figure 3.7 summarizes an assessment to see whether the curated dataset was representative of the empirical distribution of inhibitory neurons per 50 µm-depth bins. All the calculations and statistical analyses for this assessment were performed in R (R Foundation for Statistical Computing, Vienna, Austria). Figure 3.7A (left) presents the histogram of neuron counts of the curated dataset using 50 µm-depth bins. The most superficial inhibitory neuron was registered at 59.75 µm below the pial surface, whereas the deepest one was registered at 1748.85 µm. It is worth noting that between that range, there were samples at every depth 50 µm bin. Figure 3.7A (right) compares the mean ± 95% CI of the empirical density of inhibitory neurons (Meyer *et al.*, 2013) in the principal (i.e., D2) and surrounding columns (i.e., C1, C2, C3, D1, D3, E1, E2, and E3), against the scaled density of the histogram in Figure 3.7A (left). The density of the histogram was calculated with a cosine smoothing kernel from 0–2 mm. The scaling was performed only for visualization purposes, with the aim of approximately matching the peak densities of both depth distributions in L4. Qualitatively, both depth distributions are remarkably similar, even resembling the hot zones of inhibition in L2 and L5A (Meyer *et al.*, 2011). Therefore, I continued the assessment with a statistical analysis to test whether the curated sample could be a random sample of the empirical density of inhibitory neurons across cortical depth.

	Meyer *et al.* (2013)	This dissertation	Fraction (%)
L1	40 ± 6	9	23.1 ± 3.7
L2/3	427±44	53	12.5 ± 1.3
L4	557±74	99	18.1 ± 2.4
L5	820±110	74	9.2 ± 1.2
L6	459±59	71	15.7 ± 2.0
Total	2314±279	306	13.4 ± 1.6

Table 3.5: Laminar distribution of inhibitory neurons in the dataset I standardized compared to an average column (Meyer *et al.*, 2013). When applicable, numbers are mean ± 95% CI.

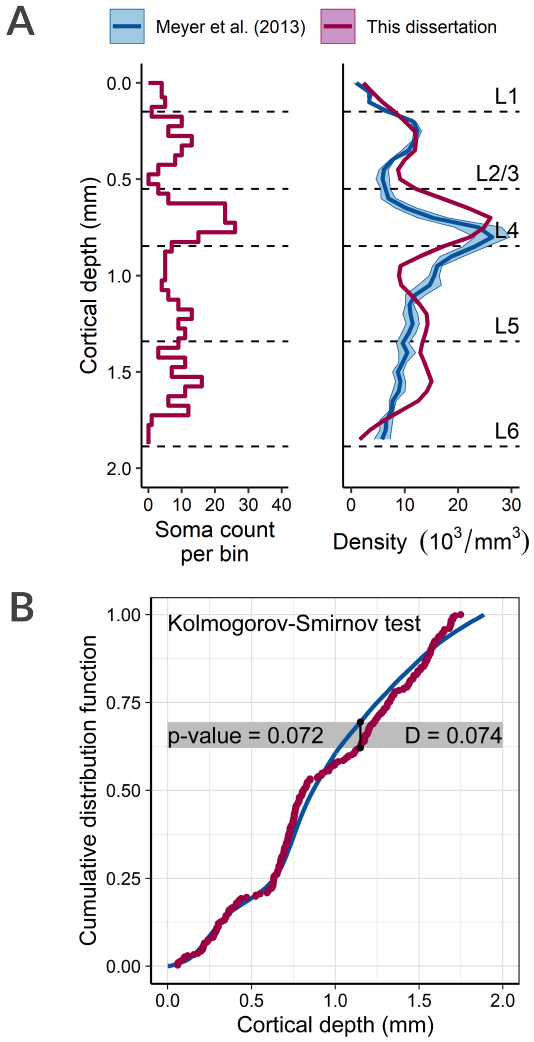

Figure 3.7: Assessment of representativeness per depth. A. Comparison of depth distributions. B. Kolmogorov-Smirnov (KS) test. Details can be found in the text.

Figure 3.7B presents the results of the one-sided Kolmogorov-Smirnov (KS) test. It compared the distribution of the curated dataset against the known cumulative distribution function (CDF) of inhibitory neurons across layers (Meyer *et al.*, 2013). I calculated the CDF using the average of the depth distribution across columns (Figure 3.7A, right). The null hypothesis was that the curated dataset came from the same distribution as the known CDF. The KS test results revealed a non-significant difference between the CDFs (D-statistic: 0.074, p-value: 0.072). This means that there was not sufficient evidence to reject the null hypothesis. In other words, there was not sufficient evidence to say that the curated dataset does not come from the distribution of inhibitory neurons in an average column measured by Meyer *et al.* (2013). The biological implication is that the curated dataset was a representative sample of an average cortical column (Meyer *et al.*, 2013).

To further evaluate the similarities and differences between the two densities in Figure 3.7A (right), I used Optimal Transport (Monge, 1781; Kantorovich, 1942; Villani, 2003) to measure their distance by finding the optimal transportation plan from one depth distribution to the other. Specifically, I utilized the Tsallis Regularized Optimal Transport (TROT) implementation (Muzellec *et al.*, 2017) with Pearson's χ^2 statistic (i.e., $q = 2$), squared Euclidean distance cost matrix, and $\lambda = 0.1$. Figure 3.8 illustrates the obtained optimal transportation plan at 50 µm resolution. The marginal distributions correspond to the inhibitory neuron densities by either Meyer *et al.* (2013) or the dataset from this dissertation. The depth distributions were normalized to be probability densities. The dashed line corresponds to the identity. In the supragranular layer (L1/3), the transportation plan lies on top of the identity. In the granular layer (L4), the transportation plan is slightly above the identity, indicating that the standardized dataset has higher density there. Finally, in the infragranular layer, the transportation plan is slightly below the identity in L5, whereas it is slightly above the identity in L6. Overall, the transportation plan shows a remarkable agreement between the inhibitory neuron density distributions from Meyer *et al.* (2013) and the standardized dataset from this dissertation.

Finally, the strategy of generating a representative dataset per cortical depth was also important for the generalizability of downstream analyses. By ensuring that the dataset accurately represented the distribution of inhibitory neurons across all cortical layers, it was possible to analyze a cortical column as a whole, rather than just specific layers. To achieve this, there are different paths. For instance, Figure 3.9 illustrates a comparison between the unique inhibitory neurons ("raw material") in the standardized dataset from this dissertation, and those used to reconstruct the microcircuitry of somatosensory cortex of juvenile rat (Markram *et al.*, 2015). Markram *et al.* (2015) reported a total of 521 inhibitory neurons, where 50 were in L1, 164 in L2/3, 113 in L4, 118 in L5, and 76 in L6. These two studies were compared against the absolute abundance of inhibitory neurons

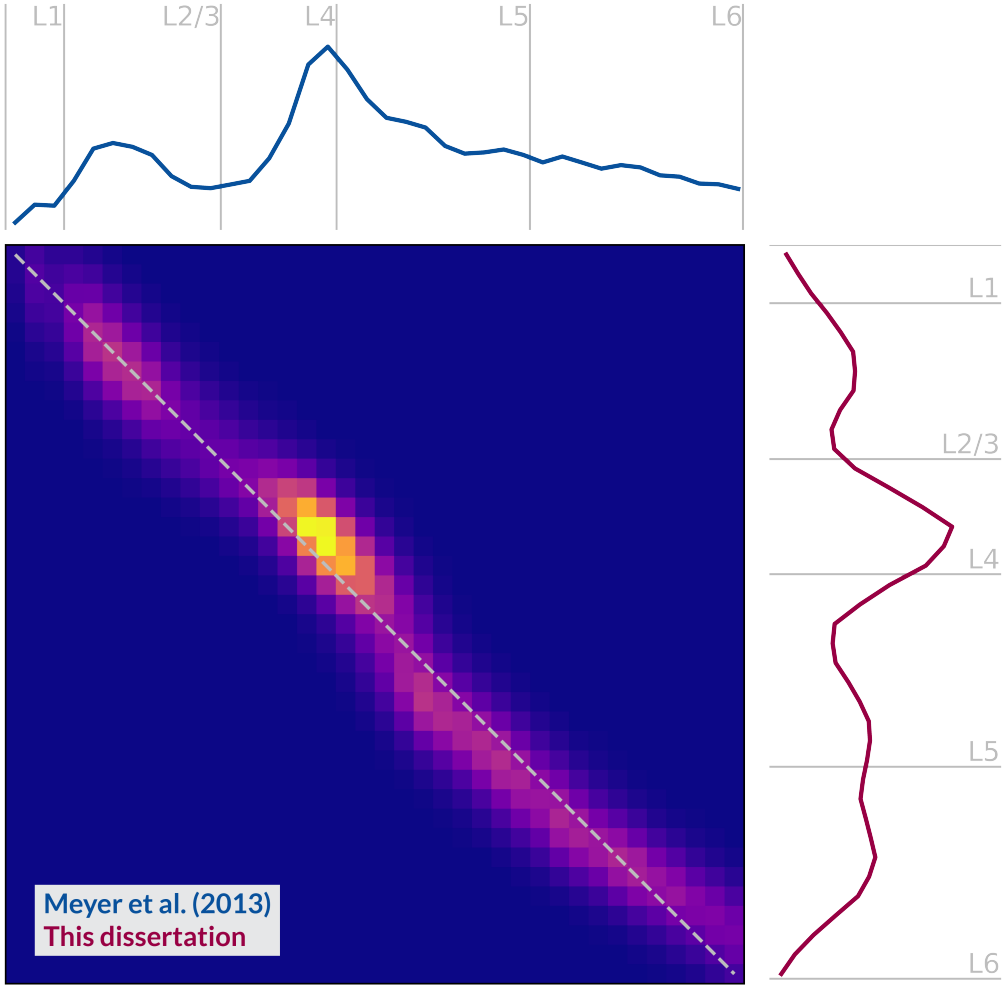

Figure 3.8: Optimal transportation plan between the dataset and average column inhibitory neuron densities. Further details can be found in the text.

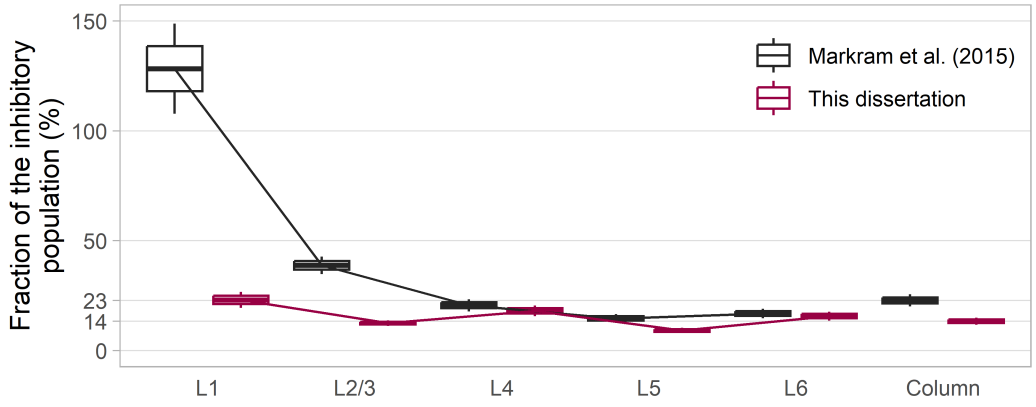

Figure 3.9: Comparison of the fraction of inhibitory neurons across cortical layers.

in an average cortical column (Meyer *et al.*, 2013). As displayed in Figure 3.9, the standardized dataset from this dissertation is homogeneous with respect to cortical layers, whereas the data from Markram *et al.* (2015) is overrepresented in the supragranular layer. This factual difference represented different strategies to generate an average cortical column: Markram *et al.* (2015) aimed at capturing the diversity of reported inhibitory neuron subtypes at the cost of inhomogeneous compensation across layers, whereas in this dissertation the aim is at producing a representative sample at the cost of not capturing all reported inhibitory neuron subtypes.

I assessed the representativeness of the generated dataset of inhibitory neurons in rat barrel cortex, and demonstrated that it accurately represented the empirical distribution as a function of cortical depth. I provided a thorough evaluation of the quality and representativeness of the generated dataset, which is essential for drawing valid conclusions from any subsequent analyses.

3.5 Summary

I analyzed the axonal and dendritic morphology (Figure 3.10A-B), as well as spiking responses to somatic current injections (Figure 3.10C) for 306 inhibitory neurons across the entire cortical depth of rat barrel cortex. For this purpose, I registered each neuron into a standardized 3D reference frame of rat barrel cortex at a resolution of 50 µm (Egger *et al.*, 2012), which allowed me to determine that 9 neurons were located in L1, 53 in L2/3, 99 in L4, 74 in L5, and 71 in L6 (Figure 3.11A). For each inhibitory neuron, the voltage trace with an initial firing frequency closest to 100 Hz was selected for analysis (Figure 3.11B). This dataset comprised diverse morphoelectric properties of inhibitory neurons, ranging from neurons with small basket morphologies and FS firing patterns (Figure 3.11A-B; orange) to neurons with Martinotti-like morphologies and non-FS firing patterns (Figure 3.11A-B; gray). The overall number of inhibitory neurons in the underlying dataset corresponded to $13.4 \pm 1.6\%$ (mean $\pm$ 95% CI) of the absolute number in an average column (Meyer *et al.*, 2013). The depth distribution of the dataset was consistent with the inhibitory neuron density in an average column. Thus, this comprehensive dataset of morphoelectric properties was representative for the depth distribution of inhibitory neurons at 50 µm resolution bins.

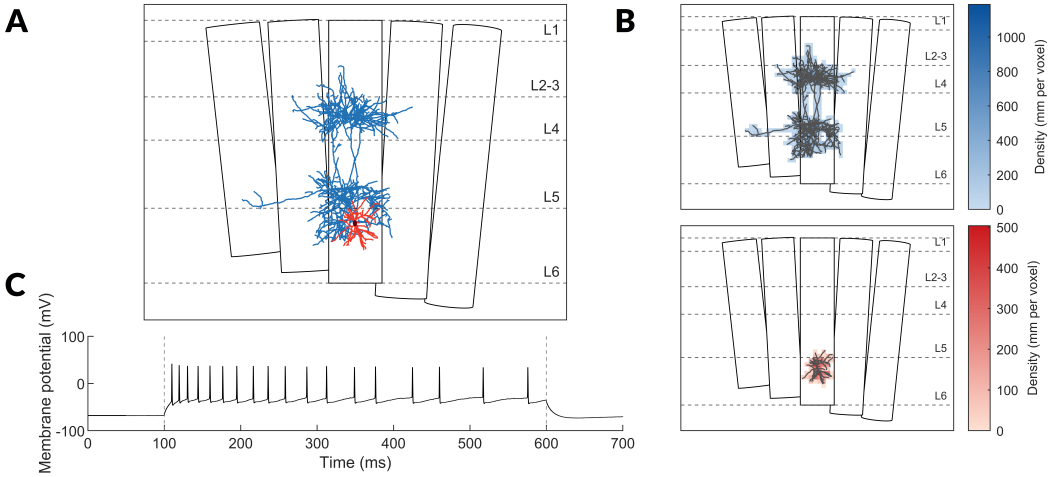

Figure 3.10: Example of a multimodal inhibitory neuron from the representative dataset, corresponding the one presented in Figure 3.1. A. Registered axonal and dendritic morphology. B. Path length density of the axonal and dendritic morphology. C. Corresponding 100 Hz voltage trace.

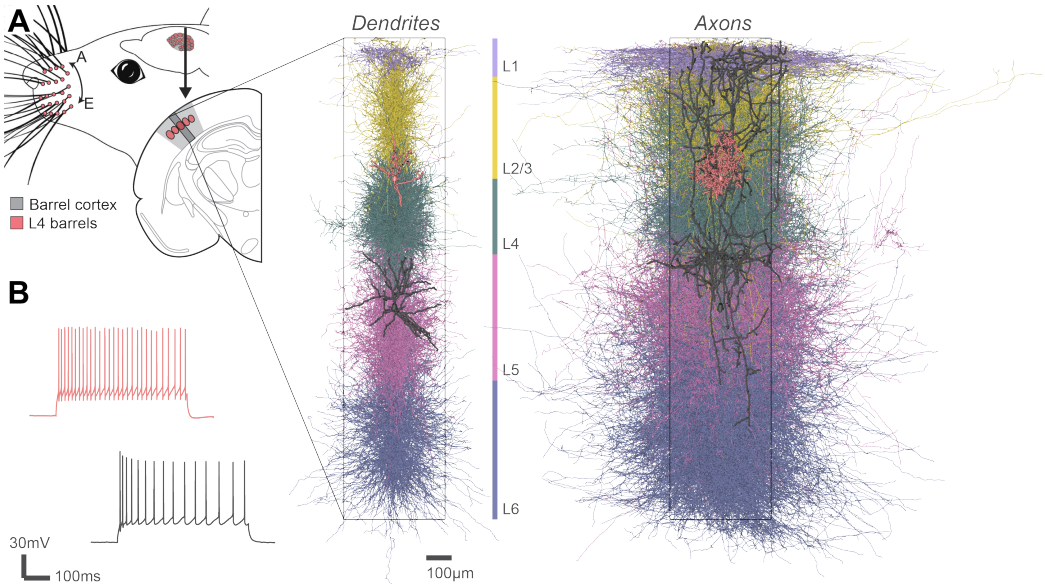

Figure 3.11: Comprehensive dataset of inhibitory neurons in rat barrel cortex. A. The dataset comprises 306 neuron morphologies from rat vS1, registered to a cortical column. The dendrites and axons are color-coded by the cortical layer where their soma was located. Two example neuron are shown to illustrate the diversity of our dataset: a L2/3 basket cell (orange) and a L5 Martinotti cell (gray). B. Example of a FS (orange) and a non-FS (gray) 100 Hz voltage trace corresponding to the neurons displayed in panel A.

Chapter 4

Single-cell characterization

I characterized the registered axonal and dendritic morphology, as well as spiking responses of 100 Hz voltage traces for a representative sample of 306 inhibitory neurons across all layers of rat barrel cortex. For each inhibitory neuron, I extracted 47 features describing the morphology and 31 features describing the electrophysiology based on previously reported studies (Ascoli *et al.*, 2008; Scorcioni *et al.*, 2008; Helmstaedter *et al.*, 2009b; Oberlaender *et al.*, 2012; DeFelipe *et al.*, 2013; Narayanan *et al.*, 2015; Koelbl *et al.*, 2015; Markram *et al.*, 2015; Emmenegger *et al.*, 2018; Gouwens *et al.*, 2019). To take advantage of the barrel cortex anatomy, I included column-specific morphological features such as the relative amount of axon or dendrites within the registered column (Oberlaender *et al.*, 2012; Narayanan *et al.*, 2015; Koelbl *et al.*, 2015; Emmenegger *et al.*, 2018). To capture different aspects of the voltage traces, ten time-dependent electrophysiological datasets were constructed, following the approach of Gouwens *et al.* (2019). To extract the most important features from each electrophysiological dataset while minimizing the number of variables needed to represent the data, I employed sparse principal component analysis. By adopting a similar characterization approach as in previous studies on mouse V1 (Gouwens *et al.*, 2019, 2020), I was able to extend my analysis across species and cortex areas.

The most important methodological results from Chapter 4 are:

- The comprehensive characterization of morphology and electrophysiology using 47 and 31 descriptive features, respectively.
- A similar characterization as reported in mouse visual cortex (Gouwens *et al.*, 2019, 2020), allowing for comparisons across species and cortex areas.

4.1 Morphology

To gain insights into the structural properties of inhibitory neurons in rat barrel cortex, I characterized their axonal and dendritic morphology using a set of 47 descriptive features, grouped in nine categories, similarly as in Gouwens *et al.* (2019). In this dissertation, the pia to white matter direction is referred to as z, and the

dorsal medial to ventral lateral direction is referred to as x. In order to perform the necessary calculations, I utilized MATLAB (The MathWorks Inc., Natick, MA, USA) along with the TREES toolbox (Cuntz *et al.*, 2010). Table 4.1 and Figures A.1–A.3 present a complete description of all morphological features and their distribution as a function of cortical layers for 302 inhibitory neurons with registered axonal and dendritic morphology.

4.1.1 Location

To determine the location of the soma, I calculated its center of mass in the $x - z$ direction. Specifically, I measured the distance between the registered pia and the soma, which is referred to as the soma depth (feature 1) in mm (see Table 4.1 for details). This measurement provides insight into the position of the neuron within the cortical mantle. Figure A.1 (first row; top to bottom) presents the distribution of inhibitory neurons grouped by cortical layer.

4.1.2 Length

To characterize the size and extent of these inhibitory neurons, I measured various aspects of their axonal and dendritic morphology. Specifically, I measured in mm the vertical and horizontal extent of both the axon and dendrites (features 2–5), respectively (see Table 4.1 for details). Figure A.1 (second row; top to bottom) illustrates a trend of increasing height from L1 to L6, while the trend in width is less apparent. This suggests that the height of axonal and dendritic arbors may be a more useful feature than width for distinguishing inhibitory neurons in different cortical layers. Additionally, I calculated the total length of all branches for both the axon and dendrites (features 6–7) in mm (see Table 4.1 for details). Figure A.1 (third row; top to bottom) shows the difference in total length between axons and dendrites, with the axons being approximately one order of magnitude larger than the dendrites.

4.1.3 Bias

To describe the directional preference of the axonal and dendritic arbors, I calculated the difference in their extent in the positive and negative directions from the soma, separately for the z and x directions (features 8–11). For the z-bias, the values were signed, indicating whether the bias was towards the pia (positive values) or the white matter (negative values). In contrast, for the x-bias, the values were unsigned, indicating the magnitude of the bias in either the dorsal or ventral direction (see Table 4.1 for details). These features are illustrated in Figure A.1 (fourth row; top to bottom). In the z direction, the axons display a trend from a preference towards the white matter to a preference towards the pia. On the other

hand, the dendrites show a symmetric bias with increasing magnitude. This trend in the x is not apparent.

4.1.4 Branch

To assess the complexity and intricacy of the axonal and dendritic arbors, I quantified various branching characteristics. Specifically, I measured the maximum branch order and the number of branches for both the axon and dendrite (features 12–15; see Table 4.1 for details). The maximum branch order represents the highest number of bifurcations encountered between the soma and all neurite tips, providing an indication of the level of branching complexity. On the other hand, the number of branches gives a measure of the total number of individual branches in the morphology, reflecting the overall size and extent of the arbor. Figure A.1 (fifth row; top to bottom) illustrates the distribution of these branching features across different cortical layers, where the most complex inhibitory neurons are concentrated towards the granular layer.

4.1.5 Distance

To characterize the spatial spread of axonal and dendritic arbors, I measured various distance metrics (see Table 4.1 for details). The maximum Euclidean distance (features 16–17) measures the direct-line distance from the soma to the most distal node in the arbor, providing insight into the overall size of the arbor. The maximum path distance (features 18–19) measures the length of the longest path from the soma to any neurite tip, indicating the maximum extent of the arbor along its branches. Figure A.2 (first row; top to bottom) illustrates an increasing trend for the dendrites from L1 to L6, while the trend for the axons is less apparent. Additionally, I calculated the mean contraction (features 20–21) as the average ratio of the summed Euclidean distance between bifurcations, and between bifurcations and tips, to the summed path distance between the same points. This metric provides a measure of how much the arbor branches and tortuosity, with higher values indicating more complex and branching arbors. Figure A.2 (second row; top to bottom) shows a higher concentration and broader range of values towards the granular layer.

4.1.6 Overlap

To describe the spatial relationship between axonal and dendritic arbors, I calculated several metrics (features 22–28; see Table 4.1 for details). Specifically, the fraction of axon nodes above, overlapping, and below the full z-extent of the dendrite was calculated (features 22–24). Figure A.2 (third row; top to bottom) shows an increasing trend in the value range for axon above and overlapping dendrite,

Category	N	Feature name	Definition
Location	1	Soma depth	Distance between the registered pia and soma.
Length	4	{Height, width}†	Extent in the $\{z, x\}$-direction.
	2	Total length†	Length across all branches.
Bias	4	$\{z, x\}$-bias†	Difference in extent in $\{z, x\}$ in one direction from the soma and the other. Values are signed for z-bias and unsigned for x-bias.
Branch	2	Max. branch order†	Maximum number of bifurcations encountered between the soma and all neurite tips.
	2	Number of branches†	Number of individual branches in the morphology.
Distance	2	Max. Euclidean distance†	Direct-line distance from the soma to the furthest neurite tip.
	2	Max. path distance†	Path distance from the soma to the furthest neurite tip.
	2	Max. mean contraction†	Average of the ratios of the summed Euclidean distance between bifurcations, and between bifurcations and tips, to the summed path distance between same.

continues on next page

Overlap	6	Axon or dendrite {above, overlapping, below} dendrite or axon	Fraction of axon or dendrite nodes {above, overlapping, below} the full z-extent of the dendrite or axon, respectively.
	1	EMD	Earth mover's distance metric calculated between the normalized and aligned axon and dendrite depth profile histograms.
Percentile	4	Soma $\{z, x\}$-percentile†	Percentile location of the $\{z, x\}$-coordinate of the soma within the $\{z, x\}$-coordinates distribution of all nodes.
Depth histogram	11	Depth histogram PCs (6 axon and 5 dendrite PCs)†	Principal components (PCs) produced by PCA to depth profile histograms aligned to our reference frame (50 µm bins) that exceed 5% explained variance.
Column	2	Home column†	Relative length within the D2 column.
	2	Adjacent columns/septa†	Relative length outside the D2 column.

Table 4.1: List of features describing morphology. The pia to white matter direction is denoted as z, whereas the dorsal medial to ventral lateral direction as x. When applicable, length units are in mm. † indicates that a particular feature is calculated independently for the axon and dendrite morphology.

while a higher concentration and broader range of values towards the granular layer for axon below dendrite. Similarly, the fraction of dendrite nodes above, overlapping, and below the full z-extent of the axon (features 25–27). Figure A.2 (fourth row; top to bottom) presents less apparent trends. Additionally, the Earth mover's distance (EMD) metric was calculated between the normalized and aligned depth profile histograms of one compartment type and another (feature 28), which provides a measure of the similarity between the axon and dendrite depth distributions. Figure A.2 (fourth row; top to bottom) shows an increasing trend in the value range from L1 to L6. These metrics provide insight into the degree of co-localization and segregation of axon and dendrite depth distributions.

4.1.7 Percentile

As illustrated in Table 4.1, I calculated the percentile location of the soma's z-coordinate within the distribution of all z-coordinates of the axon and dendrite nodes (features 29–30). I also calculated the percentile location of the soma's x-coordinate within the distribution of all x-coordinates of the axon and dendrite nodes (features 31–32), with the results symmetrized to prevent "handedness". This refers to a bias in the data towards one side or the other, which can arise due to natural variation in neuron morphology. By symmetrizing the results, the percentile values are calculated based on the absolute distance from the soma, rather than the direction, providing a more accurate representation of the soma's position relative to the arbor. Figure A.2 (fifth row; top to bottom) shows high diversity across cortical layers for the z-coordinate, and a higher concentration and broader range of values towards the granular layer for the x-coordinate.

4.1.8 Depth histogram

To analyze the axon and dendrite depth distributions, I performed principal component analysis (PCA) on depth-wise histograms of the arbors, where the depth profiles were by definition aligned to a reference frame (Egger *et al.*, 2012) and binned at 50 µm. I then identified the PCs, each of which explained more than 5% of the variance in the data. These PCs represent the aligned histogram principal components (features 33–43; see Table 4.1 for details). Specifically, I calculated six PCs for the axon histogram (features 33–38) and five PCs for the dendrite histogram (features 39–43). Figure A.3 (first to fourth rows; top to bottom) shows that these eleven features capture the variation in the depth distribution of the axonal and dendritic arbors by distinguishing laminar organization of inhibitory neurons.

4.1.9 Column

In order to analyze the distribution of axonal and dendritic structures within and outside the home column, four morphological features were utilized (features 44–47; see Table 4.1 for details). The lengths of the axon and dendrite within the home column (D2) were normalized by the total axon and dendrite length to calculate the relative axon and dendrite home column features (features 44–45), respectively. Similarly, lengths of the axon and dendrite outside the home column (D2) were normalized by the total axon and dendrite length to calculate the relative axon and dendrite septa/adjacent column features (features 46–47), respectively. Figure A.3 (fifth row; top to bottom) presents a high degree of heterogeneity of these features across cortical layers, providing insight into the projection patterns of axonal and dendritic structures within and outside the home column.

4.2 Electrophysiology

In order to characterize the electrophysiological properties of inhibitory neurons in rat barrel cortex, I first defined ten electrophysiological datasets that captured essential aspects of neuron physiology, similarly as in Gouwens *et al.* (2019). I then applied sparse principal component analysis (SPCA) to each electrophysiological dataset in order to extract a total of 31 descriptive features. These features provide a comprehensive characterization of the electrophysiological properties of inhibitory neurons. To perform the necessary calculations, I utilized MATLAB (The MathWorks Inc., Natick, MA, USA) along with the SpaSM toolbox (Sjöstrand *et al.*, 2018). Tables 4.2 and 4.3 provide the definitions of the datasets and sparse features, respectively. Figures A.4–A.5 display the distribution of these sparse features as a function of cortical layer for 303 inhibitory neurons with available 100 Hz voltage trace.

4.2.1 Descriptive datasets

I characterized electrophysiological properties of inhibitory neurons using ten different datasets, similarly as in Gouwens *et al.* (2019). The first dataset (i.e., AP V_m) consists of the membrane potential (V_m) of the first action potential (AP) for each inhibitory neuron. For each 100 Hz voltage trace, I identified the first AP and extracted the voltage from 1 ms before the peak of the AP until 2 ms after it. The total time window was 3 ms (see Table 4.2 for details). Figure 4.1 (top) illustrates the waveforms of the 303 inhibitory neurons sorted by their soma depth, from the pial surface until the white matter. The peak of the first AP of each inhibitory neuron is placed at 3 ms. The second dataset (i.e., AP dV_m/dt; Table 4.2) contains the time derivative of the AP V_m dataset. This dataset captures the rate of change

Dataset name	n	d	p	Definition
AP V_m	303	301	3	Membrane potential (V_m) of first action potential (AP). The time window is 3 ms (with a sampling rate of 100 kHz): 1 ms before the peak of the AP and 2 ms after it.
AP dV_m/dt	303	300	4	Time derivative of AP V_m.
ISI shape	303	100	2	Average of interspike interval (ISI) voltage trajectories, linearly interpolated in time to fit a standardized query of 100 points.
PSTH	303	14	2	Peristimulus time histogram (PSTH) normalized by bin width, with a bin width of 50 ms.
Inst. firing rate†	303	35	4	Instantaneous firing rate as the inverse of each ISI.
AP peak†	303	35	4	For each AP, the maximum V_m value.
AP threshold†	303	35	3	For each AP, the V_m value where dV_m/dt between pre-AP voltage and AP upstroke is maximized. The pre-AP voltage is the V_m value at half-ISI before AP (for first AP, is the half-interval between stimulus onset and AP). The AP upstroke is the maximum value of dV_m/dt between pre-AP voltage and AP peak.
AP fast trough†	303	35	3	For each AP, the minimum V_m value between AP peak and post-AP voltage, where post-AP voltage is the V_m value at half-ISI after AP (for last AP, is the half-interval between AP and stimulus offset).
AP width†	303	35	3	For each AP, the width at half-height.
Up/down ratio†	303	35	3	For each AP, the ratio of AP upstroke to AP downstroke, where AP downstroke is the minimum value of dV_m/dt between AP peak and AP fast through.

continues on next page

Table 4.2: List of datasets describing electrophysiology. Each dataset consists of n neurons representing a particular intrinsic physiological feature of dimensionality d. Dimensionality reduction is applied independently to each dataset, obtaining p sparse principal components (SPCs) with an adjusted explained variance larger than 1%. Note that $1 \leq p \leq d$. When applicable, units of time, frequency, and voltage are in ms, Hz and mV, respectively. † indicates that calculated values are placed at spike times and binned using a regular time window of 20 ms. Values falling in the same bin are averaged. Zero valued bins between non-zero valued bins are linearly interpolated.

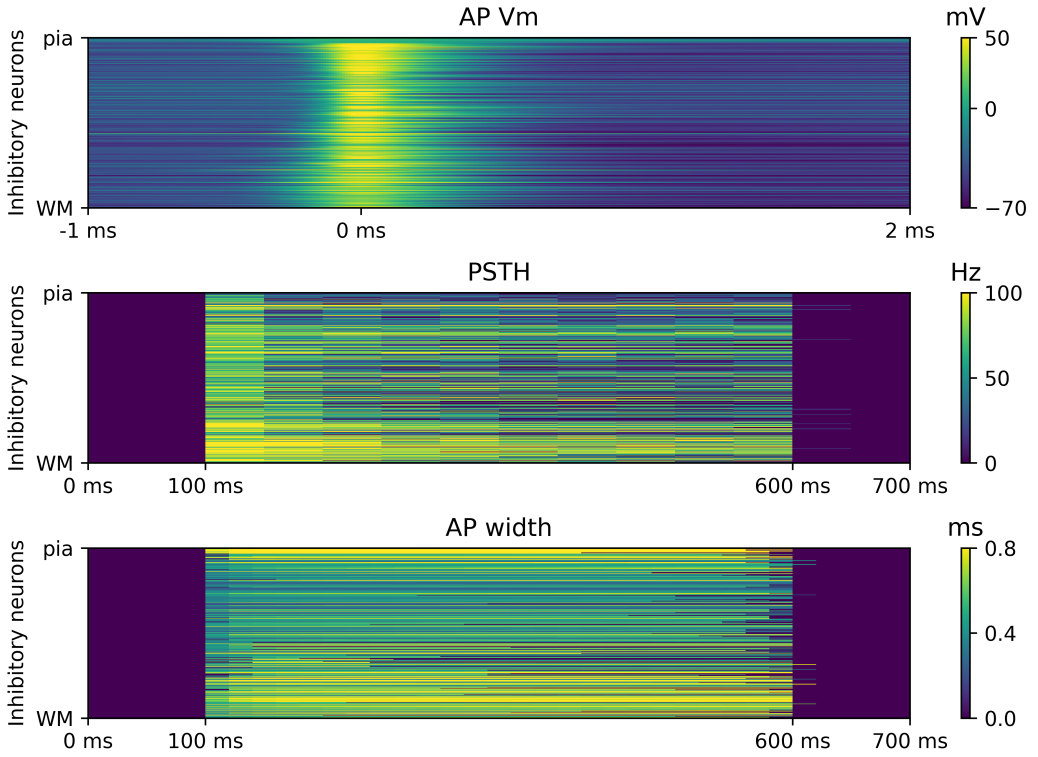

Figure 4.1: Example of three descriptive electrophysiological datasets. In each panel, inhibitory neurons are sorted by their soma depth, from the pial surface until the white matter. Dataset definitions can be found in the text.

of membrane potential during an action potential, providing information about the underlying ion channels and membrane dynamics.

The third dataset (i.e., ISI shape; Table 4.2) comprises the average of all the interspike interval (ISI) voltage trajectories in a given 100 Hz voltage trace. As the trajectories may have different durations, I linearly interpolated in time to fit a standardized query of 100 points. The fourth dataset (i.e., PSTH; Table 4.2) is a peristimulus time histogram (PSTH) that captures the temporal pattern of APs in response to a current injection. It consists of the number of APs over time, with time binned into 50 ms. As the duration of the stimulus of the standardized 100 Hz voltage traces was 500 ms, in this dataset that translates to 10 values. Figure 4.1 (center) shows the PSTHs of the 303 inhibitory neurons sorted by their soma depth. The frequency of sustained responses is gradually increasing as a function of cortical depth. The fifth dataset (i.e., Inst. firing rate; Table 4.2) corresponds to the instantaneous firing rate, which I calculated as the inverse of each ISI for a given 100 Hz voltage trace. To process this dataset, I first placed the calculated values at spike times and then binned them using a regular time window of 50 ms. If multiple values fell within the same bin, I averaged them. If there was a zero-valued bin between non-zero valued bins, I linearly interpolated them. This processing procedure was also applied to the subsequent datasets.

The sixth dataset (i.e., AP peak; Table 4.2) measures the maximum voltage reached during an AP, representing the point at which the V_m reaches its highest value before starting to repolarize back to its resting potential. I calculated the maximum V_m value for each AP in a given 100 Hz voltage trace. Then, I applied the processing procedure for each inhibitory neuron. The seventh dataset (i.e., AP threshold; Table 4.2) measures the V_m value at which an AP is initiated, typically defined as the voltage at which dV_m/dt reaches a certain threshold value, indicating that an action potential is about to occur. I calculated the V_m value where dV_m/dt between pre-AP voltage and AP upstroke, which is the rapid increase in V_m following the AP initiation, is maximized. Then, I applied the processing procedure for each inhibitory neuron. The eighth dataset (i.e., AP fast trough; Table 4.2) measures the point in an AP waveform where the V_m reaches its most negative value after the peak and before the repolarization phase. I calculated the minimum V_m value between AP peak and post-AP voltage. Then, I applied the processing procedure for each inhibitory neuron.

The ninth dataset (i.e., AP width; Table 4.2) measures the duration of an AP at half of its maximum amplitude, reflecting the properties of ion channels that underlie the generation and propagation of APs. I calculated the width at half-height for each AP. Then, I applied the processing procedure for each inhibitory neuron. Figure 4.1 (bottom) presents the AP half-widths of the 303 inhibitory neurons sorted by their soma depth. Neurons with longer AP half-widths have lower maximum firing rates and are more prone to burst firing, while neurons with

shorter AP half-widths have higher maximum firing rates and exhibit more regular spiking behavior (Erisir *et al.*, 1999). The tenth dataset (i.e., Up/down ratio; Table 4.2) corresponds to the upstroke to downstroke ratio. It is a measure of the relative speeds of the rising and falling phases of an AP. I calculated it as the ratio of the maximum rate of rise (upstroke velocity) to the maximum rate of fall (downstroke velocity) of the AP waveform.

These descriptive datasets provide a comprehensive characterization of the electrophysiological properties of inhibitory neurons in rat barrel cortex.

4.2.2 Genetic algorithm

To extract the most important features from each electrophysiological dataset while minimizing the number of variables needed to represent the data, I calculated the electrophysiological features by applying dimensionality reduction independently to each previously defined descriptive dataset. Specifically, I employed SPCA, a technique that enhances interpretability and mitigates overfitting (Tibshirani, 1996; d'Aspremont *et al.*, 2004; Zou *et al.*, 2006; Mairal *et al.*, 2010). By applying SPCA to each dataset and keeping all SPCs with a proportion of explained variance (PEV) larger than 1%, I obtained the most significant features while reducing the dimensionality of the data. The PEV of a particular SPC is the ratio of the adjusted variance of that SPC to the total explained variance using PCA, s^2_{PCA}. Besides the input data, SPCA depends on the number of components and the sparseness of each of those components. As SPCA cannot produce larger PEV than PCA, I defined an upper bound on the number of SPCs via PCA, i.e., I obtained the q PCs satisfying PEV $\geq 1\%$. Then, to cast the level of sparseness for SPCA, I defined a metric that jointly maximizes the goodness-of-fit, adjusted variance, and sparseness. This metric is a sparsity index (SI), maximized via a genetic algorithm (Goldberg, 1989; Conn *et al.*, 1991, 1997) to obtain optimal settings.

Let $\beta \in \mathbb{R}^{n\times q}$ denote the sparse loadings matrix, and $s^2 \in \mathbb{R}^q_+$ its corresponding adjusted variance, then the SI reads as follows

$$\mathrm{SI}(\beta, s^2) = \frac{\mathrm{tr}(\beta^\top \beta)}{s^2_{PCA}} \cdot \frac{\sum_{i=1}^q s_i^2}{s^2_{PCA}} \cdot \left(1 - \frac{\sum_{i=1}^q \mathbb{I}_{\mathcal{B}_i}}{nd}\right) , \tag{4.1}$$

where the first quantity corresponds to the the goodness-of-fit with $\mathrm{tr}(\cdot)$ the sum of the diagonal elements of the square matrix $\beta^\top\beta$, the second one to the total PEV, and the third one to the sparseness where $\mathbb{I}_{\mathcal{B}_i}$ is an indicator function with $\mathcal{B}_i = \{x \,|\, x = \beta_i\}$. This means, $\mathbb{I}_{\mathcal{A}}(x) = 1$ if $x \in \mathcal{A}$, and $\mathbb{I}_{\mathcal{A}}(x) = 0$ otherwise. Finally, the number of SPCs that satisfy the selection criteria would be $p \leq q$.

Dataset name	k	n	Sparsity (%)	PEV-SPCA (%)	PEV-PCA (%)
AP V_m	303	303	0.00	92.28	92.28
	285	303	5.94	4.93	4.94
	225	303	25.74	1.64	1.68
AP dV_m/dt	302	303	0.33	85.36	85.38
	294	303	2.97	8.27	8.27
	226	303	25.41	2.60	2.63
	224	303	26.07	1.53	1.58
ISI shape	301	303	0.66	98.08	98.09
	149	303	50.83	1.17	1.37
PSTH	302	303	0.33	83.01	83.46
	110	303	63.70	5.84	8.38
Inst. firing rate	303	303	0.00	78.52	78.52
	263	303	13.20	11.98	12.19
	96	303	68.32	3.23	3.77
	42	303	86.14	1.34	1.74
AP peak	300	303	0.99	85.89	85.89
	38	303	87.46	5.00	6.07
	41	303	86.47	1.83	2.87
	32	303	89.44	1.10	1.39
AP threshold	301	303	0.66	86.12	86.14
	48	303	84.16	4.97	5.72
	58	303	80.86	2.01	2.82
AP fast trough	302	303	0.33	85.77	85.78
	49	303	83.83	5.41	6.07
	65	303	78.55	2.16	2.92
AP width	300	303	0.99	87.12	87.13
	63	303	79.21	4.98	5.69
	79	303	73.93	2.23	2.90
Up/down ratio	300	303	0.99	85.31	85.34
	72	303	76.24	5.73	6.58
	58	303	80.86	1.74	2.94

continues on next page

Table 4.3: List of sparse features used to characterize the electrophysiology. The number of nonzero elements of a sparse principal component (SPC) is k, whereas the total number of elements is n, with $1 \leq k \leq n$. PEV corresponds to the proportion of explained variance.

4.2.3 Sparse principal components

As presented in Table 4.2, each descriptive dataset was calculated for 303 inhibitory neurons, with dimensionality ranging from 14 to 301. SPCA was applied independently to each dataset, obtaining 31 SPCs with an adjusted explained variance larger than 1%. The number of SPCs obtained for each dataset ranged from 2 to 4.

Table 4.3 lists the sparse features per dataset, providing the number of nonzero elements (k), the total number of elements (n), the degree of sparsity as $1-k/n$ (%), and the PEV using SPCA (PEV-SPCA) and PCA (PEV-PCA), respectively. By maximizing the SI in Equation (4.1), I obtained SPCs with a PEV equivalent to the one produced by PCA (see PEV-SPCA and PEV-PCA in Table 4.3). Specifically, the first dataset, AP V_m, had three sparse features with sparsity levels ranging from 0% (no sparsity) to 25.74%. The second dataset, AP dV_m/dt, had four sparse features with similar sparsity levels to AP V_m, in this case ranging from 0.33% to 26.07%. The third dataset, ISI shape, had two sparse features with sparsity levels of 0.66% and 50.83%, respectively. The fourth dataset, PSTH, had also two sparse features. The sparsity of these features was 0.33% and 63.70%, respectively. The fifth dataset, Inst. firing rate, had four sparse features with sparsity levels ranging from 0% (no sparsity) to 86.14% (very sparse). The sixth dataset, AP peak, had four sparse features. The sparsity of these features ranged from 0.99% to 89.44%, which was the sparsest feature. The seventh dataset, AP threshold, had three sparse features with sparsity levels of 0.66%, 84.16%, and 80.86%, respectively. Note that sparsity is not necessarily a monotonically increasing function. The eighth dataset, AP fast trough, had three sparse features with sparsity levels of 0.33%, 83.83%, and 78.55%, respectively. The ninth dataset, AP width, had three sparse features with sparsity levels of 0.99%, 79.21%, and 73.93%, respectively. The tenth dataset, Up/down ratio, had three sparse features with sparsity levels of 0.99%, 76.24%, and 80.86%, respectively.

Figures A.4–A.5 present the distribution of sparse electrophysiological features by cortical layer. Each row corresponds to the features related to a particular descriptive dataset, whereas the columns to contained SPCs ranging from 1 in the left to 4 in the right. These distributions captured the diversity and complexity of electrophysiological properties of inhibitory neurons, similarly as previously reported in mouse visual cortex (Gouwens *et al.*, 2019, 2020).

4.3 Standardization and selection

After handcrafting a comprehensive list of morphological and electrophysiological features, I performed a standardization and selection process to ensure the quality and relevance of the features used for subsequent analyses.

Firstly, I removed the features with low coefficient of variation ($CV < 0.25$). The coefficient of variation is a measure of the relative variability of a feature, calculated as the ratio of the standard deviation to the mean. Features with low coefficient of variation have little variability and are thus less informative for distinguishing differences between inhibitory neurons. Secondly, I anticipated the potential issue of highly correlated features. When features are highly correlated, they provide redundant information and can lead to overfitting in subsequent analyses. To address this, I selected a representative feature from among highly correlated columns ($r > 0.95$). This ensures that each selected feature provides unique information. Finally, the selected features were z-scored to standardize their values. Z-scoring is a process that transforms the features to have zero mean and unitary standard deviation, allowing for fair comparison and combination of features with different units or scales. This standardization and selection process ensures that the features used for subsequent analyses are informative, non-redundant, and normalized.

4.4 Summary

In this chapter, I characterized the registered axonal and dendritic morphology, as well as spiking responses of a representative sample of 306 inhibitory neurons across all layers of rat barrel cortex. Figure 4.2A illustrates the 47 features I calculated to describe the morphology. To take advantage of the barrel cortex anatomy, I included column-specific features such as the relative amount of axon or dendrites within the registered column. Similarly, Figure 4.2B shows the 31 features I calculated to describe the electrophysiology. To capture different aspects of the voltage traces, I constructed ten time-dependent electrophysiological datasets, and employed SPCA to extract the most important features from each dataset while minimizing the number of variables needed to represent the data. In both panels, neurons were sorted by their soma depth, from the pial surface (top) until the white matter (bottom); layer borders were shown; and features were z-scored. By adopting a characterization approach similar to that used in previous studies on mouse visual cortex (Gouwens *et al.*, 2019, 2020), I am able to make comparisons across species and cortex areas. The characterization of these features provides insight into the overall structure and complexity of cortical inhibitory neurons.

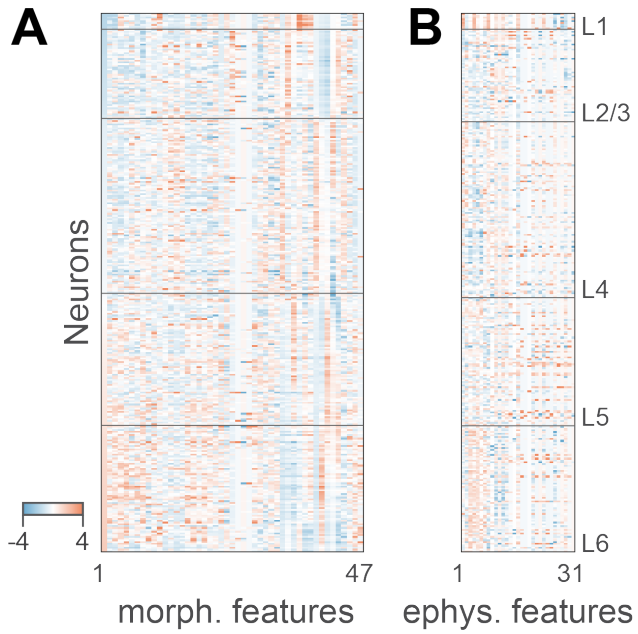

Figure 4.2: Morphological and electrophysiological features. A. Descriptive features ($n = 47$) of the axon and dendrite morphology. Neurons are sorted by cortical depth and values are z-scored. B. Descriptive features ($n = 31$) are sparse principal components (SPCs) of 10 datasets characterizing the electrophysiology.

Chapter 5

Multimodal class assignments

In the pursuit of better understanding the structural organization of the cortex, the classification of neurons into unambiguous cell types is a crucial step. The previous chapters have laid the groundwork for this endeavor by generating a representative dataset and characterizing the single-cell properties of inhibitory neurons in rat barrel cortex. Therefore, unsupervised multimodal clustering based on such descriptive features from a representative cortical column was utilized to capture the complexity and diversity of morphological and electrophysiological properties. As illustrated in Figure 5.1, I combined standardized methods (Gouwens *et al.*, 2019) to assign inhibitory neurons into 20 morphological classes (m-types), 13 electrophysiological classes (e-types), and 25 morphoelectric classes (me-types). The predictability of each clustering modality was evaluated using several classifiers, resulting in robust class assignments. However, none of the classifiers was able to perfectly predict the underlying classes. The distribution of inhibitory neurons indicated that they were predominantly organized by cortical depth. In a collaboration with a group of experts, namely, Prof. Dr. Dirk Feldmeyer (Research Center Jülich and RWTH Aachen University), Dr. Guaxiao Qi (Research Center Jülich), and Dr. Fernando Messore (Max Planck Institute for Neurobiology of Behavior – caesar), the morphology and electrophysiology of these neurons were assessed. Their classification grouped neurons into broader categories, while the multimodal clustering identified more specific subtypes. However, the overall classification of both methods was in agreement, indicating their reliability and validity in identifying distinct classes. Thus, the classification analysis allowed me to identify robust e-, m-, and me-types consistent with those reported for mouse V1 (Gouwens *et al.*, 2019, 2020).

The most important methodological results from Chapter 5 are:

- The robust classification into 20 m-types, 13 e-types, and 25 me-types using unsupervised multimodal clustering.
- The classification of morphology and electrophysiology by a consensus of experts, revealing broad categories independent of cortical depth.
- A similar classification as reported in mouse visual cortex (Gouwens *et al.*, 2019, 2020), allowing for comparisons across species and cortex areas.

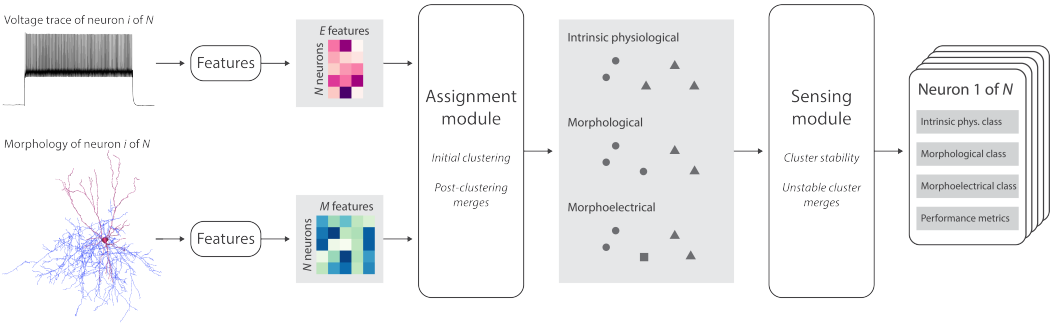

Figure 5.1: Diagram of the multimodal clustering method. (1) Descriptive features are calculated from a given morphology and voltage trace. (2) The assignment module performs a preliminary clustering step dependent on the data modality, followed by a reduction of the number of clusters using an entropy criterion. (3) The sensing module evaluates cluster stability by resampling the data, followed by an entropy criterion to merge unstable clusters. (4) The outputs are class assignments and performance metrics per data modality.

5.1 Morphology

Morphology is a fundamental modality of inhibitory neurons that provides insights into their role in cortical circuits. The characterization of dendritic and axonal morphologies reflects where the inputs to a particular inhibitory neuron are coming and where the outputs are projecting, respectively. Therefore, the classification of inhibitory neurons based on their morphology is an essential step towards understanding the organization and function of cortical circuits.

5.1.1 Classification

Machine

Figure 5.1 presents the general approach to cluster inhibitory neurons. The 47 morphological features used to characterize the 302 inhibitory neurons with both axonal and dendritic reconstructions were analyzed to ensure the quality and relevance of the features used for morphological clustering. A total of six features were removed because of low coefficient of variation ($CV < 0.25$). These features were: *axon mean contraction* (ID: 20), *dendrite mean contraction* (ID: 21), *dendrite overlapping axon* (ID: 26), *soma axon x-percentile* (ID: 31), *soma dendrite x-percentile* (ID: 32), and *axon home column* (ID: 44). IDs are according to Figures A.1–A.3. There were no highly correlated features ($r > 0.95$). Thus, the 41 remaining features were z-scored and then used for morphological class assignment.

The assignment module utilized the 41 features to calculate an initial cluster assignment by (i) creating a dendrogram using Ward's agglomeration method, and (ii) cutting this hierarchical tree where the variation between-clusters is maximized and the variation within-clusters is minimized (Langfelder *et al.*, 2007; Gouwens *et al.*, 2019). As a result, 17 clusters were initially identified. No reduction of the number of clusters using an entropy criterion was applied.

The sensing module was performed to identify robust clusters. I implemented an iterative hierarchical clustering algorithm that splits the number of inhibitory neurons in 10 consecutive folds and uses 90% of the data to assign clusters (Gouwens *et al.*, 2019). This step was repeated 100 times, each with a different seed. Thus, 1000 instances of cluster assignments with 90% of the inhibitory neurons were available. Each instance was compared with the initial cluster assignment to calculate the proportion that every pair is grouped in the same cluster. This information allowed the production of a co-clustering diagram that was used as a distance matrix to ultimately perform (i) and (ii). No merge of unstable clusters using an entropy criterion was applied. As a result, 20 robust morphological clusters were identified.

Human

In order to collect the information that has been commonly used to characterize the diversity of inhibitory neurons (Ascoli *et al.*, 2008; DeFelipe *et al.*, 2013), I implemented an evaluation system using MATLAB App Designer. Figure 5.2 presents the morphological assessment of an example inhibitory neuron performed by a human expert. The axon of the registered morphology is displayed in blue, whereas the dendrites and soma in red. The home (darker shade) and adjacent (lighter shade) columns are displayed in gray. The D2 column is placed at the center, the D1 column at the left, and the D3 column at the right. The average layer borders are also illustrated.

For each of the 306 inhibitory neurons, the self-identified user had to first determine the *Soma location*. The discrete options were: L1, L2/3, L4, L5, and L6. In the example in Figure 5.2, it was located in L5. This item served the purpose of distinguishing valid evaluations. Then, the *Axon laminar distribution* was categorized into two groups: intralaminar and translaminar. Intralaminar refers to axons that are constrained to a single layer, while translaminar indicates that the axon projects across layers. The *Confidence* had to be provided as well: High, Moderate, Slight, or No. This confidence rating also applied to the subsequent evaluation items. In the example in Figure 5.2, it was evaluated as translaminar with high confidence as the axon is predominantly projecting from L5 to L1.

The *Axon horizontal distribution* was also categorized into two groups: intracolumnar and transcolumnar. Intracolumnar refers to axons that are constrained to the home column, while transcolumnar indicates that the axon projects beyond to adjacent columns. In the example in Figure 5.2, it was evaluated as intracolumnar with high confidence as the axon is predominantly in the home column, even though, there are some weak projections to neighboring columns in L1. Then, the *Axon/dendrite relative location* was categorized into centered versus displaced. Centered refers to the dendritic arborization is predominantly located in the center of the axonal arborization, while displaced indicates that the dendritic arborization is shifted with respect to the axonal arborization. In the example in Figure 5.2, it was evaluated as centered with moderate confidence as both arbors are mostly aligned with respect to the home column.

The *Large group classification* comprised types such as small basket, large basket, bitufted, chandelier, Martinotti, and neurogliaform cells. Small basket cells have a local and dense axonal arborization, whereas their dendrites are typically short and simple, with little branching. Large basket cells are similar to small basket cells, but with transcolumnar and translaminar axonal arborization, and their dendrites are typically longer and more complex. The bitufted cells category also comprises bipolar and double bouquet cells. They are characterized by having two primary dendritic shafts that emerge from opposite poles of the soma and extend in differ-

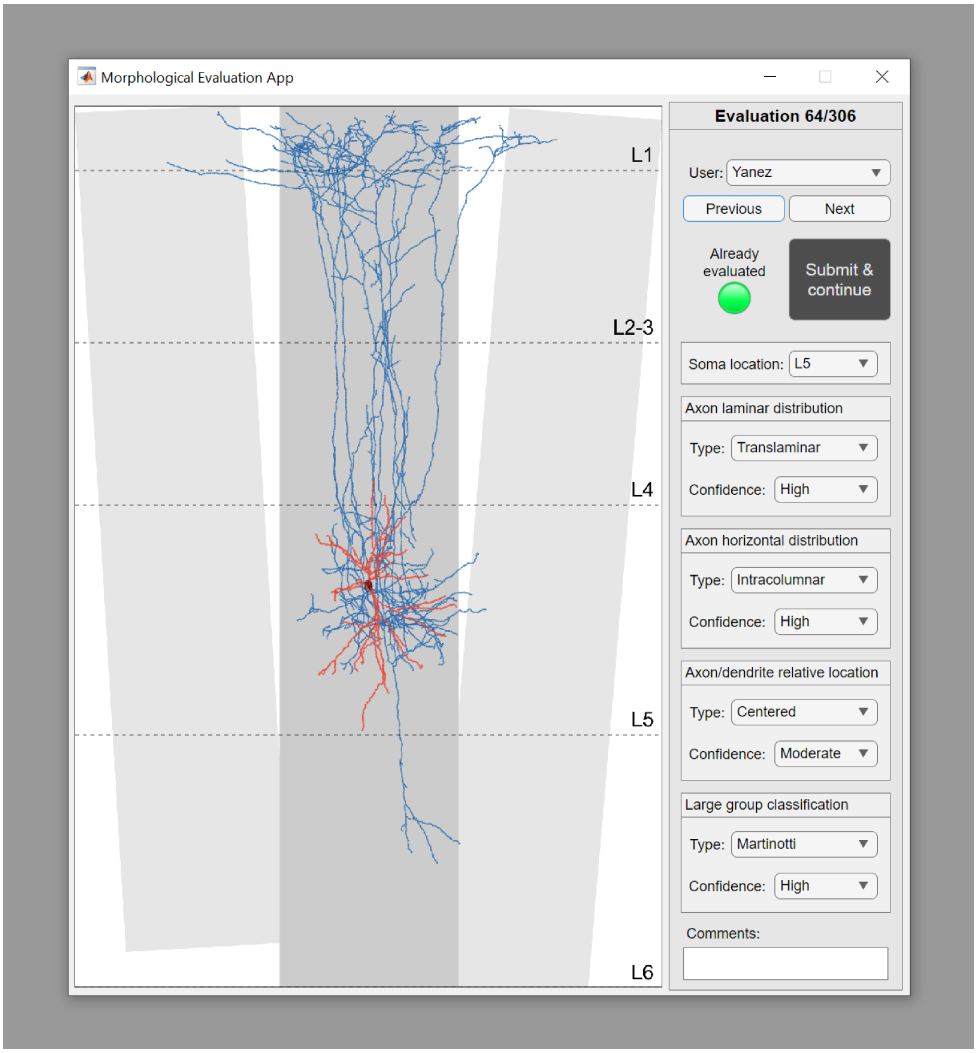

Figure 5.2: Morphological assessment of an example inhibitory neuron performed by a human expert. A detailed description of the system can be found in text.

ent directions, giving them bipolar or bitufted appearances. Double bouquet cells have a similar morphology, but with a more complex dendritic arborization that resembles two bouquets of flowers. Chandelier cells have a unique axonal morphology, with highly dense arborizations and hundreds and even thousands of branches. Their dendrites are typically above their axonal arborization. Martinotti cells are predominantly characterized by their ascending axon collaterals projecting up to L1, and their dendrites are typically local. Finally, neurogliaform cells have dense and highly branched axonal arborizations that are mainly local, and their dendrites are typically short and simple. In the example in Figure 5.2, it was evaluated as a Martinotti cell with high confidence because of the multiple axon collaterals projecting up to L1.

To conclude, there was also a text entry for comments, and inhibitory neurons were evaluated in a random order, initialized with Other and No when applicable.

5.1.2 Visualization

A representative morphology of each m-type is illustrated in Figure 5.3. Axons are displayed in lighter shades, whereas dendrites in darker shades. As previously reported (Gouwens *et al.*, 2019, 2020), m-types were predominantly depth-dependent. For instance, in the supragranular layer (i.e., L1-3), five classes were obtained (Figure 5.3; M01-05). M01 ($n = 10$) was the only m-type with neuron somata in L1. This m-type was characterized by extended horizontal axons and small dendrites. In L2/3, we observed two major groups: local (Figure 5.3; M02 and M05) and vertically-projecting (Figure 5.3; M03-04). The class M02 ($n = 19$) comprised both Martinotti and basket-like inhibitory neurons. The classes M03 ($n = 17$) and M04 ($n = 9$) resembled bipolar-like morphologies. The soma depth of the representative example of M05 ($n = 15$) was located in L2/3, however, this class spanned L2-L6. This m-type had local axons and small dendrites, resembling neurogliaform cells.

In the granular layer (i.e., L4), five classes were obtained (Figure 5.3; M06-10). The average axonal field span seemed to be monotonically increasing from M06 to M10. M06 ($n = 26$) and M07 ($n = 8$) had small local axonal and dendritic arborizations, whereas M08 ($n = 18$) and M09 ($n = 10$) had larger morphologies. The class M10 ($n = 27$) had large translaminar axons.

In the infragranular layer (i.e., L5-6), ten classes were obtained (Figure 5.3; M11-20). M11 ($n = 27$) and M12 ($n = 17$) were predominantly located in L5. These m-types were characterized by large transcolumnar axons. The classes M13 ($n = 6$), M14 ($n = 5$), and M15 ($n = 19$) were mainly L5 inhibitory neurons with large translaminar axons projecting to the supragranular layer. The soma depth of the representative example of M16 ($n = 4$) was located in L5, however, this class spanned L2-L6. M16 had dense local axonal arborizations as well as large dendrites above the axon, resembling the characteristic morphologies of chandelier

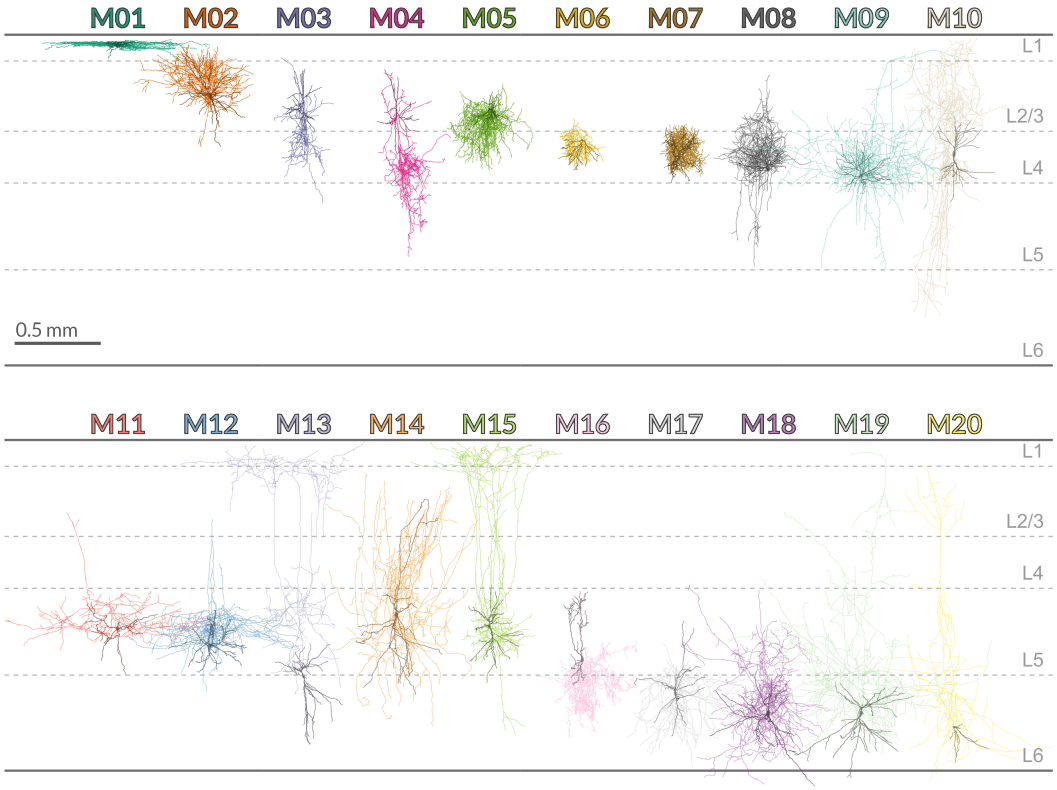

Figure 5.3: Representative example of each morphological class assignment (m-type). Axons in lighter shades; dendrites in darker shades. See text for details.

cells. The remaining m-types were to a great extent located in L6. The average axonal field span seemed to be monotonically increasing from M17 to M20. The classes M17 ($n = 12$) and M18 ($n = 22$) had large axonal and dendritic arborizations, whereas M19 ($n = 9$) and M20 ($n = 22$) had large tranlaminar axons projecting to the supragranular layer.

Thus, m-types displayed heterogeneous patterns of variation across layers, but similar relationships of this heterogeneity seemed to be present in each layer.

5.1.3 Evaluation

The clustering quality of the identified m-types was first assessed by performing the same analysis as reported in the mouse visual cortex (Gouwens *et al.*, 2019). Table 5.1 presents the out-of-bag prediction accuracy of a random forests classifier (OOB), and the leave-one-out cross-validation of a support vector classifier (LOO). OOB is calculated using the samples that are not used in training each decision tree in a random forest, while LOO is calculated by leaving out one sample at a time from the training set and testing the classifier on it. The results from this dissertation ($n = 302$) are remarkable, outperforming (Gouwens *et al.*, 2019, $n = 207$) by almost a 10% margin in each metric. A factual difference with the mouse study was the integration of the dendrite depth histogram and column features. This demonstrated the robustness of the m-types in rat barrel cortex.

Then, I continued the assessment by performing a 5-fold cross-validation across several classifiers with very different structures (Pedregosa *et al.*, 2011), meaning that they can represent the data in different ways. A 5-fold cross-validation means that the morphological features were split into 5 consecutive folds with 80% of the data used for training a classifier, and the remaining 20% to test its accuracy. The accuracy score reflects how well a particular model structure can explain the relations between morphological features and m-types. Figure 5.4 illustrates the performance of seven different classifiers, namely, a linear support vector classifier (Linear SVM), a multi-layer perceptron classifier with $\alpha = 1$ and 1000 maximum iterations (Neural Network), a Gaussian process classifier (Gaussian Process), a random forest classifier with 500 estimators (Random Forest), a 5-nearest neighbors classifier (Nearest Neighbors), a naive Bayes classifier (Naive Bayes), and a decision tree classifier with a maximum tree depth of 500 (Decision Tree). The theoretical chance level was computed as the inverse of the number of m-types ($n = 20$). This means, 5.0%. The results utilizing the original m-types as labels are shown in a lighter shade of gray, whereas with shuffled m-types in a darker shade. Figure 5.4 shows that a high performance is achieved independently of the classifier. For instance, the median accuracy of the linear SVM was 87%. If the m-types are shuffled, then the performance drops to chance level. Thus, these results further corroborate the robustness of these m-types in rat barrel cortex.

Study	OOB (%)	LOO (%)
Gouwens *et al.* (2019)	70	79
This dissertation	79.5	88.1

Table 5.1: Robustness assessment of morphological class assignments between mouse visual cortex (Gouwens *et al.*, 2019), and rat barrel cortex (this dissertation). OOB: random forests classifier out-of-bag prediction accuracy; LOO: support vector classifier leave-one-out cross-validation.

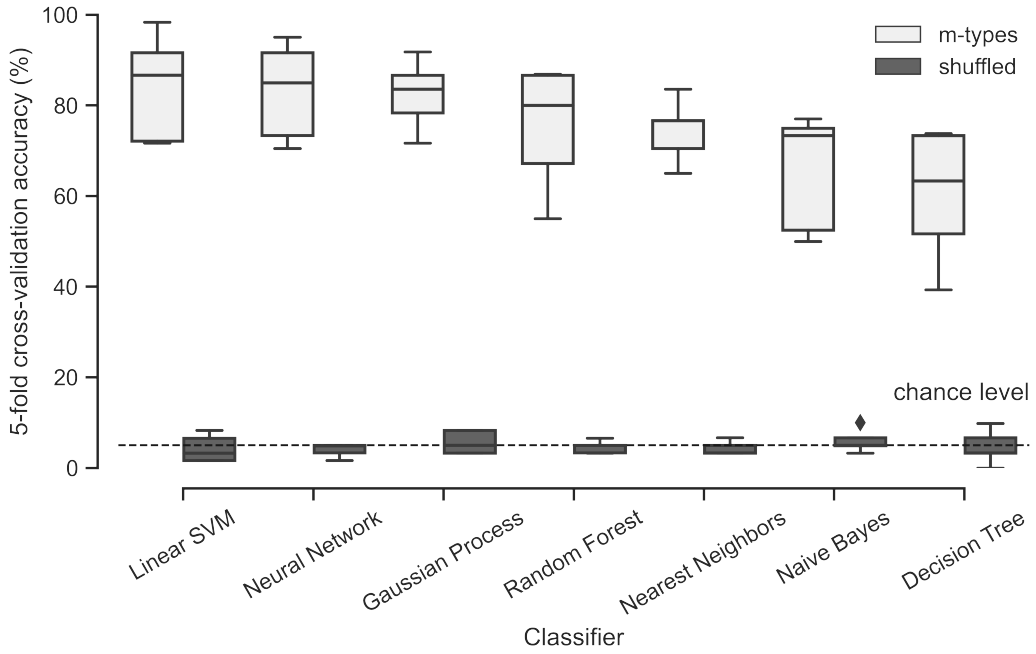

Figure 5.4: Predictability evaluation of morphological class assignments (m-types) utilizing 5-fold cross-validation accuracy. Chance level is the inverse of the number of m-types, i.e., 5.0%. Further details can be found in the text.

In order to further explore patterns and relationships in the high-dimensional morphological data, I visualized it in a two-dimensional space using a uniform manifold approximation and projection (UMAP) algorithm (McInnes *et al.*, 2018). This technique is particularly useful for this purpose because it aims to preserve both the global and local structure of the data. The 41 z-scored morphological features used for classification were embedded using 50 nearest neighbors, a minimum distance of 0.2, and a cosine similarity metric (McInnes *et al.*, 2018). Figure 5.5 presents the produced morphological UMAP (m-UMAP) color-coded according to the 20 different m-types. Each point on the m-UMAP represents an inhibitory neuron, which clusters together with neurons of the same m-type, forming three distinct supraclusters: M01-05, M06-10, and M11-20. These supraclusters resemble the morphological organization of the supragranular, granular, and infragranular layers, respectively. Similar m-types are located close to each other in the m-UMAP. For instance, in the supragranular cluster, M03 and M04 are overlapping and are located opposite to M02 and M05. In the granular layer, m-types with smaller axonal arborization (M06-07) show some overlap and are generally more distant from m-types with larger arborization (M08-10). However, there is still some degree of overlap between these groups. In the infragranular layer, this effect is also present, with m-types having small axon vertical extent (M11-12 and M16-17) being located close to each other in the m-UMAP, while m-types with large axon vertical extent (M15 and M19-20) are more distant. There seems to be a transition between the small and large m-types, as M13-14 and M18 have either *intermediate* axon vertical extent, or a combination of small and large.

I then investigated the role of different features in the morphological organization of inhibitory neurons. For this purpose, I calculated the Gini impurity per feature produced by a random forest classifier with 500 estimators (Pedregosa *et al.*, 2011). The index was computed as percentage to serve as a proxy of relative importance. Figure 5.6A presents such a relative importance for the 41 morphological features sorted in descending order. The soma depth is the most important feature, followed by the principal components (PCs) of axon and dendrite depth histograms. These results are consistent with those of (Gouwens *et al.*, 2019), who also found the soma depth and the PCs of the axon histograms to be the most important features. Note that in their study, the PCs of the dendrite depth profiles were not part of the features set. Figure 5.6B illustrates the top six features color-coding the m-UMAP. *Soma depth* (6.28%) encoded a smooth gradient across the three supraclusters. Then, the *axon* (4.80%) and *dendrite* (4.69%) *histograms PC1* were most informative in distinguishing the granular layer in the data. *Dendrite histogram PC3* (4.48%) was able to identify L5, whereas *PC2* (4.31%) did the same with L6. Similarly, *axon histogram PC2* (3.96%) separated the supragranular layer from the rest of the data. Altogether, it seems that the primary role of morphological features in the organization of inhibitory is to distinguish cortical layers.

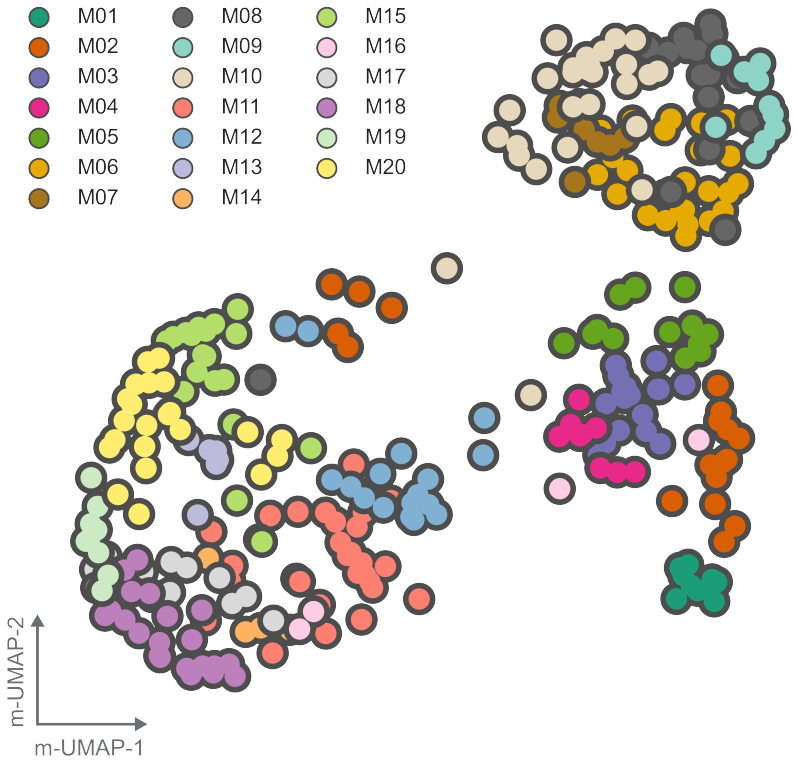

Figure 5.5: Low-dimensional morphological embedding (m-UMAP) color-coded by morphological class assignments (m-types).

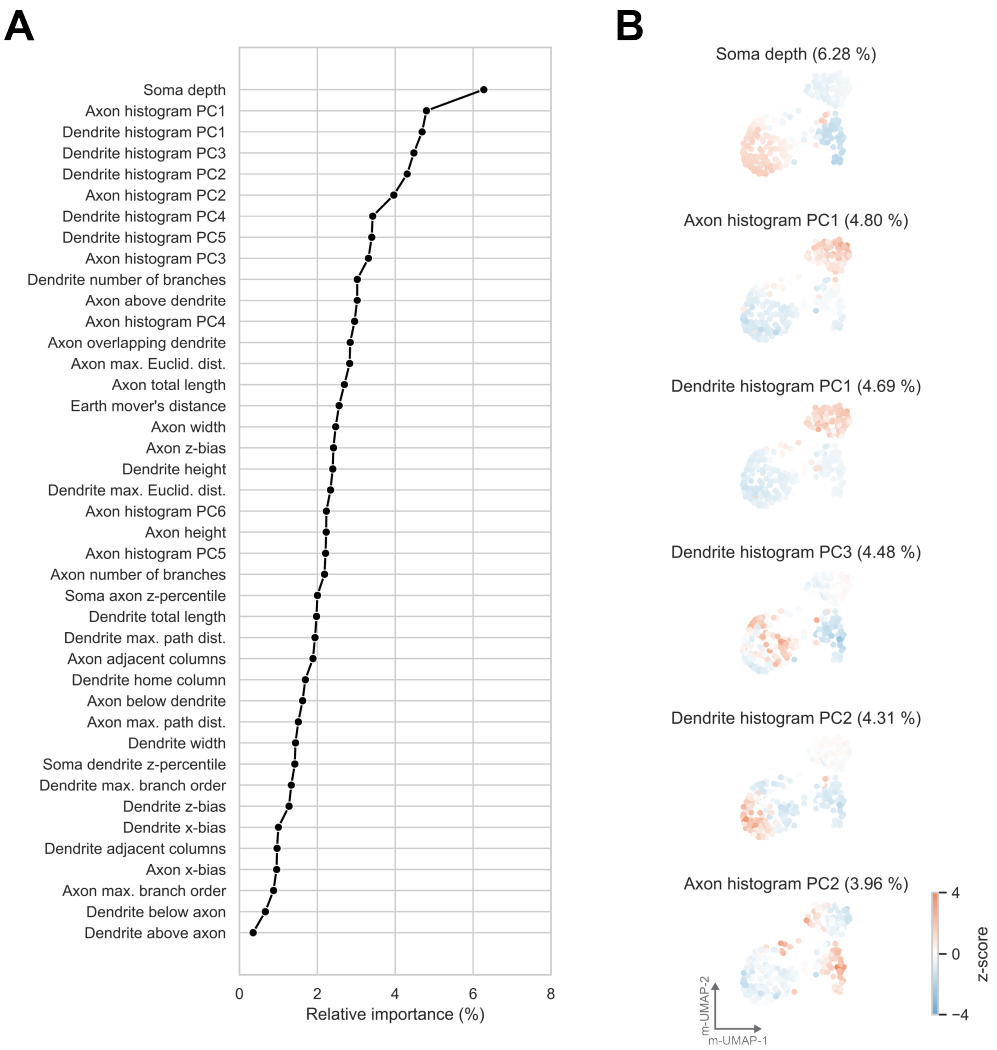

Figure 5.6: Relative importance of morphological features. A. Gini impurity index. B. Features-based projection color-coded by specific features. Details in text.

To assess the laminar organization of m-types, I reorganized Figure 5.5 by cortical layers, resulting in Figure 5.7. This new figure shows m-UMAPs colored inhibitory neurons according to m-types in the original figure. In each cortical layer, only the inhibitory neurons within that layer are colored, while all other neurons are displayed in gray. For instance, in L1 ($n = 9$) all neurons corresponded to one m-type (M01). In L2/3, 9 m-types were found among the 50 neurons: 1 neuron corresponded to M01, 14 to M02, 17 to M03, 7 to M04, 7 to M05, 1 to M06, 1 to M10, 1 to M11, and 1 to M16. Then, in L4 ($n = 98$), 12 m-types were found: 4 neurons corresponded to M02, 2 to M04, 25 to M06, 8 to M07, 18 to M08, 8 to M09, 26 to M10, 3 to M12, 1 to M13, 1 to M14, 1 to M15, and 1 to M18. In L5, 11 m-types were found among the 74 neurons: 1 neuron corresponded to M02, 5 to M05, 2 to M09, 20 to M11, 14 to M12, 3 to M13, 1 to M14, 17 to M15, 2 to M16, 1 to M19, and 8 to M20. Finally, in L6 ($n = 71$), 10 m-types were found: 3 neurons corresponded to M05, 6 to M11, 2 to M13, 3 to M14, 1 to M15, 1 to M16, 12 to M17, 21 to M18, 8 to M19, and 14 to M20.

In each cortical layer, a similar diversity of inhibitory neurons was observed. This suggests that the variety of inhibitory neurons (e.g., local versus translaminar) is consistently distributed across layers, with each layer comprising a broad range of m-types. For example, in L1, all inhibitory neurons corresponded to a single m-type, but as I delved deeper into the layers, a consistent level of diversity was observed. Interestingly, the original source of the underlying morphologies (Egger *et al.*, 2015; Helmstaedter *et al.*, 2009b,c; Koelbl *et al.*, 2015; Emmenegger *et al.*, 2018; Arzt *et al.*, 2018, and new data) did not dominate the definition of m-types. Although some m-types are restricted to a specific cortical layer, others span across them. It appears that m-types tend to form supraclusters around supragranular, granular, and infragranular layers rather than being organized by the original data sources.

Figure 5.8 illustrates the depth distribution at 50 µm bins of each m-type, further supporting the previous observations. By examining the distribution of m-types along the cortical depth, it becomes evident that certain m-types are more prevalent at specific depths, while others are more broadly distributed. For instance, some m-types, such as M01 and M03, are primarily found in superficial layers, whereas m-types like M17 and M20 are more commonly observed in deeper layers. This depth-dependent distribution of m-types provides valuable insights into the organization of inhibitory neurons, and supports the notion that m-types tend to form supraclusters around supragranular, granular, and infragranular layers, rather than being organized by the original data sources.

The comparison of m-types with the classification of human experts is important for better understanding the structural organization of inhibitory neurons. Machine classifiers offer objective criteria for identifying complex patterns, but they can be brittle and highly dependent on the selection of relevant features provided

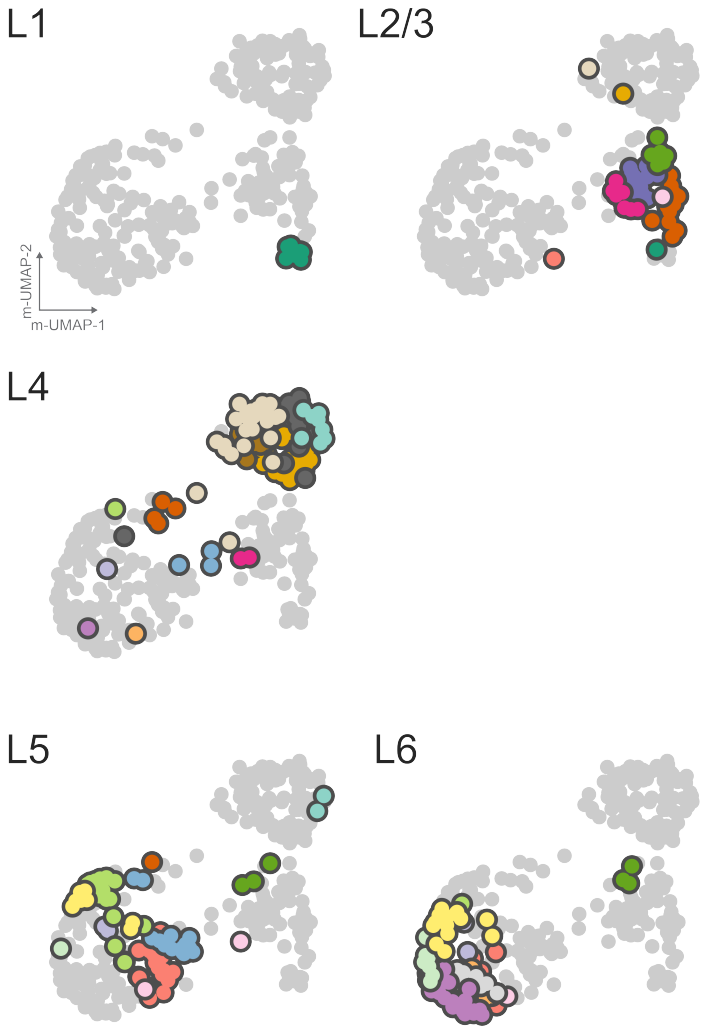

Figure 5.7: Morphological class assignments (m-types) by cortical layer. The features-based embedding and colors used for m-types are according to Figure 5.5.

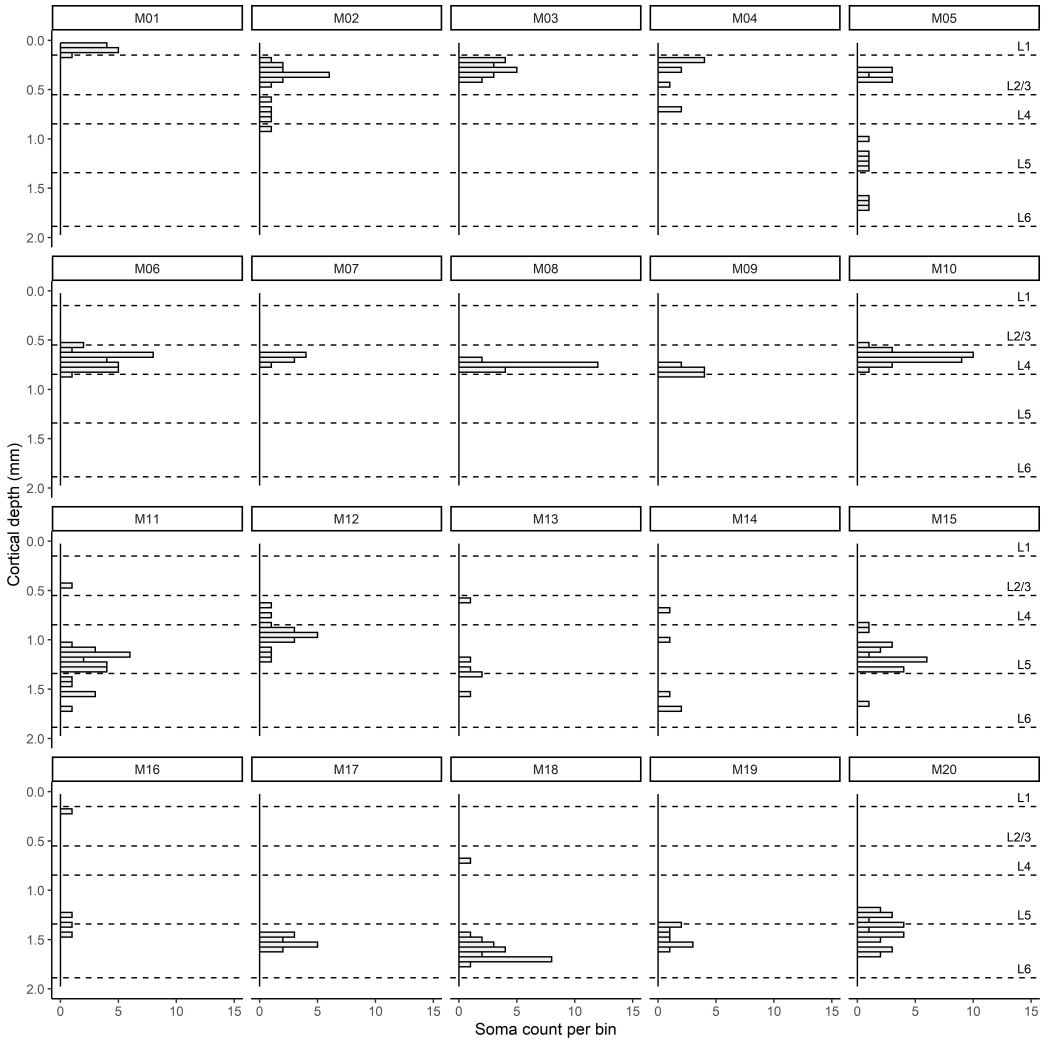

Figure 5.8: Depth distribution of morphological class assignments (m-types).

to them. On the other hand, human experts can leverage their knowledge and experience to identify subtle morphological features, however, their classifications can be subjective (DeFelipe *et al.*, 2013). In this context, Figure 5.9 illustrates a contingency matrix that compares m-types with the judgments made by human experts. The contingency matrix shows the frequency distribution of the two classification methods, with 20 m-types and 6 classes for human expert classifications. The judgments made by human experts are a consensus of heterogeneous evaluations that I curated, using only the *large group classification* item (see details in Figure 5.2) for this analysis. The remaining items are not presented in this dissertation. The comparison between m-types and human expert classifications revealed a relatively clear agreement for neurogliaform, bitufted (including bipolar and double bouquet), and chandelier cells. However, the agreement was less clear for small and large basket cells, as well as Martinotti cells. Interestingly, small basket cells were found to be primarily related to m-types located in superficial layers, whereas large basket cells were associated with m-types located in the deep layers.

To quantitatively assess the agreement between the two approaches, several statistical measures were computed: the Rand index adjusted for chance (ARI), the adjusted mutual information (AMI), and the F1 score. The ARI measures the similarity between two class assignments, adjusted for chance. An ARI value of 0.11 indicates a relatively low level of agreement between them. The AMI is another measure of the agreement, which takes into account the amount of information shared between them. An AMI value of 0.29 suggests a moderate level of agreement. The F1 score is a harmonic mean of precision and recall, which measures the balance between the two. In this context, an F1 score of 0.84 indicates that, despite the moderate level of agreement, the m-types have a high accuracy in predicting the human-assigned classes for a significant portion of the inhibitory neurons.

Morphology is necessary for understanding the role of inhibitory neurons in cortical circuits. I utilized an unsupervised clustering approach to identify 20 robust m-types. They are predominantly depth dependent. Human expert judgements were compared against m-types, revealing a good overall agreement.

5.2 Electrophysiology

Electrophysiological properties of inhibitory neurons are important for understanding their functional roles in cortical circuits. The intrinsic physiology of these neurons reflects how they integrate incoming signals and generate output signals. By identifying distinct electrophysiological classes, insights into their biophysical composition can be obtained, which is an essential step towards understanding the organization and function of cortical circuits.

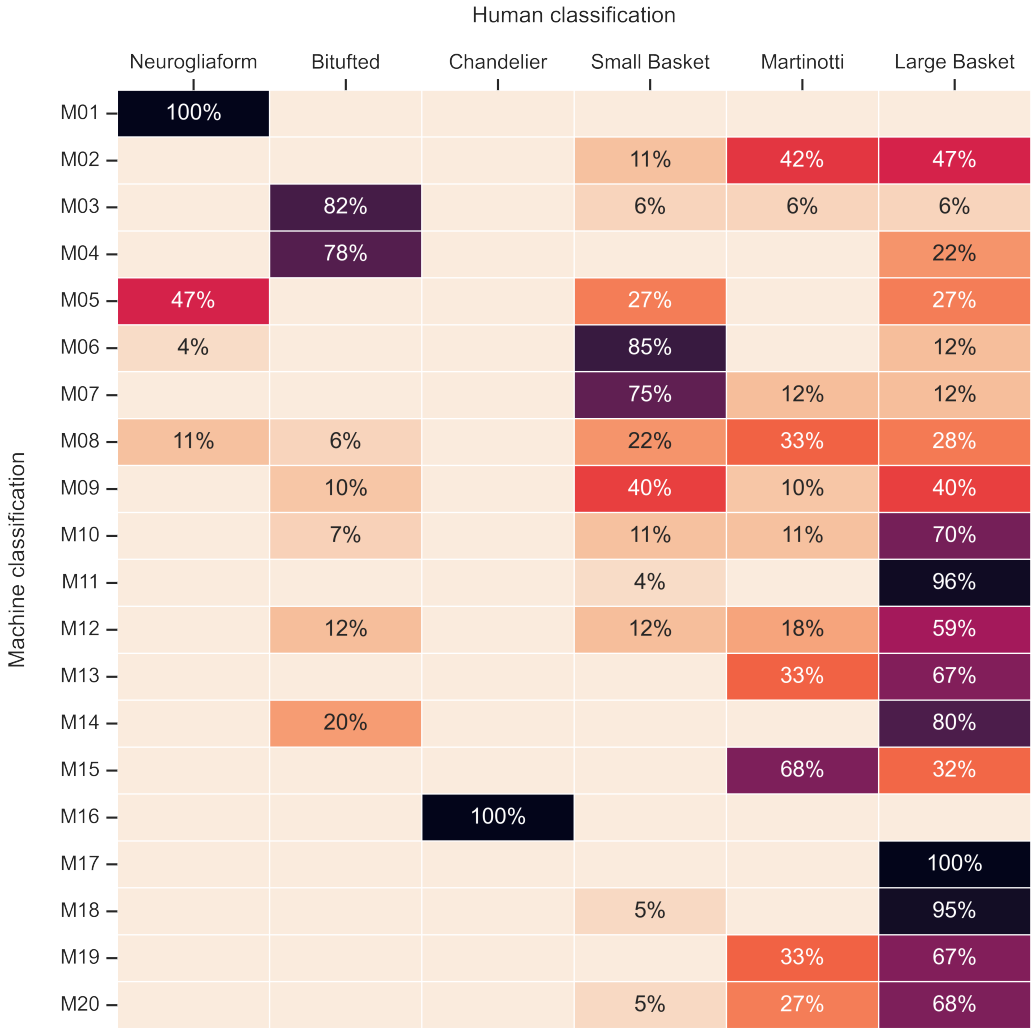

Figure 5.9: Contingency matrix comparing human (Gardner) and machine (features-based) class assignments. Numbers indicate neuron count per class.

5.2.1 Classification

Machine

Following the approach illustrated in Figure 5.1, I utilized the 31 electrophysiological features extracted from the 100 Hz voltage traces of 303 inhibitory neurons. No features were removed from this analysis (Gouwens *et al.*, 2019).

The assignment module employed those features to calculate an initial cluster assignment by fitting a Gaussian finite mixture and performing model-based clustering (Scrucca *et al.*, 2016; Gouwens *et al.*, 2019), with a *VEI* model (i.e., diagonal, varying volume, equal shape) and a maximum of 60 mixture components. The initial clustering identified 20 clusters, some of which contained as few as two inhibitory neurons. I then merged them into a smaller number of clusters using the entropy criterion described in Gouwens *et al.* (2019). The post-clustering merges reduced the number of clusters to 18.

The sensing module was performed to identify robust clusters. To assess cluster stability, I used the Jaccard similarity, which measures the similarity between two cluster sets as the ratio of the size of their intersection to the size of their union (Jaccard, 1901). This metric was calculated 100 times, each time randomly selecting 90% of the inhibitory neurons (Hennig, 2007; Gouwens *et al.*, 2019). Then, each cluster was specified as stable or unstable based on its mean Jaccard similarity. Five unstable clusters were identified and assigned to the most similar stable cluster using an entropy criterion, following the approach described in Gouwens *et al.* (2019). As a result, 13 robust electrophysiological clusters were obtained.

Human

Following the schema of the morphological assessment presented in Figure 5.2, I collected the information commonly used to characterize the diverse electrophysiology of inhibitory neurons (Ascoli *et al.*, 2008; DeFelipe *et al.*, 2013). For each of the 303 inhibitory neurons, the self-identified user evaluated the corresponding 100 Hz voltage trace on four items.

The first one was to determine whether their firing patterns were *fast* or not. *Fast-spiking* refers to neurons that can fire at frequencies greater than 50 Hz (Ascoli *et al.*, 2008) with little or no accommodation (decrease in frequency over time). The second one was to determine whether their firing patterns were *adapting* or not. *Adapting* refers to a firing pattern where the initial high-frequency firing rate decreases over time during a sustained depolarizing current injection. The third one was to determine whether their firing patterns were *irregular* or not. *Irregular-spiking* refers to firing patterns characterized by inconsistent interspike intervals (ISIs). The last one was to determine whether their firing patterns were *continuous* or not. *Continuity* refers to the uninterrupted nature of the firing pattern.

5.2.2 Visualization

Two representative 100 Hz voltage traces of each of the 13 e-types are illustrated in Figure 5.10 (right). To calculate the dendrogram (left), I first applied Principal Component Analysis (PCA) to the electrophysiological feature vectors to obtain a 2-dimensional representation of the data. I then computed the pairwise distances between the group means in this space and used the Ward method for hierarchical clustering. The optimal ordering of the leaves was also taken into account, allowing for the grouping of the electrophysiological features based on their similarity. As expected, the initial firing frequency was consistent across all e-types, with a median value of approximately 100 Hz (Figure 5.11A). In contrast with m-types, e-types are not predominantly depth-dependent (Figure 5.11B).

Based on the dendrogram, the first separation is between FS (E08-13) and non-FS (E01-07) e-types. Figure 5.11C provides quantitative evidence for this description, showing that FS e-types have an average firing rate with a median value greater than 50 Hz, while for non-FS e-types it is lower. The average firing rate was calculated as the ratio between the number of spikes and the stimulus duration in seconds (i.e., 0.5 s). The second separation involved the continuity of the firing pattern. It was assessed by the fraction of the time duration between first and last spikes to the stimulus duration (Figure 5.11D). Then, as E03-13 have a median value larger than 75%, they are considered to have continuous firing patterns, whereas E01-E02 are considered to have irregular or discontinuous firing patterns.

The third separation is between adapting (E03-06) and non-adapting (E07) e-types. As E07 is also continuous, it is described as an e-type with regular-spiking (RS) and non-adapting firing patterns. Figure 5.11E shows the spike-frequency adaptation, which is a measure of how much the firing rate of a neuron changes over time. This metric is calculated by first fitting the instantaneous firing rate (i.e., the inverse of the ISIs), and then computing the difference between first and last fitted frequencies, divided by the first fitted frequency. Adapting e-types, E03-06, displayed a spike-frequency adaptation greater than 80%, whereas all the rest (i.e., E01-02 and E07-13) presented lower median values. Interestingly, some inhibitory neurons had negative values, indicating that they have accelerating firing patterns. Figure 5.11F presents the coefficient of variation (CV) of the ISI, which provides further insight into the variability of spiking patterns among the different e-types. The CV is calculated as the standard deviation of the ISI divided by the mean ISI. FS e-types had the lowest median values, less than one quarter of the standard deviation, indicating low variability in their spiking patterns. In contrast, irregular (except E01) and adapting e-types had the highest median values, indicating high variability in their spiking patterns. No e-type had a median CV larger than one standard deviation.

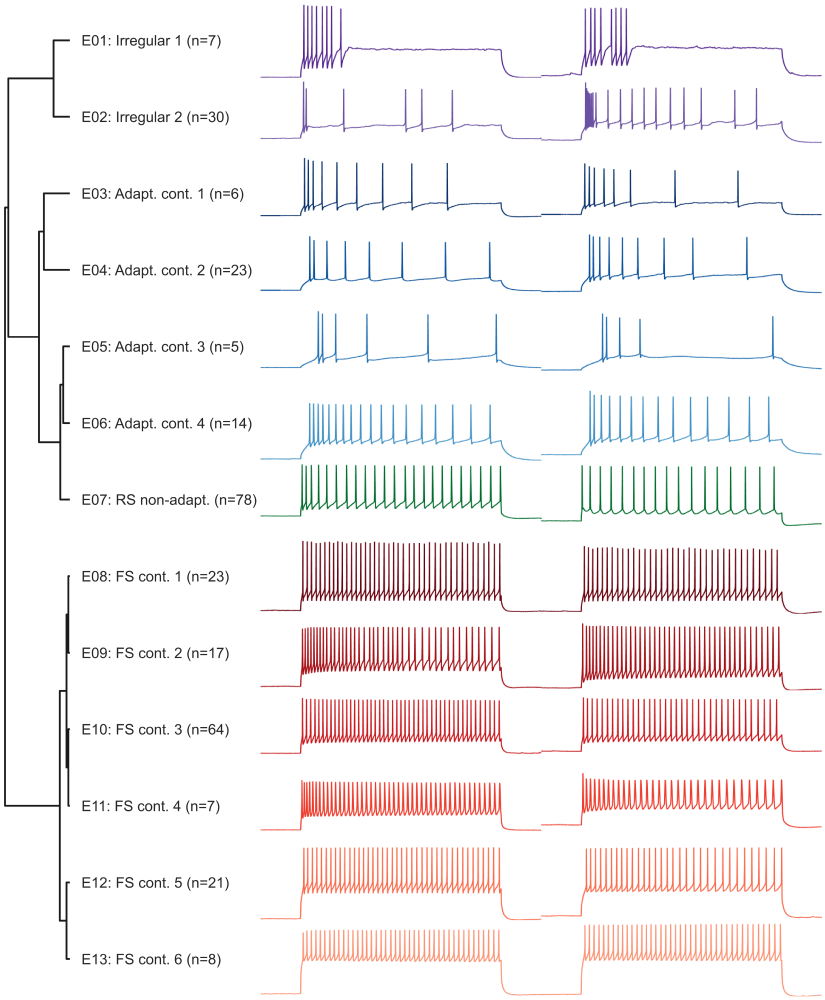

Figure 5.10: Representative examples of each electrophysiological class assignment (e-type). Dendrogram of e-types is based on electrophysiological feature similarity using Ward's method and PCA. Further details can be found in the text.

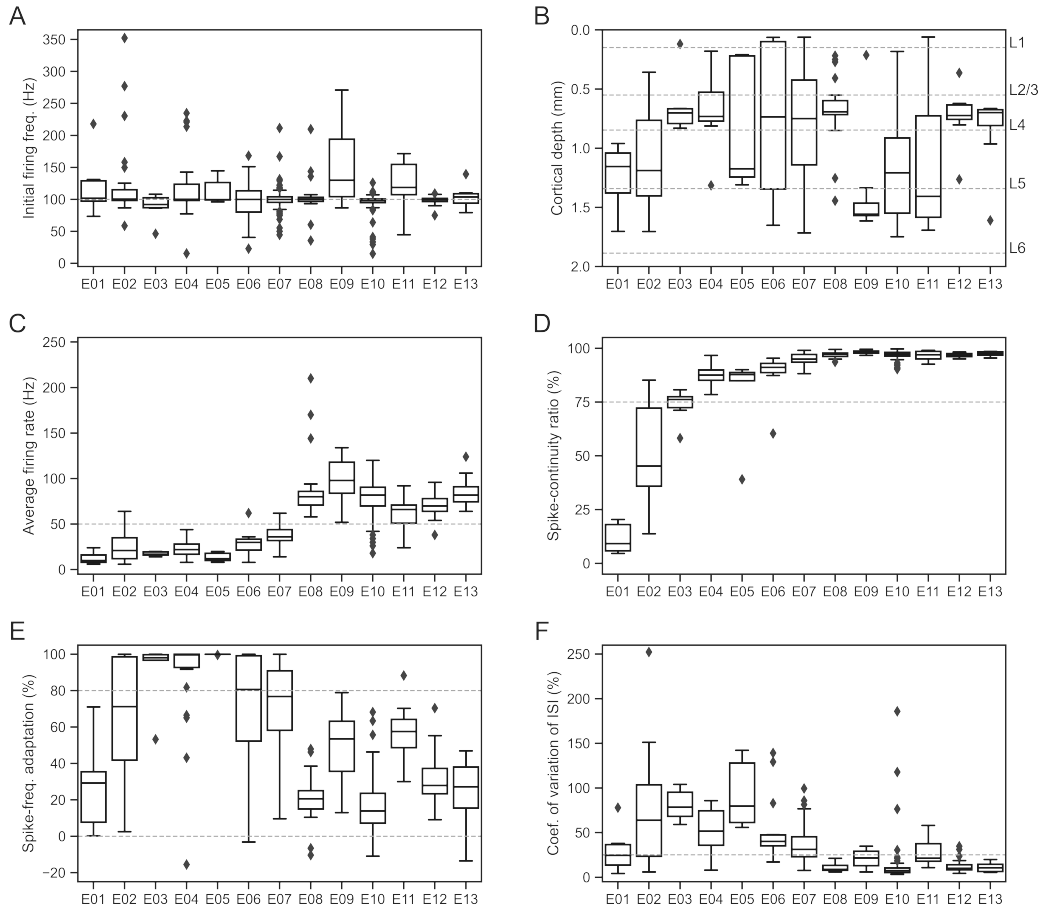

Figure 5.11: Characterization of the firing patterns by electrophysiological class assignments (e-types) using the Petilla terminology (Ascoli *et al.*, 2008). A. Initial firing frequency (Hz). B. Cortical depth (mm). C. Average spike-frequency (Hz). D. Spike-continuity ratio (%). E. Spike-frequency adaptation (%). F. Coefficient of variation of the ISI (%). Definitions and further details can be found in the text.

5.2.3 Evaluation

The clustering quality of the identified e-types was first assessed by performing a 5-fold cross-validation. Figure 5.12 illustrates the classifier performance, following the analysis already presented in Figure 5.4. However, there were two differences in the parameter settings: 1) the neural network had a regularization parameter of $\alpha = 1.1$, and 2) the nearest neighbors classifier used $k = 3$. The theoretical chance level was 7.7%, computed as the inverse of the number of e-types ($n = 13$). High performance is once again achieved independently of the classifier. For instance, the median accuracy of the linear SVM was 93%. If the e-types are shuffled, then the performance drops to chance level. Thus, these results demonstrate the robustness of these e-types in rat barrel cortex.

In order to further explore patterns and relationships in the high-dimensional electrophysiological data, I followed the analysis already presented in Figure 5.5. The 31 electrophysiological features used for classification were embedded using the same settings. Figure 5.13 presents the resulting electrophysiological UMAP (e-UMAP) color-coded according to the 13 different e-types. Each point on the e-UMAP represents an inhibitory neuron, which clusters together with neurons of the same e-type. The e-UMAP is organized by transitions from FS to non-FS, from adapting to non-adapting, and from irregular to RS. These trends are not orthogonal, meaning they are not entirely independent and may share some common dependencies. Thus, combinations of correlated features may provide useful insights into the structure of the high-dimensional electrophysiological data.

I then investigated the role of different features in the electrophysiological organization of inhibitory neurons. For this purpose, I followed the analysis already presented in Figure 5.6. Figure 5.14A presents the relative importance for the 31 electrophysiological features sorted in descending order. *AP width SPC1* is the most important feature, followed by the *PSTH SPC1* and *Inst. firing rate SPC1*. These results align with those of (Gouwens *et al.*, 2019), who also identified the same features as most important, and in the exact same order. Figure 5.14B illustrates the soma depth and the top three features color-coding the e-UMAP. *Soma depth* did not encode an informative structure that related to e-types, providing further evidence that e-types do not have a laminar-specific organization. Then, *AP width SPC1* (8.72%) was able to identify E05-07, E09, and E11 from the rest of the e-types. However, this separation was not apparent at this juncture. *PSTH SPC1* (6.69%) and *Inst. firing rate SPC1* (5.75%) were able to distinguish between FS and non-FS. Thus, it seems that the primary role of electrophysiological features in the organization of inhibitory neurons is to identify fast-spiking patterns.

To assess the laminar organization of e-types, I reorganized Figure 5.13 by cortical layers, resulting in Figure 5.15. This new figure shows e-UMAPs colored inhibitory neurons according to e-types in the original figure. In each cortical layer, only

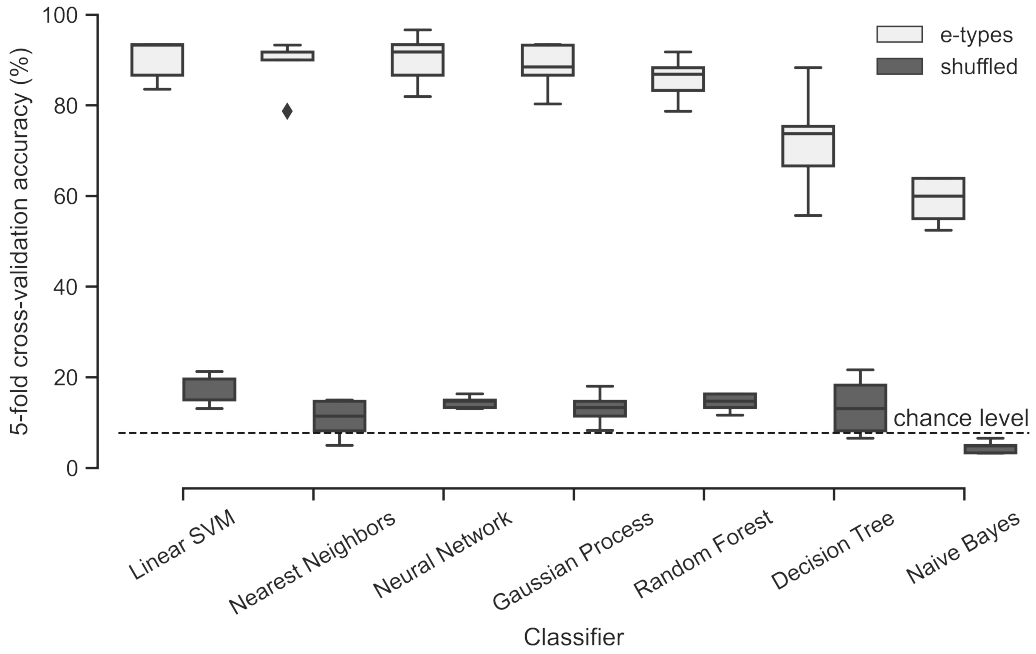

Figure 5.12: Predictability evaluation of electrophysiological class assignments (e-types) utilizing 5-fold cross-validation accuracy. Chance level is the inverse of the number of e-types, i.e., 7.7%. Further details can be found in the text.

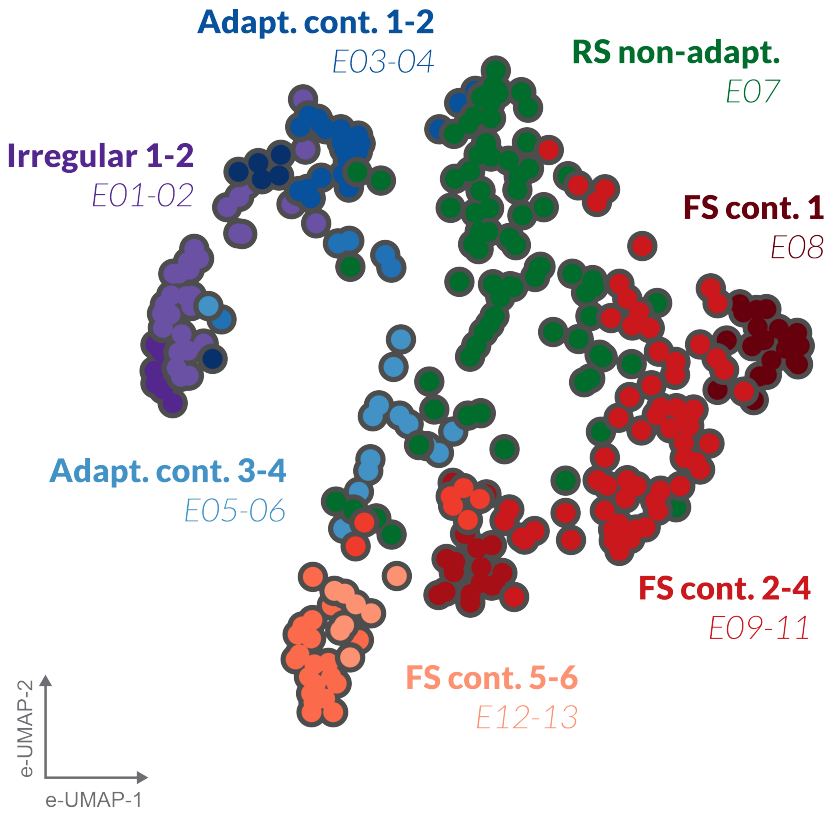

Figure 5.13: Low-dimensional electrophysiological embedding (e-UMAP) color-coded by electrophysiological class assignments (e-types). E-types are also described based on the Petilla terminology (Ascoli *et al.*, 2008).

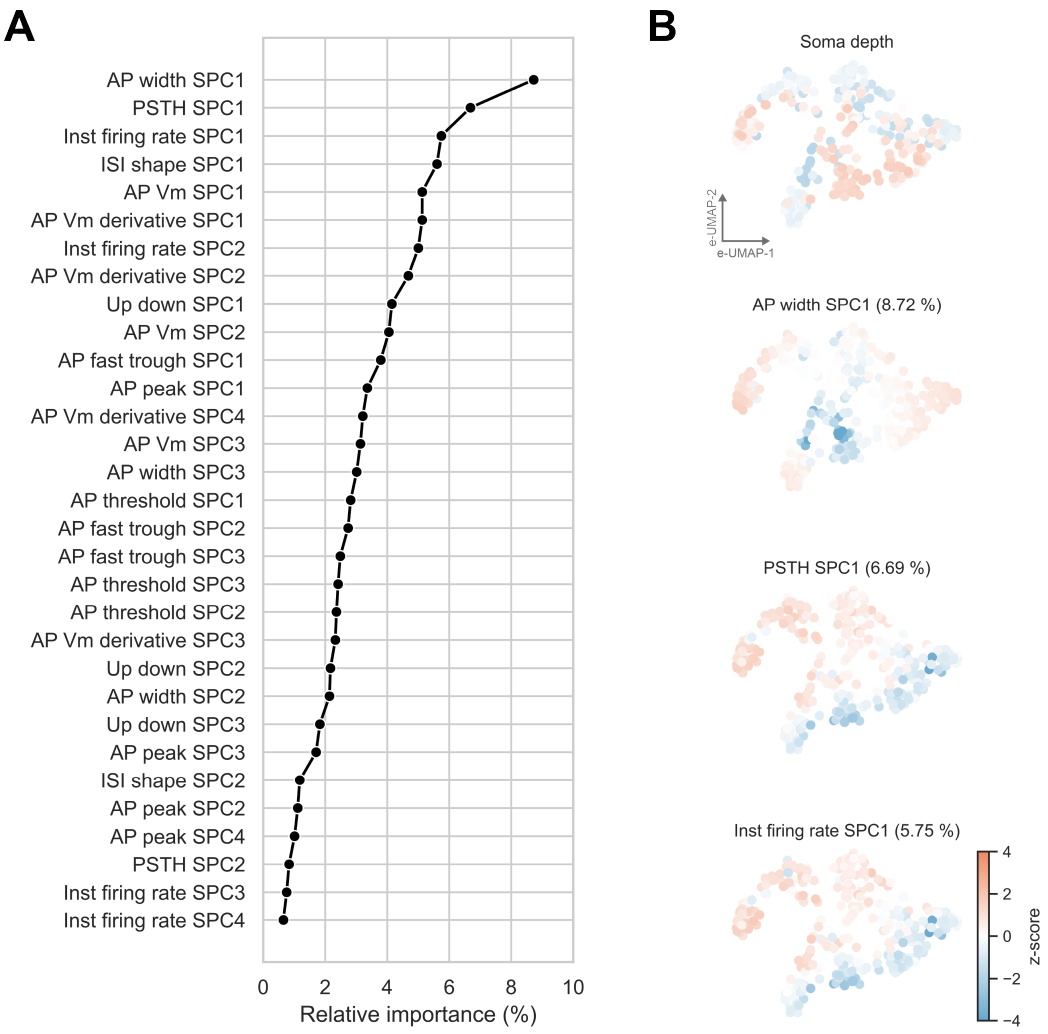

Figure 5.14: Relative importance of electrophysiological features. A. Gini impurity index. B. Features-based projection color-coded by specific features. Details in text.

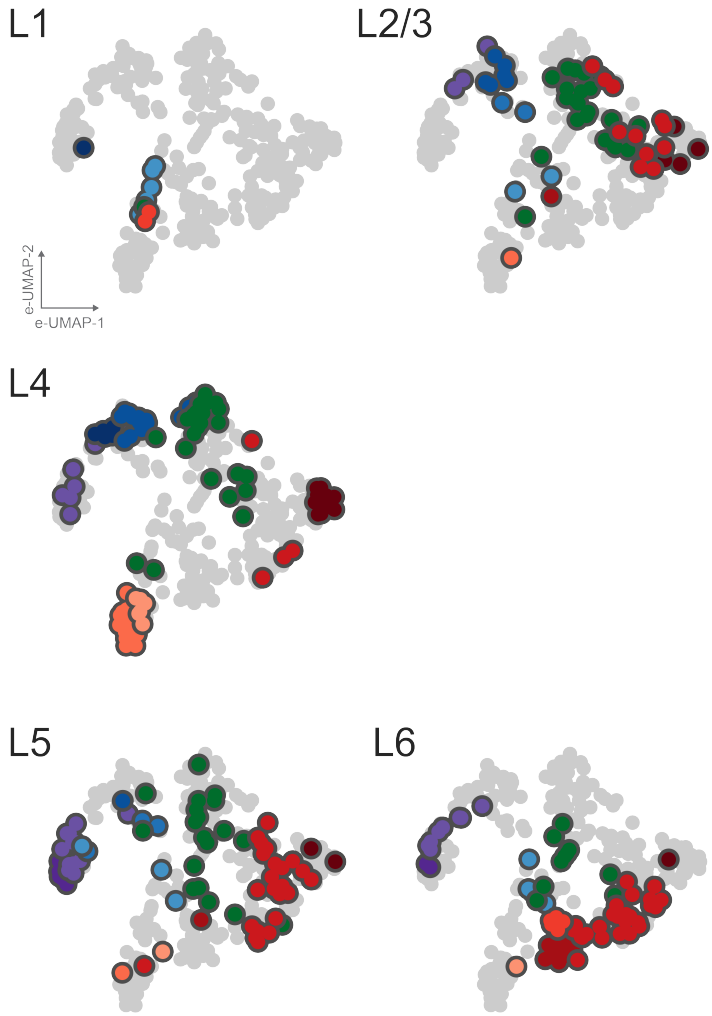

Figure 5.15: Electrophysiological class assignments (e-types) by cortical layer. The features-based embedding and colors used for e-types are according to Figure 5.13.

the inhibitory neurons within that layer are colored, while all other neurons are displayed in gray. For instance, in L1 ($n = 9$), 4 e-types were found: 1 neuron corresponded to E03, 5 to E06, 1 to E07, and 2 to E11. In L2/3, 9 e-types were found among the 52 neurons: 3 neurons corresponded to E02, 6 to E04, 2 to E05, 2 to E06, 22 to E07, 4 to E08, 1 to E09, 11 to E10, and 1 to E12. Then, in L4 ($n = 99$), 8 e-types were found: 7 neurons corresponded to E02, 5 to E03, 16 to E04, 26 to E07, 16 to E08, 4 to E10, 19 to E12, and 6 to E13. In L5, 11 e-types were found among the 72 neurons: 5 neurons corresponded to E01, 12 to E02, 1 to E04, 3 to E05, 3 to E06, 19 to E07, 2 to E08, 1 to E09, 24 to E10, 1 to E12, and 1 to E13. Finally, in L6 ($n = 71$), 9 e-types were found: 2 neurons corresponded to E01, 8 to E02, 4 to E06, 10 to E07, 1 to E08, 15 to E09, 25 to E10, 5 to E11, and 1 to E13.

In each cortical layer, a similar diversity of inhibitory neurons was observed. This suggests that the variety of inhibitory neurons (e.g., FS, RS, adapting, and irregular-spiking) is consistently distributed across layers, with each layer comprising a broad range of e-types. Interestingly, the original source of the underlying 100 Hz voltage traces (Egger *et al.*, 2015; Helmstaedter *et al.*, 2009b,c; Koelbl *et al.*, 2015; Emmenegger *et al.*, 2018; Arzt *et al.*, 2018, and new data) did not dominate the definition of e-types. The vast majority of e-types span across cortical layers, although some of them are restricted to a specific laminar location. Furthermore, it appears that e-types tend to form supraclusters with similar firing patterns, such as FS, RS, adapting, or irregular-spiking, rather than being organized by the original data sources.

Figure 5.16 illustrates the depth distribution at 50 µm bins of each e-type, further supporting the previous observations. By examining the distribution of e-types along the cortical depth, it becomes evident that most e-types are broadly distributed. For instance, some e-types, such as E08 and E10, are composed of FS inhibitory neurons that span multiple layers, while another e-type like E02 comprises irregular-spiking neurons that are also found across layers. This distribution of e-types provides valuable insights into the organization of inhibitory neurons, and supports the notion that e-types tend to form supraclusters with similar firing patterns, such as FS, RS, adapting, or irregular-spiking, rather than being organized by the original data sources.

Similarly as the analysis presented in Figure 5.9, the comparison of e-types with the classification of human experts is important for better understanding the functional organization of inhibitory neurons. Figure 5.17 illustrates a contingency matrix that compares e-types with the judgments made by human experts. The contingency matrix shows the frequency distribution of the two classification methods, with 13 e-types and 5 classes for human expert classifications. The judgments made by human experts are a consensus of heterogeneous evaluations that I curated. The *Adapt./irreg. spiking* class corresponds to a group of inhibitory neurons for

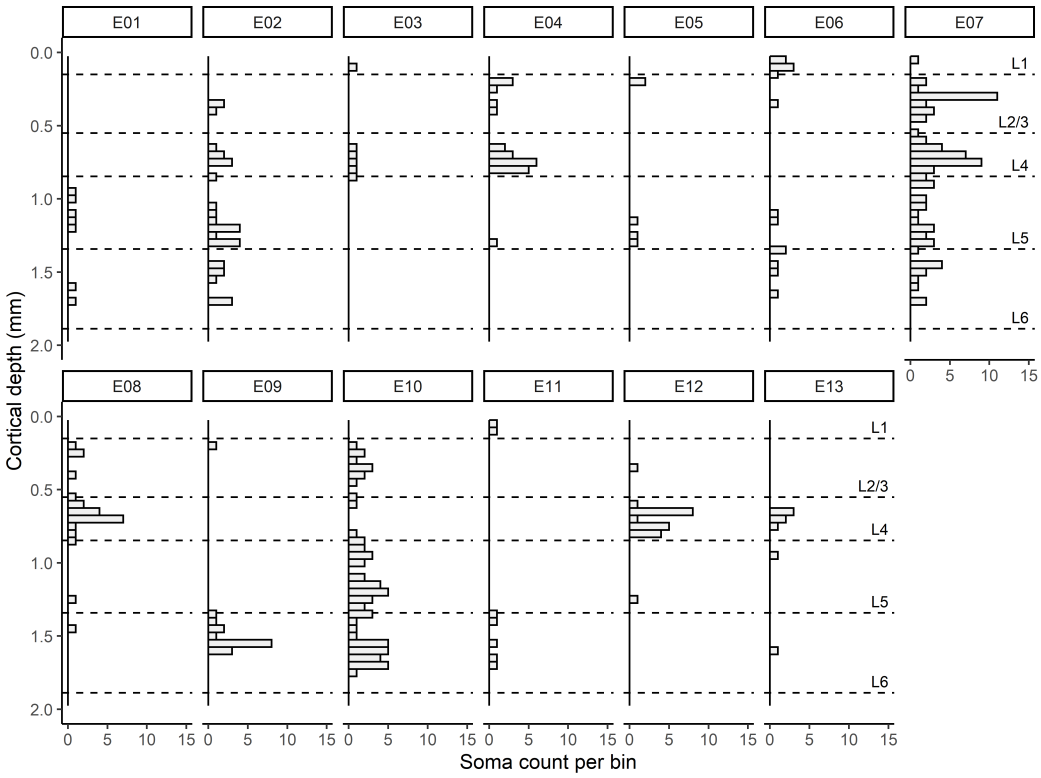

Figure 5.16: Depth distribution of electrophysiological class assignments (e-types).

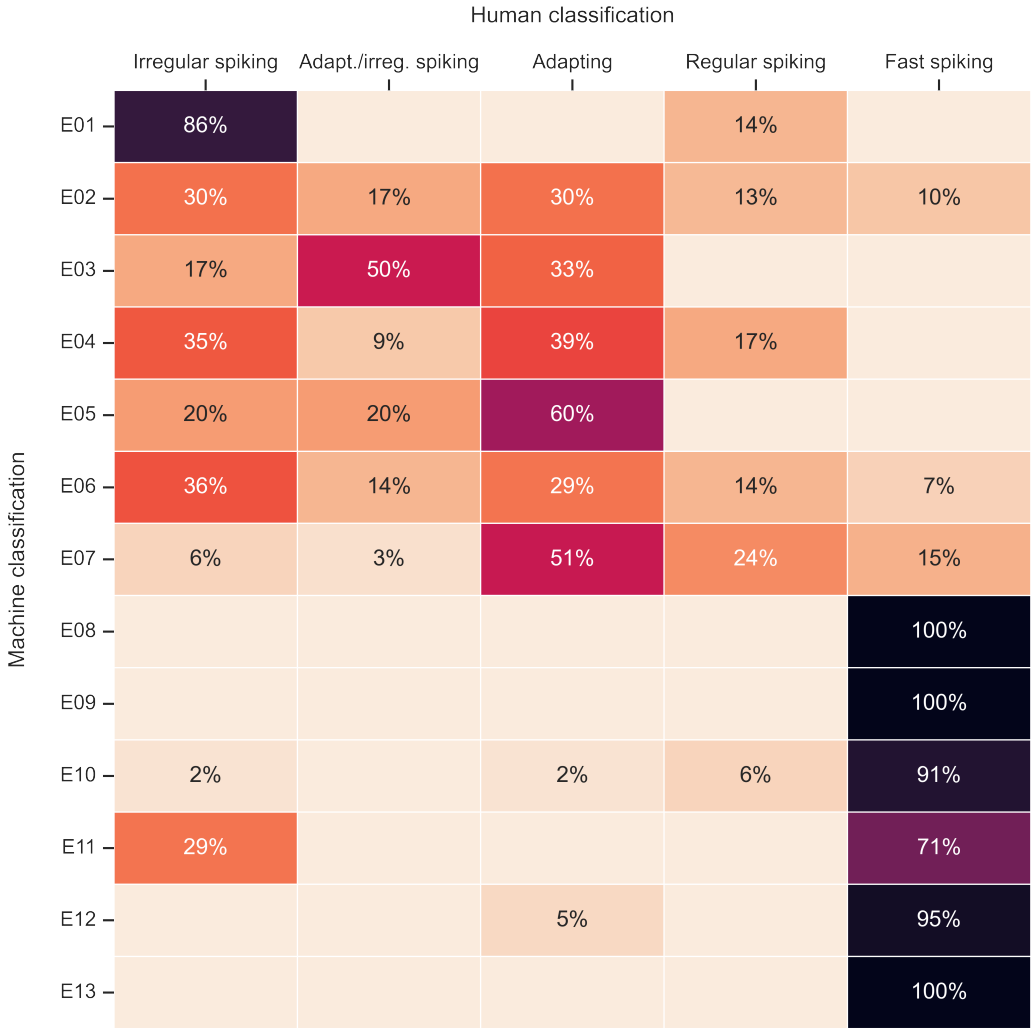

Figure 5.17: Contingency matrix comparing human (Gardner) and machine (features-based) class assignments. Numbers indicate inhibitory count per class.

which there was not sufficient confidence to determine whether they had an adapting or an irregular-spiking firing pattern. The comparison between e-types and human expert classifications revealed a clear agreement for FS inhibitory neurons. However, the agreement was less clear for the rest.

To quantitatively assess the agreement between the two approaches, the ARI, AMI, and F1 score were computed. The ARI was 0.17, indicating a relatively low level of agreement between them. On the other hand, the AMI was 0.28, suggesting a moderate level of agreement. Finally, the F1 score was 0.80, indicating that, despite the moderate level of agreement, the e-types have a high accuracy in predicting the human-assigned classes for a significant portion of the inhibitory neurons. Interestingly, the human-machine comparisons revealed similar levels of uncertainty for morphology and electrophysiology.

Electrophysiology is a necessary component for understanding the role of inhibitory neurons in cortical circuits. I utilized an unsupervised clustering approach to identify 13 robust e-types. These e-types present diverse firing patterns that broadly span across layers. Human expert judgements were compared against e-types, revealing a good overall agreement.

5.3 Joint morphology and electrophysiology

The joint analysis of morphology and electrophysiology of inhibitory neurons provides insights into their organization. Therefore, their classification is an essential step towards understanding their structural and functional roles in cortical circuits.

5.3.1 Classification

I jointly clustered the morphology and electrophysiology of 299 inhibitory neurons, following the approach presented in Figure 5.1. To ensure the quality and relevance of the features used for morphoelectric clustering, I analyzed the 47 morphological and 31 electrophysiological features used to characterize inhibitory neurons. From the 78 morphoelectric features, a total of ten were removed. Six because of low coefficient of variation ($CV < 0.25$). These features were: *axon mean contraction* (ID: 20), *dendrite mean contraction* (ID: 21), *dendrite overlapping axon* (ID: 26), *soma axon x-percentile* (ID: 31), *soma dendrite x-percentile* (ID: 32), and *axon home column* (ID: 44). IDs are according to Figures A.1–A.3. Aditionally, four because of high correlation with other features ($r > 0.95$). *PSTH SPC1* (ID: 10), *AP threshold SPC1* (ID:20), *AP threshold SPC2* (ID: 21), and *AP threshold SPC3* (ID: 22). IDs are according to Figures A.4–A.5. Thus, the 68 remaining features were z-scored and then used for morpholelectric class assignment.

The assignment module utilized the 41 morphological and 27 electrophysiological features to calculate multiple class assignments through an initial clustering process.

This process involved several steps (Gouwens *et al.*, 2019), each with different settings for the four clustering algorithms used, namely, agglomerative hierarchical clustering with and without connectivity constraints, Gaussian mixture model clustering, and spectral clustering. For the agglomerative hierarchical clustering with connectivity constraints, the number of nearest neighbors was set to 4, 7, and 10, and the number of clusters was set to 10, 15, 20, and 25. The morphological features were clustered based on connectivity constraints derived from pairwise distances between the electrophysiological features. This step produced 12 different class assignments. For the agglomerative hierarchical clustering without connectivity constraints, the number of clusters was also set to 10, 15, 20, or 25. The morphological features were concatenated with weighted electrophysiological features, and clustered using Ward's method. The weights were 0.5, 0.75, 1, and 1.5, as described in Gouwens *et al.* (2019). This step produced 16 different class assignments. For the Gaussian mixture model clustering, the number of clusters was the same as before, the covariance type was set to diagonal, and the number of initializations was set to 20 to increase the likelihood of finding the optimal solution. The weights were also set to 0.5, 0.75, 1, and 1.5. This step produced 16 different class assignments. For the spectral clustering, the number of clusters and initializations, as well as the weights were set as for the previous algorithm. The "scale" method was utilized for normalizing the data. This step produced 16 different class assignments. Overall, the initial clustering process comprised 60 different instances of class assignments, where the number of clusters in each class assignment were not reduced at this juncture.

The sensing module was performed to identify robust clusters. A consensus clustering algorithm calculated pairwise similarity scores between inhibitory neuron pairs based on how often they are grouped together in each of the initial 60 class assignments. The consensus class assignments were obtained through iterative hierarchical clustering, cluster merging, and individual inhibitory neuron reassignment based on pairwise similarity. In each iteration, hierarchical clustering was performed on each cluster from the previous iteration and split it into two sub-clusters, unless the sub-cluster size is smaller than a minimum size of five. Then, pairs of clusters were merged based on a similarity criterion. A refinement step was performed by iteratively reassigning inhibitory neurons to different clusters based on the similarity between a single neuron and all the other ones in each cluster. The consensus procedure identified 25 robust morphoelectric clusters.

5.3.2 Visualization

A representative inhibitory neuron of each me-type is illustrated in Figure 5.18. The axons are displayed in lighter shades, whereas the dendrites in darker shades. The corresponding 100 Hz voltage traces are in the same lighter shades as the axons.

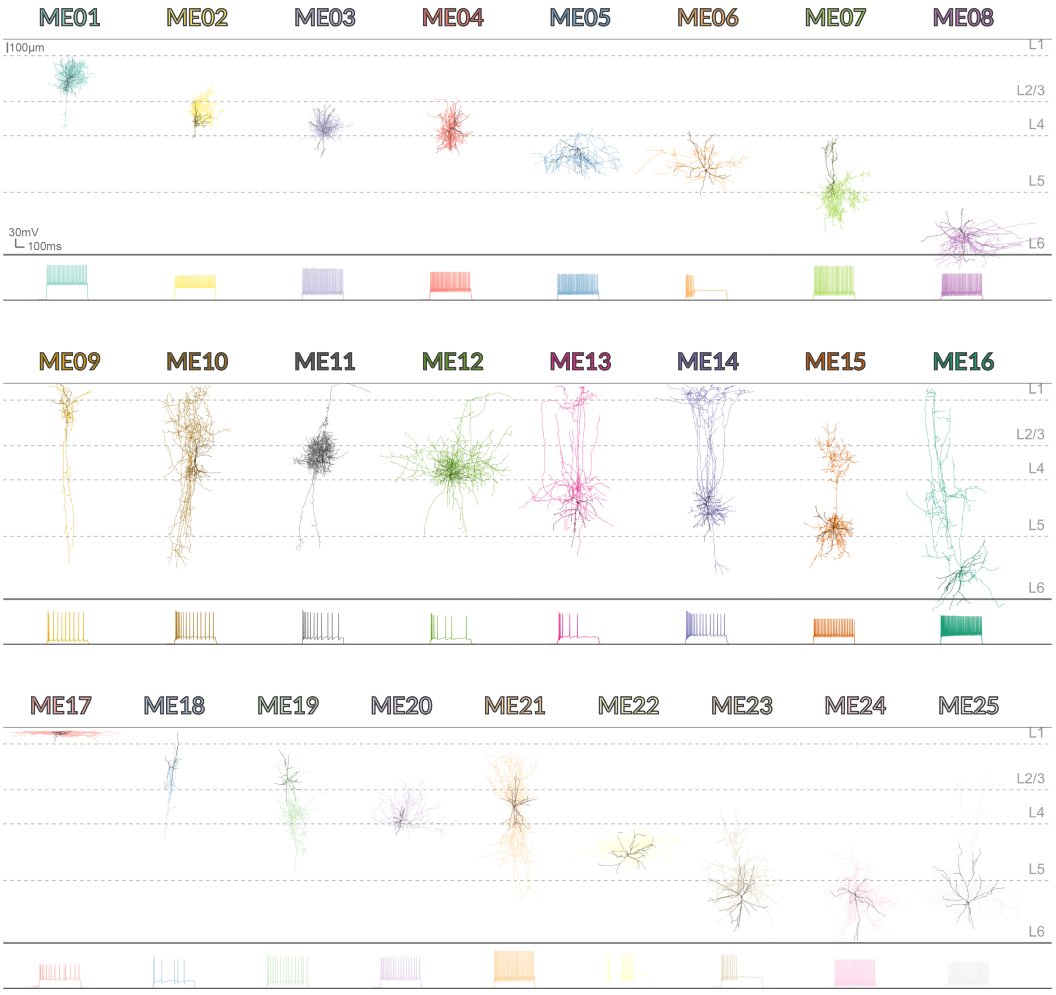

Figure 5.18: Representative example of each morphoelectric class assignment (me-type). Axons in lighter shades; dendrites in darker shades. See text for details.

As previously reported (Gouwens *et al.*, 2019, 2020), me-types were predominantly depth-dependent. For instance, the 8 me-types in Figure 5.18 (top) spanned from L2 to L6. ME01 ($n = 15$) was mainly restricted to the supragranular layer, ME02 ($n = 18$), ME03 ($n = 11$), and ME04 ($n = 11$) to the granular layer, and ME05 ($n = 31$), ME06 ($n = 6$), ME07 ($n = 7$), and ME08 ($n = 7$) to the infragranular layer. All these 8 me-types were characterized by small axonal and dendritic morphology, and FS firing patterns. ME01-06 and ME08 resembled previously reported FS basket cells (Kubota *et al.*, 1994; Kawaguchi and Kubota, 1997), whereas ME07 with dense axonal arborizations and elaborated dendrites resembled chandelier cells (Szentágothai and Arbib, 1974; Somogyi, 1977; Somogyi *et al.*, 1982).

Then, the 8 me-types in Figure 5.18 (center) also spanned from L2 to L6. ME09 ($n = 6$) was predominantly located in the supragranular layer, ME10 ($n = 9$), ME11 ($n = 19$), and ME12 ($n = 17$) in the granular layer, and ME13 ($n = 13$), ME14 ($n = 9$), ME15 ($n = 7$), and ME16 ($n = 10$) in the infragranular layer. All these 8 me-types were characterized by large axonal and dendritic morphology, and adapting firing patterns. For instance, ME09 comprised bipolar and bitufted cells (Bayraktar *et al.*, 2000; Prönneke *et al.*, 2015), ME11-12 displayed translaminar basket-like morphologies (Tremblay *et al.*, 2016; Nigro *et al.*, 2018), and ME10 and ME13-16 corresponded to Martinotti cells (Martinotti, 1889).

Finally, the 9 me-types in Figure 5.18 (bottom) spanned from L1 to L6. ME17 ($n = 10$) was the only class with somata in L1 and, along with ME20 ($n = 12$), were mainly characterized by RS firing patterns and small dendrite vertical extents, resembling previously reported neurogliaform cells (Tamás *et al.*, 2003). ME18 ($n = 7$) and ME19 ($n = 19$) were bipolar or bitufted cells with different degrees of accommodation. ME21 ($n = 8$) was FS with large vertically-projecting axons, resembling hourglass-like morphologies, specific to the barrel cortex (Feldmeyer *et al.*, 2018). ME22 ($n = 8$), ME23 ($n = 6$), ME24 ($n = 8$), and ME25 ($n = 25$) were large FS basket cells located in the infragranular layer.

Thus, me-types displayed diverse patterns of variation across layers, but as in the previous analyses, the same relationships of this diversity were present in each layer.

5.3.3 Evaluation

The clustering quality of the identified me-types was first assessed by performing a 5-fold cross-validation. Figure 5.19 illustrates the classifier performance, following the analysis already presented in Figure 5.4. However, the only difference was that the nearest neighbors used $k = 8$. The theoretical chance level was 4.0%. High performance is once again achieved independently of the classifier. For instance, the median accuracy of the neural network was 78%. If the me-types are shuffled, then the performance drops to chance level. Thus, these results demonstrate the robustness of these me-types in rat barrel cortex.

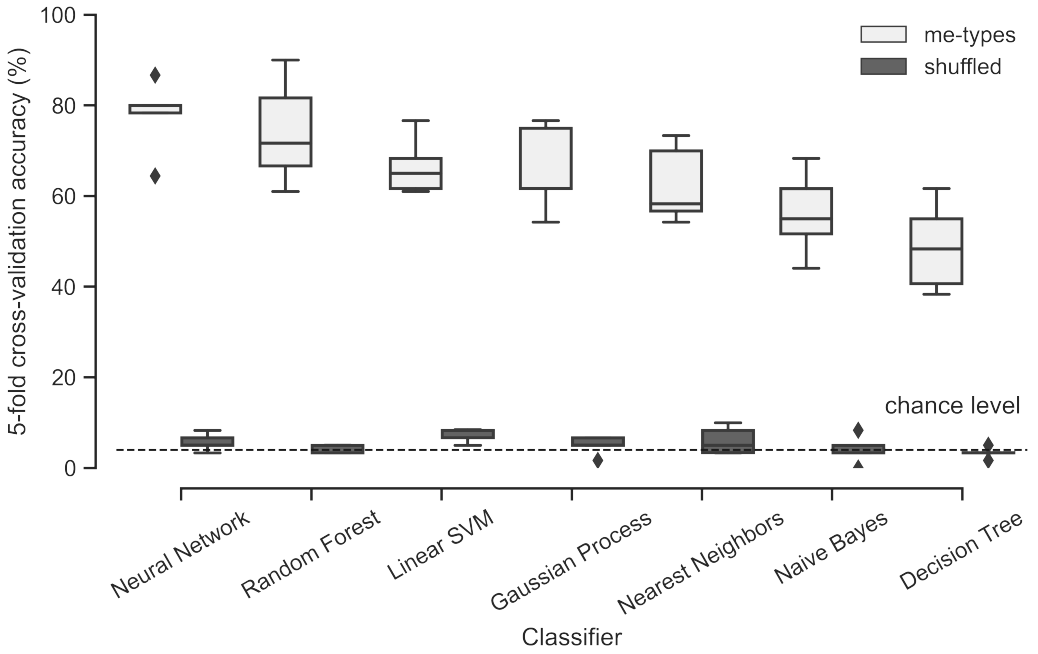

Figure 5.19: Predictability evaluation of morphoelectric class assignments (me-types) utilizing 5-fold cross-validation accuracy. Chance level is the inverse of the number of me-types, i.e., 4.0%. Further details can be found in the text.

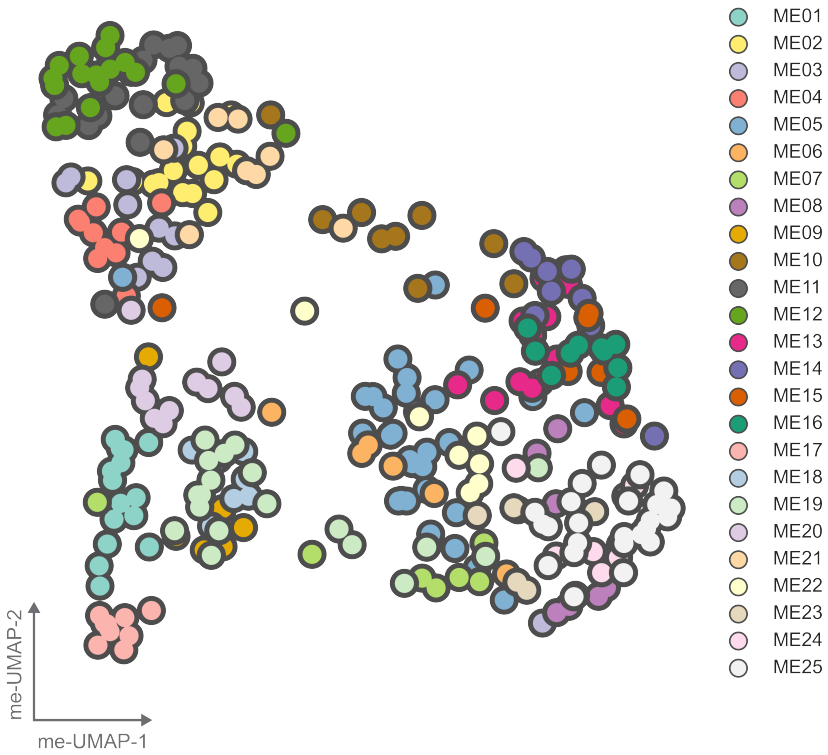

Figure 5.20: Low-dimensional morphoelectric embedding (me-UMAP) color-coded by morphoelectric class assignments (me-types).

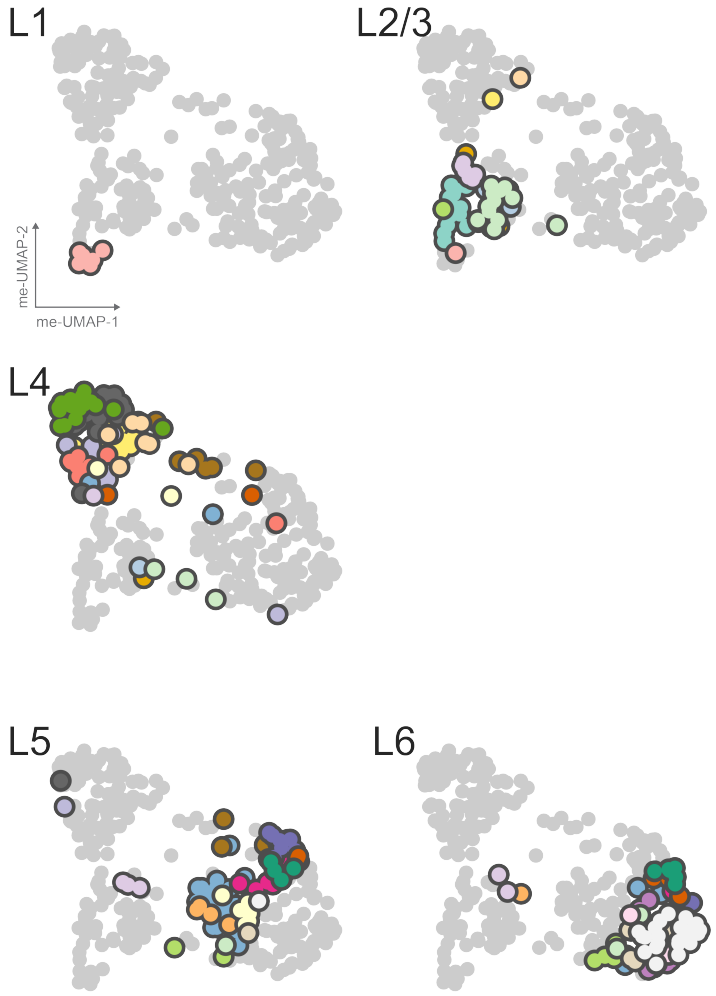

Figure 5.21: Morphoelectric class assignments (me-types) by cortical layer. The features-based embedding and colors used for me-types are according to Figure 5.20.

In order to further explore patterns and relationships in the high-dimensional electrophysiological data, I followed the analysis already presented in Figure 5.5. The morphological features ($n = 41$) were concatenated with weighted electrophysiological features ($n = 27$) using weights of 0.5, 0.75, 1, and 1.5, as previously described in Gouwens *et al.* (2019). The out-of-bag prediction accuracy of a random forests classifier was used to determine the best weight. The best weight was 0.5, which was then used to compute the embedding with the same settings. Figure 5.13 presents the resulting morphoelectric UMAP (me-UMAP) color-coded according to the 25 different me-types. Each point on the me-UMAP represents an inhibitory neuron, which clusters together with neurons of the same me-type. Furthermore, similar me-types are located close to each other in the me-UMAP.

To assess the laminar organization of me-types, I reorganized Figure 5.20 by cortical layers, resulting in Figure 5.21. This new figure shows me-UMAPs colored inhibitory neurons according to me-types in the original figure. In each cortical layer, only the inhibitory neurons within that layer are colored, while all other neurons are displayed in gray. For instance, in L1 ($n = 9$) all neurons corresponded to one me-type (ME17). In L2/3, 9 me-types were found among the 49 neurons: 15 neurons corresponded to ME01, 1 to ME02, 1 to ME07, 5 to ME09, 1 to ME17, 6 to ME18, 13 to ME19, 6 to ME20, and 1 to ME21. Then, in L4 ($n = 98$), 14 me-types were found: 17 neurons corresponded to ME02, 10 to ME03, 11 to ME04, 2 to ME05, 1 to ME09, 6 to ME10, 18 to ME11, 17 to ME12, 2 to ME15, 1 to ME18, 3 to ME19, 1 to ME20, 7 to ME21, and 2 to ME22. In L5, 15 me-types were found among the 72 neurons: 1 neuron corresponded to ME03, 24 to ME05, 4 to ME06, 2 to ME07, 3 to ME10, 1 to ME11, 11 to ME13, 8 to ME14, 2 to ME15, 4 to ME16, 1 to ME19, 3 to ME20, 6 to ME22, 1 to ME23, and 1 to ME25. Finally, in L6 ($n = 71$), 13 m-types were found: 5 neurons corresponded to M05, 2 to ME06, 4 to ME07, 7 to ME08, 2 to ME13, 1 to ME14, 3 to ME15, 6 to ME16, 2 to ME19, 2 to ME20, 5 to ME23, 8 to ME24, and 24 to ME25. In each cortical layer, a similar diversity of inhibitory neurons was observed. This suggests that the variety of inhibitory neurons (e.g., local versus translaminar, or FS versus non-FS) is consistently distributed across layers, with each layer comprising a broad range of me-types. Although some me-types are restricted to a specific cortical layer, others span across multiple layers.

Figure 5.22 illustrates the depth distribution at 50 µm bins of each me-type, further supporting the previous observations. By examining the distribution of me-types along the cortical depth, it becomes evident that certain me-types are more prevalent at specific depths, while others are more broadly distributed. For instance, some me-types, such as ME01 and ME17, are primarily found in superficial layers, whereas me-types like ME08 and ME13 are more commonly observed in deeper layers. This depth-dependent distribution of me-types provides valuable insights into the organization of inhibitory neurons.

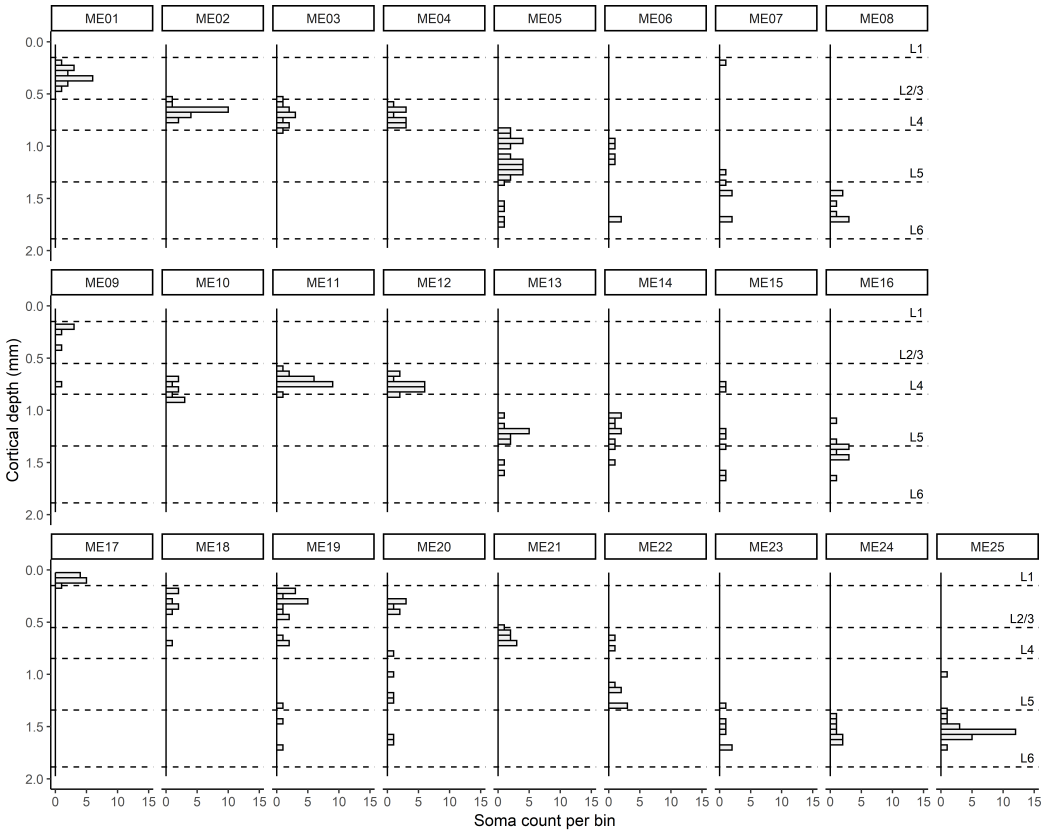

Figure 5.22: Depth distribution of morphoelectric class assignments (me-types).

5.4 Summary

Unsupervised multimodal clustering was used to classify inhibitory neurons based on their morphological and electrophysiological properties in a representative column of rat barrel cortex. The clustering resulted in the identification of 20 morphological classes (m-types), 13 electrophysiological classes (e-types), and 25 morphoelectric classes (me-types). The predictability of each clustering modality was evaluated using several classifiers, resulting in robust class assignments. It is worth noting that although the classifiers achieved high accuracy rates, none of them was able to perfectly predict the underlying classes. The distribution of inhibitory neurons indicated that they were predominantly organized by cortical depth. In a collaboration with a group of experts, the morphology and electrophysiology of these neurons were assessed. Their classification grouped neurons into broader categories with resulting distributions that were independent of laminar location, while the multimodal clustering identified more specific depth-dependent subtypes. The overall classification of both methods was in moderate agreement, indicating that they captured different but complementary aspects of inhibitory neuron diversity. Therefore, the classification analysis allowed for the identification of robust e-, m-, and me-types consistent with those reported for mouse V1.

Chapter 6

Molecular composition of barrel cortex

In collaboration with Dr. Fernando Messore (Max Planck Institute for Neurobiology of Behavior – caesar), we developed a framework to quantify the 3D distribution of the most predominant molecular markers for inhibitory neurons, namely parvalbumin (Pvalb), somatostatin (Sst), and vasoactive intestinal polypeptide (Vip). This procedure involved a series of six experiments, each of which consisted of double-immunolabeling 50 µm-thick tissue sections against Gad67 and one of the three molecular markers. He was responsible for implementing the staining protocols and acquiring the confocal images of the double-immunolabeled tissue sections. The manual quantification of neuron somata was jointly performed by both of us. To reduce experimental bias, we double-checked each other's counts. The data shown here represents the consensus result between both of us. I utilized those soma counts to produce the 3D density distributions and absolute soma number for Gad67+, Pvalb+, Sst+, and Vip+ neurons throughout the entire barrel cortex. To validate the accuracy of this quantification methodology, I compared the 3D distribution of inhibitory neurons against a comprehensive previously reported study (Meyer *et al.*, 2013), obtaining remarkable correspondence. The distributions of these molecular markers were heterogeneous across layers and barrel columns. For Pvalb+ neurons, there was even a significant difference across experiments. It turns out that the relative abundance of Pvalb+ and Gad67+ neurons is linked, indicating that their fraction is preserved across cortical depth. Furthermore, the fraction of inhibitory neurons expressing each of these molecular markers across cortical depth was consistent with previous studies (Helmstaedter *et al.*, 2009b; Meyer *et al.*, 2011; Koelbl *et al.*, 2015; Emmenegger *et al.*, 2018; Arzt *et al.*, 2018). Thus, providing a reliable estimate of the molecular composition of rat barrel cortex.

The most important methodological results from Chapter 6 are:

- The 3D density distribution of Pvalb+, Sst+, and Vip+ neurons throughout the entire barrel cortex.
- The absolute number of Pvalb+, Sst+, and Vip+ neurons throughout the entire barrel cortex.

6.1 Experimental design

A series of six experiments was performed in order to investigate the molecular composition of inhibitory neurons in rat barrel cortex. The 3D distribution of neuron somata expressing the most predominant non-overlapping molecular markers were quantified across layers throughout the entire barrel field. Specifically, the analysis comprised parvalbumin (Pvalb), somatostatin (Sst), and vasoactive intestinal polypeptide (Vip). Each experiment consisted of one of these molecular markers and glutamic acid decarboxylase 67 (Gad67). Two experiments were performed for each marker (i.e., Pvalb, Sst, and Vip).

Figure 6.1 illustrates the quantification procedure. For each experiment, 50 µm thick slices were double-immunolabeled against Gad67 and either Pvalb, Sst, or Vip according to previously established methodologies (Meyer *et al.*, 2011, 2013; Messore, 2024). All images were acquired using a confocal laser scanning system (Leica Application Suite Advanced Fluorescence SP5, Leica Microsystems, Wetzlar, Germany) equipped with glycerol/oil immersion objectives (HC PL APO 10× 0.04 N.A., HC PL APO 20× 0.7 N.A., and HCX PL APO 63× 1.3 N.A.), a tandem scanning system (Resonance Scanner: 8 kHz scanning speed), spectral detectors with hybrid technology (GaAsP photocathode; 8× line average), and mosaic scanning software (Matrix Screener, beta version provided by Frank Sieckmann, Leica Microsystems). For each experiment, a single optical image was acquired from each of the 40 to 48 tissue sections that covered the entire cortical depth. These sections were 50 µm thick and spanned the complete barrel field. The 40-48 images from the Gad67 channel were used to manually reconstruct the contours of the pia, barrels, and white matter in AmiraZIBEdition (Dercksen *et al.*, 2014). As blood vessels are approximately orthogonal to the barrel field, they were used as a reference to manually align subsequent contours. The affine transformation matrix of each manually aligned section, which comprised only translation and rotation, was saved for later use. These aligned contours allowed the reconstruction of the pial and white matter surfaces, as well as the barrel cortex, which was identified as the volume defined by the convex-hull of the barrel columns (Egger *et al.*, 2012).

A region of interest (ROI) was defined in the center of the barrel cortex, containing the D2 column, in order to allow a systematic assessment in 3D. This ROI had a horizontal extent of size 1 mm×1 mm. To determine the exact location for acquiring a 3D stack in each slice, the corresponding inverse transformation was applied to the contour of the ROI. Each 3D image stack for the two molecular markers was acquired in a way that completely covered the ROI. The horizontal extent of the acquisition area was set to 3 mm×3 mm. The 3D image stack of each 50 µm thick tissue section comprised approximately 100 optical sections. The contours containing the complete barrel field were manually aligned to their corresponding 3D image stacks. These second slice-specific affine transformation matrices were

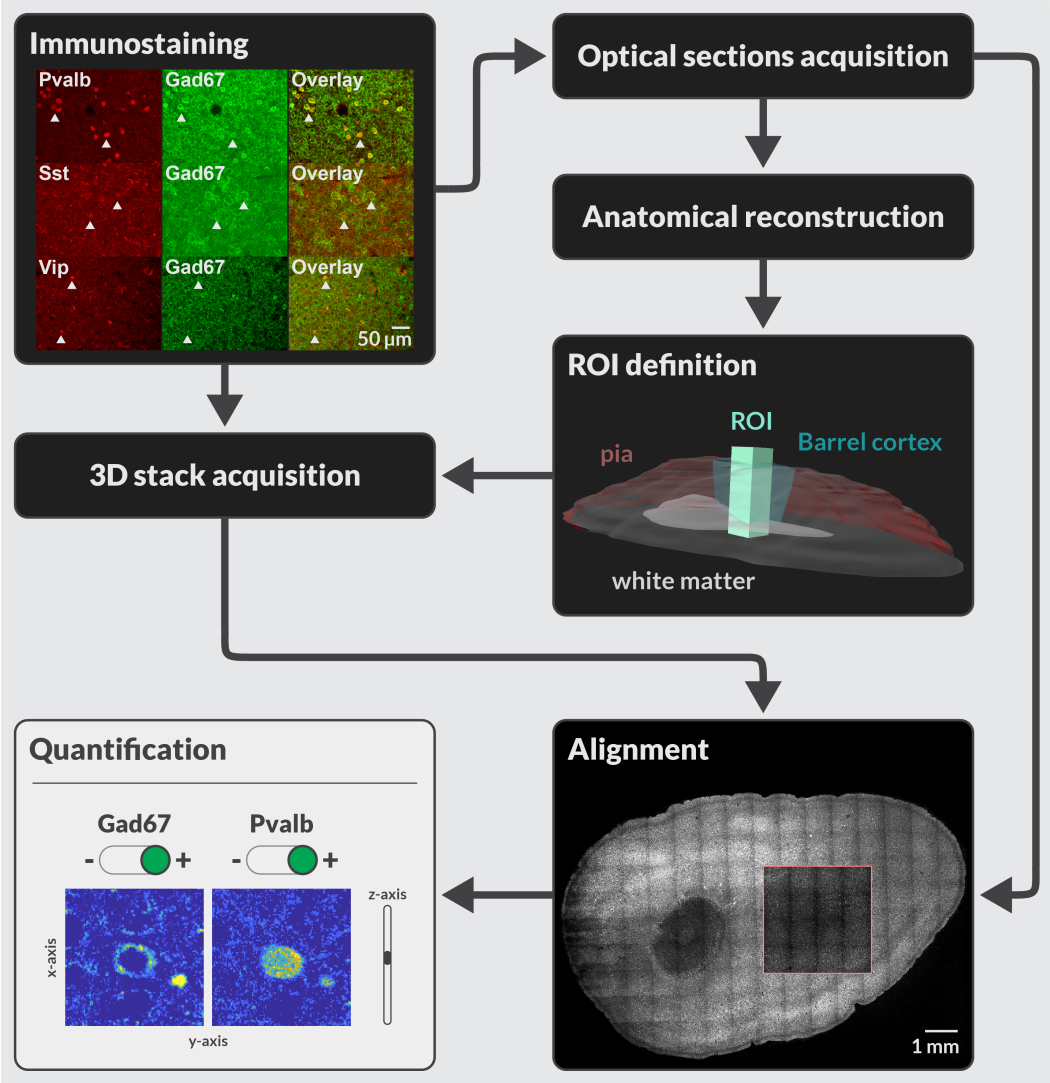

Figure 6.1: Diagram of method for quantifying molecular markers. Details in text.

also saved to later align the soma counts from the 3D image stacks. A manual soma identification procedure was performed in both channels for the optical sections containing the entire barrel field and the 3D image stacks containing the D2 column. Each identified soma in the 3D image stacks was assessed with respect to the two molecular markers for a given experiment (e.g., Gad67 and Pvalb) using an evaluation tool developed in Matlab App Designer. The 3D distribution of each molecular marker was obtained by applying the corresponding transformations to identified neuron somata in individual sections.

6.2 Glutamic acid decarboxylase 67

The organization of Gad67-expressing neurons was the ideal scenario to benchmark the quantification protocol (Figure 6.1) as their 3D distribution has been previously reported (Meyer *et al.*, 2013). Figure 6.2A illustrates the laminar organization of Gad67+ neurons. I used previously acquired MIP images by Dr. Jason M. Guest (Max Planck Institute for Neurobiology of Behavior – caesar) to calculate the average density distribution of neuron somata along the columns A2, B2, C2, D2, E2, and the mean distribution across all barrel columns. Black lines indicate the mean and shaded regions its corresponding 95% CI. The sample size is $n = 3$ for the C2 column and $n = 2$ for the rest. For each experiment, the mean density distribution obtained with MIP images was scaled to fit the reported mean distribution (Meyer *et al.*, 2013). Those experiment-specific scaling factors were applied to all columns. Blue lines correspond to the six Gad67-profiles obtained from the 3D quantification in the ROI. There was no significant difference between them and the average quantification in the D2 column (1-way ANOVA: $p = 0.589$). Dashed lines represent column-specific layer borders (Meyer *et al.*, 2013). The mean distribution displayed remarkable similarities with the hot zones of inhibition in L2 and L5A (Meyer *et al.*, 2011). Figure 6.2B shows the horizontal organization of Gad67+ neurons. The average neuron density per barrel column remained constant across the entire barrel field. In other words, there was no specific gradient or pattern of neuron density observed across the barrel cortex (two-tailed t-test: $p = 0.725$). The boxplot inserted in the colorbar summarizes the overall density in the barrel field, with a median of 10 628 neurons/mm^3.

Table 6.1 presents the whisker-specific organization of Gad67+ neurons, and the corresponding volume of each barrel column. The volumes of barrel columns within the same whisker row were almost identical. However, there was an orderly increase in their volume from the A-row towards the E-row (1-way ANOVA: $p < 1.5 \cdot 10^{-5}$) (Meyer *et al.*, 2013). The average number of inhibitory neurons per cortical barrel column was found to be proportional to the column volume. Consistent with the results by Meyer *et al.* (2013), a relatively constant number of inhibitory neurons

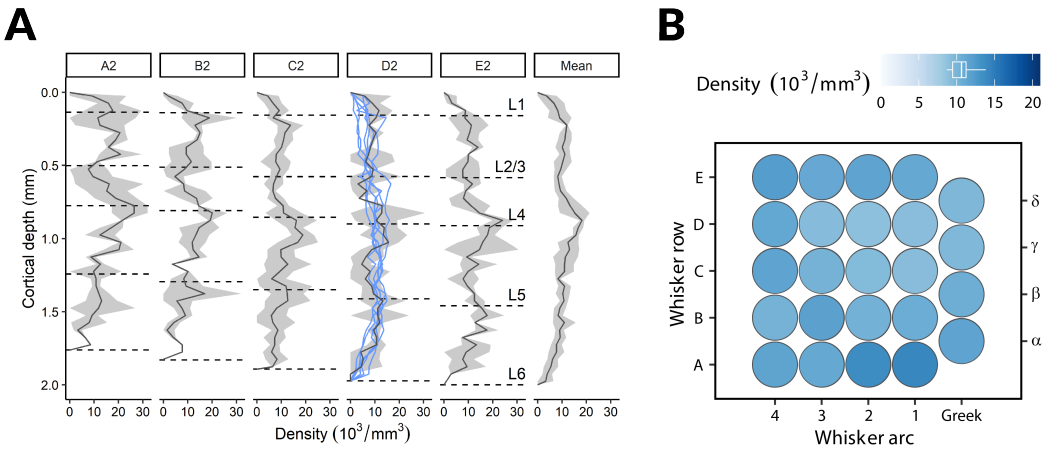

Figure 6.2: Laminar and horizontal organization of Gad67+ neurons. A. Average distribution of Gad67+ neuron somata along the vertical column axis for columns in arc-2, namely, A2, B2, C2, D2, E2, and the mean distribution across all barrel columns. Black lines indicate the mean and shaded regions its corresponding 95% CI. The sample size is $n = 3$ for the C2 column and $n = 2$ for the rest. Blue lines correspond to the six Gad67-profiles obtained from the 3D quantification in the ROI. Dashed lines represent column-specific layer borders. B. The average Gad67+ neuron density per barrel column is constant across the barrel field. The boxplot inserted in the colorbar summarizes the overall density in the barrel field.

Whisker	Volume	Neurons	Whisker	Volume	Neurons
A1	0.15 ± 0.03	2140 ± 865	D1	0.20 ± 0.001	1786 ± 520
A2	0.15 ± 0.03	2124 ± 952	D2	0.27 ± 0.001	2464 ± 1194
A3	0.13 ± 0.06	1535 ± 1190	D3	0.24 ± 0.003	2163 ± 697
A4	0.15 ± 0.07	1760 ± 1048	D4	0.27 ± 0.05	3060 ± 451
A-row	0.14 ± 0.02	1890 ± 430	D-row	0.25 ± 0.02	2368 ± 452
B1	0.18 ± 0.08	1933 ± 896	E1	0.31 ± 0.07	3320 ± 801
B2	0.19 ± 0.09	2075 ± 1068	E2	0.38 ± 0.06	4337 ± 513
B3	0.17 ± 0.03	2068 ± 669	E3	0.33 ± 0.05	3672 ± 751
B4	0.19 ± 0.06	1979 ± 601	E4	0.26 ± 0.01	3142 ± 175
B-row	0.18 ± 0.03	2014 ± 317	E-row	0.32 ± 0.04	3618 ± 410
C1	0.21 ± 0.03	1935 ± 50	α	0.13 ± 0.005	1479 ± 6
C2	0.22 ± 0.05	2117 ± 561	β	0.17 ± 0.04	1917 ± 759
C3	0.22 ± 0.02	2221 ± 662	γ	0.20 ± 0.01	1867 ± 913
C4	0.21 ± 0.01	2398 ± 183	δ	0.25 ± 0.05	2577 ± 1096
C-row	0.21 ± 0.01	2162 ± 227	Mean	0.22 ± 0.02	2332 ± 222

Table 6.1: Whisker-specific organization of Gad67+ neurons. Displayed numbers are mean ± 95% CI. The sample size is $n = 3$ for the C2 column and $n = 2$ for the rest. Volume units are given in mm^3.

	Avg.†	D2†	Avg.‡	D2‡	ROI‡
L1	40 ± 6	64 ± 26	135 ± 16	205 ± 64	97 ± 53
L2/3	427 ± 44	522 ± 97	541 ± 53	534 ± 147	423 ± 116
L4	557 ± 74	842 ± 576	438 ± 64	451 ± 416	440 ± 160
L5	820 ± 110	1026 ± 287	772 ± 77	707 ± 206	789 ± 153
L6	459 ± 59	552 ± 134	445 ± 58	567 ± 362	524 ± 96
Total	2314 ± 279	3005 ± 827	2332 ± 222	2464 ± 1194	2274 ± 372

Table 6.2: Assessment of the laminar distribution of Gad67+ neurons. Avg. corresponds to the average across columns ($n = 24$), D2 to the D2-column, and ROI to a region of interest in the center of the barrel cortex. † indicates that the quantification is from Meyer *et al.* (2013), and ‡ from this dissertation. Numbers are mean ± 95% CI. Further details can be found in the text.

for columns within the same whisker row was obtained, as shown in Table 6.1. Then, similarly as for the volumes, there was an orderly increase in the number of neurons from the A-row towards the E-row (1-way ANOVA: $p < 5.0 \cdot 10^{-5}$), with the average number of inhibitory neurons in the E-row being approximately 1.9 times higher than that in the A-row (1890 ± 430 inhibitory neurons in the A-row). The whisker-specific organization of Gad67+ neurons across cortical layers can be found in Tables B.1 (L1), B.5 (L2/3), B.9 (L4), B.13 (L5), and B.17 (L6).

The laminar distribution of Gad67+ neurons is presented in Table 6.2. The quantification performed by Meyer *et al.* (2013) and the quantification obtained in this dissertation were consistent with each other. For instance, no significant differences were found in the average across columns (two-tailed t-test: $p = 0.973$), or the D2 column (two-tailed t-test: $p = 0.750$). Furthermore, the ROI in the center of the barrel cortex was indistinguishable from the rest (1-way ANOVA: $p = 0.895$).

Thus, the 3D quantification obtained in this dissertation provides a reliable estimate of the average distribution of inhibitory neurons in the barrel cortex.

6.3 Parvalbumin

In order to measure the organization of Pvalb-expressing neurons throughout the entire barrel cortex, the neurons in the optical images were quantified. However, these measurements provide only an estimate based on a subset of the neurons, as a single image every 50 mm is utilized. Therefore, I compensated the neuron density obtained from the optical images compared to the one obtained from 3D image stacks by calculating a scaling factor. Specifically, consider the given data pairs $\{x_i, y_i\}_{i=1}^{n}$ corresponding to the neuron density in single optical sections and 3D image stacks, both restricted only to the ROI. The scaling factor β across n consecutive tissue sections satisfies

$$y_i = \beta x_i + \epsilon \; \forall i = 1, \ldots, n \tag{6.1}$$

independently for each of the two experiments. Then, after applying Equation (6.1) to each experiment, I obtained $\beta = 3.8$ ($R^2 = 0.98$, $p < 7.39 \cdot 10^{-29}$) and $\beta = 3.6$ ($R^2 = 0.95$, $p < 3.93 \cdot 10^{-19}$), respectively.

Figure 6.3A illustrates the laminar organization of Pvalb+ neurons. The scaling factors were applied to neuron density measurements from each of the two experiments in order to calculate the average density distribution of neuron somata along the columns A2, B2, C2, D2, E2, and the mean distribution across all barrel columns (shown in black). Blue lines correspond to the two Pvalb-profiles obtained from the 3D quantification in the ROI. There was no significant difference between them and their corresponding quantification in the D2 column (two-tailed t-test: $p = 0.789$ and $p = 0.445$). However, there was a significant difference between ex-

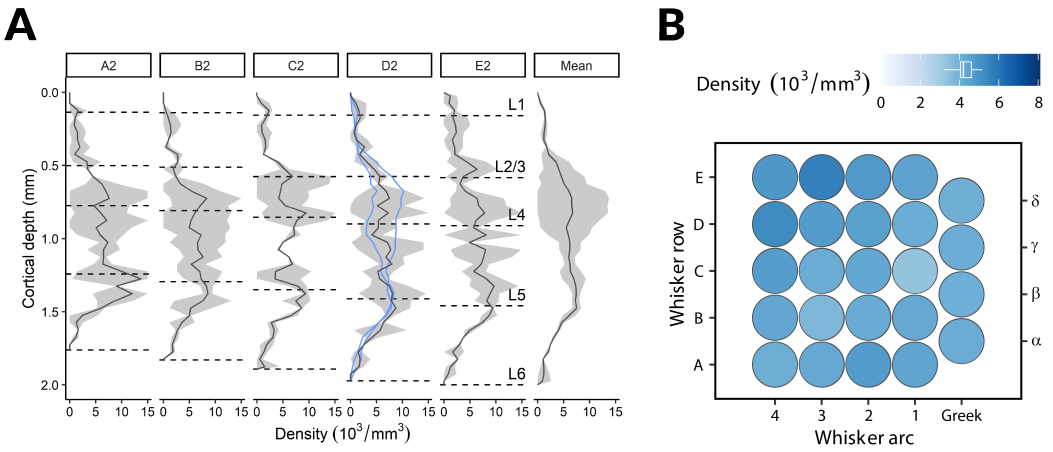

Figure 6.3: Laminar and horizontal organization of Pvalb+ neurons. A. Average distribution of Pvalb+ neuron somata along the vertical column axis for columns in arc-2, namely, A2, B2, C2, D2, E2, and the mean distribution across all barrel columns. Black lines indicate the mean and shaded regions its corresponding 95% CI. The sample size is $n = 2$ for all columns. Blue lines correspond to the two Pvalb-profiles obtained from the 3D quantification in the ROI. Dashed lines represent column-specific layer borders. B. The average Pvalb+ neuron density per barrel column is constant across the barrel field. The boxplot inserted in the colorbar summarizes the overall density in the barrel field.

Whisker	Volume	Neurons	Whisker	Volume	Neurons
A1	0.16 ± 0.05	744 ± 564	D1	0.22 ± 0.08	937 ± 687
A2	0.15 ± 0.03	686 ± 208	D2	0.31 ± 0.05	1420 ± 669
A3	0.10 ± 0.004	442 ± 278	D3	0.25 ± 0.03	1162 ± 304
A4	0.12 ± 0.05	516 ± 584	D4	0.24 ± 0.08	1212 ± 75
A-row	0.13 ± 0.02	597 ± 190	D-row	0.25 ± 0.03	1183 ± 229
B1	0.15 ± 0.01	608 ± 286	E1	0.27 ± 0.07	1243 ± 520
B2	0.18 ± 0.02	764 ± 481	E2	0.30 ± 0.06	1408 ± 148
B3	0.15 ± 0.01	568 ± 183	E3	0.33 ± 0.06	1821 ± 274
B4	0.14 ± 0.05	635 ± 538	E4	0.28 ± 0.01	1366 ± 403
B-row	0.16 ± 0.02	644 ± 160	E-row	0.30 ± 0.03	1460 ± 212
C1	0.20 ± 0.01	635 ± 203	α	0.15 ± 0.04	631 ± 539
C2	0.19 ± 0.02	802 ± 294	β	0.16 ± 0.05	675 ± 404
C3	0.23 ± 0.01	951 ± 387	δ	0.29 ± 0.15	1202 ± 746
C4	0.21 ± 0.04	1033 ± 699	γ	0.19 ± 0.001	799 ± 295
C-row	0.21 ± 0.02	855 ± 200	Mean	0.21 ± 0.02	928 ± 119

Table 6.3: Whisker-specific organization of Pvalb+ neurons. Displayed numbers are mean ± 95% CI, with a sample size of $n = 2$. Volume units are given in mm^3.

	Avg. column		D2 column		ROI	
	Neurons	Fraction	Neurons	Fraction	Neurons	Fraction
L1	12 ± 3	9.0 ± 3	21 ± 8	10.4 ± 5	20 ± 16	29.1 ± 18
L2/3	100 ± 18	18.5 ± 4	131 ± 36	24.6 ± 10	209 ± 166	50.7 ± 18
L4	205 ± 42	46.7 ± 12	354 ± 280	78.4 ± 95	328 ± 278	49.9 ± 19
L5	363 ± 51	47.0 ± 8	536 ± 390	75.8 ± 59	597 ± 267	59.3 ± 14
L6	248 ± 22	55.7 ± 9	377 ± 27	66.5 ± 43	202 ± 91	48.9 ± 15
Total	928 ± 119	39.8 ± 6	1420 ± 669	57.6 ± 39	1356 ± 787	53.3 ± 15

Table 6.4: Assessment of the laminar distribution of Pvalb+ neurons. Avg. column corresponds to the average across columns ($n = 24$), and ROI to a region of interest in the center of the barrel cortex. Numbers are mean ± 95% CI. The quantification in the ROI was performed in 3D, whereas for the rest, it was in 2D with subsequent scaling. Further details can be found in the text.

periments in the D2 column (two-tailed t-test: $p < 0.037$) and 3D ROI (two-tailed t-test: $p < 0.014$) quantification. Figure 6.3B shows the horizontal organization of Pvalb+ neurons. Similarly as for Gad67, the average neuron density per barrel column remained constant across the entire barrel field (two-tailed t-test: $p = 0.587$). The boxplot inserted in the colorbar summarizes the overall density in the barrel field, with a median of 4205 neurons/mm^3.

Table 6.3 presents the whisker-specific organization of Pvalb+ neurons, and the corresponding volume of each barrel column. From these experiments, the total volume of the barrel cortex was 6.28 ± 0.46 mm^3, consistent with 6.60 ± 0.57 mm^3 previously reported in (Meyer *et al.*, 2013). Similarly as in the Gad67 case, the barrel column volumes within the same whisker row were almost identical and increased from the A-row towards the E-row (1-way ANOVA: $p < 5.8 \cdot 10^{-5}$). The average number of Pvalb+ neurons per cortical barrel column was proportional to the column volume. A relatively constant number of Pvalb+ neurons for columns within the same whisker row was obtained, as shown in Table 6.3. Then, similarly as for the volume, there was an increase in the number of neurons from the A-row towards the E-row (1-way ANOVA: $p < 4.0 \cdot 10^{-5}$), with the average number of Pvalb+ neurons in the E-row being approximately 2.4 times higher than that in the A-row (597 ± 190 inhibitory neurons in the A-row). The whisker-specific organization of Pvalb+ neurons across cortical layers can be found in Tables B.2 (L1), B.6 (L2/3), B.10 (L4), B.14 (L5), and B.18 (L6).

The laminar distribution of Pvalb+ neurons is presented in Table 6.4. Similarly as in the Gad67 case, no significant differences were found in the number of Pvalb+ neurons across the average column, the D2 column, and the ROI in the center of the barrel cortex (1-way ANOVA: $p = 0.676$). Furthermore, their ratio to Gad67 was also indistinguishable between them (1-way ANOVA: $p = 0.529$).

Thus, the 3D quantification obtained in this dissertation provides a reliable estimate of the average distribution of Pvalb+ neurons in the barrel cortex.

6.4 Somatostatin

The previous methodology is now applied to assess the organization of Sst-expressing neurons throughout the entire barrel cortex. The first step was to scale the number of Sst+ neurons obtained from single optical images by applying Equation (6.1) to each experiment. I obtained $\beta = 3.6$ ($R^2 = 0.94$, $p < 8.70 \cdot 10^{-22}$) and $\beta = 4.5$ ($R^2 = 0.86$, $p < 1.40 \cdot 10^{-16}$), respectively.

Figure 6.4A illustrates the laminar organization of Sst+ neurons. The scaled density distribution of neuron somata along the columns A2, B2, C2, D2, E2, and the mean distribution across all barrel columns are shown in black. Blue lines correspond to the two Sst-profiles obtained from the 3D quantification in

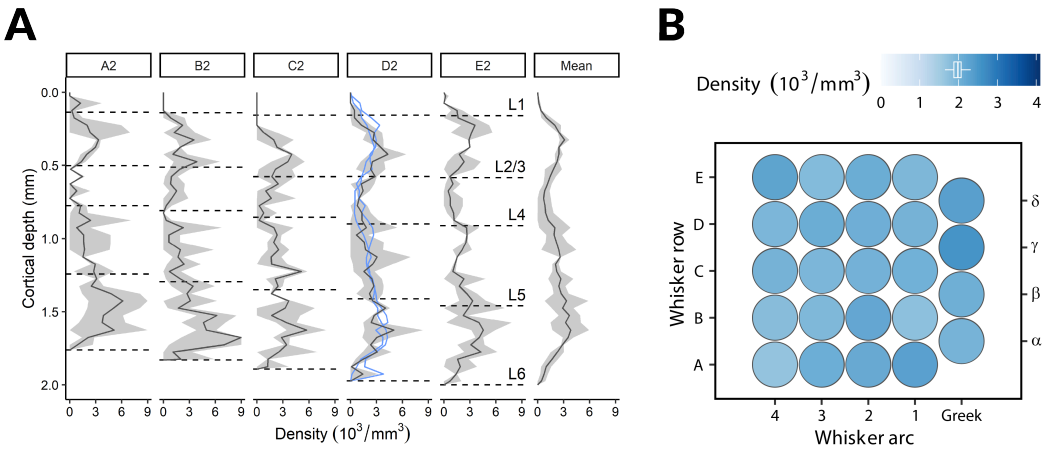

Figure 6.4: Laminar and horizontal organization of Sst+ neurons. A. Average distribution of Sst+ neuron somata along the vertical column axis for columns in arc-2, namely, A2, B2, C2, D2, E2, and the mean distribution across all barrel columns. Black lines indicate the mean and shaded regions its corresponding 95% CI. The sample size is $n = 2$ for all columns. Blue lines correspond to the two Sst-profiles obtained from the 3D quantification in the ROI. Dashed lines represent column-specific layer borders. B. The average Sst+ neuron density per barrel column is constant across the barrel field. The boxplot inserted in the colorbar summarizes the overall density in the barrel field.

Whisker	Volume	Neurons	Whisker	Volume	Neurons
A1	0.11 ± 0.12	203 ± 125	D1	0.22 ± 0.03	447 ± 314
A2	0.13 ± 0.08	259 ± 73	D2	0.30 ± 0.08	616 ± 304
A3	0.09 ± 0.05	185 ± 49	D3	0.31 ± 0.08	636 ± 201
A4	0.09 ± 0.01	144 ± 120	D4	0.25 ± 0.05	480 ± 201
A-row	0.10 ± 0.03	198 ± 48	D-row	0.27 ± 0.04	545 ± 116
B1	0.16 ± 0.05	286 ± 259	E1	0.36 ± 0.03	672 ± 170
B2	0.16 ± 0.11	339 ± 252	E2	0.43 ± 0.01	866 ± 241
B3	0.17 ± 0.09	317 ± 296	E3	0.37 ± 0.14	685 ± 516
B4	0.16 ± 0.02	276 ± 31	E4	0.28 ± 0.14	652 ± 451
B-row	0.16 ± 0.03	304 ± 90	E-row	0.36 ± 0.05	719 ± 155
C1	0.24 ± 0.06	490 ± 383	α	0.13 ± 0.02	251 ± 136
C2	0.24 ± 0.11	489 ± 393	β	0.15 ± 0.01	296 ± 103
C3	0.25 ± 0.06	464 ± 143	δ	0.16 ± 0.15	355 ± 286
C4	0.28 ± 0.04	550 ± 201	γ	0.15 ± 0.05	352 ± 49
C-row	0.25 ± 0.03	498 ± 116	Mean	0.22 ± 0.03	430 ± 64

Table 6.5: Whisker-specific organization of Sst+ neurons. Displayed numbers are mean ± 95% CI, with a sample size of $n = 2$. Volume units are given in mm^3.

	Avg. column		D2 column		ROI	
	Neurons	Fraction	Neurons	Fraction	Neurons	Fraction
L1	4 ± 2	2.8 ± 1	4 ± 8	2.0 ± 4	19 ± 37	8.3 ± 16
L2/3	105 ± 18	19.4 ± 4	157 ± 63	29.3 ± 14	115 ± 59	22.7 ± 3
L4	36 ± 8	8.1 ± 2	80 ± 45	17.6 ± 19	29 ± 14	9.0 ± 3
L5	124 ± 22	16.0 ± 3	164 ± 105	23.1 ± 16	112 ± 54	17.7 ± 6
L6	161 ± 21	36.2 ± 7	212 ± 83	37.4 ± 28	189 ± 81	29.0 ± 5
Total	430 ± 64	18.4 ± 3	616 ± 304	25.0 ± 17	464 ± 246	20.2 ± 2

Table 6.6: Assessment of the laminar distribution of Sst+ neurons. Avg. column corresponds to the average across columns ($n = 24$), and ROI to a region of interest in the center of the barrel cortex. Numbers are mean ± 95% CI. The quantification in the ROI was performed in 3D, whereas for the rest, it was in 2D with subsequent scaling. Further details can be found in the text.

the ROI. There was no significant difference between them and their corresponding quantification in the D2 column (two-tailed t-test: $p = 0.616$ and $p = 0.627$). And in this case, also between experiments in the D2 column (two-tailed t-test: $p = 0.142$) and 3D ROI (two-tailed t-test: $p = 0.465$) quantification. Figure 6.4B shows the horizontal organization of Sst+ neurons. Similarly as in the previous cases, the average density per barrel column remained constant across the entire barrel field (two-tailed t-test: $p = 0.538$). The boxplot inserted in the colorbar summarizes the overall density in the barrel field, with a median of 1981 neurons/mm^3.

Table 6.5 presents the whisker-specific organization of Sst+ neurons, and the corresponding volume of each barrel column. The total volume of the barrel cortex from these experiments was 6.52 ± 0.07 mm^3, consistent with (Meyer *et al.*, 2013). Similarly as in the previous cases, the volumes of barrel columns within the same whisker row were almost identical, and increased from the A-row towards the E-row (1-way ANOVA: $p < 1.2 \cdot 10^{-8}$). The average number of Sst+ neurons per cortical barrel column was proportional to the column volume. A relatively constant number of Sst+ neurons for columns within the same whisker row was obtained, as shown in Table 6.5. Then, similarly as for the volume, there was an increase in the number of neurons from the A-row towards the E-row (1-way ANOVA: $p < 1.4 \cdot 10^{-8}$)., with the average number of Sst+ neurons in the E-row being approximately 3.6 times higher than that in the A-row (198 ± 48 inhibitory neurons in the A-row). The whisker-specific organization of Sst+ neurons across cortical layers can be found in Tables B.3 (L1), B.7 (L2/3), B.11 (L4), B.15 (L5), and B.19 (L6).

The laminar distribution of Sst+ neurons is presented in Table 6.6. Similarly as in the previous cases, no significant differences were found in the number of Sst+ neurons across the average column, the D2 column, and the ROI in the center of the barrel cortex (1-way ANOVA: $p = 0.693$). Furthermore, their ratio to Gad67 was also indistinguishable between them (1-way ANOVA: $p = 0.747$).

Thus, the 3D quantification obtained in this dissertation provides a reliable estimate of the average distribution of Sst+ neurons in the barrel cortex.

6.5 Vasoactive intestinal polypeptide

To assess the organization of Vip-expressing neurons throughout the entire barrel cortex, the same methodology is applied. The number of Vip+ neurons obtained from single optical images are scaled by applying Equation (6.1) to each experiment. I obtained $\beta = 5.6$ ($R^2 = 0.85$, $p < 4.59 \cdot 10^{-15}$) and $\beta = 5.2$ ($R^2 = 0.89$, $p < 6.03 \cdot 10^{-16}$), respectively.

Figure 6.5A illustrates the laminar organization of Vip+ neurons. The scaled density distribution of neuron somata along the columns A2, B2, C2, D2, E2, and the mean distribution across all barrel columns are shown in black. Blue

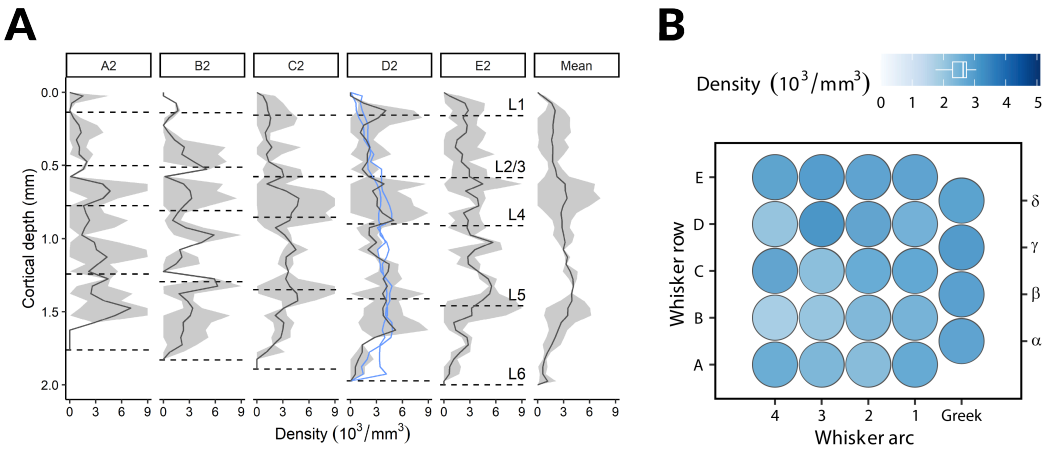

Figure 6.5: Laminar and horizontal organization of Vip+ neurons. A. Average distribution of Vip+ neuron somata along the vertical column axis for columns in arc-2, namely, A2, B2, C2, D2, E2, and the mean distribution across all barrel columns. Black lines indicate the mean and shaded regions its corresponding 95% CI. The sample size is $n = 2$ for all columns. Blue lines correspond to the two Vip- profiles obtained from the 3D quantification in the ROI. Dashed lines represent column-specific layer borders. B. The average Vip+ neuron density per barrel column is constant across the barrel field. The boxplot inserted in the colorbar summarizes the overall density in the barrel field.

Whisker	Volume	Neurons	Whisker	Volume	Neurons
A1	0.16 ± 0.05	425 ± 63	D1	0.17 ± 0.03	432 ± 19
A2	0.15 ± 0.01	323 ± 58	D2	0.24 ± 0.01	643 ± 59
A3	0.10 ± 0.01	241 ± 178	D3	0.24 ± 0.09	747 ± 411
A4	0.11 ± 0.02	289 ± 189	D4	0.23 ± 0.06	460 ± 100
A-row	0.13 ± 0.02	319 ± 72	D-row	0.22 ± 0.03	571 ± 126
B1	0.16 ± 0.02	382 ± 127	E1	0.32 ± 0.08	890 ± 143
B2	0.16 ± 0.04	368 ± 82	E2	0.33 ± 0.19	954 ± 792
B3	0.13 ± 0.003	252 ± 33	E3	0.37 ± 0.06	1092 ± 395
B4	0.15 ± 0.05	266 ± 129	E4	0.26 ± 0.03	720 ± 258
B-row	0.15 ± 0.02	317 ± 57	E-row	0.32 ± 0.05	914 ± 202
C1	0.19 ± 0.03	500 ± 142	α	0.16 ± 0.03	433 ± 220
C2	0.21 ± 0.01	540 ± 215	β	0.19 ± 0.01	557 ± 73
C3	0.22 ± 0.03	491 ± 132	δ	0.29 ± 0.01	797 ± 33
C4	0.19 ± 0.04	502 ± 22	γ	0.25 ± 0.01	749 ± 251
C-row	0.20 ± 0.02	508 ± 57	Mean	0.21 ± 0.02	544 ± 74

Table 6.7: Whisker-specific organization of Vip+ neurons. Displayed numbers are mean ± 95% CI, with a sample size of $n = 2$. Volume units are given in mm^3.

	Avg. column		D2 column		ROI	
	Neurons	Fraction	Neurons	Fraction	Neurons	Fraction
L1	24 ± 6	17.8 ± 5	34 ± 24	16.7 ± 13	18 ± 4	22.5 ± 13
L2/3	88 ± 18	16.2 ± 4	92 ± 87	17.3 ± 17	96 ± 11	27.1 ± 3
L4	99 ± 22	22.7 ± 6	141 ± 147	31.2 ± 43	149 ± 15	43.5 ± 5
L5	193 ± 32	25.0 ± 5	200 ± 18	28.3 ± 9	242 ± 71	31.9 ± 3
L6	140 ± 17	31.4 ± 6	176 ± 113	31.0 ± 28	173 ± 5	33.3 ± 1
Total	544 ± 74	23.3 ± 4	643 ± 59	26.1 ± 13	677 ± 77	33.0 ± 0

Table 6.8: Assessment of the laminar distribution of Vip+ neurons. Avg. column corresponds to the average across columns ($n = 24$), and ROI to a region of interest in the center of the barrel cortex. Numbers are mean ± 95% CI. The quantification in the ROI was performed in 3D, whereas for the rest, it was in 2D with subsequent scaling. Further details can be found in the text.

lines correspond to the two Vip-profiles obtained from the 3D quantification in the ROI. There was no significant difference between them and their corresponding quantification in the D2 column (two-tailed t-test: $p = 0.365$ and $p = 0.556$). And in this case, also between experiments in the D2 column (two-tailed t-test: $p = 0.657$) and 3D ROI (two-tailed t-test: $p = 0.879$) quantification. Figure 6.5B shows the horizontal organization of Vip+ neurons. Similarly as in the previous cases, the average density per barrel column remained constant across the entire barrel field (two-tailed t-test: $p = 0.480$). The boxplot inserted in the colorbar summarizes the overall density in the barrel field, with a median of 2632 neurons/mm^3.

Table 6.7 presents the whisker-specific organization of Vip+ neurons, and the corresponding volume of each barrel column. The total volume of the barrel cortex from these experiments was 6.26 ± 0.09 mm^3, consistent with (Meyer *et al.*, 2013). Similarly as in the previous cases, the volumes of barrel columns within the same whisker row were almost identical, and increased from the A-row towards the E-row (1-way ANOVA: $p < 9.2 \cdot 10^{-6}$). The average number of Vip+ neurons per cortical barrel column was proportional to the column volume. A relatively constant number of Vip+ neurons for columns within the same whisker row was obtained, as shown in Table 6.7. Then, similarly as for the volume, there was an increase in the number of neurons from the A-row towards the E-row (1-way ANOVA: $p < 1.3 \cdot 10^{-5}$)., with the average number of Vip+ neurons in the E-row being approximately 2.7 times higher than that in the A-row (425 ± 63 inhibitory neurons in the A-row). The whisker-specific organization of Vip+ neurons across cortical layers can be found in Tables B.4 (L1), B.8 (L2/3), B.12 (L4), B.16 (L5), and B.20 (L6).

The laminar distribution of Vip+ neurons is presented in Table 6.8. Similarly as in the previous cases, no significant differences were found in the number of Vip+ neurons across the average column, the D2 column, and the ROI in the center of the barrel cortex (1-way ANOVA: $p = 0.832$). Furthermore, their ratio to Gad67 was also indistinguishable between them (1-way ANOVA: $p = 0.156$).

Thus, the 3D quantification obtained in this dissertation provides a reliable estimate of the average distribution of Vip+ neurons in the barrel cortex.

6.6 Evaluation

The density of inhibitory neurons, including those expressing molecular markers such as Pvalb, Sst, and Vip, can vary significantly across cortical depth, and these variations can have important implications in the organization of cortical circuits (Xu *et al.*, 2010; Meyer *et al.*, 2011, 2013; Tremblay *et al.*, 2016). Thus, I first assessed whether the variability of the presented empirical distributions is due to neurobiological factors or technical limitations. For instance, Figure 6.3 showed that the 3D density distribution of Pvalb+ neurons from two experiments

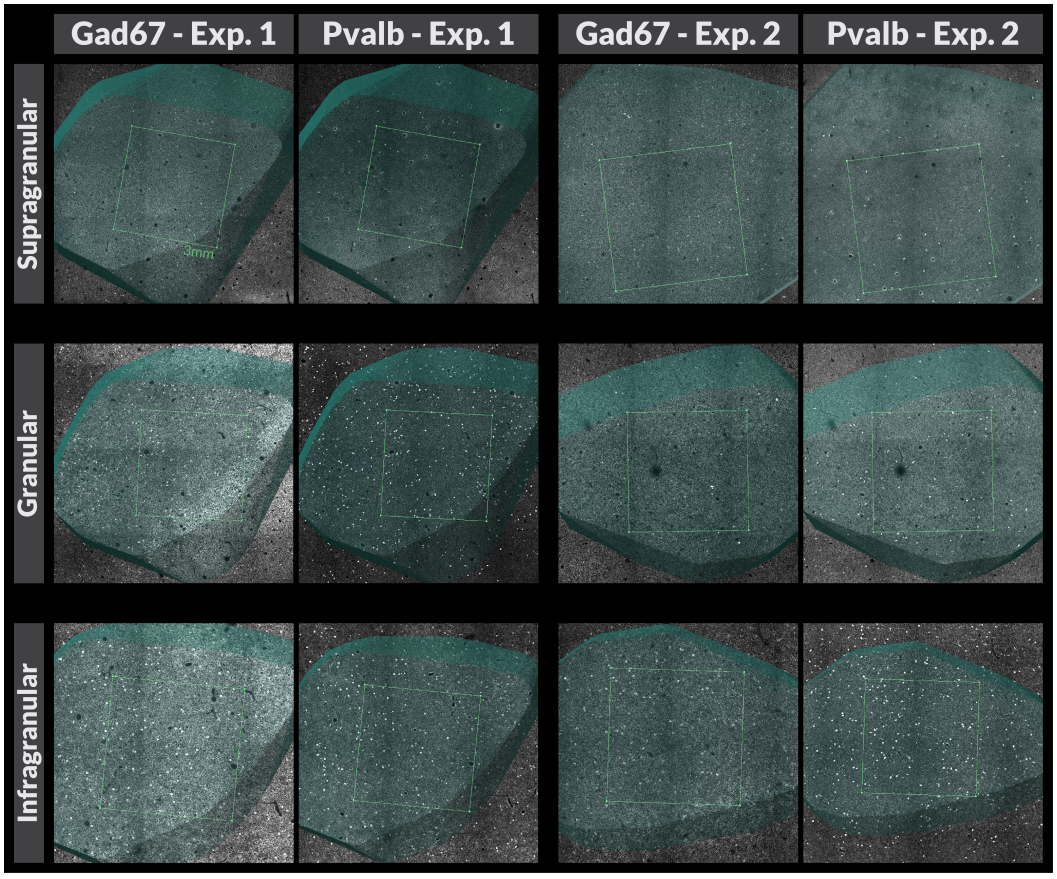

Figure 6.6: Assessment of the variability of Pvalb+ neurons. Example Pvalb-images with their corresponding Gad67-image across laminar locations and experiments. In each image, the convex-hull of the barrel cortex and the 3 mm side region of interest (ROI) are visible. Further details can be found in the text.

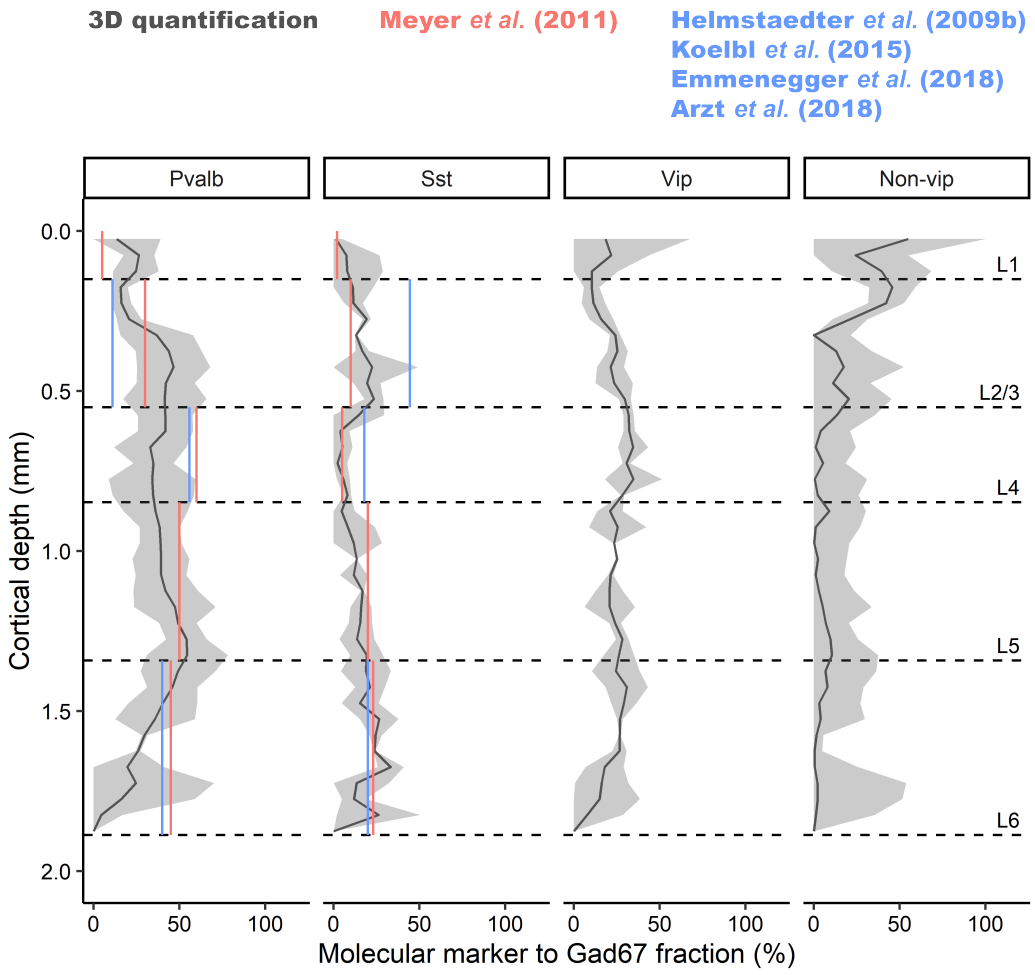

Figure 6.7: Validation of the laminar distribution. For each molecular marker, the fraction to its corresponding Gad67-distribution is illustrated. Black lines indicate the mean and shaded regions its corresponding 95% CI. Red and blue lines correspond to reported fractions. Further details can be found in the text.

(blue lines) were remarkably different (two-sample KS test: $p < 3.6 \cdot 10^{-3}$), predominantly in the granular layer. In contrast, the 3D density distributions of Sst+ and Vip+ neurons, shown in blue in Figures 6.4 and 6.5, were similar across experiments (two-sample KS test: $p = 0.773$ and $p = 0.279$, respectively).

Figure 6.6 illustrates the variability of Pvalb+ neurons across cortical depth. Each experiment includes Pvalb and Gad67 confocal images from three different laminar locations: supragranular (approximately at 300 µm from the pial surface), granular (700 µm), and infragranular (1200 µm). In each image, the convex-hull of the barrel cortex and the 3 mm side ROI are shown. The large difference in the number of Pvalb+ neurons between experiments is also seen in the number of Gad67+ neurons from the same experiments, predominantly in the granular layer. By calculating the fraction of each molecular marker's 3D density distribution relative to its corresponding Gad67 3D density distribution at 50 µm-depth bins, I obtained consistent and indistinguishable distributions across experiments. Specifically, the two-sample KS test revealed no significant differences for Pvalb ($p = 0.738$), Sst ($p = 0.545$), or Vip ($p = 0.545$) fractions.

Figure 6.7 shows the 3D quantification of these fractions as a function of cortical depth. The Non-vip distribution corresponds to the serotonin 5-HT(3A)R group that is simultaneously negative to Vip (Tremblay *et al.*, 2016). It was calculated as the difference between Gad67 and the remaining molecular markers (i.e., Pvalb, Sst, and Vip). I only compared the obtained Pvalb and Sst distributions with available measurements in rat barrel cortex, as no Vip measurements were found at this juncture. Specifically, Meyer *et al.* (2011) measured the fractions from L1 to L6 in two cortical columns. Helmstaedter *et al.* (2009b) tested their expression in 9 neurons in L2/3, while Koelbl *et al.* (2015) and Emmenegger *et al.* (2018) in 10 and 20 neurons in L4, respectively. In L6, Arzt *et al.* (2018) tested their expression in 5 neurons. Overall, the fractions of Pvalb and Sst distribution show a remarkable agreement with previously reported measurements.

6.7 Summary

In order to investigate the molecular composition of inhibitory neurons in the rat barrel cortex, a series of experiments using double-immunolabeling against Gad67 and either Pvalb, Sst, or Vip were performed. Confocal images of the double-immunolabeled tissue sections were analyzed to quantify the 3D density distribution and absolute number of neuron somata expressing these molecular markers across cortical depth throughout the entire barrel field. The distribution of these molecular markers was heterogeneous across layers and barrel columns. The fraction of inhibitory neurons expressing each of these molecular markers across cortical depth provides a reliable estimate of the composition of the rat barrel cortex.

Chapter 7

Depth-dependent gradients of morphoelectric properties

I investigated the role of different morphoelectric properties in inhibitory neuron diversity. For this purpose, I color-coded the morphoelectric embedding (me-UMAP) by z-scores of morphoelectric features, relevant for defining morphoelectric class assignments (me-types). When color-coding by cortical depth, a depth-specific trend across layers was identified. By unfolding the manifold with affine transformations, the horizontal axis displayed a smooth gradient of neuron somata ranging from the pial surface to the white matter, independent of me-type. Among the morphological features, the most important ones after cortical depth were those related to the axon and dendrite depth distributions, which had the role of defining cortical layers. Interestingly, other morphological features, such as the axon and dendrite vertical extent, increased with cortical depth, regardless of me-type. The axon vertical extent also displayed a bimodal distribution with larger neurons on the upper part of the me-UMAP, and smaller neurons on the lower part of it. I then performed the same analysis for electrophysiological features, where some of them displayed smooth gradients as a function of cortical depth. Furthermore, they could be associated to intrinsic properties such as the frequency and adaptation of the firing patterns. The frequency of the firing patterns increased with cortical depth and at the same time displayed a bimodal distribution with fast-spiking (FS) neurons on the lower and non-FS neurons on the upper part of the me-UMAP. The adaptation of the firing patterns was higher on the upper part of the me-UMAP, regardless of cortical depth. Remarkable similarities were obtained when analyzing mouse visual cortex (Gouwens *et al.*, 2019, 2020). Thus, depth-dependent gradients of morphoelectric properties are conserved across species and cortex areas.

The most important neurobiological results from Chapter 7 are:

- The size of inhibitory neurons increases with cortical depth.
- The frequency of their firing patterns also increases with cortical depth.
- The adaptation, however, is independent of cortical depth.
- These depth-dependent gradients are also observed in mouse visual cortex.

7.1 The organizing role of cortical depth

Morphoelectric class assignments (me-types) are predominantly depth-dependent. Thus, I assessed the impact of cortical depth in the diversity of inhibitory neurons.

Figure 7.1 illustrates the morphoelectric embedding (me-UMAP) color-coded by cortical depth, the most important feature for defining me-types. A depth-specific trend across layers was identified by fitting a spline at a resolution of 100 µm bins (Figure 7.1; top-left). This trend was unfolded, in order to obtain an approximately smooth gradient of neuron somata ranging from the pial surface to the white matter (WM). The method to unfold or detrend the me-UMAP was as follows. First, each inhibitory neuron in the me-UMAP was mapped to a closed unitary ball around the origin given by $B = \{x \in \mathbb{R}^n : ||x||_2 \leq 1\}$. Then, the me-UMAP was clustered into three layers, namely supra-, infra-, and granular layers, using a Gaussian mixture model with three components. The predicted labels were used to identify the inhibitory neurons belonging to each layer. The supra- and granular layers were flipped vertically and horizontally, respectively, to align them with the infragranular layer. A linear regression was applied per layer in order to obtain the angle with respect to the origin. The respective angle and an inverse rotation matrix were used in each layer to place it along the horizontal axis. Then, all layers were centered at the origin. Finally, the supra- and infragranular layers were shifted symmetrically along the horizontal axis. The unfolded me-UMAP is presented in Figure 7.2. L1 to L6 are placed from left to right in the me-UMAP. The overall gradient (Figure 7.2; top-left) was calculated via linear regression between the spatial coordinates of the me-UMAP and the corresponding cortical depth values.

Thus, the horizontal axis displayed a smooth gradient of neuron somata ranging from the pial surface to WM, independent of me-type.

7.2 Morphological properties

Figure 7.3 presents the most important morphological features used for classification, after cortical depth. These features, namely the axon and dendrite depth distributions, were able to distinguish cortical layers. For instance, the *axon* and *dendrite histogram PC1* separated the granular layer (L4) from the rest. The *axon histogram PC2* did the same but for the supragranular layer, i.e., L1/3. Then, the *dendrite histogram PC2* exclusively targeted inhibitory neurons in the deep layers, specifically in L6. Both the *axon* and *dendrite histogram PC3* also targeted the infragranular layer, but specifically L5. The remaining features related to the axon and dendrite depth distributions, namely the *axon histogram PC4-6* and *dendrite histogram PC4-5*, are not shown in Figure 7.3. However, the *axon histogram PC4* focused exclusively in separating the small number of inhibitory neurons in L1 from

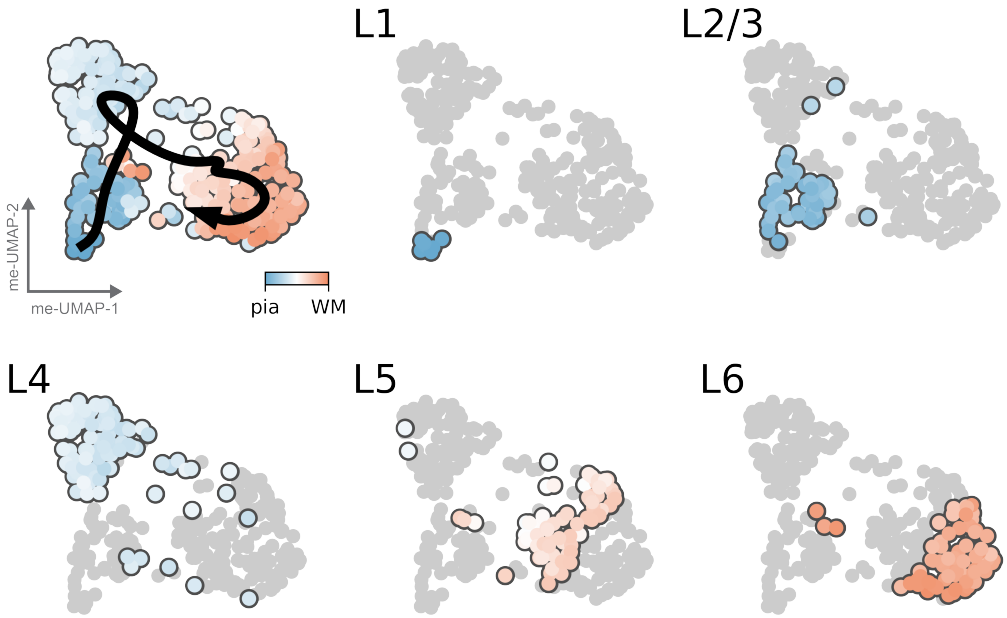

Figure 7.1: Unfolding the low-dimensional morphoelectric embedding (me-UMAP) by cortical depth. The me-UMAPs are color-coded by soma depth and subdivided by laminar location when indicated. In the top-left panel, the trend from pia to white matter is also shown. Further details can be found in the text.

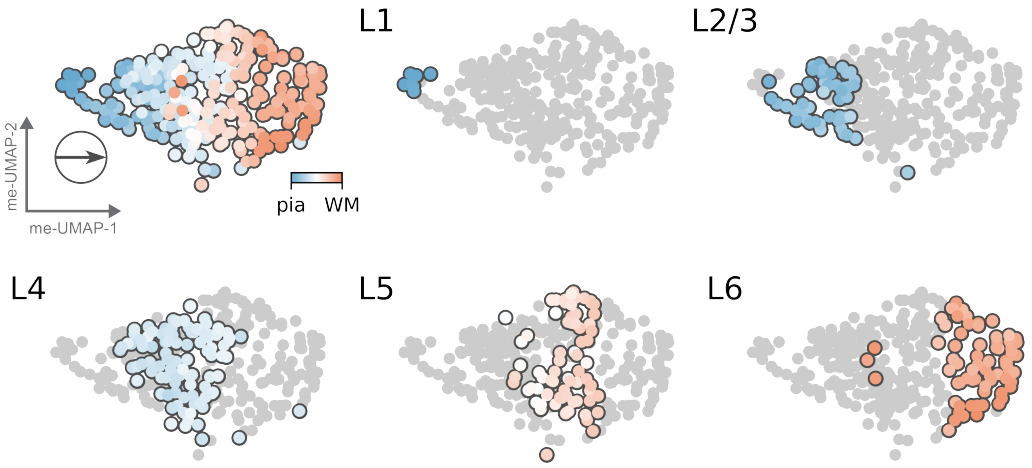

Figure 7.2: Low-dimensional morphoelectric embedding (me-UMAP) unfolded via affine transformations. The me-UMAPs are color-coded by soma depth and subdivided by laminar location when indicated. In the top-left panel, the overall gradient of this feature is also shown. Further details can be found in the text.

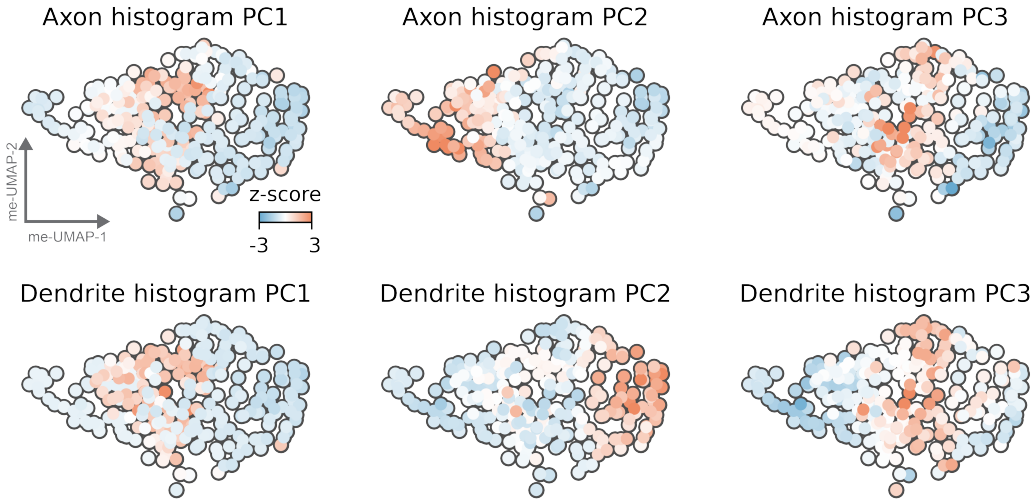

Figure 7.3: Low-dimensional morphoelectric embedding (me-UMAP) color-coded by most important morphological features after cortical depth.

the rest. Finally, the *axon histogram PC5-6* and *dendrite histogram PC4-5* did not show apparent layer-specific patterns.

I then assessed other morphological features, specifically the ones related to the length of the axons and dendrites. These features characterized their height, width, and total length. Figure 7.4 illustrates the me-UMAP color-coded by these six features. Each panel contains an arrow that represents the overall gradient of the corresponding feature, which is obtained by fitting a linear regression between the spatial coordinates of the me-UMAP and the z-scored values of the underlying feature. In contrast to Figure 7.3, these six features display smooth gradients as a function of cortical depth. For instance, the *axon height* (or *axon vertical extent*) and *dendrite height* (or *dendrite vertical extent*) increased with cortical depth, regardless of me-type. At the same time, the *axon height* displayed a bimodal distribution with larger neurons on the upper part of the me-UMAP, and smaller neurons on the lower part of it. This suggested that the y-axis may in part encode neuron size. Something similar was observed for the *dendrite height*, however, as the overall gradient was closer to the x-axis, the effect was less apparent. The *axon* and *dendrite width* also presented depth-dependent gradients, with larger inhibitory neurons located in the deeper layers. In the case of the width, the bimodal distribution separating small and large neurons was not present. This indicates, for example, that the axonal arborization of basket and Martinotti cells in the deep layers would be similar with respect to width but very different with respect to height. Furthermore, those same Martinotti cells and L2/3 bipolar cells would be similar with respect to height but very different with respect to width. Then, for the *axon* and *dendrite total length* the depth-dependent gradients displayed a similar pattern as in the previous cases, however, the distribution was not so smooth. The overall depth-dependent gradients were present in many morphological features, despite factual differences between them.

The volume of the axonal and dendritic arborizations of inhibitory neurons was then calculated to evaluate whether the neuron size was increasing with cortical depth. Figure 7.5A shows the me-UMAP color-coded by *axon* and *dendrite volume*. The volumes were approximated by counting the number of 50 µm voxels for each registered morphology. As the dataset comprised inhibitory neurons with different slice-thicknesses, I compared the raw count of voxels to the count of voxels in the xz-plane for axons and dendrites separately. The median of the underlying unimodal distributions was 2.7 for axons and 2.0 for dendrites. Thus, the volumes were approximated as the voxel count in the xz-plane times 2.7 for axons and 2.0 for dendrites. The overall trend in the presented features is very similar to the one from the *axon* and *dendrite vertical extent*. Figure 7.5B groups the z-scored features by cortical layer. Each point corresponds to the mean and the range to the 95% CI. For axons and dendrites, the smallest mean volumes are in L1, whereas the largest ones are located in L6. There is a mean volume increase from superficial to

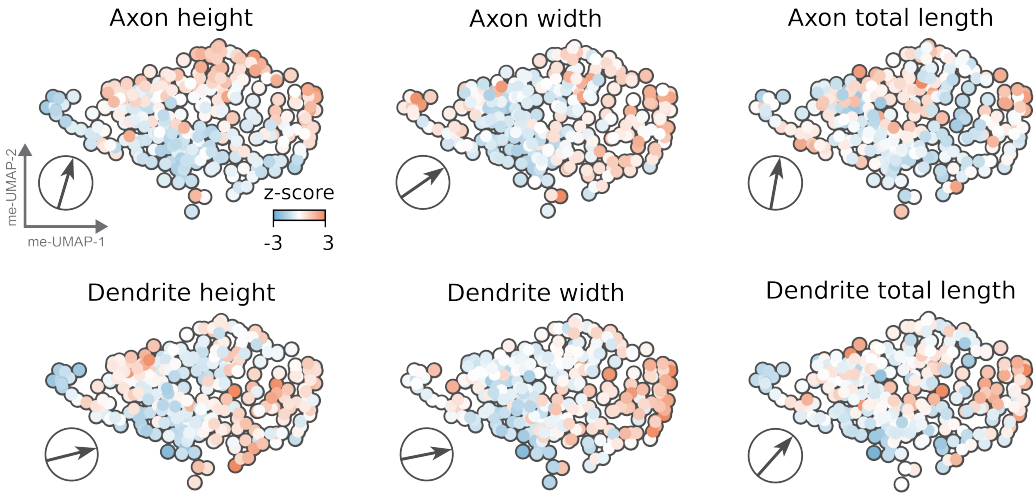

Figure 7.4: Low-dimensional morphoelectric embedding (me-UMAP) color-coded by morphological features. These features display smooth gradients as a function of cortical depth. Further details can be found in the text.

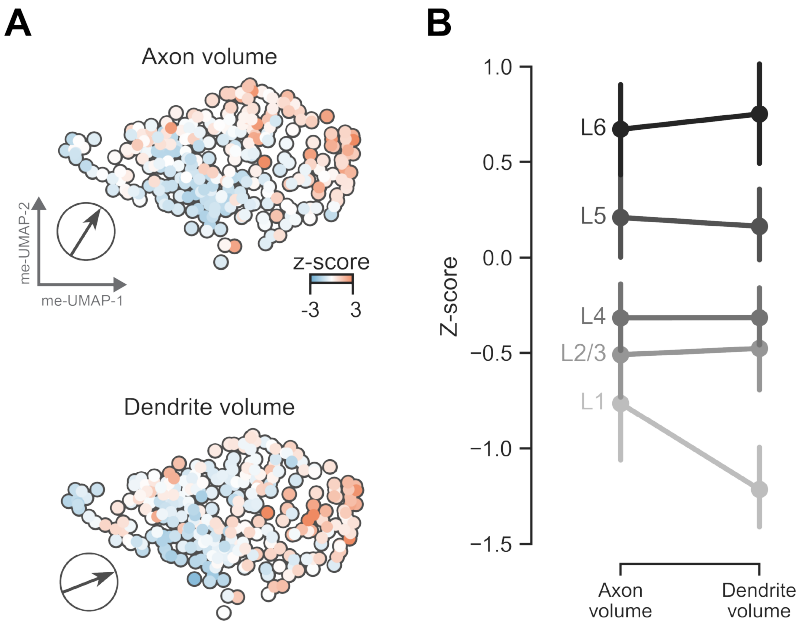

Figure 7.5: Overall inhibitory neuron size increases with cortical depth. A. Low-dimensional morphoelectric embedding (me-UMAP) color-coded by the volume of the axonal and dendritic arborizations. B. Point plot of the features by cortical layer, using mean ± 95% CI. Further details can be found in the text.

deep layers, although, some of them display an overlap in their 95% CI. Altogether, these overall trends suggested that the size of inhibitory neurons was increasing with cortical depth, regardless of me-type.

7.3 Electrophysiological properties

Following the analysis from the previous section, I assessed the most important electrophysiological features used for classification. These features were characterizing the AP half-width, PSTH, and instantaneous firing rate. As *PSTH SPC1* and *Inst firing rate SPC1* were very similar, I included *Inst firing rate SPC2* that displayed an interesting bimodal distribution. Figure 7.6 (top row) illustrates the me-UMAP color-coded by these three features. The *AP width SPC1* (top; left) does not present a depth-dependent gradient, and its distribution distinguishes inhibitory neurons in L1 and L6. Then, *PSTH SPC1* (top; center) presents a depth-dependent gradient that increases with cortical depth. At the same time, it displays a bimodal distribution with larger values on the upper part of the me-UMAP, and smaller values on the lower part of it (see the overall gradient). The same effect was observed for *Inst firing rate SPC1*. In contrast, *Inst firing rate SPC2* (top; right) does not present a depth-dependent gradient that increases with cortical depth, the overall gradient is orthogonal to the cortical depth axis. However, it displays a bimodal distribution that separates the upper and lower parts of the me-UMAP.

In order to better understand the physiological basis of SPC features, I calculated traditional electrophysiological features that correlate with them. For instance, *PSTH SPC1* correlated with the *spike-frequency* (bottom; center), which was defined as the fraction of the number of spikes to the time duration between first and last spikes. The coefficient of determination between them was $R^2 = 0.70$, suggesting that they are strongly correlated. The p-value was significant ($p < 3.05 \cdot 10^{-80}$), indicating that the observed R^2 was highly unlikely to have occurred by chance. To make the relationship between *PSTH SPC1* and *spike-frequency* more clear, I multiplied the z-scores of *PSTH SPC1* by -1. This changed the sign of the z-scores, allowing for a more apparent visual correlation between the two features. Similarly, *Inst firing rate SPC2* was found to be correlated with the *spike-frequency adaptation* (bottom; right). To calculate this, the instantaneous firing rate was first fit to an exponential function. Then, the fraction of the difference between the first and last fitted frequencies was computed and divided by the first fitted frequency. In this case, the coefficient of determination between them was $R^2 = 0.46$ with $p < 5.61 \cdot 10^{-42}$, suggesting a moderate to strong correlation between them. The overall depth-dependent gradients were also present in electrophysiological features, with different degrees of relations to cortical depth.

Figure 7.7 groups the z-scores of the *spike-frequency* and the *spike-frequency*

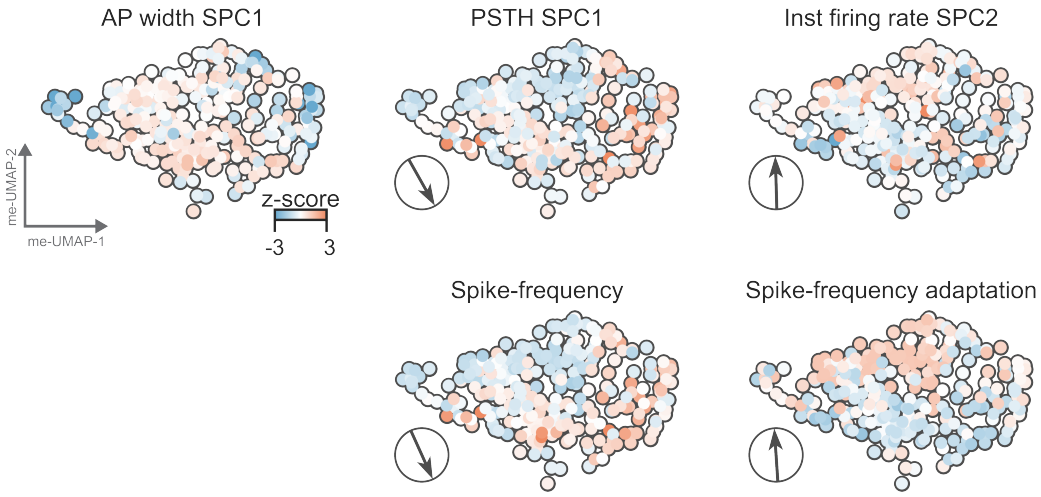

Figure 7.6: Low-dimensional morphoelectric embedding (me-UMAP) color-coded by electrophysiological features. Not all of the most important features display smooth gradients as a function of cortical depth (top). SPC features can be related to common features (bottom). Further details can be found in the text.

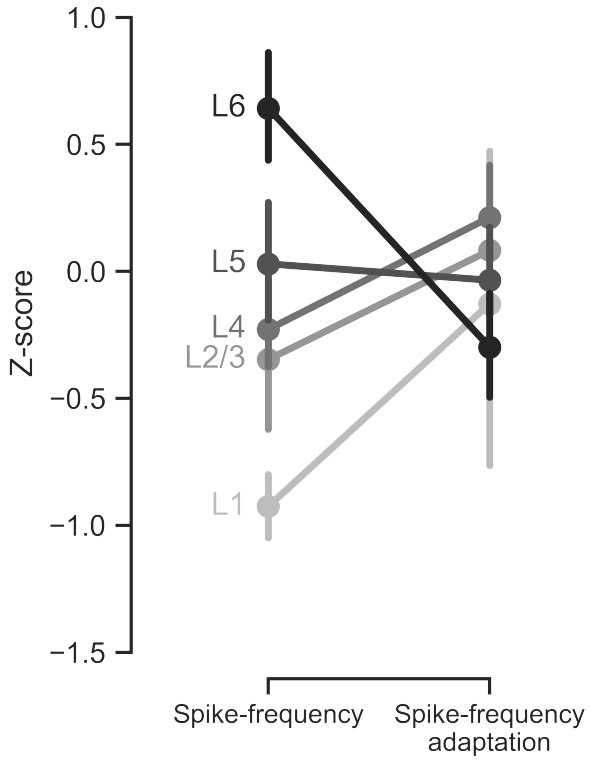

Figure 7.7: Distinct firing patterns display different depth dependencies. Point plot of the spike-frequency and the spike-frequency adaptation by cortical layer, using mean ± 95% CI.

adaptation by cortical layer. Each point corresponds to the mean and the range to the 95% CI. There is a general trend of increasing firing frequency of inhibitory neurons from layer L1 to L6. The overlap in the 95% CIs for some of the layers indicate that while the overall gradient depends on depth, there may be other factors at play that contribute to the variability in *spike-frequency* within and across layers. In contrast, the adaptation of inhibitory neurons does not show a clear trend with respect to depth, as the *spike-frequency adaptation* values overlap across layers. Altogether, these overall trends suggested that the frequency of the firing patterns increases with cortical depth, whereas the adaptation is independent of it.

7.4 Conservation across species and cortex areas

Multiple morphoelectric features display depth-dependent gradients. I defined the minimal set of features that reflected the underlying effect. Two features characterizing the morphology, namely the *axon vertical extent* (or *axon height*), and the *dendrite vertical extent* (or *dendrite height*). And two features characterizing the electrophysiology, namely the *spike-frequency*, and the *spike-frequency adaptation*. These four features were also calculated for 466 inhibitory neurons in mouse visual cortex (Gouwens *et al.*, 2019, 2020). The axodendritic morphological reconstructions in SWC-format were obtained from the Brain Image Library, while the raw electrophysiological traces in NWB-format were obtained from the DANDI Archive (dandiset #000020). The layer borders used in (Gouwens *et al.*, 2019, 2020) were kindly provided by Dr. Staci Sorensen (Allen Institute for Brain Science).

Figure 7.8 illustrates a cross-species comparison of morphological properties across cortical layers. The absolute values of the *axon* and *dendrite vertical extents* are displayed as laminar box plots. Additionally, points representing inhibitory neurons in each layer are overlaid on top of the box plots, and these points are color-coded by the z-score of the respective feature. Figure 7.8A presents the results in rat S1, whereas Figure 7.8B for mouse V1. The absolute scale of axons and dendrites in rat S1 is larger than in mouse V1. However, the relative distributions of these morphological features are remarkably similar between the two species. By visualizing the z-scored data, it is possible to see how both morphological features increase on average across layers in each species, and how the diversity of individual neurons is similar in each layer.

The same cross-species comparison but for electrophysiological properties is presented in Figure 7.9. In this case, the absolute scale and relative distributions of the *spike-frequency* and *spike-frequency adaptation* are remarkably similar between the two species. The overall trend of the *spike-frequency* indicates an increase as a function of cortical depth. In contrast, the level of adaptation in both species remains unaffected by cortical depth.

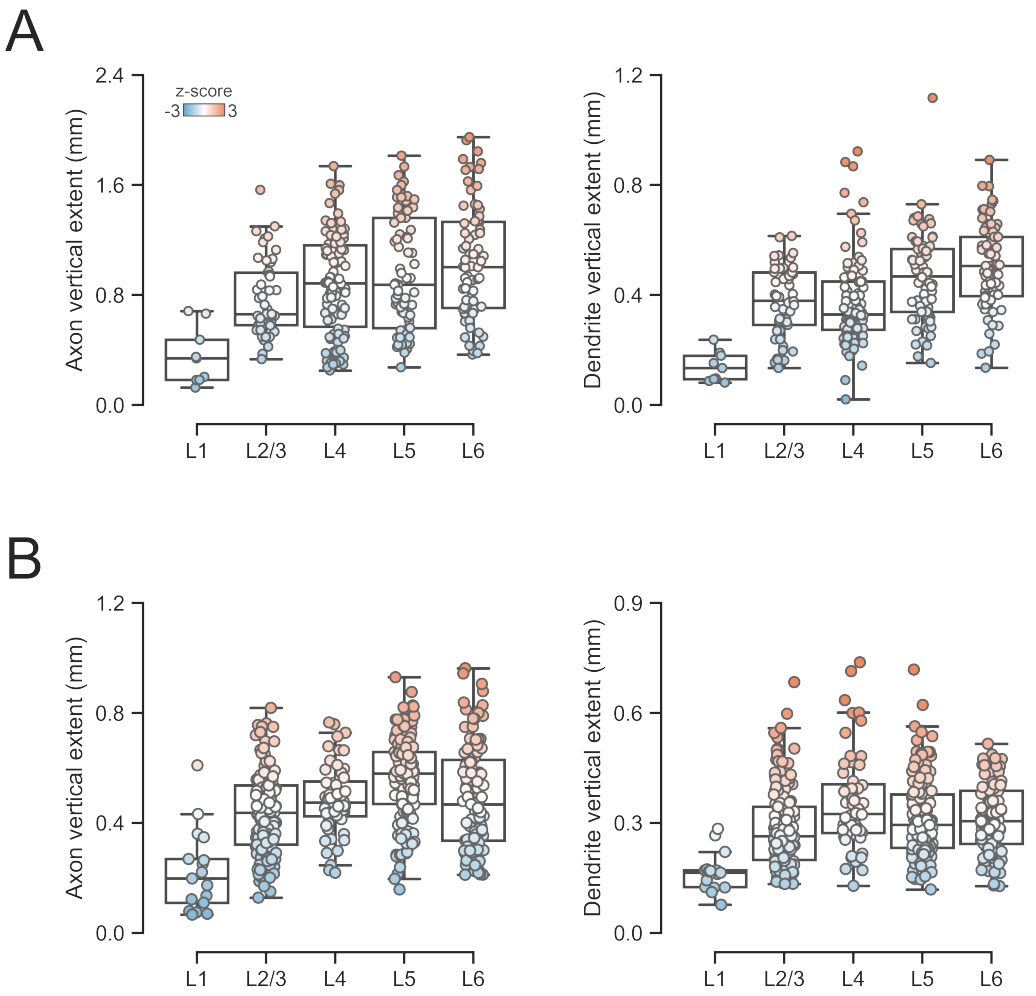

Figure 7.8: Cross-species comparison of the axon and dendrite vertical extents by cortical layer. Inhibitory neurons are color-coded by the respective feature on top of each box plot. A. Rat S1. B. Mouse V1.

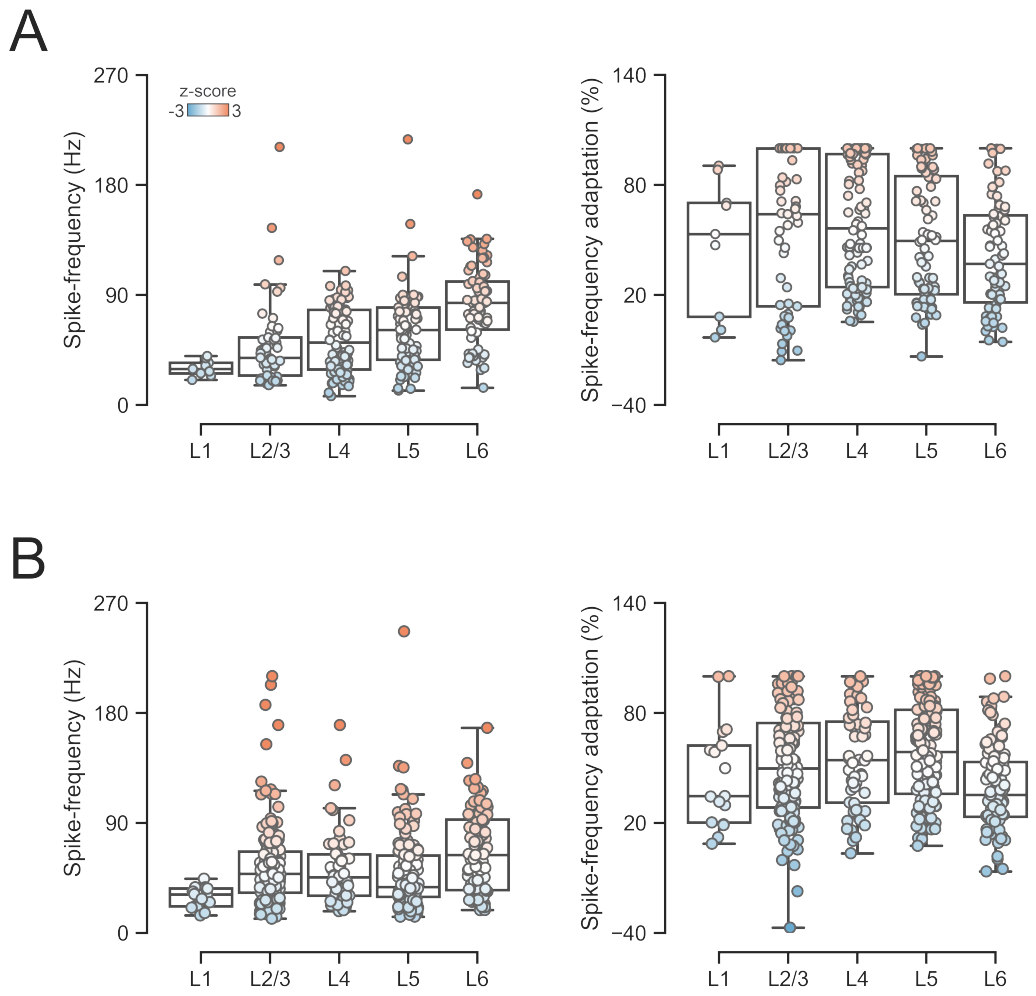

Figure 7.9: Cross-species comparison of the spike-frequency and spike-frequency adaptation by cortical layer. Inhibitory neurons are color-coded by the respective feature on top of each box plot. A. Rat S1. B. Mouse V1.

Therefore, the relative distributions of morphological and electrophysiological properties in rat S1 and mouse V1 are remarkably similar at any given depth location. At the same time, these distributions systematically shift as a function of cortical depth, regardless of me-type.

7.5 Summary

In this chapter, the role of different morphoelectric properties in inhibitory neuron diversity was investigated. The me-UMAP has been color-coded by z-scores of relevant morphoelectric features. A depth-specific trend across layers was identified (Figure 7.10). The most important morphological features after cortical depth were related to the axon and dendrite depth distributions, that defined cortical layers. Other morphological features, such as axon and dendrite vertical extent, increased with cortical depth regardless of me-type. The axon vertical extent displayed a bimodal distribution with larger neurons on the upper part of the me-UMAP and smaller neurons on the lower part. Electrophysiological features were also analyzed, and some displayed smooth gradients as a function of cortical depth. These features could be associated with intrinsic properties such as the frequency and adaptation of firing patterns. The frequency of firing patterns increased with cortical depth and displayed a bimodal distribution, while adaptation was higher on the upper part of the me-UMAP regardless of cortical depth. Remarkable similarities have been observed when jointly analyzing rat barrel and mouse visual cortices, suggesting that depth-dependent gradients of morphoelectric properties are conserved across species and cortex areas.

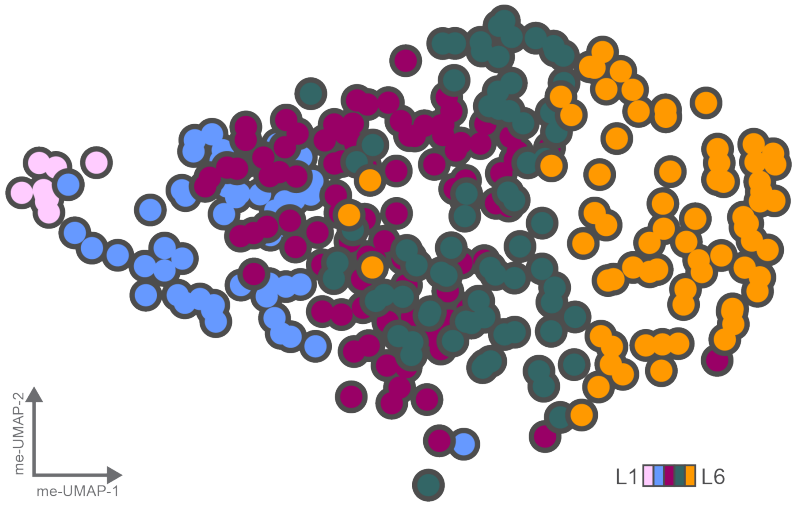

Figure 7.10: Low-dimensional morphoelectric embedding (me-UMAP) color-coded by cortical layer.

Chapter 8

The organizing principles

Cortical inhibitory neurons are characterized by a variety of single-cell attributes that enable their specialized roles in regulating information processing in the brain (Tremblay *et al.*, 2016; Feldmeyer *et al.*, 2018; Fishell and Kepecs, 2020). Molecular identity provides the major subtype specification, with striking differences in morphology and electrophysiology across layers (Tasic *et al.*, 2016; Gouwens *et al.*, 2020). Some well-established morphoelectric types by human experts (Ascoli *et al.*, 2008; DeFelipe *et al.*, 2013), such as FS basket, chandelier, or Martinotti cells, have been reported to link to a particular molecular identity (Fishell and Rudy, 2011; Kepecs and Fishell, 2014; Tremblay *et al.*, 2016). However, it is unknown whether morphoelectric properties systematically relate to molecular identity to organize the structure underlying cortical circuits. To investigate this, I systematically assessed the degree and character of the variability in morphoelectric properties across the entire depth of rat barrel and mouse visual cortices. It turns out that the variability has a particular structure that allows the definition of relationships that reveal the molecular identity of inhibitory neurons based on their respective morphoelectric properties. These relationships are largely homogeneous with respect to human morphological and electrophysiological classification assessments and appear to link to a particular molecular identity. For instance, inhibitory neurons with high spike-frequency and low spike-frequency adaptation z-scores delineate the parvalbumin class, including small to large basket, chandelier, and translaminar cells. This relationship is conserved across layers. Strong correspondences between morphoelectric properties and molecular identity are also observed in the remaining major inhibitory neuron subtypes. Thus, simple organizing principles may largely account for the diversity of inhibitory neurons in cortex.

The most important neurobiological results from Chapter 8 are:

- Depth-specific relationships of morphoelectric properties reliably predict the molecular identity of cortical inhibitory neurons.
- Mouse V1 and rat vS1 share the same depth-specific relationships.

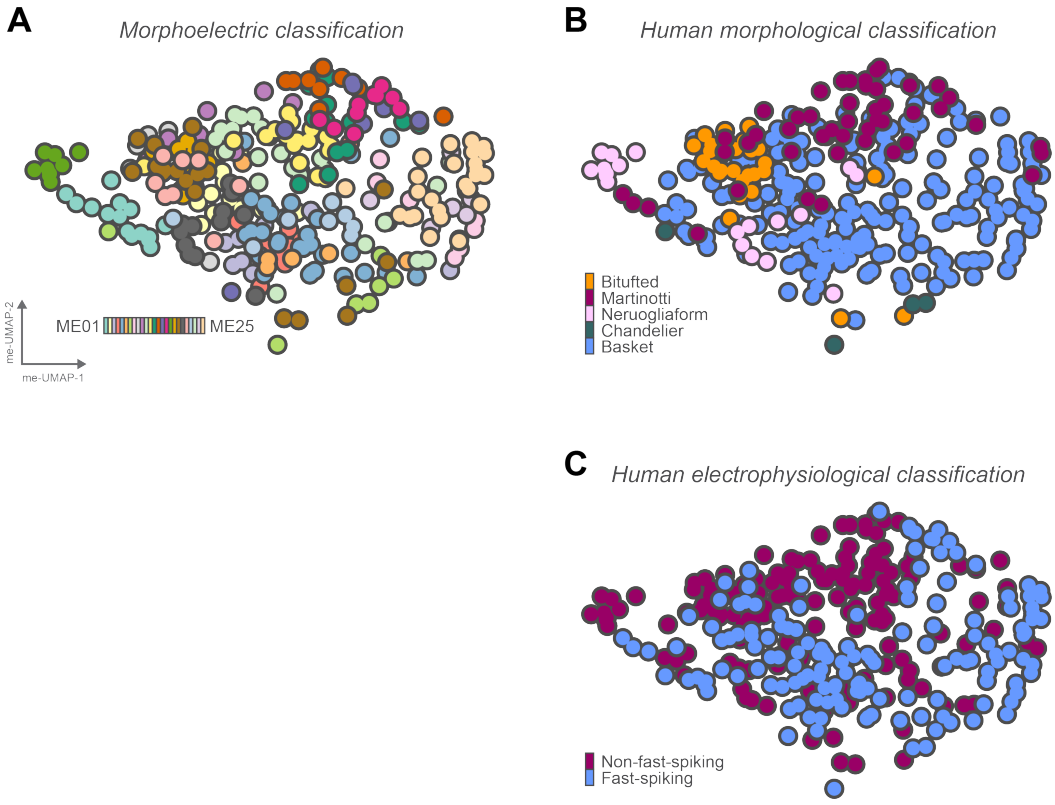

Figure 8.1: Low-dimensional morphoelectric embedding (me-UMAP) color-coded by different class assignments. A. Morphoelectric class assignments (me-types). B. Morphological human assessment. C. Electrophysiological human assessment.

8.1 Depth-driven analysis

Cortical depth is paramount in the organization of inhibitory neurons. Figure 8.1A illustrates the unfolded morphoelectric embedding (me-UMAP) color-coded by morphoelectric class assignments (me-types). The distribution of inhibitory neurons indicates that me-types are depth-dependent, from L1 to L6. Figure 8.1B shows the same me-UMAP color-coded by a human morphological assessment. This revealed that bitufted, Martinotti, and basket cells were located on the upper part of the me-UMAP, while neurogliaform and basket cells were found on the central part of it. Chandelier and basket cells, on the other hand, were located on the lower part of this UMAP. Figure 8.1C illustrates the me-UMAP color-coded by a human electrophysiological assessment. Fast-spiking neurons were predominantly located on the lower part of the me-UMAP, whereas non-FS neurons were located on the upper part. It is worth noting that some FS neurons were also located on the upper part of the me-UMAP.

In order to assess the impact of depth-dependent gradients across me-types, I characterized me-types according to a concise set of z-scored morphoelectric features, namely, the axon and dendrite vertical extents, the spike-frequency, and the spike-frequency adaptation. Their average absolute values in barrel cortex are as follows: 0.90 ± 0.05 mm, 0.42 ± 0.02 mm, 61 ± 4 Hz, and 51 ± 4 %, respectively.

ME01-08 were located on the lower part of the me-UMAP, spanning from L2 to L6 (Figure 8.2A; left). A gallery with a representative neuron for each me-type is illustrated in Figure 8.2A (right). These 8 me-types were characterized by low axon vertical extent (1-way ANOVA: $p < 2.10 \cdot 10^{-18}$), high spike-frequency (1-way ANOVA: $p < 9.16 \cdot 10^{-14}$) and low spike-frequency adaptation (1-way ANOVA: $p < 7.77 \cdot 10^{-19}$) with respect to the rest of the me-types. Although there were not significant differences in dendrite vertical extent between ME01-08 and the rest of the me-types (1-way ANOVA: $p > 0.21$), within ME01-08, the dendrite vertical extent increased as a function of cortical depth (Linear regression: Slope = 0.42; $p < 3.79 \cdot 10^{-5}$). As previously mentioned, ME01-06 and ME08 comprise FS basket cells, whereas ME07 comprises FS chandelier cells.

In contrast, ME09-16 were located on the upper part of the me-UMAP, opposite to ME01-08, also spanning from L2 to L6 (Figure 8.2B; left). A gallery with a representative neuron for each me-type is illustrated in Figure 8.2B (right). These 8 me-types were characterized by high axon vertical extent (1-way ANOVA: $p < 9.14 \cdot 10^{-16}$), low spike-frequency (1-way ANOVA: $p < 8.97 \cdot 10^{-13}$) and high spike-frequency adaptation (1-way ANOVA: $p < 1.58 \cdot 10^{-21}$) with respect to the rest of the me-types. When analyzing the variability within ME09-16, the four features displayed significant trends as a function of cortical depth. The axon (Linear regression: Slope = 0.20; $p < 0.008$) and dendrite (Linear regression: Slope = 0.28; $p < 0.002$) vertical extent, and spike-frequency (Linear regression: Slope = 0.33;

Figure 8.2: Morphoelectric properties indicate relationships in each cortical layer. A. Left: Low-dimensional morphoelectric embedding (me-UMAP) color-coded by classes ME01-08 that are characterized to be small and FS. Right: The morphology and corresponding 100 Hz voltage trace of a representative inhibitory neuron example of each class. B. Same as in panel A, but for translaminar non-FS classes ME09-16. C. Same as in panel A, but for the remaining classes ME17-25. Axons are in lighter shades, and dendrites in darker shades. See text for details.

$p < 0.0002$) were increasing, whereas the spike-frequency adaptation (Linear regression: Slope $= -0.15$; $p < 0.041$) was decreasing. These translaminar and non-FS me-types comprised bitufted (ME09), basket (ME11-12), and Martinotti (ME10, ME13-16) cells.

Then, the remaining me types (i.e., ME17-25) were located on the central part of the me-UMAP, spanning from L1 to L6 (Figure 8.2C; left). A gallery with a representative neuron for each me-type revealed that these 9 me-types were diverse in terms of morphology and electrophysiology (Figure 8.2C; right). The only significant characteristic shared among these 9 me-types, with respect to the rest of them, was a high dendrite vertical extent (1-way ANOVA: $p < 0.014$). It is worth noting that within ME17-25, the axon (Linear regression: Slope $= 0.58$; $p < 1.52 \cdot 10^{-6}$) and dendrite (Linear regression: Slope $= 0.46$; $p < 3.54 \cdot 10^{-6}$) vertical extent, and spike-frequency (Linear regression: Slope $= 0.75$; $p < 2.08 \cdot 10^{-10}$) were increasing as a function of depth. This heterogeneous group of me-types comprised regular-spiking neurogliaform (ME17 and ME20), irregular-spiking bitufted (ME18-19), FS hourglass (ME21), and FS basket (ME22-25) cells.

By resorting me-types based on these four morphoelectric features, groups that shared common relative relationships (R1-4) were revealed, which are preserved across cortical depth (Figure 8.3). For instance, the me-types that shared high spike-frequency (z-score > 0.15) and low spike-frequency adaptation (z-score < -0.35) delineated a group of FS neurons with diverse morphology (Figure 8.3; R1). However, "fast" in R1 was changing relative to cortical depth. Of the remaining me-types, those with low spike-frequency (z-score < -1.0) and low dendrite vertical extent (z-score < -0.5) were characterized by regular-spiking and local morphology (Figure 8.3; R2). It is worth noting that these depth-specific relationships are not unique. For example, in R2, the axon vertical extent could have been used instead of the dendrite vertical extent to define the group. From the remaining unassigned me-types, R3 comprised those with either low axon vertical extent or high dendrite vertical extent. Specifically, this group satisfied the following inequality:

$$\text{axon vertical extent} < 0.15 \cdot \text{dendrite vertical extent} + 0.35 \; .$$

Of the remaining me-types, R4 comprised those that shared low spike-frequency and high spike-frequency adaptation through the following inequality:

$$\text{spike-frequency} < 3.0 \cdot \text{spike-frequency adaptation} + 0.05 \; .$$

The me-types that did not satisfy the previous inequality were assigned to R3.

The underlying depth-specific relationships appeared to be largely homogeneous with respect to human morphological and electrophysiological assessments (Figure 8.1B-C). These traditional cell types, such as FS basket, chandelier, or

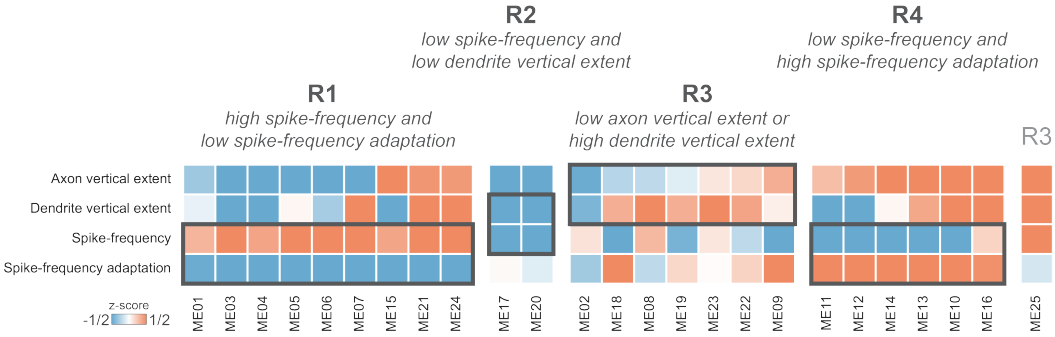

Figure 8.3: Depth-specific relationships indicate a link between morphoelectric properties and molecular identity. Descriptive features of morphoelectric class assignments (me-types) are grouped by depth-specific relationships (R1-4).

Martinotti cells, have been previously reported to link to a particular molecular identity (Fishell and Rudy, 2011; Kepecs and Fishell, 2014; Tremblay *et al.*, 2016; Feldmeyer *et al.*, 2018; Fishell and Kepecs, 2020).

Thus, depth-specific relationships seemed to provide a homogeneous grouping that linked morphoelectric properties to molecular identity.

8.2 Linking morphoelectric properties to molecular identity

I evaluated the accuracy of depth linking morphoelectric properties to molecular identity. For that purpose, I clustered inhibitory neurons in a depth-specific manner. First, the neurons were binned by cortical depth. The bin size was set to 900 µm, resulting in two groups, the minimum number possible. The groups approximately covered L1-4 ($n = 160$) and L5-6 ($n = 139$). The clustering procedure was performed according to (Gouwens *et al.*, 2019), but utilizing a simple hierarchical algorithm (Langfelder *et al.*, 2007). As a result, 67 me-types were obtained. Finally, those me-types were assigned to R1-4 based on their axon and dendrite vertical extent, the spike-frequency, and the spike-frequency adaptation.

In Figure 8.4, I color-coded the me-UMAP based on R1-4 applied to depth-specific me-types. These depth-specific relationships were largely distributed along the vertical axis, orthogonal to cortical depth. R1 was located at the bottom of the me-UMAP, with R2 and R3 in the center, and R4 at the top.

I then compared R1-4 to actual molecular identities for the few cells ($n = 14$) where it was known (Figure 8.5A). Pvalb-positive neurons were always assigned to R1 (100%; 2/2), whereas Pvalb-negative neurons were almost never assigned to R1 (8%; 1/12). Then, Sst-positive neurons were always assigned to R4 (100%; 6/6), and at the same time Sst-negative neurons were never assigned to R4 (0%; 0/8). Finally, Pvalb-negative and Sst-negative neurons were most likely assigned to R2-3 (80%; 4/5), and not to R1 or R4 (20%; 1/5). To further asses these relationships, I utilized the previously quantified 3D distributions of Pvalb-, Sst-, Vip-, and Gad67-positive neurons across a cortical column in barrel cortex. The 1D profiles of the fraction of Pvalb ($n = 2$), Sst ($n = 2$), Vip ($n = 2$), and Non-vip (inferred; Gad67+ neurons that are simultaneously Pvalb-, Sst-, and Vip-) with respect to the total number of inhibitory neurons (i.e., Gad67) were computed as a function of cortical depth (Figure 8.5B; black lines). As the distribution of inhibitory neurons was representative per 50 µm-depth bins, I predicted the 1D depth profiles of R1-4. (Figure 8.5B; colored lines). There was a remarkable correspondence between the depth profiles of Pvalb and R1, Non-vip and R2, Vip and R3, and Sst and R4.

Figure 8.6 displays a gallery of representative morphological reconstructions and their corresponding voltage traces for each depth-specific relationship. The putative Pvalb class (Figure 8.6; R1) comprised small to large basket, chandelier,

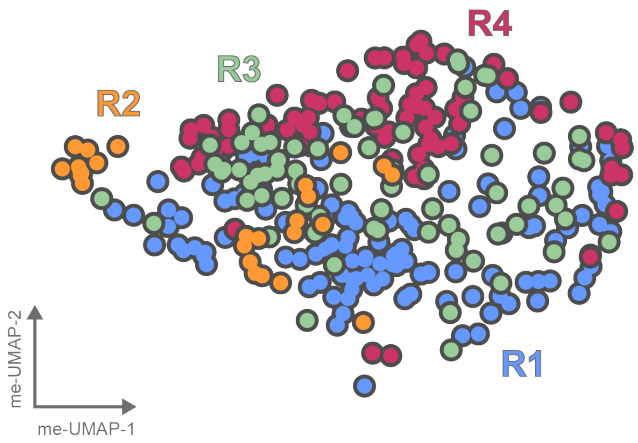

Figure 8.4: Organization of depth-specific relationships (R1-4), the low-dimensional morphoelectric embedding (me-UMAP) is color-coded by R1-4.

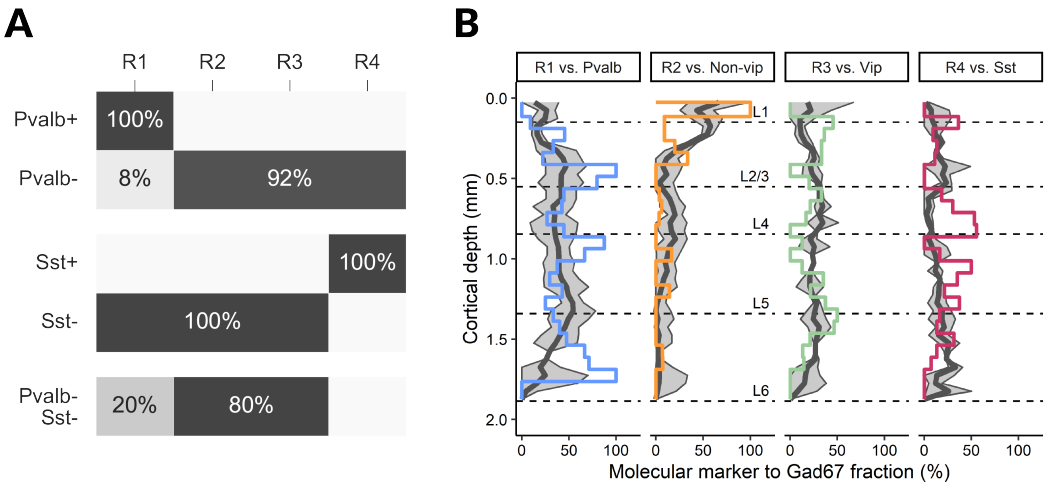

Figure 8.5: Depth-specific relationships (R1-4) reliably predict molecular identity. A. Prediction accuracy of R1-4 for a subset of the inhibitory neurons with known molecular identity. B. Empirical depth distribution of Pvalb, Sst, Vip, and Non-vip (black; mean ± 95% CI) and the predicted profiles by R1-4. For each molecular marker, the fraction to Gad67 is shown. Further details can be found in text.

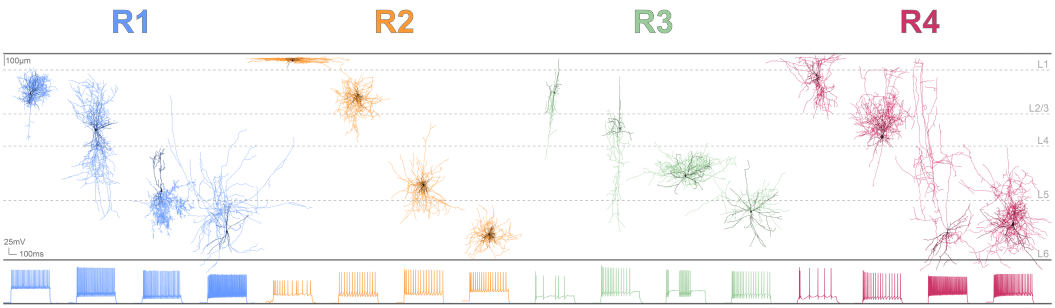

Figure 8.6: Gallery of morphoelectric properties grouped by depth-specific relationships (R1-4). For each class, the morphology and corresponding 100 Hz voltage trace of four representative inhibitory neuron examples are shown. Axons are in lighter shades, and dendrites in darker shades. See text for details.

and translaminar cells. The shared relative properties were high spike-frequency (z-score: 0.75 ± 0.16; absolute: 86 ± 5 Hz) and low spike-frequency adaptation (z-score: -0.77 ± 0.11; absolute: 25 ± 4 %). The morphologies of this class were on average small, i.e., the axon vertical extent was 0.77 ± 0.06 mm and the dendrite vertical extent was 0.44 ± 0.03 mm. The putative Non-vip class (Figure 8.6; R2) comprised neurgliaform cells. The shared relative properties were low spike-frequency (z-score: -0.80 ± 0.11; absolute: 34 ± 4 Hz) and low dendrite vertical extent (z-score: -1.43 ± 0.13; absolute: 0.18 ± 0.02 mm). The axon vertical extent was also low (z-score: -0.88 ± 0.23; absolute: 0.55 ± 0.09 mm). This class displayed regular to adapting spiking behavior (48 ± 12 %). The putative Vip class (Figure 8.6; R3) comprised bitufted, bipolar, and basket-like cells. The morphology was the shared relative property of this class. They displayed a relation of low to average axon vertical extent (z-score: -0.07 ± 0.17; absolute: 0.87 ± 0.07 mm) with wide ranging dendrite vertical extent (z-score: 0.09 ± 0.21; absolute: 0.43 ± 0.04 mm). The spiking behavior of this class displayed high heterogeneity, i.e., spike-frequency was 51 ± 6 Hz and the spike-frequency adaptation was 63 ± 7 %. The putative Sst class (Figure 8.6; R4) comprised Martinotti and basket-like cells. The spiking behavior was the shared property of this class. They displayed a relation of low spike-frequency (z-score: -0.66 ± 0.14; absolute: 39 ± 5 Hz) and high spike-frequency adaptation (z-score: 0.97 ± 0.12; absolute: 85 ± 4 %). The morphologies of this class were on average large, i.e., the axon vertical extent was 1.27 ± 0.07 mm and the dendrite vertical extent was 0.45 ± 0.04 mm.

Thus, R1-4, relationships that were shared across all me-types, reliably predict the molecular identity at any given depth location.

8.3 Conservation across species and cortex areas

In order to further assess the robustness of these depth-specific relationships, I performed the same analysis in mouse visual cortex, where the molecular identity of each neuron is known from transcriptomics (Gouwens *et al.*, 2019, 2020). The transcriptomic-validated morphoelectric class assignments (met-types) defined in (Gouwens *et al.*, 2020) were kindly provided by Dr. Staci Sorensen (Allen Institute for Brain Science). In the previous Chapter, it was observed that, in rat S1 and mouse V1, the laminar distribution of the axon and dendrite vertical extent, the spike-frequency, and the spike-frequency adaptation displayed overall gradients, representing a shift in the distribution.

Figure 8.7 presents the original met-types, resorted following a similar analysis as in Figure 8.3. The morphoelectric features characterization revealed that R1 comprised all Pvalb-MET types, R2 all Lamp5-MET types, R3 all Sncg-MET and Vip-MET types, and R4 all Sst-MET types but Sst-MET-5 that was assigned to R3.

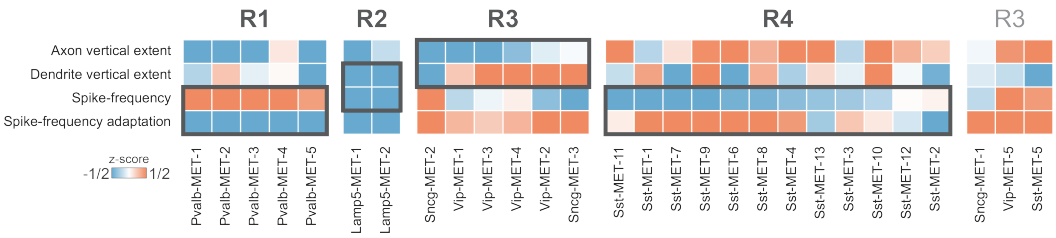

Figure 8.7: Descriptive features of transcriptomic-validated morphoelectric class assignments (met-types) in mouse visual cortex are grouped by depth-specific relationships (R1-4) according to Figure 8.3.

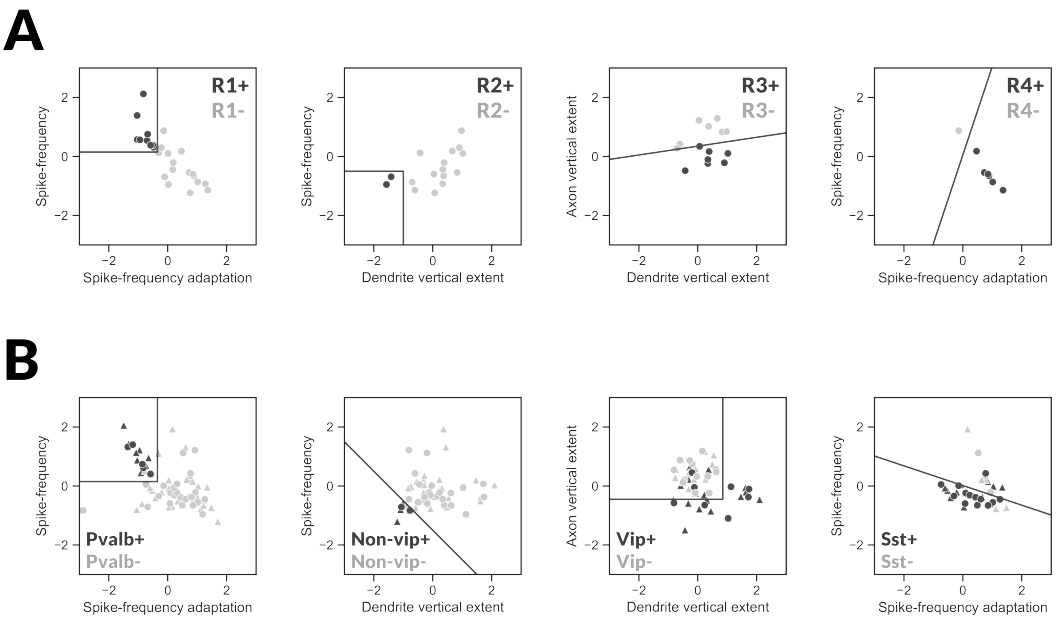

Figure 8.8: Shared depth-specific relationships across species. Scatter plot of the features that define depth-specific relationships (R1-4), according to Figure 8.3. A. Rat barrel cortex, where points correspond to morphoelectric class assignments (me-types). Darker shades are me-types that satisfy the decision boundaries R1-4. B. Mouse visual cortex, where points and triangles correspond to transcriptomic-validated morphoelectric (met-types) and transcriptomic (t-types) class assignments, respectively. Darker shades represent types positive to a particular molecular marker. Decision boundaries are R1-4. Further details can be found in text.

Depth-specific relationships in rat S1 and mouse V1 were qualitatively the same, but with some quantitative differences. For instance, R1 was identical in both species. However, R2 satisfied the following inequality in mouse V1:

$$\text{spike-frequency} < -1 \cdot \text{dendrite vertical extent} - 1.5 \ .$$

Then, R3 comprised met-types with low axon vertical extent (z-score < -0.45) or high dendrite vertical extent (z-score > 0.85). Finally, R4 was defined through the following inequality:

$$\text{spike-frequency} < -1/3 \cdot \text{spike-frequency adaptation} + 0.05 \ .$$

Figure 8.8 summarizes the decision boundaries for assigning inhibitory neurons to depth-specific relationships in rat barrel cortex and mouse visual cortex. In panel A, each point corresponds to one of the 25 me-types identified in rat barrel cortex. Its corresponding feature coordinates are given by the average across class members, with darker shades representing classes that satisfy the criteria for R1-4. Panel B presents a similar plot for mouse visual cortex. Here, points correspond to met-types ($n = 28$) and triangles represent t-types ($n = 53$), with darker shades corresponding to the molecular identity of either met- or t-types. Lamp5+ neurons were assigned to R2 in mouse visual cortex, and for consistency with rat barrel cortex, I renamed them to the broad serotonin 5-HT(3A)R group that are simultaneously Vip-, i.e., Non-vip. Similarly, Sncg+ and Serpinf1+ neurons were assigned to R3 and grouped with the Vip class. It is worth noting that surprisingly, it was possible to formulate R1-4 in both species using the same feature combinations and targeting similar regions in the feature space. An evaluation of all feature combinations color-coded by molecular identity was performed for met-types (Figure A.6) and t-types (Figure A.7).

Then, I quantified the predictive accuracy of linking morphoelectric properties to molecular identity grouping by met-types and by t-types (Figure 8.9). The overall average accuracy was 97% (453 out of 466) and 89% (415 out of 466), respectively. When assessing by met-types (left panel), it is observed that all Pvalb+ neurons (88 out of 88) were assigned to R1. There was one Lamp5+ neuron (t-type: Lamp5 Lsp1) that was assigned to R1. The reason for that misclassification is because it belonged to Pvalb-MET4. The remaining 43 Lamp5+ (i.e., Non-vip+) neurons were assigned to R2. 103 out of 103 Vip+ neurons were assigned to R3. Finally, 219 out of 231 Sst+ neurons were assigned to R4. When assessing by t-types (right panel), all Pvalb+ and Non-vip+ neurons are assigned to R1 and R2, respectively. Note that the previous misclassification is gone when grouping by t-types. Then, 90 out of 103 Vip+ neurons were assigned to R3, and 193 out of 231 Sst+ neurons were assigned to R4. Note that the overlap between Sst and Vip comes from the fact that the spike-frequency adaptation is not able to distinguish irregular from

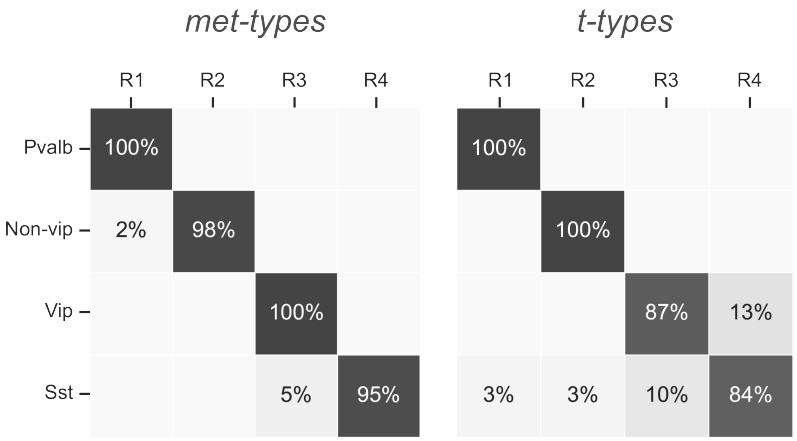

Figure 8.9: Depth-specific relationships (R1-4) robustly predict molecular identity in mouse visual cortex. Prediction tasks are based on transcriptomic-validated morphoelectric (met-types; left) and transcriptomic (t-types; right) class assignments according to Figure 8.8. Further details can be found in text.

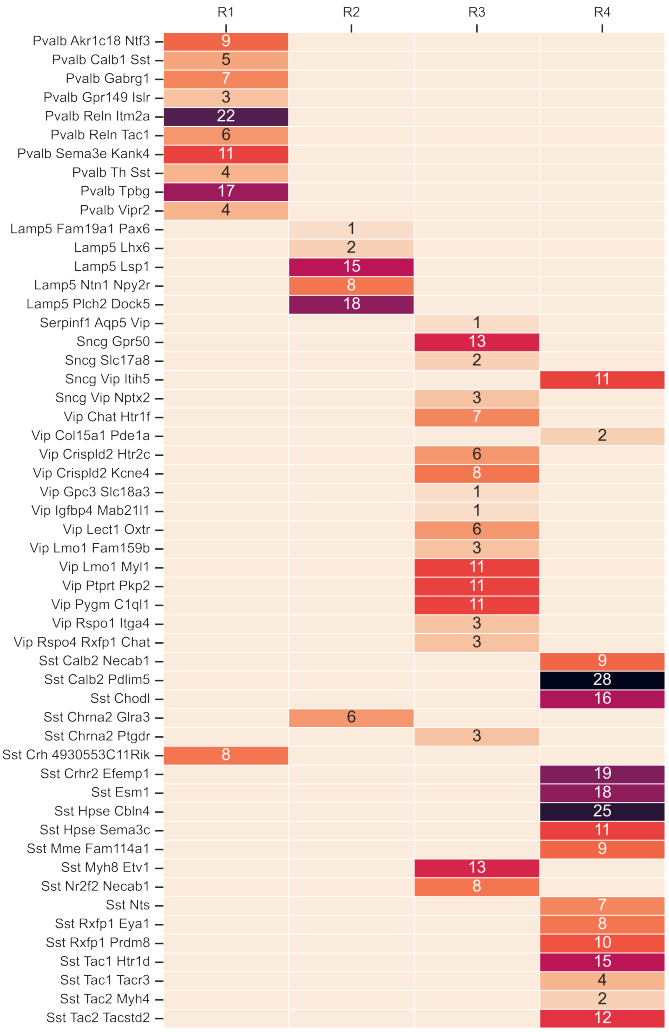

Figure 8.10: Actual number of inhibitory neurons per transcriptomic class assignment (t-type) given by depth-specific relationships (R1-4). See text for details.

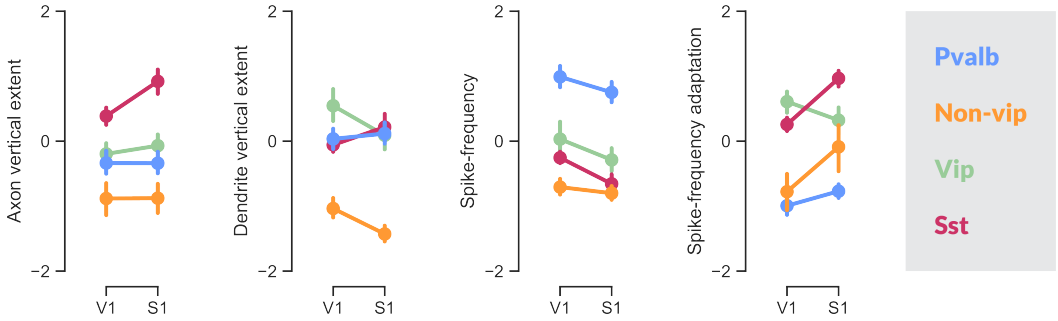

Figure 8.11: Overall relationships between morphoelectic properties and molecular identity across species. Point plots (mean ± 95% CI) of the features by molecular marker. V1 corresponds to mouse visual cortex, whereas S1 to rat barrel cortex. Further details can be found in text.

adapting behavior. In contrast, the coefficient of variation of the ISI could provide a more accurate distinction between them. Figure 8.10 shows the actual number of inhibitory neurons per t-type, grouped by R1-4. For instance, among the Vip+ neurons, two t-types were misclassified and assigned to R4: Sncg Vip Itih5 ($n = 11$) and Vip Col15a1 Pde1a ($n = 2$). Similarly, among the Sst+ neurons, five t-types were misclassified. One was assigned to R1, Sst Crh 4930553C11Rik ($n = 8$). Another one to R2, Sst Chrna2 Glra3 ($n = 6$). And three to R3, Sst Chrna2 Ptgdr ($n = 3$), Sst Myh8 Etv1 ($n = 13$), and Sst Nr2f2 Necab1 ($n = 8$). Nonetheless, the molecular identity of the vast majority of the t-types was accurately predicted.

Figure 8.11 illustrates the overall relationships between morphoelectic properties and molecular identity in rat S1 and mouse V1. In both species, Sst+ neurons have the largest axon vertical extent, while Non-vip+ neurons have the smallest. Although there is some overlap, Vip+ neurons appear to have larger axon vertical extents than Pvalb+ neurons. Interestingly, Pvalb+, Vip+, and Non-vip+ neurons seem to have the same relative positions across rat S1 and mouse V1. The dendrite vertical extent of Non-vip+ neurons is remarkably different to the rest in both species. In rat S1, the dendrite vertical extents of the other molecular types are indistinguishable. However, in mouse V1, Vip+ neurons have the largest ones. The trend in spike-frequency is preserved in both species, with Pvalb+ neurons displaying extreme levels, followed by Vip+, Sst+, and Non-vip+ neurons with some overlap. In terms of spike-frequency adaptation, Pvalb+ and Non-vip+ neurons have the lowest values in both species. It is worth noting that the higher values in rat S1 come from Sst+ neurons, whereas in mouse V1 from Vip+ neurons.

Altogether, depth-specific relationships provided robust predictions that link morphoelectric properties to molecular identity across species (rat and mouse) and cortex areas (S1 vs V1).

8.4 Summary

Depth-specific relationships of morphoelectric properties have been established as a reliable link to the molecular identity of inhibitory neurons. Cortical depth is a critical factor in the organization of these neurons, as similar degrees of diversity were observed at different depth locations. A concise set of morphoelectric features was used to characterize me-types, revealing shared properties among them. At any given depth location, these relationships predicted their molecular identity. Rat S1 and mouse V1 comprised similar shared properties, indicating that these depth-specific relationships are conserved across species and cortex areas. Figure 8.12 schematically illustrates how to link depth-specific relationships of morphoelectric properties to Pvalb, Sst, Vip, and Non-vip. The chapter provides important insights into the organizing principles of inhibitory neurons in the cortex.

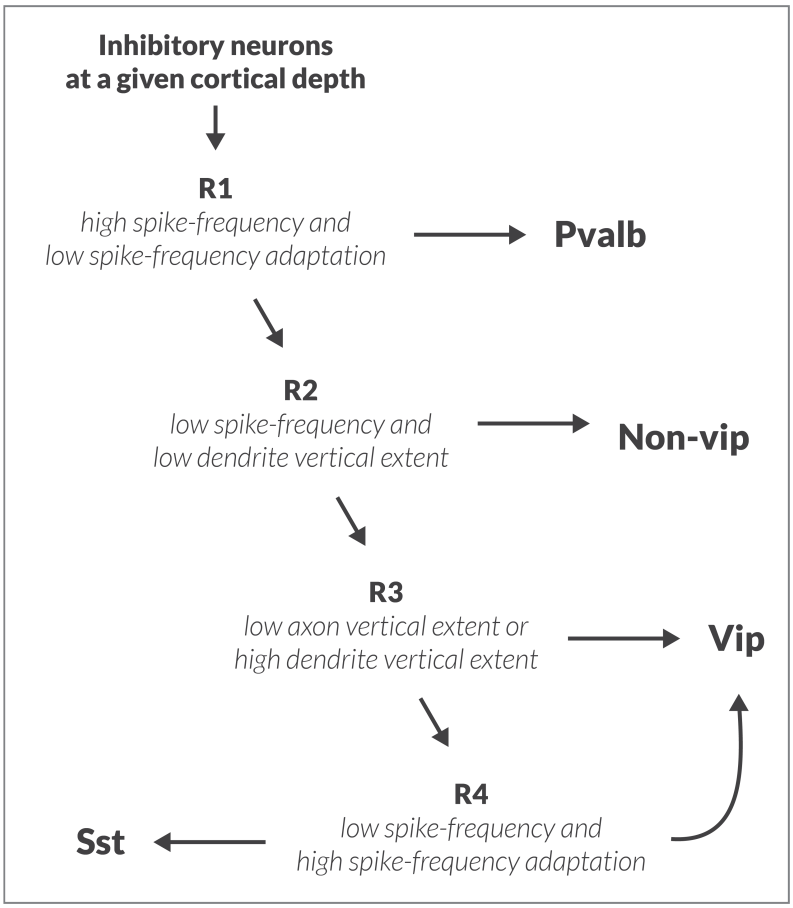

Figure 8.12: Schematic that links morphoelectric properties to molecular identity.

Chapter 9

Discussion

In this dissertation, I have presented the standardization, curation, and analysis of a comprehensive dataset of inhibitory neurons in rat barrel cortex. This dataset included morphological reconstructions and intrinsic physiological responses of 306 neurons, displaying their diversity and complexity. The overall soma density distribution of inhibitory neurons in an average cortical column (Meyer *et al.*, 2013) was indistinguishable from the distribution of registered somata in this dataset (one-sample Kolmogorov-Smirnov test: $p = 0.072$).

Inhibitory neurons were characterized by a rich set of morphological and electrophysiological features. These neurons were then classified into distinct morphological, electrophysiological, and morphoelectric types using 88 morphoelectric features and standardized clustering techniques (Gouwens *et al.*, 2019). These morphological reconstructions and electrphysiological responses were also assessed by a group of human experts, grouping neurons into broader categories (DeFelipe *et al.*, 2013). The main difference between machine and human types was their dependency on soma depth. While human evaluations were largely independent of laminar location, features-based clustering identified more specific depth-dependent subtypes.

I then investigated the role of different morphoelectric features with respect to cortical depth. For the machine classification of morphology, the most important features after cortical depth were those related to the axon and dendrite depth distributions, which had the role of defining cortical layers. Other morphological features, such as the axon and dendrite vertical extent, increased with cortical depth, regardless of subtype. With regard to electrophysiological features, the spike-frequency increased with cortical depth, while the spike-frequency adaptation was independent of it.

Depth-dependent variations defined relationships that indicated a link to the molecular identity of inhibitory neurons based on their respective morphoelectric properties. A quantification of the 3D depth-distribution of the most predominant molecular markers, known molecularly identified neurons from the morphoelectric dataset, and a replication in mouse visual cortex (Gouwens *et al.*, 2019, 2020) were used to verify that depth-dependent variations in morphoelectric properties reveal the molecular identity of cortical inhibitory neurons.

In the following sections, I discuss previous studies on cortical inhibitory neuron diversity, challenges and opportunities of reanalyzing previously published data, the impact of well-constrained inhibition, predicting *in vivo* subtypes with missing information, homologies and divergences of inhibitory neurons across species, and close with the question "are inhibitory neurons adjusting their cellular properties to local cortical circuits?"

9.1 On cortical inhibitory neuron diversity

Cortical inhibitory neurons are a rich and diverse class of neurons (Fishell and Kepecs, 2020; Huang and Paul, 2019; Feldmeyer *et al.*, 2018; Tremblay *et al.*, 2016; Kepecs and Fishell, 2014; Ascoli *et al.*, 2008; Markram *et al.*, 2004; Gupta *et al.*, 2000). At the single-cell level, attributes such as morphology, intrinsic physiology, gene expression profiles, connectivity patterns, developmental history, circuit and behavioral function exhibit complex patterns of variation, making them difficult to characterize (Huang and Paul, 2019; Zeng, 2022). On the one hand, classifications by consensus of expert neuroscientists have produced ambiguous and sometimes arbitrary results (DeFelipe *et al.*, 2013), agreeing on well-established subtypes such as chandelier cells (Szentágothai and Arbib, 1974; Somogyi, 1977; Somogyi *et al.*, 1982) and Martinotti cells (Martinotti, 1889), but not reaching a clear consensus on the remaining subtypes such as basket cells (Kubota *et al.*, 1994; Kawaguchi and Kubota, 1997). On the other hand, statistical methods based on cellular features introduce an objective criteria, producing a large number of subtypes (Gouwens *et al.*, 2019, 2020). These methods are designed to find boundaries in multimodal data in order to define homogeneous groups. This implies that with larger datasets, more subtypes should be expected. As the size of a particular group decreases, it tends to be more depth-dependent (Gouwens *et al.*, 2020), meaning that depth-dependent gradients of morphoelectric properties would become readily apparent within the population. Conceptually, this dissertation aims at defining unifying principles by the utilization of depth-dependent gradients of morphoelectric properties.

9.2 Reutilization of existing resources

Combining previously published datasets in order to generate a new one offers the opportunity to address questions beyond the scope of the original data. As the sample size becomes larger, it affords more accurate estimates of effects. The utilization of different species and cortex areas improves the robustness of the findings. It also encourages the adoption of open science practices, such as data sharing and transparency. The challenges are related to the consistency and compatibility of the data. The protocols utilized to collect the different dataseta were similar but

not identical. For instance, this implied defining a unifying protocol for electrophysiology based on 100 Hz voltage traces with a stimulus duration of 500 ms. The sample in L4 included datasets targeting fast-spiking (FS) (Koelbl *et al.*, 2015) and non-FS (Emmenegger *et al.*, 2018) neurons. Although consistent with the empirical composition (Markram *et al.*, 2015), it is worth considering this limitation when interpreting results. In terms of compatibility, the morphological reconstructions comprised different slice thicknesses. Thus, the y-axis was not considered for feature calculation or any further analysis. Once the data was curated, the process of integration was straightforward due to previously developed pipelines (Egger *et al.*, 2012, 2014; Udvary *et al.*, 2022).

9.3 The impact of well-constrained inhibition

Constraining inhibition is challenging, because of the diversity and relative abundance of inhibitory neurons. The variability of cellular features, high wiring specificity, and distinct developmental origin, make inhibitory neurons diverse and difficult to characterize (Huang and Paul, 2019; Feldmeyer *et al.*, 2018). The number of inhibitory neurons is low with respect to excitatory neurons, below 15% (Meyer *et al.*, 2013; Feldmeyer *et al.*, 2018), posing a laborious task to acquire a sufficiently large sample that comprises their diversity. The "In Silico Brain Sciences" group at the Max Planck Institute for Neurobiology of Behavior – caesar has produced a digital model of the entire rat barrel cortex (Udvary *et al.*, 2022; Egger *et al.*, 2014). This effort included the characterization of 213 inhibitory neurons, with 9 of them in L1, 53 in L2/3, 41 in L4, 43 in L5, and 67 in L6. The distribution of these neurons is significantly different from the the previously reported soma density of inhibitory neurons (one-sample Kolmogorov-Smirnov test: $p < 2.8 \cdot 10^{-3}$). This dissertation aims to mitigate this limitation by including 93 new neurons, i.e., a 44% increase in the size of the dataset. With this integration, the underlying soma distribution is now representative of the number of inhibitory neurons per 50 µm-depth bin (Meyer *et al.*, 2013). The number of neurons in L1-3 remained unchanged. In L4, 58 new neurons were included (i.e., a 141% increase). In L5, 31 (i.e., a 72% increase), and in L6, 4 (i.e., a 6% increase). Figure 9.1A illustrates in black the empirical soma density (mean ± 95% CI) of inhibitory neurons (Meyer *et al.*, 2013) in the principal (i.e., D2) and surrounding columns (i.e., C1, C2, C3, D1, D3, E1, E2, and E3). Shaded in green, the histogram of neuron counts of the current dataset (Udvary *et al.*, 2022; Egger *et al.*, 2014) using 100 µm-depth bins is presented. It is worth noting that this histogram corresponds to the "raw material" that was used to generate the digital model of the rat barrel cortex (Udvary *et al.*, 2022; Egger *et al.*, 2014). The green edges display the histogram of the dataset presented in this dissertation.

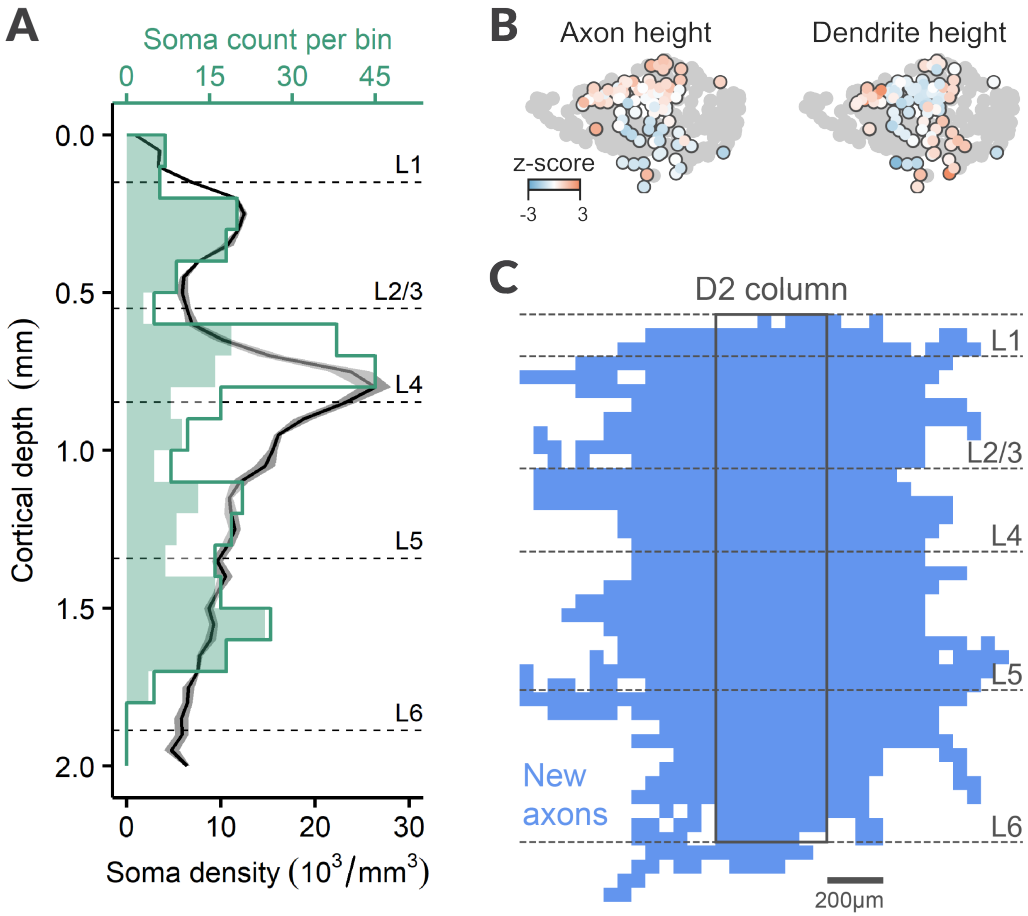

Figure 9.1: The impact of well-constrained inhibition. A. Comparison of the depth histograms of current and new datasets, and the overall soma density distribution. B. Axonal and dendritic height of the 93 new neurons. C. Axon projections of the new neurons in the D2 column. Further details can be found in the text.

To investigate the composition of the new "raw material," I compared axonal and dendritic features from the current and new datasets. The 93 neurons included in this dissertation are predominantly located in L4/5, and present significant differences in axonal features with respect to the current dataset. For instance, axon height (two-tailed t-test: $p < 0.011$), axon width (two-tailed t-test: $p < 0.005$), and axon total length (two-tailed t-test: $p < 0.003$). In contrast, dendritic features are similar in both datasets: dendrite height (two-tailed t-test: $p = 0.656$), dendrite width (two-tailed t-test: $p = 0.561$), and dendrite total length (two-tailed t-test: $p = 0.268$). Figure 9.1B shows the axon and dendrite height of the 93 inhibitory neurons embedded in the me-UMAP. The main difference between new and current dataset is the integration of translaminar neurons in L4/5, largely because of the data by Emmenegger *et al.* (2018). This difference has been described as a limitation of the current dataset (Udvary, 2020, Section 4.3.1), and this dissertation aimed to address it. As the main difference between datasets is with respect to axon morphology, I investigated the projecting patterns of the new neurons in the home (i.e., D2) column. In Figure 9.1C, each 50 µm voxel is colored if any of the 93 registered axons is passing through it. These new neurons have an impact in the entire D2 column, from the pial surface to the white matter, septa, and surrounding columns. Note that these projections come from neurons that were registered in the central part of D2 along the dorsal medial to ventral lateral direction.

The current barrel cortex model (Udvary *et al.*, 2022; Egger *et al.*, 2014) was generated with "raw material" that introduced an overrepresentation of local inhibitory neurons and an underrepresentation of translaminar neurons in L4/5. This has an impact on the organization of inhibitory neurons. For instance, depth-dependent gradients of morphoelectric properties are no longer present. Systematic differences from empirical measurements may introduce propagating errors in downstream tasks that rely on the distribution of inhibitory neurons, such as estimations of connectivity rules or biophysical modeling.

9.4 *In vivo* prediction with missing information

As more data characterizing different aspects of cortical circuits are becoming available, the development of methods to reliably transfer information between datasets that were independently collected is of particular relevance (Zeng, 2022). One alternative is to use the standardized dataset described in this dissertation to learn the diversity of inhibitory neurons in a cortical column. As the registered neurons are tensors composed of 50 µm voxels and the 100 Hz voltage traces are arrays, a joint-embedding predictive architecture (JEPA) can be utilized (Bardes *et al.*, 2022). In this setting, the morphology and the electrophysiology of a given neuron are encoded by different modules, where their resulting internal representation in

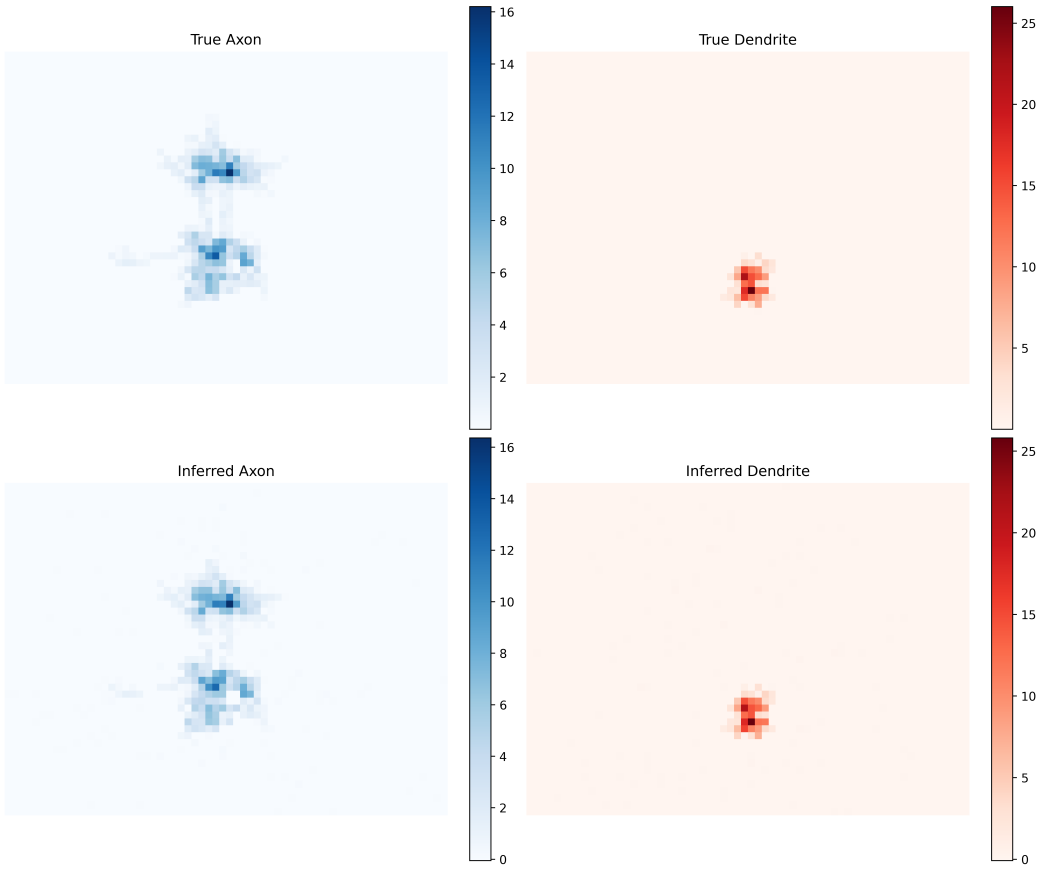

Figure 9.2: Joint-embedding predictive architecture of cortical inhibitory neurons.

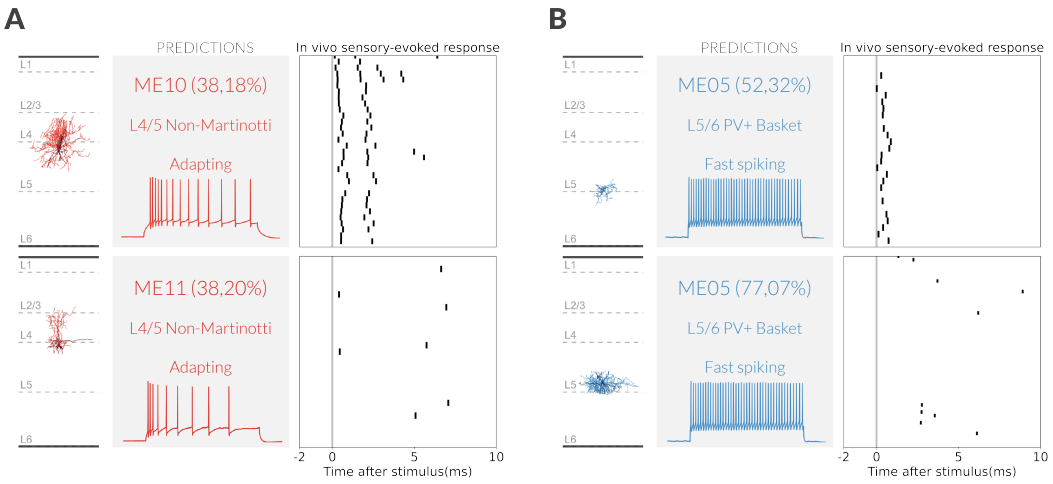

Figure 9.3: Highly accurate me-type prediction of *in vivo* recorded neurons with missing information.

the embedding is identical. Two different decoding modules are in charge of reconstructing the morphology and the electrophysiology. Figure 9.2 illustrates the precise reconstruction of an example inhibitory neuron with an embedding comprising only 10 latent dimensions. Similar precision is obtained when reconstructing the underlying 100 Hz voltage trace. This scalable approach learns directly from data, therefore, there is no longer a need of handcrafted features characterizing different data modalities.

There are experimental settings where data acquisition is complex and not all variables can be always recorded. For instance, the acquisition of cortical inhibitory neurons *in vivo*. Due to their scarcity, approximately in one out of seven successful blind experiments, the collected neuron would be inhibitory. Then, the experimental procedure begins, where several complications may prevent the acquisition of a particular data modality for a given neuron. A dataset comprising 22 inhibitory neurons in the deep layers was provided by Dr. Fernando Messore (Max Planck Institute for Neurobiology of Behavior – caesar) to transfer information from the standardized dataset with predicted molecular identities.

In this case, the input to the JEPA is masked (He *et al.*, 2022). This means that during training only a subset of the inputs are provided, however, the complete outputs are still required. Then, a classifier can trained on top to provide morphoelectric class assignments. Figure 9.3 shows how the morphoelectric labels and other related properties are reliably transferred to *in vivo* recorded inhibitory neurons. This approach links two independently collected datasets in order to provide access to cellular information that may otherwise be inaccessible.

9.5 Homology and divergence of cell types across species

Understanding which cell types are canonical and which ones are specialized is an important question to better understand the organization and function of cortical circuits (Zeng, 2022; Hardcastle *et al.*, 2017). By performing the same analysis on two different species and cortex areas, similarities and differences can be quantified. Figure 9.4 shows a joint analysis of 4554 inhibitory neurons from rat barrel cortex and mouse visual cortex Gouwens *et al.* (2019, 2020). The embedding is calculated using only electrphysiological features. In light gray are neurons from the mouse and in dark gray from the rat. A classifier was trained on morphological and electrophysiological features and class labels from mouse inhibitory neurons to predict corresponding mouse-like classes in rat neurons.

Homologous subtypes are ME11-12 and Sst-MET-3. It is worth noting that although only morphological and electrophysiological properties were utilized for classification, their underlying molecular identities corresponded. A divergence between these two species is ME21. It comprises fast-spiking neurons with large

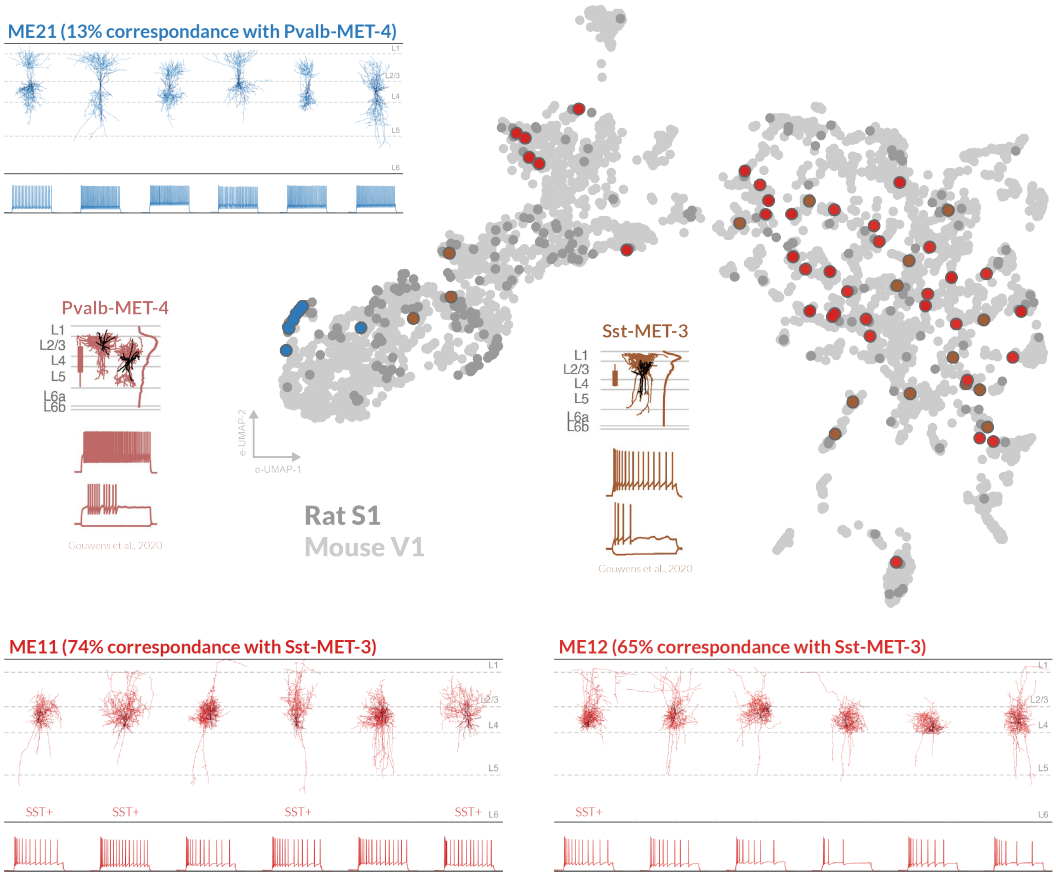

Figure 9.4: Convergent and divergent me-types in rat S1 and mouse V1.

vertically-projecting axons, resembling hourglass-like morphologies. ME21 neurons are restricted to the granular layer. Pvalb-MET-4 is the most similar class found in the mouse, however, this class comprises predominantly large basket cells across layers. Thus, cross-species and cross-area analyses of cell types can contribute to assessing the impact of the local environment in which these inhibitory neurons are embedded.

9.6 Are inhibitory neurons adjusting their cellular properties to local cortical circuits?

Newly born inhibitory neurons disperse throughout the brain to populate distinct structures including cortex (Fishell and Kepecs, 2020; Hu *et al.*, 2017; Kepecs and Fishell, 2014). Remarkably, they integrate into cortical circuits following the arrival of excitatory neurons (Kwan *et al.*, 2012). This sequential integration is a fundamental process in the development and organization of neural circuits (Fishell and Kepecs, 2020; Kwan *et al.*, 2012). Each cortical layer is characterized by diverse morphoelectric and molecular properties, allowing inhibitory neurons to fulfill specific roles within cortical circuits (Tremblay *et al.*, 2016). The placement of a given inhibitory neuron has been shown to be stochastic (Bandler *et al.*, 2022; Fishell and Kepecs, 2020), suggesting an adjustment of cellular properties once integrated into the circuitry of a cortical area (Pouchelon *et al.*, 2021). In this dissertation, it has been demonstrated the presence of systematic variations in morphoelectric properties of inhibitory neurons as a function of cortical depth. These depth-dependent variations defined relationships that reveal their molecular identity based on their respective morphoelectric properties. These depth-specific relationships are conserved across cortex areas and species. Thus, one key question that follows up on this observation is whether inhibitory neurons adjust their cellular properties to local circuits. An answer to this question would provide further evidence to formulate simplifying principles to better understand the diversity of inhibitory neurons.

Chapter 10

Conclusion

Cortical inhibitory neurons are characterized by diverse cellular attributes that enable their specialized roles in regulating the balance and dynamic organization of pyramidal neurons (Fishell and Kepecs, 2020; Huang and Paul, 2019; Feldmeyer *et al.*, 2018; Roux and Buzsáki, 2015; Kepecs and Fishell, 2014). Molecular identity provides the major subtype specification (Rudy *et al.*, 2011; Fishell and Rudy, 2011; Tremblay *et al.*, 2016; Gouwens *et al.*, 2019; Fishell and Kepecs, 2020; Yuste *et al.*, 2020; Zeng, 2022; Mao and Staiger, 2024), with striking differences in morphology and electrophysiology across and within layers (Gouwens *et al.*, 2020; Huang and Paul, 2019; Nigro *et al.*, 2018; Markram *et al.*, 2015; DeFelipe *et al.*, 2013). However, it is unknown whether such diverse morphoelectric properties systematically relate to molecular identity to organize the structure underlying cortical circuits.

In this dissertation, I have systematically assessed variations in morphological and electrophysiological properties of inhibitory neurons across the entire depth of rat barrel cortex. These variations defined relationships that reveal the molecular identity of inhibitory neurons based on their respective morphological and electrophysiological properties. I conducted the same analysis in mouse visual cortex, finding that the identified depth-specific relationships are conserved in both species.

In collaboration with the laboratories of Prof. Dr. Bert Sakmann (Max Planck Institute for Biological Intelligence) and Prof. Dr. Dirk Feldmeyer (Research Center Jülich and RWTH Aachen University), we created a comprehensive dataset of morphological and electrophysiological properties of inhibitory neurons across all layers of rat barrel cortex. The dataset comprises a combination of published (Egger *et al.*, 2015; Helmstaedter *et al.*, 2009a,b,c; Koelbl *et al.*, 2015; Emmenegger *et al.*, 2018; Arzt *et al.*, 2018) and unpublished neurons from their laboratories. The reutilization of existing resources allowed me to standardize, curate, and annotate a dataset of 306 inhibitory neurons that is representative for the overall density distribution (Meyer *et al.*, 2013) per 50 µm-depth bins. In the pursuit of better characterizing the structural the complexity and diversity of morphological and electrophysiological properties of inhibitory neurons, I classified them using features-based multimodal clustering (Gouwens *et al.*, 2019, 2020). A total of 47 morphological and 31 electrophysiological descriptive features based on previously

reported studies (Ascoli *et al.*, 2008; Scorcioni *et al.*, 2008; Helmstaedter *et al.*, 2009b; Oberlaender *et al.*, 2012; DeFelipe *et al.*, 2013; Narayanan *et al.*, 2015; Koelbl *et al.*, 2015; Markram *et al.*, 2015; Emmenegger *et al.*, 2018; Gouwens *et al.*, 2019) were extracted. As a result, inhibitory neurons were assigned into 20 morphological, 13 electrophysiological, and 25 morphoelectric robust subtypes. The distribution of inhibitory neuron types indicated that they were predominantly organized by cortical depth. In a collaboration with a group of experts, namely, Prof. Dr. Dirk Feldmeyer, Dr. Guaxiao Qi (Research Center Jülich), and Dr. Fernando Messore (Max Planck Institute for Neurobiology of Behavior – caesar), the morphology and electrophysiology of these neurons were also assessed, grouping them into broader categories (DeFelipe *et al.*, 2013). The main difference between machine and human types was their depth-dependency. While human evaluations were largely independent of laminar location, features-based clustering methods identified more specific depth-dependent subtypes.

As laminar location was a relevant distinguishing factor between human and machine assessments, I investigated the role of different morphological and electrophysiological features with respect to cortical depth. Among the morphological features, the most important ones to define subtypes, after cortical depth, were those related to the axon and dendrite depth distributions, which had the role of defining cortical layers. Interestingly, other morphological features, such as the axon and dendrite vertical extent, increased with cortical depth, regardless of subtype. With regard to electrophysiological features, two of the three most important sparse features used for classification displayed smooth depth-dependent gradients. Furthermore, they correlated with well-established features such as the spike-frequency and the spike-frequency adaptation. Interestingly, the former increased with cortical depth, while the latter was independent of it. These depth-dependent variations defined relationships that grouped inhibitory neurons regardless of their laminar location, similarly as in the human assessment. For instance, inhibitory neurons with high spike-frequency and low spike-frequency adaptation z-scores delineated a class of neurons that included small to large basket, chandelier, and translaminar cells. This relationship, resembling Pvalb+ neurons, was conserved across layers. Thus, depth-specific relationships indicated a link to the molecular identity of inhibitory neurons based on their respective morphological and electrophysiological properties.

In order to assess the validity of depth-specific relationships, I quantified the 3D depth-distribution of Pvalb-, Sst-, and Vip-positive neurons across the barrel cortex in collaboration with Dr. Fernando Messore. As the morphoelectric dataset of inhibitory neurons was representative per 50 µm-depth bins, I calculated the 1D-profiles for each depth-specific relationship. A remarkable correspondence was obtained between them and the empirical distribution of Pvalb-, Sst-, and Vip-positive neurons across cortical depth. The few known molecularly identified neurons from the morphoelectric dataset were accurately assigned to the major

inhibitory subtypes by depth-specific relationships. I replicated the multimodal analysis described in this dissertation in mouse visual cortex (Gouwens *et al.*, 2019, 2020). Surprisingly, depth-specific relationships were conserved in two different cortex areas in two different species. Thus, depth-dependent variations in morphoelectric properties reveal the molecular identity of cortical inhibitory neurons.

A thorough multimodal analysis of cortical inhibitory neurons has been herein presented. By introducing transparent unifying protocols, different data sources can be combined in order to generate a comprehensive dataset to investigate questions beyond the scope of the original publications. The intentional focus on reliably constraining inhibition is the foundation of the results presented in this dissertation. The design, acquisition, and analysis of the molecular composition of the barrel cortex provides another avenue to understand the variability of inhibitory neurons. The methodological procedures and generated datasets can provide insight for applications beyond the ones I described herein. A direct application may be related to the study of *in vivo* inhibitory neurons where the morphoelectric and molecular datasets can aid at providing population statistics for a setting that is characterized by small sample sizes. Another application may be the comparison of cell types across species and cortex in order to assess the impact of the local environment for homology and divergence of cell types. Implications of the presented results may be related to the developmental origin of inhibitory neurons, by investigating whether they adjust their cellular properties to local cortical circuits after radially migrating to their final positions in cortex.

The present dissertation provides new insight into the nature of cellular diversity in cortex, as depth-dependent variations in morphological and electrophysiological properties reveal the molecular identity of inhibitory neurons. This should not be seen as a definitive answer, rather as a starting point for questioning and understanding the organization of the brain.

Appendix A

Supplementary Figures

Figure A.1: Distribution of morphological features by cortical layer, with overall spread summarized in boxplot. Definitions of features can be found in the text.

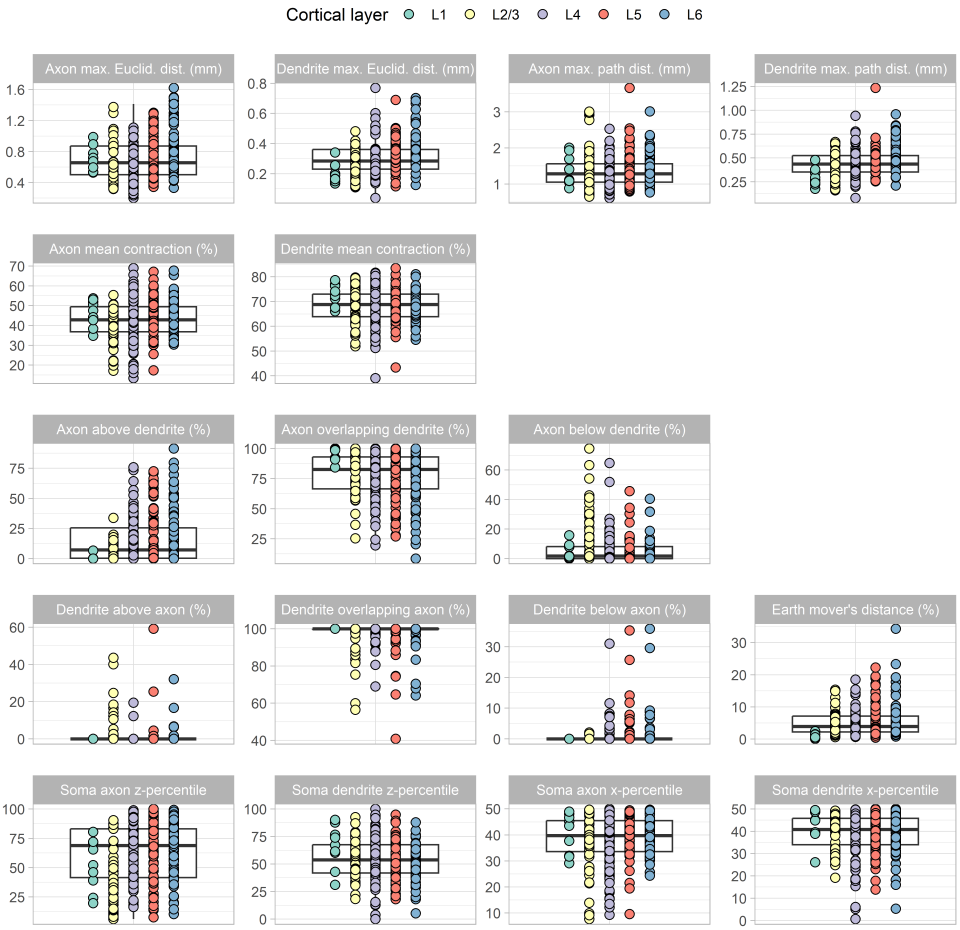

Figure A.2: Distribution of morphological features by cortical layer, with overall spread summarized in boxplot. Definitions of features can be found in the text.

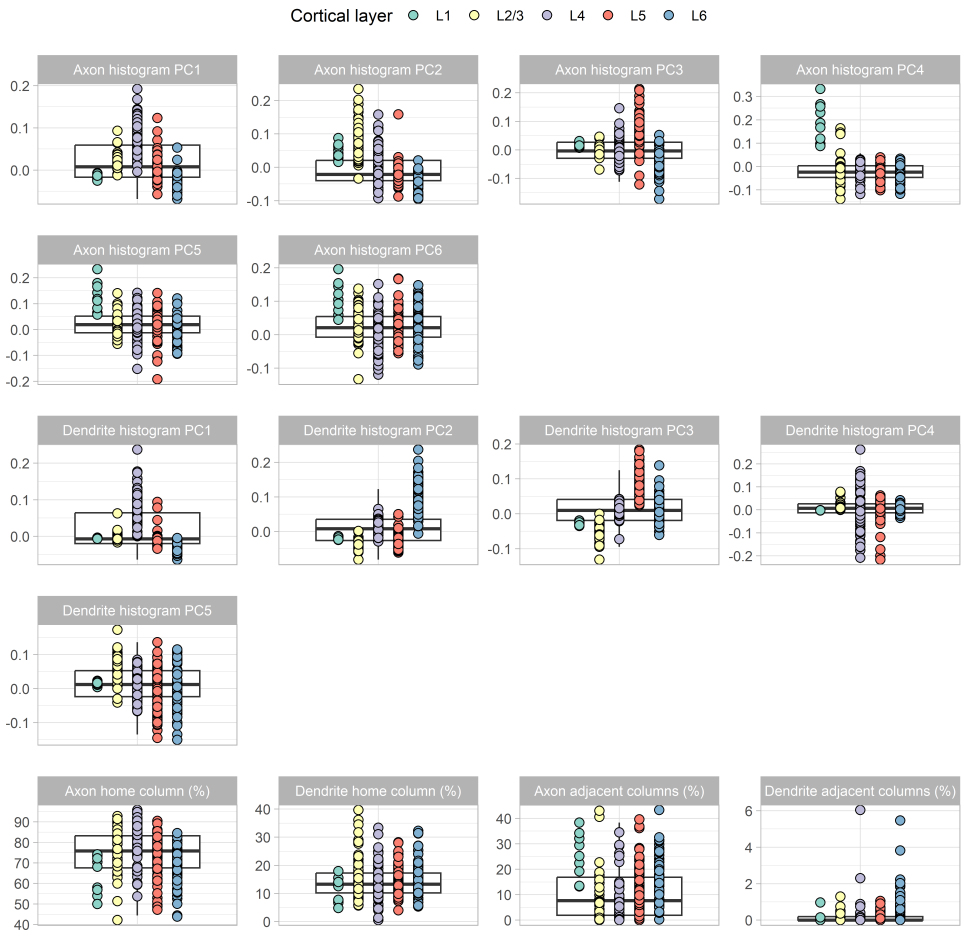

Figure A.3: Distribution of morphological features by cortical layer, with overall spread summarized in boxplot. Definitions of features can be found in the text.

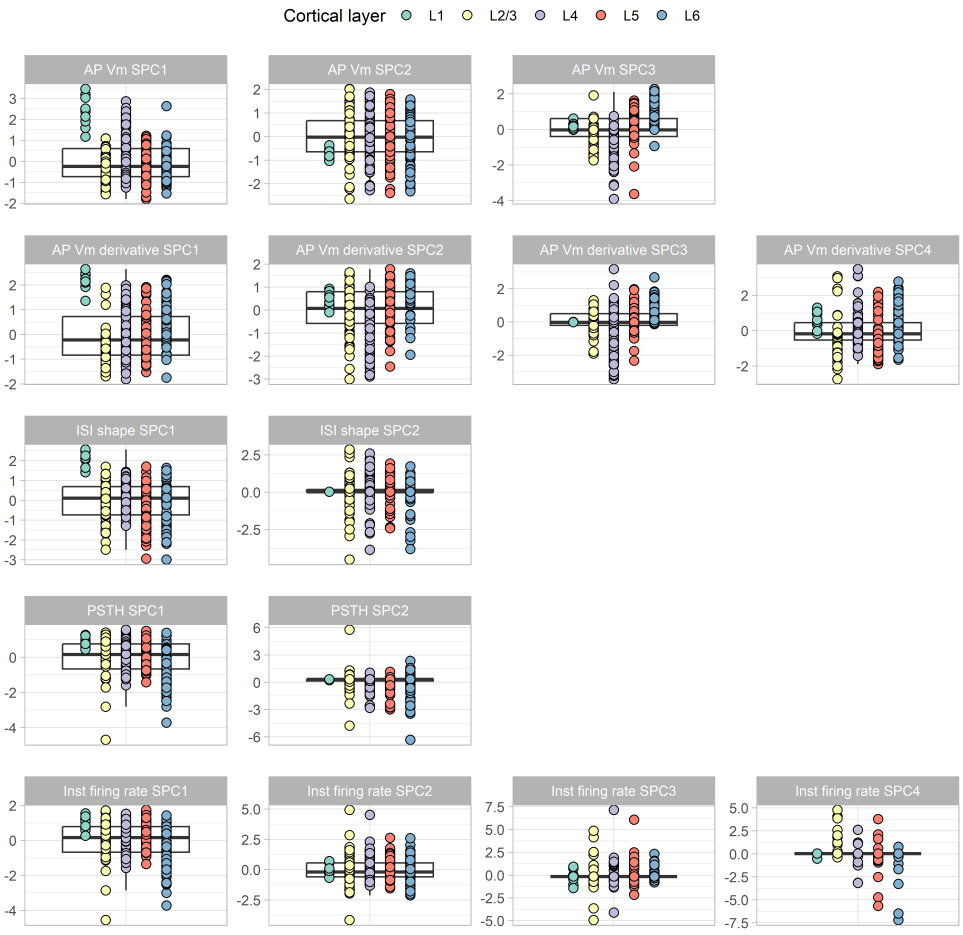

Figure A.4: Distribution of electrophysiological features by cortical layer, with overall spread summarized in boxplot. Definitions of features can be found in the text.

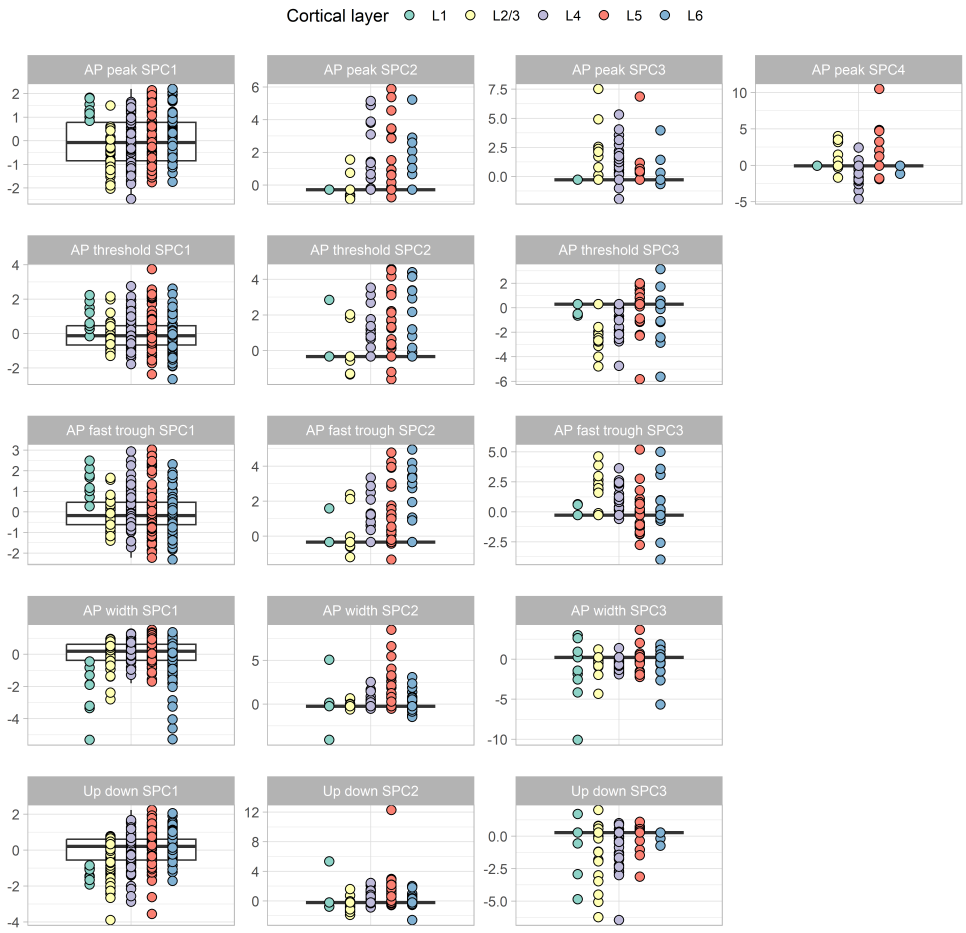

Figure A.5: Distribution of electrophysiological features by cortical layer, with overall spread summarized in boxplot. Definitions of features can be found in the text.

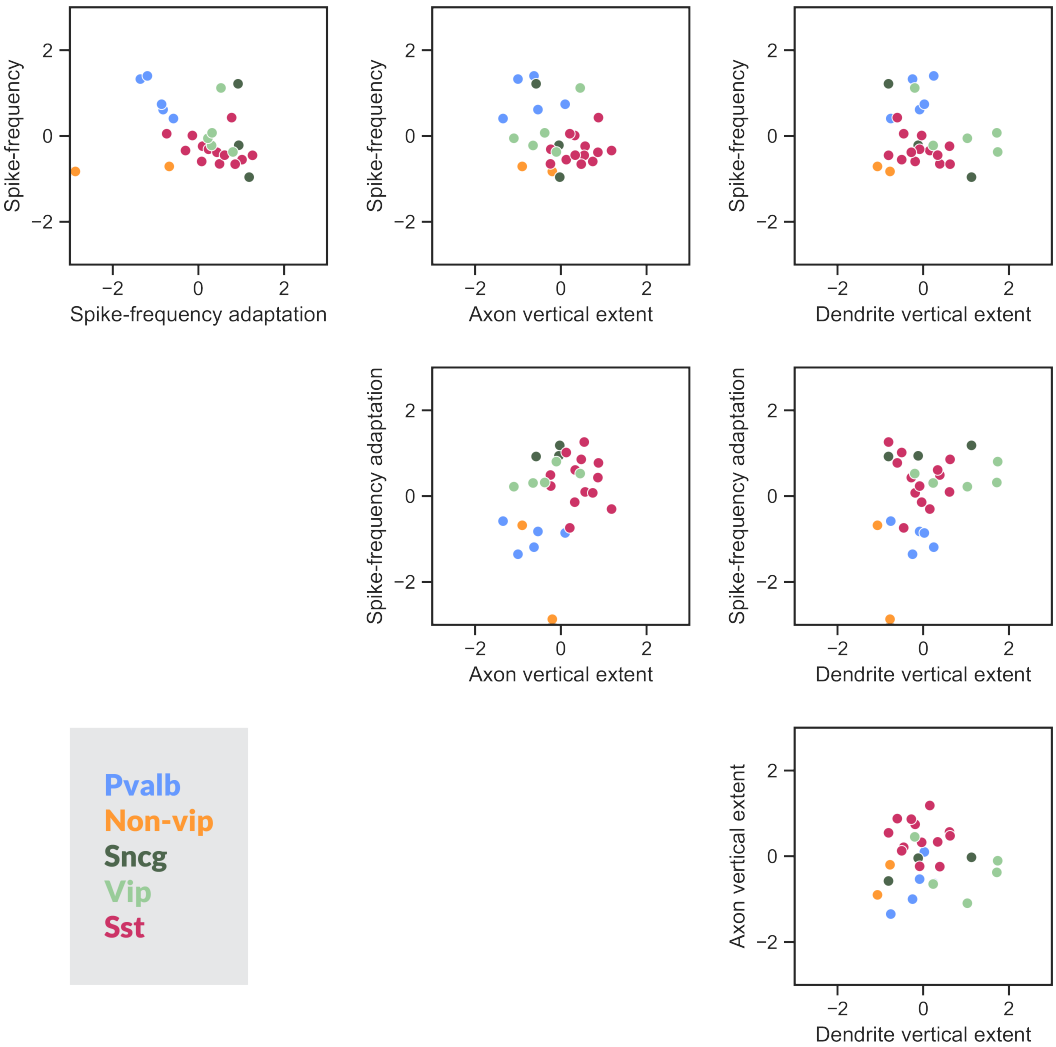

Figure A.6: Evaluation of met-types in mouse V1. Scatter plot shows all the z-scored feature-pair combinations. Points are met-types, colored by molecular identity.

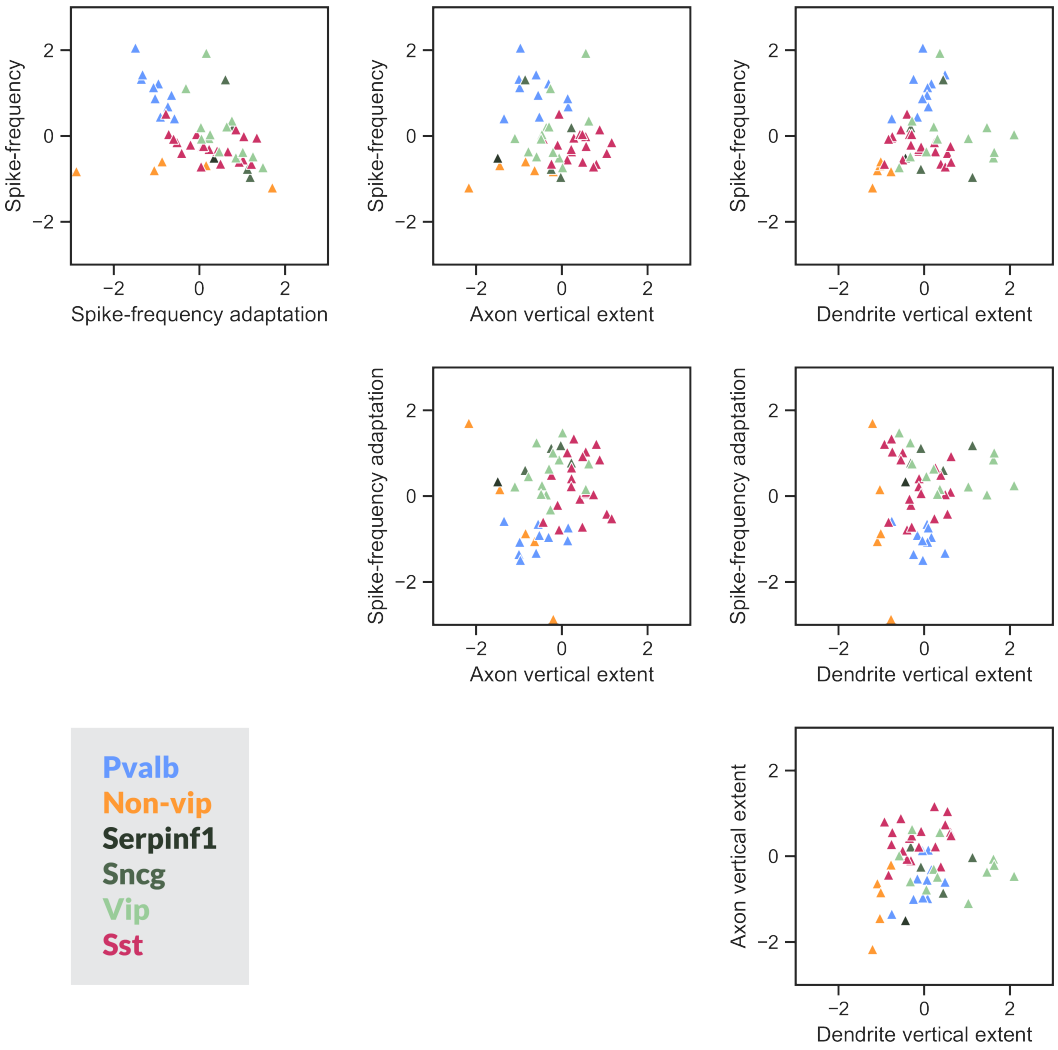

Figure A.7: Evaluation of t-types in mouse V1. Scatter plot shows all the z-scored feature-pair combinations. Points are t-types, colored by molecular identity.

Appendix B

Supplementary Tables

B.1 Molecular composition of L1

Whisker	Volume	Neurons	Whisker	Volume	Neurons
A1	1.36 ± 0.35	181 ± 56	D1	1.91 ± 0.06	153 ± 112
A2	1.30 ± 0.35	175 ± 81	D2	2.35 ± 0.05	205 ± 64
A3	1.18 ± 0.46	61 ± 13	D3	1.88 ± 0.03	137 ± 69
A4	1.24 ± 0.63	61 ± 13	D4	2.24 ± 0.35	176 ± 26
A-row	1.27 ± 0.18	119 ± 48	D-row	2.09 ± 0.16	168 ± 34
B1	1.64 ± 0.83	160 ± 32	E1	2.53 ± 0.49	98 ± 60
B2	1.80 ± 0.78	114 ± 38	E2	3.14 ± 0.53	143 ± 1
B3	1.48 ± 0.22	84 ± 34	E3	2.71 ± 0.28	116 ± 78
B4	1.58 ± 0.54	77 ± 18	E4	2.22 ± 0.08	139 ± 47
B-row	1.62 ± 0.26	109 ± 27	E-row	2.65 ± 0.29	124 ± 25
C1	1.88 ± 0.34	140 ± 217	α	1.17 ± 0.19	138 ± 101
C2	1.59 ± 1.01	131 ± 105	β	1.62 ± 0.46	185 ± 62
C3	1.81 ± 0.18	134 ± 95	γ	1.85 ± 0.02	170 ± 52
C4	1.64 ± 0.02	126 ± 59	δ	2.29 ± 0.54	143 ± 1
C-row	1.72 ± 0.31	132 ± 51	Mean	1.84 ± 0.16	135 ± 16

Table B.1: Whisker-specific organization of L1 Gad67+ neurons in S1. Displayed numbers are mean ± 95% CI. The sample size is $n = 3$ for the C2 column and $n = 2$ for the rest. Volume units are given in 10^{-2} mm^3.

Whisker	Volume	Neurons	Whisker	Volume	Neurons
A1	1.47 ± 0.48	3 ± 6	D1	1.78 ± 0.72	13 ± 25
A2	1.31 ± 0.29	6 ± 6	D2	2.41 ± 0.35	21 ± 8
A3	0.87 ± 0.02	4 ± 7	D3	1.90 ± 0.22	9 ± 7
A4	0.94 ± 0.40	6 ± 5	D4	1.87 ± 0.55	12 ± 2
A-row	1.15 ± 0.23	5 ± 3	D-row	1.99 ± 0.26	14 ± 6
B1	1.28 ± 0.08	10 ± 19	E1	2.09 ± 0.45	14 ± 20
B2	1.50 ± 0.13	2 ± 4	E2	2.26 ± 0.44	31 ± 14
B3	1.24 ± 0.09	2 ± 4	E3	2.58 ± 0.42	31 ± 11
B4	1.10 ± 0.42	7 ± 2	E4	2.20 ± 0.02	31 ± 24
B-row	1.28 ± 0.14	5 ± 4	E-row	2.28 ± 0.20	26 ± 9
C1	1.65 ± 0.07	4 ± 2	α	1.39 ± 0.36	0 ± 0
C2	1.49 ± 0.19	15 ± 9	β	1.51 ± 0.42	6 ± 12
C3	1.77 ± 0.02	13 ± 8	δ	2.48 ± 1.33	16 ± 4
C4	1.66 ± 0.38	11 ± 21	γ	1.71 ± 0.02	25 ± 37
C-row	1.64 ± 0.11	11 ± 5	Mean	1.69 ± 0.15	12 ± 3

Table B.2: Whisker-specific organization of L1 Pvalb+ neurons in S1. Displayed numbers are mean ± 95% CI. The sample size is $n = 2$ for all columns. Volume units are given in 10^{-2} mm^3.

Whisker	Volume	Neurons	Whisker	Volume	Neurons
A1	0.98 ± 1.06	0 ± 0	D1	1.78 ± 0.30	0 ± 0
A2	1.15 ± 0.74	8 ± 15	D2	2.37 ± 0.65	4 ± 8
A3	0.80 ± 0.48	6 ± 13	D3	2.34 ± 0.63	9 ± 7
A4	0.70 ± 0.01	0 ± 0	D4	1.92 ± 0.39	9 ± 7
A-row	0.91 ± 0.29	4 ± 5	D-row	2.10 ± 0.27	5 ± 4
B1	1.40 ± 0.41	0 ± 0	E1	2.77 ± 0.10	6 ± 12
B2	1.36 ± 1.03	0 ± 0	E2	3.42 ± 0.14	19 ± 11
B3	1.38 ± 0.79	2 ± 5	E3	2.87 ± 1.06	8 ± 16
B4	1.27 ± 0.19	2 ± 4	E4	2.17 ± 1.02	13 ± 17
B-row	1.35 ± 0.26	1 ± 1	E-row	2.81 ± 0.43	12 ± 7
C1	1.99 ± 0.55	2 ± 4	α	1.21 ± 0.14	0 ± 0
C2	1.92 ± 0.89	0 ± 0	β	1.36 ± 0.07	0 ± 0
C3	1.97 ± 0.61	4 ± 8	δ	1.29 ± 1.19	0 ± 0
C4	2.17 ± 0.37	0 ± 0	γ	1.28 ± 0.46	0 ± 0
C-row	2.01 ± 0.25	2 ± 2	Mean	1.74 ± 0.21	4 ± 2

Table B.3: Whisker-specific organization of L1 Sst+ neurons in S1. Displayed numbers are mean ± 95% CI. The sample size is $n = 2$ for all columns. Volume units are given in 10^{-2} mm^3.

Whisker	Volume	Neurons	Whisker	Volume	Neurons
A1	1.46 ± 0.42	26 ± 1	D1	1.40 ± 0.25	15 ± 3
A2	1.29 ± 0.12	8 ± 15	D2	1.83 ± 0.04	34 ± 24
A3	0.85 ± 0.06	13 ± 8	D3	1.81 ± 0.67	33 ± 1
A4	0.88 ± 0.16	12 ± 24	D4	1.76 ± 0.43	15 ± 30
A-row	1.12 ± 0.21	15 ± 8	D-row	1.70 ± 0.20	24 ± 10
B1	1.36 ± 0.18	38 ± 55	E1	2.46 ± 0.69	12 ± 12
B2	1.32 ± 0.38	14 ± 2	E2	2.53 ± 1.50	50 ± 35
B3	1.02 ± 0.04	9 ± 17	E3	2.96 ± 0.44	77 ± 15
B4	1.16 ± 0.42	6 ± 5	E4	2.07 ± 0.17	59 ± 82
B-row	1.21 ± 0.15	17 ± 14	E-row	2.51 ± 0.40	49 ± 25
C1	1.56 ± 0.27	14 ± 11	α	1.49 ± 0.25	31 ± 6
C2	1.66 ± 0.04	17 ± 16	β	1.80 ± 0.11	15 ± 29
C3	1.71 ± 0.27	13 ± 9	δ	2.34 ± 0.07	22 ± 9
C4	1.42 ± 0.32	31 ± 36	γ	2.18 ± 0.10	17 ± 21
C-row	1.59 ± 0.13	19 ± 10	Mean	1.68 ± 0.16	24 ± 6

Table B.4: Whisker-specific organization of L1 Vip+ neurons in S1. Displayed numbers are mean ± 95% CI. The sample size is $n = 2$ for all columns. Volume units are given in 10^{-2} mm^3.

B.2 Molecular composition of L2/3

Whisker	Volume	Neurons	Whisker	Volume	Neurons
A1	3.16 ± 0.82	487 ± 225	D1	5.08 ± 0.16	391 ± 17
A2	3.02 ± 0.81	493 ± 289	D2	6.26 ± 0.13	534 ± 147
A3	3.14 ± 1.22	397 ± 327	D3	5.65 ± 0.10	450 ± 245
A4	3.30 ± 1.67	444 ± 460	D4	6.71 ± 1.06	639 ± 128
A-row	3.16 ± 0.45	455 ± 130	D-row	5.92 ± 0.50	504 ± 91
B1	3.83 ± 1.94	476 ± 323	E1	7.59 ± 1.48	808 ± 141
B2	4.19 ± 1.81	555 ± 318	E2	9.43 ± 1.58	922 ± 64
B3	3.94 ± 0.60	505 ± 340	E3	8.12 ± 0.83	699 ± 209
B4	4.22 ± 1.44	471 ± 313	E4	5.92 ± 0.21	565 ± 20
B-row	4.05 ± 0.60	502 ± 125	E-row	7.77 ± 1.03	749 ± 110
C1	4.39 ± 0.80	435 ± 122	α	2.73 ± 0.43	323 ± 164
C2	5.57 ± 1.49	529 ± 139	β	3.77 ± 1.07	573 ± 394
C3	4.83 ± 0.47	485 ± 193	γ	4.94 ± 0.06	515 ± 320
C4	4.92 ± 0.07	512 ± 140	δ	6.10 ± 1.44	792 ± 265
C-row	5.00 ± 0.55	494 ± 65	Mean	5.04 ± 0.50	541 ± 53

Table B.5: Whisker-specific organization of L2/3 Gad67+ neurons in S1. Displayed numbers are mean ± 95% CI. The sample size is $n = 3$ for the C2 column and $n = 2$ for the rest. Volume units are given in 10^{-2} mm^3.

Whisker	Volume	Neurons	Whisker	Volume	Neurons
A1	3.42 ± 1.13	23 ± 45	D1	4.74 ± 1.92	128 ± 89
A2	3.05 ± 0.67	48 ± 8	D2	6.43 ± 0.92	131 ± 36
A3	2.32 ± 0.04	31 ± 62	D3	5.71 ± 0.65	149 ± 25
A4	2.51 ± 1.06	37 ± 32	D4	5.60 ± 1.66	186 ± 38
A-row	2.82 ± 0.45	35 ± 17	D-row	5.62 ± 0.69	149 ± 26
B1	2.98 ± 0.19	63 ± 35	E1	6.27 ± 1.35	125 ± 20
B2	3.51 ± 0.29	55 ± 29	E2	6.79 ± 1.33	199 ± 32
B3	3.31 ± 0.25	50 ± 10	E3	7.74 ± 1.27	241 ± 20
B4	2.94 ± 1.12	63 ± 73	E4	5.86 ± 0.05	137 ± 89
B-row	3.18 ± 0.29	58 ± 17	E-row	6.66 ± 0.68	176 ± 40
C1	3.85 ± 0.17	49 ± 4	α	3.24 ± 0.84	47 ± 59
C2	4.48 ± 0.57	120 ± 21	β	3.53 ± 0.98	67 ± 8
C3	4.72 ± 0.05	105 ± 73	δ	6.61 ± 3.55	119 ± 63
C4	4.99 ± 1.15	122 ± 161	γ	4.55 ± 0.05	113 ± 49
C-row	4.51 ± 0.40	99 ± 40	Mean	4.55 ± 0.46	100 ± 18

Table B.6: Whisker-specific organization of L2/3 Pvalb+ neurons in S1. Displayed numbers are mean ± 95% CI. The sample size is $n = 2$ for all columns. Volume units are given in 10^{-2} mm^3.

Whisker	Volume	Neurons	Whisker	Volume	Neurons
A1	2.28 ± 2.48	41 ± 8	D1	4.75 ± 0.80	109 ± 12
A2	2.68 ± 1.73	62 ± 72	D2	6.32 ± 1.72	157 ± 63
A3	2.14 ± 1.28	56 ± 38	D3	7.01 ± 1.90	197 ± 9
A4	1.87 ± 0.02	46 ± 9	D4	5.75 ± 1.16	153 ± 1
A-row	2.24 ± 0.66	51 ± 17	D-row	5.96 ± 0.83	154 ± 26
B1	3.26 ± 0.95	48 ± 43	E1	8.31 ± 0.30	173 ± 26
B2	3.18 ± 2.40	69 ± 59	E2	10.26 ± 0.41	234 ± 96
B3	3.67 ± 2.11	61 ± 1	E3	8.62 ± 3.18	183 ± 124
B4	3.38 ± 0.50	55 ± 20	E4	5.78 ± 2.72	171 ± 82
B-row	3.37 ± 0.65	58 ± 15	E-row	8.24 ± 1.43	190 ± 39
C1	4.64 ± 1.28	98 ± 48	α	2.82 ± 0.33	35 ± 28
C2	5.75 ± 2.68	111 ± 96	β	3.17 ± 0.16	62 ± 1
C3	5.26 ± 1.62	106 ± 8	δ	3.44 ± 3.16	89 ± 85
C4	6.50 ± 1.12	138 ± 12	γ	3.41 ± 1.23	71 ± 11
C-row	5.54 ± 0.84	113 ± 23	Mean	4.76 ± 0.68	105 ± 18

Table B.7: Whisker-specific organization of L2/3 Sst+ neurons in S1. Displayed numbers are mean ± 95% CI. The sample size is $n = 2$ for all columns. Volume units are given in 10^{-2} mm^3.

Whisker	Volume	Neurons	Whisker	Volume	Neurons
A1	3.41 ± 0.98	82 ± 57	D1	3.74 ± 0.67	68 ± 18
A2	3.01 ± 0.28	34 ± 30	D2	4.88 ± 0.11	92 ± 87
A3	2.28 ± 0.15	17 ± 33	D3	5.43 ± 2.01	121 ± 47
A4	2.34 ± 0.42	63 ± 60	D4	5.27 ± 1.30	57 ± 3
A-row	2.76 ± 0.41	49 ± 26	D-row	4.83 ± 0.68	85 ± 26
B1	3.18 ± 0.43	39 ± 52	E1	7.38 ± 2.06	154 ± 94
B2	3.09 ± 0.88	42 ± 47	E2	7.59 ± 4.50	185 ± 195
B3	2.71 ± 0.12	25 ± 32	E3	8.88 ± 1.31	204 ± 83
B4	3.09 ± 1.11	36 ± 3	E4	5.52 ± 0.46	139 ± 105
B-row	3.02 ± 0.31	35 ± 15	E-row	7.34 ± 1.32	171 ± 52
C1	3.63 ± 0.63	82 ± 0	α	3.47 ± 0.59	71 ± 23
C2	4.98 ± 0.12	84 ± 39	β	4.20 ± 0.26	137 ± 131
C3	4.57 ± 0.72	47 ± 24	δ	6.24 ± 0.19	159 ± 127
C4	4.26 ± 0.95	72 ± 3	γ	5.80 ± 0.27	92 ± 72
C-row	4.36 ± 0.44	71 ± 14	Mean	4.54 ± 0.52	88 ± 18

Table B.8: Whisker-specific organization of L2/3 Vip+ neurons in S1. Displayed numbers are mean ± 95% CI. The sample size is $n = 2$ for all columns. Volume units are given in 10^{-2} mm^3.

B.3 Molecular composition of L4

Whisker	Volume	Neurons	Whisker	Volume	Neurons
A1	2.26 ± 0.59	393 ± 279	D1	4.45 ± 0.14	442 ± 116
A2	2.16 ± 0.58	306 ± 281	D2	5.47 ± 0.12	451 ± 416
A3	1.96 ± 0.76	313 ± 229	D3	3.76 ± 0.07	264 ± 199
A4	2.06 ± 1.04	349 ± 234	D4	5.22 ± 0.82	723 ± 123
A-row	2.11 ± 0.30	340 ± 100	D-row	4.72 ± 0.52	470 ± 153
B1	3.28 ± 1.66	304 ± 172	E1	4.22 ± 0.82	513 ± 475
B2	3.59 ± 1.56	369 ± 326	E2	6.29 ± 1.06	823 ± 260
B3	2.95 ± 0.45	461 ± 240	E3	6.32 ± 0.65	870 ± 338
B4	3.17 ± 1.08	500 ± 238	E4	5.18 ± 0.18	733 ± 137
B-row	3.25 ± 0.51	409 ± 110	E-row	5.50 ± 0.70	735 ± 160
C1	3.76 ± 0.69	297 ± 92	α	1.95 ± 0.31	259 ± 149
C2	3.10 ± 0.83	263 ± 121	β	2.69 ± 0.77	227 ± 61
C3	4.23 ± 0.42	509 ± 249	γ	3.09 ± 0.04	235 ± 102
C4	3.28 ± 0.05	532 ± 86	δ	4.58 ± 1.08	473 ± 648
C-row	3.54 ± 0.41	385 ± 103	Mean	3.70 ± 0.38	438 ± 64

Table B.9: Whisker-specific organization of L4 Gad67+ neurons in S1. Displayed numbers are mean ± 95% CI. The sample size is $n = 3$ for the C2 column and $n = 2$ for the rest. Volume units are given in 10^{-2} mm^3.

Whisker	Volume	Neurons	Whisker	Volume	Neurons
A1	2.44 ± 0.80	158 ± 174	D1	4.15 ± 1.68	281 ± 337
A2	2.18 ± 0.48	118 ± 86	D2	5.62 ± 0.81	354 ± 280
A3	1.45 ± 0.03	98 ± 176	D3	3.80 ± 0.44	255 ± 192
A4	1.57 ± 0.66	84 ± 142	D4	4.35 ± 1.29	310 ± 268
A-row	1.91 ± 0.38	115 ± 60	D-row	4.48 ± 0.67	300 ± 107
B1	2.55 ± 0.16	133 ± 125	E1	3.48 ± 0.75	223 ± 164
B2	3.01 ± 0.25	144 ± 113	E2	4.52 ± 0.88	248 ± 129
B3	2.48 ± 0.19	112 ± 88	E3	6.02 ± 0.99	465 ± 370
B4	2.20 ± 0.84	126 ± 200	E4	5.13 ± 0.05	302 ± 295
B-row	2.56 ± 0.27	129 ± 53	E-row	4.79 ± 0.74	310 ± 120
C1	3.30 ± 0.14	132 ± 192	α	2.31 ± 0.60	192 ± 214
C2	2.49 ± 0.31	146 ± 177	β	2.52 ± 0.70	141 ± 224
C3	4.13 ± 0.05	213 ± 240	δ	4.96 ± 2.66	303 ± 402
C4	3.32 ± 0.77	207 ± 242	γ	2.85 ± 0.03	165 ± 157
C-row	3.31 ± 0.46	175 ± 85	Mean	3.37 ± 0.37	205 ± 42

Table B.10: Whisker-specific organization of L4 Pvalb+ neurons in S1. Displayed numbers are mean ± 95% CI. The sample size is $n = 2$ for all columns. Volume units are given in 10^{-2} mm^3.

Whisker	Volume	Neurons	Whisker	Volume	Neurons
A1	1.63 ± 1.77	6 ± 3	D1	4.16 ± 0.70	30 ± 45
A2	1.91 ± 1.23	8 ± 0	D2	5.53 ± 1.51	80 ± 45
A3	1.34 ± 0.80	7 ± 1	D3	4.67 ± 1.27	38 ± 45
A4	1.17 ± 0.01	8 ± 16	D4	4.47 ± 0.90	45 ± 56
A-row	1.51 ± 0.48	7 ± 3	D-row	4.71 ± 0.57	48 ± 23
B1	2.80 ± 0.82	38 ± 23	E1	4.62 ± 0.17	36 ± 58
B2	2.72 ± 2.06	31 ± 28	E2	6.84 ± 0.28	59 ± 54
B3	2.76 ± 1.58	21 ± 40	E3	6.70 ± 2.47	64 ± 67
B4	2.53 ± 0.37	37 ± 24	E4	5.06 ± 2.38	41 ± 32
B-row	2.70 ± 0.52	32 ± 12	E-row	5.80 ± 0.97	50 ± 22
C1	3.98 ± 1.10	54 ± 48	α	2.01 ± 0.24	12 ± 9
C2	3.20 ± 1.49	42 ± 39	β	2.26 ± 0.11	22 ± 29
C3	4.60 ± 1.42	62 ± 64	δ	2.58 ± 2.37	33 ± 32
C4	4.33 ± 0.75	43 ± 53	γ	2.13 ± 0.77	39 ± 21
C-row	4.03 ± 0.61	50 ± 20	Mean	3.50 ± 0.49	36 ± 8

Table B.11: Whisker-specific organization of L4 Sst+ neurons in S1. Displayed numbers are mean ± 95% CI. The sample size is $n = 2$ for all columns. Volume units are given in 10^{-2} mm^3.

Whisker	Volume	Neurons	Whisker	Volume	Neurons
A1	2.44 ± 0.70	50 ± 68	D1	3.27 ± 0.59	101 ± 119
A2	2.15 ± 0.20	58 ± 58	D2	4.27 ± 0.10	141 ± 147
A3	1.42 ± 0.09	38 ± 23	D3	3.62 ± 1.34	197 ± 287
A4	1.46 ± 0.26	32 ± 12	D4	4.10 ± 1.01	101 ± 73
A-row	1.87 ± 0.36	45 ± 19	D-row	3.81 ± 0.45	135 ± 73
B1	2.72 ± 0.37	79 ± 24	E1	4.10 ± 1.14	125 ± 141
B2	2.65 ± 0.76	77 ± 93	E2	5.06 ± 3.00	161 ± 56
B3	2.03 ± 0.09	57 ± 63	E3	6.91 ± 1.02	246 ± 93
B4	2.32 ± 0.83	47 ± 61	E4	4.83 ± 0.41	90 ± 67
B-row	2.43 ± 0.30	65 ± 27	E-row	5.23 ± 1.00	156 ± 56
C1	3.11 ± 0.54	89 ± 31	α	2.48 ± 0.42	45 ± 58
C2	2.76 ± 0.07	100 ± 128	β	3.00 ± 0.19	79 ± 96
C3	4.00 ± 0.63	135 ± 195	δ	4.68 ± 0.14	128 ± 153
C4	2.84 ± 0.64	81 ± 98	γ	3.63 ± 0.17	125 ± 141
C-row	3.18 ± 0.41	101 ± 50	Mean	3.33 ± 0.38	99 ± 22

Table B.12: Whisker-specific organization of L4 Vip+ neurons in S1. Displayed numbers are mean ± 95% CI. The sample size is $n = 2$ for all columns. Volume units are given in 10^{-2} mm^3.

B.4 Molecular composition of L5

Whisker	Volume	Neurons	Whisker	Volume	Neurons
A1	4.03 ± 1.12	611 ± 376	D1	5.03 ± 0.04	533 ± 163
A2	4.27 ± 1.26	770 ± 421	D2	7.46 ± 0.19	707 ± 206
A3	3.83 ± 1.70	498 ± 485	D3	6.82 ± 0.14	772 ± 107
A4	4.12 ± 2.07	542 ± 399	D4	7.10 ± 1.18	969 ± 25
A-row	4.06 ± 0.61	605 ± 177	D-row	6.60 ± 0.73	745 ± 127
B1	4.79 ± 2.55	678 ± 414	E1	9.05 ± 2.00	1169 ± 275
B2	5.71 ± 2.70	733 ± 269	E2	11.13 ± 1.84	1453 ± 300
B3	4.75 ± 1.00	650 ± 187	E3	9.18 ± 1.55	1215 ± 112
B4	5.22 ± 1.77	581 ± 210	E4	7.52 ± 0.53	1030 ± 51
B-row	5.12 ± 0.85	661 ± 115	E-row	9.22 ± 1.12	1217 ± 139
C1	6.12 ± 1.07	719 ± 202	α	3.11 ± 0.51	517 ± 243
C2	5.99 ± 1.46	757 ± 167	β	4.84 ± 1.38	648 ± 435
C3	5.90 ± 0.32	677 ± 278	γ	5.55 ± 0.07	654 ± 405
C4	5.92 ± 0.19	839 ± 211	δ	7.03 ± 1.21	811 ± 116
C-row	5.98 ± 0.47	749 ± 91	Mean	6.02 ± 0.56	772 ± 77

Table B.13: Whisker-specific organization of L5 Gad67+ neurons in S1. Displayed numbers are mean ± 95% CI. The sample size is $n = 3$ for the C2 column and $n = 2$ for the rest. Volume units are given in 10^{-2} mm^3.

Whisker	Volume	Neurons	Whisker	Volume	Neurons
A1	4.40 ± 1.45	353 ± 302	D1	5.33 ± 2.15	256 ± 134
A2	4.35 ± 0.96	273 ± 142	D2	8.03 ± 1.16	536 ± 390
A3	2.88 ± 0.08	176 ± 53	D3	6.97 ± 0.80	458 ± 156
A4	3.14 ± 1.33	215 ± 259	D4	6.17 ± 1.89	417 ± 59
A-row	3.69 ± 0.66	254 ± 94	D-row	6.63 ± 0.95	417 ± 113
B1	3.83 ± 0.25	233 ± 131	E1	7.66 ± 1.66	487 ± 352
B2	5.01 ± 0.42	327 ± 275	E2	8.29 ± 1.62	605 ± 130
B3	4.14 ± 0.31	212 ± 82	E3	9.33 ± 1.55	756 ± 89
B4	3.67 ± 1.40	237 ± 205	E4	7.96 ± 0.21	592 ± 23
B-row	4.16 ± 0.48	252 ± 78	E-row	8.31 ± 0.70	610 ± 102
C1	5.51 ± 0.24	210 ± 90	α	3.70 ± 0.96	242 ± 176
C2	4.97 ± 0.63	296 ± 117	β	4.54 ± 1.25	275 ± 164
C3	5.88 ± 0.11	324 ± 135	δ	8.15 ± 4.22	467 ± 255
C4	6.07 ± 1.36	472 ± 263	γ	5.12 ± 0.06	285 ± 82
C-row	5.61 ± 0.42	325 ± 94	Mean	5.63 ± 0.55	363 ± 51

Table B.14: Whisker-specific organization of L5 Pvalb+ neurons in S1. Displayed numbers are mean ± 95% CI. The sample size is $n = 2$ for all columns. Volume units are given in 10^{-2} mm^3.

Whisker	Volume	Neurons	Whisker	Volume	Neurons
A1	2.93 ± 3.19	50 ± 34	D1	5.34 ± 0.90	132 ± 159
A2	3.82 ± 2.47	58 ± 16	D2	7.87 ± 2.08	164 ± 105
A3	2.59 ± 1.43	56 ± 21	D3	8.56 ± 2.31	195 ± 84
A4	2.31 ± 0.06	37 ± 56	D4	6.35 ± 1.21	118 ± 115
A-row	2.91 ± 0.91	50 ± 15	D-row	7.03 ± 1.14	152 ± 50
B1	4.19 ± 1.22	72 ± 76	E1	10.08 ± 0.54	207 ± 133
B2	4.48 ± 3.31	71 ± 118	E2	11.99 ± 0.74	256 ± 52
B3	4.52 ± 2.51	93 ± 83	E3	10.27 ± 3.65	193 ± 184
B4	4.17 ± 0.55	78 ± 8	E4	7.93 ± 3.71	215 ± 238
B-row	4.34 ± 0.83	79 ± 31	E-row	10.07 ± 1.46	218 ± 65
C1	6.63 ± 1.83	135 ± 105	α	3.22 ± 0.38	81 ± 35
C2	6.36 ± 2.90	143 ± 90	β	4.07 ± 0.20	90 ± 40
C3	6.36 ± 1.62	140 ± 79	δ	4.30 ± 3.95	92 ± 52
C4	7.87 ± 1.23	182 ± 86	γ	3.83 ± 1.39	115 ± 7
C-row	6.81 ± 0.88	150 ± 37	Mean	5.84 ± 0.80	124 ± 22

Table B.15: Whisker-specific organization of L5 Sst+ neurons in S1. Displayed numbers are mean ± 95% CI. The sample size is $n = 2$ for all columns. Volume units are given in 10^{-2} mm^3.

Whisker	Volume	Neurons	Whisker	Volume	Neurons
A1	4.39 ± 1.26	143 ± 93	D1	4.20 ± 0.75	119 ± 18
A2	4.28 ± 0.36	104 ± 10	D2	6.10 ± 0.14	200 ± 18
A3	2.83 ± 0.21	95 ± 13	D3	6.63 ± 2.45	236 ± 73
A4	2.91 ± 0.56	88 ± 3	D4	5.85 ± 1.45	178 ± 131
A-row	3.60 ± 0.61	108 ± 24	D-row	5.70 ± 0.87	183 ± 43
B1	4.08 ± 0.55	107 ± 74	E1	9.02 ± 2.52	401 ± 48
B2	4.41 ± 1.26	119 ± 34	E2	9.26 ± 5.46	385 ± 287
B3	3.39 ± 0.14	82 ± 23	E3	10.24 ± 1.46	394 ± 277
B4	3.87 ± 1.39	96 ± 37	E4	7.54 ± 0.68	296 ± 107
B-row	3.94 ± 0.46	101 ± 20	E-row	9.02 ± 1.38	369 ± 85
C1	5.19 ± 0.91	172 ± 117	α	3.96 ± 0.67	128 ± 143
C2	5.53 ± 0.13	193 ± 78	β	5.40 ± 0.33	165 ± 105
C3	5.71 ± 0.90	160 ± 54	δ	7.79 ± 0.22	313 ± 18
C4	5.21 ± 1.17	207 ± 33	γ	6.53 ± 0.30	254 ± 187
C-row	5.41 ± 0.37	183 ± 32	Mean	5.60 ± 0.60	193 ± 32

Table B.16: Whisker-specific organization of L5 Vip+ neurons in S1. Displayed numbers are mean ± 95% CI. The sample size is $n = 2$ for all columns. Volume units are given in 10^{-2} mm^3.

B.5 Molecular composition of L6

Whisker	Volume	Neurons	Whisker	Volume	Neurons
A1	3.90 ± 0.24	467 ± 40	D1	3.61 ± 0.40	268 ± 112
A2	3.92 ± 0.19	380 ± 42	D2	5.92 ± 0.57	567 ± 362
A3	3.10 ± 1.54	265 ± 136	D3	5.46 ± 0.07	540 ± 215
A4	4.04 ± 1.17	364 ± 57	D4	5.80 ± 1.55	554 ± 149
A-row	3.74 ± 0.46	369 ± 61	D-row	5.20 ± 0.76	482 ± 127
B1	4.28 ± 1.05	315 ± 20	E1	7.14 ± 1.93	732 ± 253
B2	4.06 ± 2.10	304 ± 117	E2	8.17 ± 1.23	996 ± 15
B3	3.87 ± 0.63	367 ± 63	E3	6.28 ± 1.41	772 ± 239
B4	4.79 ± 0.72	349 ± 178	E4	5.52 ± 0.14	675 ± 63
B-row	4.25 ± 0.54	334 ± 46	E-row	6.78 ± 0.89	794 ± 112
C1	5.04 ± 0.26	344 ± 149	α	3.57 ± 0.98	243 ± 121
C2	5.46 ± 0.35	437 ± 205	β	4.56 ± 0.16	283 ± 68
C3	5.17 ± 0.11	416 ± 234	γ	4.55 ± 0.88	293 ± 137
C4	5.00 ± 0.70	390 ± 390	δ	5.26 ± 0.60	358 ± 66
C-row	5.20 ± 0.21	401 ± 102	Mean	4.95 ± 0.36	445 ± 58

Table B.17: Whisker-specific organization of L6 Gad67+ neurons in S1. Displayed numbers are mean ± 95% CI. The sample size is $n = 3$ for the C2 column and $n = 2$ for the rest. Volume units are given in 10^{-2} mm^3.

Whisker	Volume	Neurons	Whisker	Volume	Neurons
A1	4.57 ± 1.36	207 ± 139	D1	6.04 ± 1.96	258 ± 102
A2	4.15 ± 1.09	241 ± 34	D2	8.10 ± 1.29	377 ± 27
A3	2.96 ± 0.23	133 ± 19	D3	6.38 ± 0.63	291 ± 63
A4	3.41 ± 1.59	175 ± 145	D4	5.99 ± 2.22	287 ± 174
A-row	3.77 ± 0.65	189 ± 49	D-row	6.63 ± 0.89	304 ± 52
B1	4.12 ± 0.54	169 ± 14	E1	7.95 ± 2.58	394 ± 4
B2	5.29 ± 0.89	235 ± 59	E2	7.91 ± 1.43	325 ± 93
B3	4.22 ± 0.13	192 ± 2	E3	7.42 ± 1.85	329 ± 16
B4	4.03 ± 1.48	202 ± 59	E4	6.91 ± 0.71	304 ± 20
B-row	4.41 ± 0.51	199 ± 24	E-row	7.55 ± 0.74	338 ± 31
C1	5.25 ± 0.62	240 ± 77	α	4.02 ± 1.14	149 ± 90
C2	5.14 ± 0.67	224 ± 11	β	4.32 ± 1.21	187 ± 12
C3	6.64 ± 0.94	296 ± 69	δ	7.30 ± 3.48	297 ± 22
C4	5.35 ± 0.62	220 ± 13	γ	5.19 ± 0.03	210 ± 29
C-row	5.59 ± 0.53	245 ± 30	Mean	5.53 ± 0.47	248 ± 22

Table B.18: Whisker-specific organization of L6 Pvalb+ neurons in S1. Displayed numbers are mean ± 95% CI. The sample size is $n = 2$ for all columns. Volume units are given in 10^{-2} mm^3.

Whisker	Volume	Neurons	Whisker	Volume	Neurons
A1	3.02 ± 3.10	106 ± 96	D1	6.15 ± 0.78	175 ± 99
A2	3.54 ± 2.15	124 ± 2	D2	8.19 ± 2.21	212 ± 83
A3	2.53 ± 0.94	59 ± 21	D3	8.26 ± 2.05	196 ± 73
A4	2.56 ± 0.50	53 ± 57	D4	6.77 ± 0.91	156 ± 25
A-row	2.91 ± 0.80	86 ± 31	D-row	7.34 ± 0.91	185 ± 33
B1	4.48 ± 1.51	129 ± 117	E1	9.94 ± 1.52	250 ± 7
B2	4.12 ± 2.43	169 ± 48	E2	10.37 ± 0.12	298 ± 28
B3	4.34 ± 1.90	139 ± 177	E3	8.26 ± 3.83	235 ± 126
B4	4.55 ± 0.62	103 ± 39	E4	7.56 ± 4.00	212 ± 115
B-row	4.37 ± 0.67	135 ± 45	E-row	9.03 ± 1.38	249 ± 40
C1	6.57 ± 1.74	201 ± 178	α	3.51 ± 0.65	123 ± 64
C2	6.38 ± 2.83	193 ± 168	β	4.07 ± 0.20	122 ± 34
C3	6.45 ± 0.30	152 ± 16	δ	4.27 ± 3.99	142 ± 118
C4	7.08 ± 1.00	187 ± 52	γ	4.21 ± 1.44	128 ± 46
C-row	6.62 ± 0.69	183 ± 49	Mean	5.71 ± 0.70	161 ± 21

Table B.19: Whisker-specific organization of L6 Sst+ neurons in S1. Displayed numbers are mean ± 95% CI. The sample size is $n = 2$ for all columns. Volume units are given in 10^{-2} mm^3.

Whisker	Volume	Neurons	Whisker	Volume	Neurons
A1	4.47 ± 1.18	124 ± 39	D1	4.86 ± 0.58	129 ± 62
A2	3.90 ± 0.39	118 ± 80	D2	6.57 ± 0.43	176 ± 113
A3	2.79 ± 0.11	79 ± 101	D3	6.29 ± 2.05	161 ± 6
A4	3.22 ± 0.89	95 ± 121	D4	6.02 ± 1.71	108 ± 9
A-row	3.60 ± 0.56	104 ± 37	D-row	5.94 ± 0.71	143 ± 31
B1	4.47 ± 0.49	118 ± 26	E1	9.26 ± 1.90	198 ± 130
B2	4.59 ± 1.05	116 ± 1	E2	8.44 ± 4.36	172 ± 219
B3	3.43 ± 0.11	80 ± 38	E3	7.84 ± 1.49	172 ± 113
B4	4.41 ± 1.52	82 ± 28	E4	6.37 ± 1.09	136 ± 30
B-row	4.22 ± 0.50	99 ± 17	E-row	7.98 ± 1.24	170 ± 55
C1	5.14 ± 0.97	142 ± 18	α	4.22 ± 0.76	158 ± 48
C2	5.83 ± 0.40	146 ± 64	β	4.99 ± 0.33	162 ± 32
C3	6.46 ± 0.55	137 ± 102	δ	7.51 ± 0.25	176 ± 85
C4	4.96 ± 1.25	111 ± 48	γ	7.08 ± 0.31	261 ± 17
C-row	5.60 ± 0.55	134 ± 27	Mean	5.55 ± 0.51	140 ± 17

Table B.20: Whisker-specific organization of L6 Vip+ neurons in S1. Displayed numbers are mean ± 95% CI. The sample size is $n = 2$ for all columns. Volume units are given in 10^{-2} mm^3.

Bibliography

Agmon, A. and Connors, B. W. (1991). Thalamocortical responses of mouse somatosensory (barrel) cortex in vitro. *Neuroscience*, **41**(2-3), 365–379.

Arzt, M., Sakmann, B., and Meyer, H. S. (2018). Anatomical Correlates of Local, Translaminar, and Transcolumnar Inhibition by Layer 6 GABAergic Interneurons in Somatosensory Cortex. *Cerebral Cortex*, **28**(8), 2763–2774.

Ascoli, G. A., Alonso-Nanclares, L., Anderson, S. A., Barrionuevo, G., Benavides-Piccione, R., Burkhalter, A., Buzsáki, G., Cauli, B., DeFelipe, J., Fairén, A., Feldmeyer, D., Fishell, G., Fregnac, Y., Freund, T. F., Gardner, D., Gardner, E. P., Goldberg, J. H., Helmstaedter, M., Hestrin, S., Karube, F., Kisvárday, Z. F., Lambolez, B., Lewis, D. A., Marin, O., Markram, H., Muñoz, A., Packer, A., Petersen, C. C. H., Rockland, K. S., Rossier, J., Rudy, B., Somogyi, P., Staiger, J. F., Tamas, G., Thomson, A. M., Toledo-Rodriguez, M., Wang, Y., West, D. C., and Yuste, R. (2008). Petilla terminology: nomenclature of features of GABAergic interneurons of the cerebral cortex. *Nature Reviews Neuroscience*, **9**(7), 557–568.

Bandler, R. C., Vitali, I., Delgado, R. N., Ho, M. C., Dvoretskova, E., Ibarra Molinas, J. S., Frazel, P. W., Mohammadkhani, M., Machold, R., Maedler, S., Liddelow, S. A., Nowakowski, T. J., Fishell, G., and Mayer, C. (2022). Single-cell delineation of lineage and genetic identity in the mouse brain. *Nature*, **601**, 404–409.

Bardes, A., Ponce, J., and LeCun, Y. (2022). VICReg: Variance-Invariance-Covariance Regularization for Self-Supervised Learning. In *Proceedings of the Tenth International Conference on Learning Representations*.

Bast, A. and Oberlaender, M. (2022). Ion channel distributions in cortical neurons are optimized for energy-efficient active dendritic computations. *bioRxiv preprint*. 2021.12.11.472235.

Bast, A., Guest, J. M., Fruengel, R., Narayanan, R. T., de Kock, C. P., and Oberlaender, M. (2023). Thalamus drives active dendritic computations in cortex. *bioRxiv preprint*. 2021.10.21.465325.

Bayraktar, T., Welker, E., Freund, T. F., Zilles, K., and Staiger, J. F. (2000). Neurons immunoreactive for vasoactive intestinal polypeptide in the rat primary somatosensory cortex: morphology and spatial relationship to barrel-related columns. *Journal of Comparative Neurology*, **420**(3), 291–304.

Beierlein, M., Gibson, J. R., and Connors, B. W. (2003). Two Dynamically Distinct Inhibitory Networks in Layer 4 of the Neocortex. *Journal of Neurophysiology*, **90**(5), 2987–3000.

Brodmann, K. (1909). *Vergleichende Lokalisationslehre Der Grosshirnrinde in Ihren Prinzipien Dargestellt Aufgrund Des Zellenbaues*. Johann Ambrosius Barth.

Carnevale, N. T. and Hines, M. L. (2006). *The NEURON Book*. Cambridge University Press.

Conn, A. R., Gould, N. I. M., and Toint, P. L. (1991). A Globally Convergent Augmented Lagrangian Algorithm for Optimization with General Constraints and Simple Bounds. *SIAM Journal on Numerical Analysis*, **28**(2), 545–575.

Conn, A. R., Gould, N. I. M., and Toint, P. L. (1997). A Globally Convergent Augmented Lagrangian Barrier Algorithm for Optimization with General Inequality Constraints and Simple Bounds. *Mathematics of Computation*, **66**(217), 261–288.

Connors, B. W. and Gutnick, M. J. (1990). Intrinsic firing patterns of diverse neocortical neurons. *Trends in Neurosciences*, **13**(3), 99–104.

Connors, B. W., Gutnick, M. J., and Prince, D. A. (1982). Electrophysiological properties of neocortical neurons in vitro. *Journal of Neurophysiology*, **48**(6), 1302–1320.

Cuntz, H., Forstner, F., Borst, A., and Häusser, M. (2010). One Rule to Grow Them All: A General Theory of Neuronal Branching and Its Practical Application. *PLOS Computational Biology*, **6**(8), e1000877.

d'Aspremont, A., El Ghaoui, L., Jordan, M. I., and Lanckriet, G. R. G. (2004). A direct formulation for sparse PCA using semidefinite programming. In *Advances in Neural Information Processing Systems*, volume 17.

DeFelipe, J., López-Cruz, P. L., Benavides-Piccione, R., Bielza, C., Larrañaga, P., Anderson, S., Burkhalter, A., Cauli, B., Fairén, A., Feldmeyer, D., Fishell, G., Fitzpatrick, D., Freund, T. F., González-Burgos, G., Hestrin, S., Hill, S., Hof, P. R., Huang, J., Jones, E. G., Kawaguchi, Y., Kisvárday, Z., Kubota, Y., Lewis, D. A., Marín, O., Markram, H., McBain, C. J., Meyer, H. S., Monyer,

H., Nelson, S. B., Rockland, K., Rossier, J., Rubenstein, J. L. R., Rudy, B., Scanziani, M., Shepherd, G. M., Sherwood, C. C., Staiger, J. F., Tamás, G., Thomson, A., Wang, Y., Yuste, R., and Ascoli, G. A. (2013). New insights into the classification and nomenclature of cortical GABAergic interneurons. *Nature Reviews Neuroscience*, **14**(3), 202–216.

Dercksen, V. J., Hege, H.-C., and Oberlaender, M. (2014). The Filament Editor: An Interactive Software Environment for Visualization, Proof-Editing and Analysis of 3D Neuron Morphology. *Neuroinformatics*, **12**, 325–339.

Egger, R., Narayanan, R. T., Helmstaedter, M., de Kock, C. P. J., and Oberlaender, M. (2012). 3D Reconstruction and Standardization of the Rat Vibrissal Cortex for Precise Registration of Single Neuron Morphology. *PLOS Computational Biology*, **8**(12), e1002837.

Egger, R., Dercksen, V. J., Udvary, D., Hege, H.-C., and Oberlaender, M. (2014). Generation of dense statistical connectomes from sparse morphological data. *Frontiers in Neuroanatomy*, **8**.

Egger, R., Schmitt, A. S., Wallace, D. J., Sakmann, B., Oberlaender, M., and Kerr, J. N. D. (2015). Robustness of sensory-evoked excitation is increased by inhibitory inputs to distal apical tuft dendrites. *Proceedings of the National Academy of Sciences of the United States of America*, **112**(45), 14072–14077.

Egger, R., Narayanan, R. T., Guest, J. M., Bast, A., Udvary, D., Messore, L. F., Das, S., Kock, C. P. D., and Oberlaender, M. (2020). Cortical output is gated by horizontally projecting neurons in the deep layers. *Neuron*, **105**(1), 122–137.

Emmenegger, V., Qi, G., Wang, H., and Feldmeyer, D. (2018). Morphological and Functional Characterization of Non-fast-Spiking GABAergic Interneurons in Layer 4 Microcircuitry of Rat Barrel Cortex. *Cerebral Cortex*, **28**(4), 1439–1457.

Erisir, A., Lau, D., Rudy, B., and Leonard, C. S. (1999). Function of Specific K+ Channels in Sustained High-Frequency Firing of Fast-Spiking Neocortical Interneurons. *Journal of Neurophysiology*, **82**(5), 2476–2489.

Feldmeyer, D., Egger, V., Lübke, J., and Sakmann, B. (1999). Reliable synaptic connections between pairs of excitatory layer 4 neurones within a single 'barrel' of developing rat somatosensory cortex. *Journal of Physiology*, **521**(1), 169–190.

Feldmeyer, D., Brecht, M., Helmchen, F., Petersen, C. C., Poulet, J. F., Staiger, J. F., Luhmann, H. J., and Schwarz, C. (2013). Barrel cortex function. *Progress in Neurobiology*, **103**, 3–27.

Feldmeyer, D., Qi, G., Emmenegger, V., and Staiger, J. F. (2018). Inhibitory Interneurons and their Circuit Motifs in the Many Layers of the Barrel Cortex. *Neuroscience*, **368**, 132–151.

Fishell, G. and Kepecs, A. (2020). Interneuron Types as Attractors and Controllers. *Annual Review of Neuroscience*, **43**, 1–30.

Fishell, G. and Rudy, B. (2011). Mechanisms of Inhibition within the Telencephalon: "Where the Wild Things Are". *Annual Review of Neuroscience*, **34**, 535–567.

Goldberg, D. E. (1989). *Genetic Algorithms in Search, Optimization, and Machine Learning*. Addison-Wesley Longman Publishing Co., Inc.

Golgi, C. (1885). *Sulla Fina Anatomia Degli Organi Centrali del Sistema Nervoso*. Reggio Emilia: S. Calderini e Figlio.

Golgi, C. (1903). *Opera Omnia*. Milan: Hoepli.

Gouwens, N. W., Sorensen, S. A., Berg, J., Lee, C., Jarsky, T., Ting, J., Sunkin, S. M., Feng, D., Anastassiou, C. A., Barkan, E., Bickley, K., Blesie, N., Braun, T., Brouner, K., Budzillo, A., Caldejon, S., Casper, T., Castelli, D., Chong, P., Crichton, K., Cuhaciyan, C., Daigle, T. L., Dalley, R., Dee, N., Desta, T., Ding, S.-L., Dingman, S., Doperalski, A., Dotson, N., Egdorf, T., Fisher, M., de Frates, R. A., Garren, E., Garwood, M., Gary, A., Gaudreault, N., Godfrey, K., Gorham, M., Gu, H., Habel, C., Hadley, K., Harrington, J., Harris, J. A., Henry, A., Hill, D., Josephsen, S., Kebede, S., Kim, L., Kroll, M., Lee, B., Lemon, T., Link, K. E., Liu, X., Long, B., Mann, R., McGraw, M., Mihalas, S., Mukora, A., Murphy, G. J., Ng, L., Ngo, K., Nguyen, T. N., Nicovich, P. R., Oldre, A., Park, D., Parry, S., Perkins, J., Potekhina, L., Reid, D., Robertson, M., Sandman, D., Schroedter, M., Slaughterbeck, C., Soler-Llavina, G., Sulc, J., Szafer, A., Tasic, B., Taskin, N., Teeter, C., Thatra, N., Tung, H., Wakeman, W., Williams, G., Young, R., Zhou, Z., Farrell, C., Peng, H., Hawrylycz, M. J., Lein, E., Ng, L., Arkhipov, A., Bernard, A., Phillips, J. W., Zeng, H., and Koch, C. (2019). Classification of electrophysiological and morphological neuron types in the mouse visual cortex. *Nature Neuroscience*, **22**(7), 1182–1195.

Gouwens, N. W., Sorensen, S. A., Baftizadeh, F., Budzillo, A., Lee, B. R., Jarsky, T., Alfiler, L., Baker, K., Barkan, E., Berry, K., Bertagnolli, D., Bickley, K., Bomben, J., Braun, T., Brouner, K., Casper, T., Crichton, K., Daigle, T. L., Dalley, R., de Frates, R. A., Dee, N., Desta, T., Lee, S. D., Dotson, N., Egdorf, T., Ellingwood, L., Enstrom, R., Esposito, L., Farrell, C., Feng, D., Fong, O., Gala, R., Gamlin, C., Gary, A., Glandon, A., Goldy, J., Gorham, M., Graybuck, L., Gu, H., Hadley, K., Hawrylycz, M. J., Henry, A. M., Hill, D. J., Hupp, M.,

Kebede, S., Kim, T. K., Kim, L., Kroll, M., Lee, C., Link, K. E., Mallory, M., Mann, R., Maxwell, M., McGraw, M., McMillen, D., Mukora, A., Ng, L., Ng, L., Ngo, K., Nicovich, P. R., Oldre, A., Park, D., Peng, H., Penn, O., Pham, T., Pom, A., Popović, Z., Potekhina, L., Rajanbabu, R., Ransford, S., Reid, D., Rimorin, C., Robertson, M., Ronellenfitch, K., Ruiz, A., Sandman, D., Smith, K., Sulc, J., Sunkin, S. M., Szafer, A., Tieu, M., Torkelson, A., Trinh, J., Tung, H., Wakeman, W., Ward, K., Williams, G., Zhou, Z., Ting, J. T., Arkhipov, A., Sümbül, U., Lein, E. S., Koch, C., Yao, Z., Tasic, B., Berg, J., Murphy, G. J., and Zeng, H. (2020). Integrated Morphoelectric and Transcriptomic Classification of Cortical GABAergic Cells. *Cell*, **183**(4), 935–953.

Gupta, A., Wang, Y., and Markram, H. (2000). Organizing principles for a diversity of gabaergic interneurons and synapses in the neocortex. *Science*, **287**(5451), 273–278.

Hamill, O. P., Marty, A., Neher, E., Sakmann, B., and Sigworth, F. J. (1981). Improved patch-clamp techniques for high-resolution current recording from cells and cell-free membrane patches. *Pflügers Archiv: European Journal of Physiology*, **391**(2), 85–100.

Hardcastle, K., Ganguli, S., and Giocomo, L. M. (2017). Cell types for our sense of location: where we are and where we are going. *Nature Neuroscience*, **20**(11), 1474–1482.

He, K., Chen, X., Xie, S., Li, Y., Dollár, P., and Girshick, R. (2022). Masked Autoencoders Are Scalable Vision Learners. In *Proceedings of the Thirty-Third IEEE/CVF Conference on Computer Vision and Pattern Recognition ()*.

Helmstaedter, M., Sakmann, B., and Feldmeyer, D. (2009a). Neuronal Correlates of Local, Lateral, and Translaminar Inhibition with Reference to Cortical Columns. *Cerebral Cortex*, **19**(4), 926–937.

Helmstaedter, M., Sakmann, B., and Feldmeyer, D. (2009b). The Relation between Dendritic Geometry, Electrical Excitability, and Axonal Projections of L2/3 Interneurons in Rat Barrel Cortex. *Cerebral Cortex*, **19**(4), 938–950.

Helmstaedter, M., Sakmann, B., and Feldmeyer, D. (2009c). L2/3 Interneuron Groups Defined by Multiparameter Analysis of Axonal Projection, Dendritic Geometry, and Electrical Excitability. *Cerebral Cortex*, **19**(4), 951–962.

Hennig, C. (2007). Cluster-wise assessment of cluster stability. *Computational Statistics and Data Analysis*, **52**, 258–271.

Horikawa, K. and Armstrong, W. E. (1988). A versatile means of intracellular labeling: injection of biocytin and its detection with avidin conjugates. *Journal of Neuroscience Methods*, **25**(1), 1–11.

Hu, J. S., Vogt, D., Sandberg, M., and Rubenstein, J. L. (2017). Cortical interneuron development: a tale of time and space. *Development*, **144**(21), 3867–3878.

Huang, Z. and Paul, A. (2019). The diversity of GABAergic neurons and neural communication elements. *Nature Reviews Neuroscience*, **20**(9), 563–572.

Jaccard, P. (1901). Distribution de la Flore Alpine dans le Bassin des Dranses. *Bulletin de la Société Vaudoise des Sciences Naturelles*, **37**(140), 241–272.

Kantorovich, L. V. (1942). On the translocation of masses. *Comptes Rendus (Doklady) de l'Academie des Sciences de l'URSS*, **37**(7–8).

Kawaguchi, Y. and Kubota, Y. (1997). GABAergic cell subtypes and their synaptic connections in rat frontal cortex. *Cerebral Cortex*, **7**(6), 476–486.

Kepecs, A. and Fishell, G. (2014). Interneuron cell types are fit to function. *Nature*, **505**, 318–326.

Koelbl, C., Helmstaedter, M., Lübke, J., and Feldmeyer, D. (2015). A Barrel-Related Interneuron in Layer 4 of Rat Somatosensory Cortex with a High Intrabarrel Connectivity. *Cerebral Cortex*, **25**(3), 713–725.

Kubota, Y., Hattori, R., and Yui, Y. (1994). Three distinct subpopulations of GABAergic neurons in rat frontal agranular cortex. *Brain Research*, **649**(1-2), 159–173.

Kwan, K. Y., Šestan, N., and Anton, E. S. (2012). Transcriptional co-regulation of neuronal migration and laminar identity in the neocortex. *Development*, **139**(9), 1535–1546.

Land, P. W. and Kandler, K. (2002). Somatotopic organization of rat thalamocortical slices. *Journal of Neuroscience Methods*, **119**(1), 15–21.

Landau, I. D., Egger, R., Dercksen, V. J., Oberlaender, M., and Sompolinsky, H. (2016). The Impact of Structural Heterogeneity on Excitation-Inhibition Balance in Cortical Networks. *Neuron*, **92**(5), 1106–1121.

Langfelder, P., Zhang, B., and Horvath, S. (2007). Defining clusters from a hierarchical cluster tree: the Dynamic Tree Cut package for R. *Bioinformatics*, **24**(5), 719–720.

Maeda, J. (2006). *The Laws of Simplicity*. MIT Press.

Mairal, J., Bach, F., Ponce, J., and Sapiro, G. (2010). Online Learning for Matrix Factorization and Sparse Coding. *Journal of Machine Learning Research*, **11**(2), 19–60.

Mao, X. and Staiger, J. F. (2024). Multimodal cortical neuronal cell type classification. *Pflügers Archiv - European Journal of Physiology*, **476**(5), 721–733.

Markram, H., Toledo-Rodriguez, M., Wang, Y., Gupta, A., Silberberg, G., and Wu, C. (2004). Interneurons of the neocortical inhibitory system. *Nature Reviews Neuroscience*, **5**(10), 793–807.

Markram, H., Muller, E., Ramaswamy, S., Reimann, M. W., Abdellah, M., Sanchez, C. A., Ailamaki, A., Alonso-Nanclares, L., Antille, N., Arsever, S., Kahou, G. A. A., Berger, T. K., Bilgili, A., Buncic, N., Chalimourda, A., Chindemi, G., Courcol, J.-D., Delalondre, F., Delattre, V., Druckmann, S., Dumusc, R., Dynes, J., Eilemann, S., Gal, E., Gevaert, M. E., Ghobril, J.-P., Gidon, A., Graham, J. W., Gupta, A., Haenel, V., Hay, E., Heinis, T., Hernando, J. B., Hines, M., Kanari, L., Keller, D., Kenyon, J., Khazen, G., Kim, Y., King, J. G., Kisvarday, Z., Kumbhar, P., Lasserre, S., Bé, J.-V. L., Magalhães, B. R., Merchán-Pérez, A., Meystre, J., Morrice, B. R., Muller, J., Muñoz-Céspedes, A., Muralidhar, S., Muthurasa, K., Nachbaur, D., Newton, T. H., Nolte, M., Ovcharenko, A., Palacios, J., Pastor, L., Perin, R., Ranjan, R., Riachi, I., Rodríguez, J.-R., Riquelme, J. L., Rössert, C., Sfyrakis, K., Shi, Y., Shillcock, J. C., Silberberg, G., Silva, R., Tauheed, F., Telefont, M., Toledo-Rodriguez, M., Tränkler, T., Geit, W. V., Díaz, J. V., Walker, R., Wang, Y., Zaninetta, S. M., DeFelipe, J., Hill, S. L., Segev, I., and Schürmann, F. (2015). Reconstruction and Simulation of Neocortical Microcircuitry. *Cell*, **163**(2), 456–492.

Martinotti, C. (1889). Contributo allo studio della corteccia cerebrale, ed all'origine centrale dei nervi. *Annali di Freniatria e Scienze Affini*, **1**, 14–381.

Marx, M. and Feldmeyer, D. (2013). Morphology and Physiology of Excitatory Neurons in Layer 6b of the Somatosensory Rat Barrel Cortex. *Cerebral Cortex*, **23**(12), 2803–2817.

McInnes, L., Healy, J., Saul, N., and Großberger, L. (2018). UMAP: Uniform Manifold Approximation and Projection. *Journal of Open Source Software*, **3**(29), 861.

Messore, F. (2024). *Organization principles of thalamocortical input onto deep-layer inhibitory neurons of the barrel cortex*. Ph.D. thesis, Rheinische Friedrich-Wilhelms-Universität Bonn.

Meyer, H. S., Wimmer, V. C., Oberlaender, M., de Kock, C. P., Sakmann, B., and Helmstaedter, M. (2010). Number and Laminar Distribution of Neurons in a Thalamocortical Projection Column of Rat Vibrissal Cortex. *Cerebral Cortex*, **20**(10), 2277–2286.

Meyer, H. S., Schwarz, D., Wimmer, V. C., Schmitt, A. C., Kerr, J. N. D., Sakmann, B., and Helmstaedter, M. (2011). Inhibitory interneurons in a cortical column form hot zones of inhibition in layers 2 and 5A. *Proceedings of the National Academy of Sciences of the United States of America*, **108**(40), 16807–16812.

Meyer, H. S., Egger, R., Guest, J. M., Foerster, R., Reissl, S., and Oberlaender, M. (2013). Cellular organization of cortical barrel columns is whisker-specific. *Proceedings of the National Academy of Sciences of the United States of America*, **110**(47), 19113–19118.

Monge, G. (1781). Mémoire sur la théorie des déblais et des remblais. *Histoire de l'Académie Royale des Sciences*, pages 666–704.

Muzellec, B., Nock, R., Patrini, G., and Nielsen, F. (2017). Tsallis Regularized Optimal Transport and Ecological Inference. In *Proceedings of the Thirty-First AAAI Conference on Artificial Intelligence*.

Narayanan, R. T., Egger, R., Johnson, A. S., Mansvelder, H. D., Sakmann, B., de Kock, C. P. J., and Oberlaender, M. (2015). Beyond Columnar Organization: Cell Type- and Target Layer-Specific Principles of Horizontal Axon Projection Patterns in Rat Vibrissal Cortex. *Cerebral Cortex*, **25**(11), 4450–4468.

Narayanan, R. T., Udvary, D., and Oberlaender, M. (2017). Cell Type-Specific Structural Organization of the Six Layers in Rat Barrel Cortex. *Frontiers in Neuroanatomy*, **11**.

Neher, E. and Sakmann, B. (1976). Single-channel currents recorded from membrane of denervated frog muscle fibres. *Nature*, **260**, 799–802.

Nigro, M. J., Hashikawa-Yamasaki, Y., and Rudy, B. (2018). Diversity and Connectivity of Layer 5 Somatostatin-Expressing Interneurons in the Mouse Barrel Cortex. *Journal of Neuroscience*, **38**(7), 1622–1633.

Oberlaender, M. (2019). Neuronal Morphology and Its Significance. In W. Singer, T. J. Sejnowski, and P. Rakic, editors, *The Neocortex*, pages 125–138. MIT Press.

Oberlaender, M. (2023). Anatomical and Physiological Basis for the Flow of Thalamocortical Inputs across the Layers of the Primary Sensory Cortex. In W. M. Usrey and S. M. Sherman, editors, *The Cerebral Cortex and Thalamus*, pages 55–64. Oxford University Press.

Oberlaender, M., Dercksen, V. J., Egger, R., Gensel, M., Sakmann, B., and Hege, H.-C. (2009). Automated three-dimensional detection and counting of neuron somata. *Journal of Neuroscience Methods*, **180**(1), 147–160.

Oberlaender, M., Boudewijns, Z. S. R. M., Kleele, T., Mansvelder, H. D., Sakmann, B., and de Kock, C. P. J. (2011). Three-dimensional axon morphologies of individual layer 5 neurons indicate cell type-specific intracortical pathways for whisker motion and touch. *Proceedings of the National Academy of Sciences of the United States of America*, **108**(10), 4188–4193.

Oberlaender, M., de Kock, C. P. J., Bruno, R. M., Ramirez, A., Meyer, H. S., Dercksen, V. J., Helmstaedter, M., and Sakmann, B. (2012). Cell Type–Specific Three-Dimensional Structure of Thalamocortical Circuits in a Column of Rat Vibrissal Cortex. *Cerebral Cortex*, **22**(10), 2375–2391.

Pedregosa, F., Varoquaux, G., Gramfort, A., Michel, V., Thirion, B., Grisel, O., Blondel, M., Prettenhofer, P., Weiss, R., Dubourg, V., Vanderplas, J., Passos, A., Cournapeau, D., Brucher, M., Perrot, M., and Duchesnay, E. (2011). Scikit-learn: Machine Learning in Python. *Journal of Machine Learning Research*, **12**, 2825–2830.

Petersen, C. C. H. (2019). Sensorimotor processing in the rodent barrel cortex. *Nature Reviews Neuroscience*, **20**(9), 533–546.

Pouchelon, G., Dwivedi, D., Bollmann, Y., Agba, C. K., Xu, Q., Mirow, A. M., Kim, S., Qiu, Y., Sevier, E., Ritola, K. D., Cossart, R., and Fishell, G. (2021). The organization and development of cortical interneuron presynaptic circuits are area specific. *Cell Reports*, **37**(6), 109993.

Prönneke, A., Scheuer, B., Wagener, R. J., Möck, M., Witte, M., and Staiger, J. F. (2015). Characterizing VIP neurons in the barrel cortex of VIPcre/tdTomato mice reveals layer-specific differences. *Cerebral Cortex*, **25**(12), 4854–4868.

Ramón y Cajal, S. (1899). Estudios sobre la corteza cerebral humana II: Estructura de la corteza motriz del hombre y mamíferos superiores. *Rev. Trimest. Microgr.*, **4**, 117–200.

Ramón y Cajal, S. (1903). Sobre un sencillo método de impregnación de las fibrillas interiores del protoplasma nervioso. *Arch. Latinos Med. Biol.*, **1**, 3–8.

Ramón y Cajal, S. (1909). *Histologie du Système Nerveux de l'homme et Des Vertébrés*. Paris: Maloine.

Roux, L. and Buzsáki, G. (2015). Tasks for inhibitory interneurons in intact brain circuits. *Neuropharmacology*, **88**, 10–23.

Rudy, B., Fishell, G., Lee, S., and Hjerling-Leffler, J. (2011). Three groups of interneurons account for nearly 100% of neocortical GABAergic neurons. *Developmental Neurobiology*, **71**(1), 45–61.

Sakmann, B. (1992). Nobel Lecture: elementary steps in synaptic transmission revealed by currents through single ion channels. In T. Frängsmyr, editor, *Les Prix Nobel 1991*, pages 137–169. Almqvist & Wiksell, Stockholm, Sweden.

Sakmann, B. (2017). From single cells and single columns to cortical networks: dendritic excitability, coincidence detection and synaptic transmission in brain slices and brains. *Experimental Physiology*, **102**(5), 489–521.

Scorcioni, R., Polavaram, S., and Ascoli, G. A. (2008). L-Measure: a web-accessible tool for the analysis, comparison and search of digital reconstructions of neuronal morphologies. *Nature Protocols*, **3**(5), 866–876.

Scrucca, L., Fop, M., Murphy, T. B., and Raftery, A. E. (2016). mclust 5: clustering, classification and density estimation using Gaussian finite mixture models. *The R Journal*, **8**(1), 205–233.

Sjöstrand, K., Clemmensen, L. H., Larsen, R., Einarsson, G., and Ersbøll, B. (2018). SpaSM: A MATLAB Toolbox for Sparse Statistical Modeling. *Journal of Statistical Software*, **84**(10), 1–37.

Somogyi, P. (1977). A specific 'axo-axonal' interneuron in the visual cortex of the rat. *Brain Research*, **136**(2), 345–350.

Somogyi, P., Freund, T. F., and Cowey, A. (1982). The axo-axonic interneuron in the cerebral cortex of the rat, cat and monkey. *Neuroscience*, **7**(11), 2577–2607.

Swanson, L. W. and Lichtman, J. W. (2016). From Cajal to Connectome and Beyond. *Annual Review of Neuroscience*, **39**, 197–216.

Szentágothai, J. and Arbib, M. A. (1974). Conceptual models of neural organization. *Neurosciences Research Program Bulletin*, **12**(3), 305–510.

Takahashi, N., Ebner, C., Sigl-Glöckner, J., Moberg, S., Nierwetberg, S., and Larkum, M. E. (2020). Active dendritic currents gate descending cortical outputs in perception. *Nature Neuroscience*, **23**(10), 1277–1285.

Tamás, G., Lorincz, A., Simon, A., and Szabadics, J. (2003). Identified sources and targets of slow inhibition in the neocortex. *Science*, **299**(5614), 1902–1905.

Tasic, B., Menon, V., Nguyen, T. N., Kim, T. K., Jarsky, T., Yao, Z., Levi, B., Gray, L. T., Sorensen, S. A., lbeare, T., rtagnolli, D., Goldy, J., Shapovalova, N., Parry,

S., Lee, C., Smith, K., Bernard, A., Madisen, L., Sunkin, S. M., Hawrylycz, M., Koch, C., and Zeng, H. (2016). Adult mouse cortical cell taxonomy revealed by single cell transcriptomics. *Nature Neuroscience*, **19**(2), 335–346.

Tasic, B., Yao, Z., Graybuck, L. T., mith, K. A., Nguyen, T. N., Bertagnolli, D., Goldy, J., Garren, E., Economo, M. N., Viswanathan, S., Penn, O., Bakken, T., Menon, V., Miller, J., Fong, O., Hirokawa, K. E., Lathia, K., Rimorin, C., Tieu, M., Larsen, R., Casper, T., Barkan, E., Kroll, M., Parry, S., Shapovalova, N. V., Hirschstein, D., Pendergraft, J., Sullivan, H. A., Kim, T. K., Szafer, A., Dee, N., oblewski, P., Wickersham, I., Cetin, A., Harris, J. A., Levi, B. P., Sunkin, S. M., Madisen, L., Daigle, T. L., Looger, L., Bernard, A., Phillips, J., Lein, E., Hawrylycz, M., Svoboda, K., Jones, A. R., Koch, C., and Zeng, H. (2018). Shared and distinct transcriptomic cell types across neocortical areas. *Nature*, **563**, 72–78.

Tibshirani, R. (1996). Regression Shrinkage and Selection via the Lasso. *Journal of the Royal Statistical Society. Series B (Methodological)*, **58**(1), 267–288.

Tremblay, R., Lee, S., and Rudy, B. (2016). GABAergic Interneurons in the Neocortex: From Cellular Properties to Circuits. *Neuron*, **91**(2), 260–292.

Udvary, D. (2020). *Three-dimensional reverse engineering of neuronal microcircuits: The barrel cortex in silico*. Ph.D. thesis, Eberhard Karls Universität Tübingen.

Udvary, D., Harth, P., Macke, J. H., Hege, H.-C., de Kock, C. P., Sakmann, B., and Oberlaender, M. (2022). The impact of neuron morphology on cortical network architecture. *Cell Reports*, **39**(2), 110677.

Villani, C. (2003). *Topics in Optimal Transportation*. Graduate Studies in Mathematics Series. American Mathematical Society.

Xu, X., Roby, K. D., and Callaway, E. M. (2010). Immunochemical characterization of inhibitory mouse cortical neurons: Three chemically distinct classes of inhibitory cells. *Journal of Comparative Neurology*, **518**(3), 389–404.

Yuste, R., Hawrylycz, M., Aalling, N., Aguilar-Valles, A., Arendt, D., Armañanzas, R., Ascoli, G. A., Bielza, C., Bokharaie, V., Bergmann, T. B., Bystron, I., Capogna, M., Chang, Y., Clemens, A., de Kock, C. P. J., DeFelipe, J., Dos Santos, S. E., Dunville, K., Feldmeyer, D., Fiáth, R., Fishell, G. J., Foggetti, A., Gao, X., Ghaderi, P., Goriounova, N. A., Güntürkün, O., Hagihara, K., Hall, V. J., Helmstaedter, M., Herculano-Houzel, S., Hilscher, M. M., Hirase, H., Hjerling-Leffler, J., Hodge, R., Huang, J., Huda, R., Khodosevich, K., Kiehn, O., Koch, H., Kuebler, E. S., Kühnemund, M., Larrañaga, P., Lelieveldt, B., Louth, E. L.,

Lui, J. H., Mansvelder, H. D., Marin, O., Martinez-Trujillo, J., Chameh, H. M., Mohapatra, A. N., Munguba, H., Nedergaard, M., Němec, P., Ofer, N., Pfisterer, U. G., Pontes, S., Redmond, W., Rossier, J., Sanes, J. R., Scheuermann, R. H., Serrano-Saiz, E., Staiger, J. F., Somogyi, P., Tamás, G., Tolias, A. S., Tosches, M. A., García, M. T., Wozny, C., Wuttke, T. V., Liu, Y., Yuan, J., Zeng, H., and Lein, E. (2020). A community-based transcriptomics classification and nomenclature of neocortical cell types. *Nature Neuroscience*, **23**(12), 1456–1468.

Zeng, H. (2022). What is a cell type and how to define it? *Cell*, **185**(15), 2739–2755.

Zou, H., Hastie, T., and Tibshirani, R. (2006). Sparse Principal Component Analysis. *Journal of Computational and Graphical Statistics*, **15**(2), 265–286.